UNIVERSITA' DEL SALENTO

DIPARTIMENTO DI MATEMATICA E FISICA *"Ennio De Giorgi"*
CORSO DI DOTTORATO IN FISICA E NANOSCIENZE XXXV CICLO

The ultralight drift chambers: from MEG II to the future colliders

Tutors:
Prof. Marco Panareo, Dott. Giovanni Francesco Tassielli
Tutors esterni:
Prof. Nicola de Filippis, Prof. Francesco Grancagnolo

Dottoranda:
Federica Cuna

ANNO ACCADEMICO 2019/2020

To my family,
for the endless love, support and encouragement

«No one you have been and no place you have gone ever leaves you.
The new parts of you simply jump in the car and go along for the rest of the ride.
The success of your journey and your destination all depend on who's driving»
Bruce Springsteen

Contents

Introduction

Ultralight drift chambers are a new generation of gas detector which aim to provide competitive performances about the tracking and the particle identification.
To pursue this goal, this chambers sum up hardware and software innovations.
Custom mechanical designs are necessary to ensure high transparency, which means reducing the impact of the multiple coulomb scattering to the track reconstruction while ensuring the mechanical stability of the whole structure. High innovative technological solutions combined with the cluster counting/timing technique will ensure high competitive tracking performances.
An example of the ultralight drift chamber is the tracking detector of the MEGII experiment at PSI, in Zurich, which is described in this thesis.
Thank to extremely successful operation of this chamber, the tracking detector proposed for IDEA detector at future collider consists of an ultralight drift chamber.
This thesis describes in details the performances, the techniques and all the elements connected to the capabilities of the ultralight drift chambers from the one operated at MEGII up to the future one of the IDEA detector, which are the main focus of my research project.
Indeed I worked on the study of the MEG II drift chambers constants, by developing a monitoring drift chamber which allows to measure variations of drift velocity in few minutes at per mil level. This is an important tools to ensure the accuracy of the positron track reconstruction, since any contamination or impurities in the gas mixture used in the drift chamber inevitably affect the tracking performances. The project of the monitoring drift chamber is quite challenging: the first step consists of a detailed simulation phase to analyze the electric field configuration and the drift velocity measurement sensitivity. The second phase consists of the mechanical design and the construction of the chamber. The third phase, which is under development, is the test of the chamber.
Another important item which I developed for the PhD project is the simulation of the new time to distance relations (txy tables) for the MEG II drift chamber. For particle tracking, the drift time-space relations play a key role, since any uncertainty or misknowledge of the drift space-time relations will affect the tracking performances. The simulation of the txy tables, made by using the Garfield++ toolkit, requires a great effort and consists of many steps, from the reconstruction of the geometrical sector of the chamber to the study of the txy tables effect on the tracking performances.
The second part of my research project deals with drift chambers for future colliders, by exploiting the expertise gained thanks to the MEG II drift chamber. In details, I developed a new mechanical design which maximizes:

- the transparency in terms of radiation length,
- the mechanical stability by reducing to acceptable limits the deformations of the end-

plates under the total load of the wires.

This design, developed in the contest of the CMD3 experiment, will be useful to the development of the new IDEA drift chamber.
In the end, I performed an intensive and detailed study of the cluster counting/timing techniques, where great expectations have been placed in order to deeply improve the particle identification capabilities.
By starting from some analytical study, I performed a simulations campaign, by using Garfield++, to carefully study the ionization process in Helium/Isobutane gas mixture. Then I developed three version of an algorithm which can easily reproduce the number of clusters and the cluster size in Geant4. Indeed besides being a great and powerful tool to study a full scale detector, Geant4 cannot reproduce the sensible element of the drift chamber (the drift cells). Then to validate the simulations results and ascertain some questions arisen from them, two beam tests at CERN/H8 have been performed: I took part in the experimental setup development, in the data collection at CERN and in the data analysis.
The preliminary results obtained from the analysis of the huge amount of the collected data are in agreement with what expected from the physics of the process.
The thesis is structured as follows:

- chapter1 describes briefly the phenomenological panorama of MEGII and future collider experiments,
- chapter 2 summarizes the basic concept of the gaseous detector, with a particular focus on the drift chambers,
- chapter 3 describes the MEG and MEGII experiments, highlighting the main improvements between the old and the new sub-detectors,
- chapter 4 deals with the MEGII drift chamber constants, by describing the construction of a drift velocity monitoring chamber and the time-to-distance relations,
- chapter 5 describes in details the implementation of the new set of time-to-distance relations and the improvement on the MEGII tracking performances,
- chapter 6 describes the IDEA detector and the development of the mechanical design for its ultralight drift chamber in the contest of the CMD3 and SCTF experiment,
- chapter 7 deals with the detailed analysis of the cluster counting technique for the improvement of the particle identification capabilities: it reports the simulations studies and the description of two beam tests performed at CERN/H8 to prove the expected improvement of this technique.

Chapter 1

The Standard Model and beyond

Everything in the Universe origins from few basic building blocks called *fundamental particles*, governed by four fundamental forces. The Standard Model (SM) describes the visible matter in the Universe and three of the four forces between matter: the **strong interaction** which reflects the invariance under the local SU(3) colour gauge group, the **electromagnetic and weak interactions** which are described by a Lagrangian that is invariant under local weak isospin and hypercharge gauge transformation, described using the $SU(2) \otimes U(1)$ group [1]. Even though the Standard Model is currently the best description of the subatomic world, it cannot explain the complete picture: a lot of important questions remain unanswered. These missing peaces in the Standard Model puzzle can be divided in two categories:

- *theoretical*
  - gravitation is not taken into account (that is the fourth of the four fundamental forces);
  - hierarchy problem of the Higgs scalar mass and its loop divergence [2];
  - the great number of free parameters of the theory that account for the observed masses and mixing of quarks and leptons;
- *observational*
  - the Dark Matter (DM) of non-baryonic nature and the baryon (matter-antimatter) asymmetry in the universe [3];
  - neutrino mixing and neutrino masses can be ad hoc included, but there is no hint concerning the mass difference with respect to other fermions [4];
  - cosmological problems related with inflation, which is, by definition, a period of superluminal expansion in the very early universe [5].

1.1 The Standard Model: a brief overview

In a nutshell, the Standard Model is the description of the building blocks of matter (quarks and leptons) and their interactions (strong, weak and electromagnetic interactions) in terms of certain symmetries, named *gauge symmetries*. A gauge theory is one that possesses invariance under a set of local transformations i.e. transformations whose parameters are space-time dependent.

The matter fields are organized in families. The interactions are described in terms of vector bosons, which mediate them. A scalar field, the Higgs boson, is added to generate the vector-boson and fermion masses. The SM sums up two disjoint theories: the Quantum Cromo–Dynamics (QCD) [6] that describes the strong interactions between quarks and gluons and the Glashow–Salam–Weinberg electroweak theory [7], [8].
It is a renormalizable theory based on the gauge symmetry group $G = SU(3)_C \otimes SU(2)_L^{weak} \otimes U(1)_Y^{weak}$, where $SU(3)_C$ is related to the color quantum number, $SU(2)_L^{weak}$ is generated by the weak isospin operators $\overrightarrow{T}$ and $U(1)_Y^{weak}$ is generated by the weak hypercharge operator Y [9].
The components of matter are fermions, which can be distinguished in leptons and quarks, as shown in Figure 1.1, where the gauge bosons are also listed.

Figure 1.1: Standard Model particles: quarks, leptons, gauge bosons and Higgs.

The two groups of fermions contain different flavours or families, in each family there is a weak isospin doublet with left helicity, two weak isospin singlet with right helicity for the quarks and one weak isospin singlet with right helicity for the leptons, in the assumption of massless neutrinos. Quarks exist in three different colors (strong charge) for each flavour family [10].
The mediators of the electroweak and strong forces are vector bosons: an interaction between two fermions can be described by the exchange of one of these bosons [10].
The gluons are eight massless vector bosons that couple to quarks of different color but same family according to the symmetry structure of $SU(3)_C$ (defined by the Gell–Mann matrices, generators of the group) with strength g_s, the strong coupling constant. The non-abelian gauge structure $SU(3)_C$ implies that three and four point self-interactions among gluons are allowed and actually observed experimentally [10].
The electroweak theory is based on the gauge group $SU(2)_L \otimes U(1)_Y$, where the four physical vector bosons, $\gamma, Z_0, W^{\pm}$, correspond to the linear combinations of the fields (W^i and B) associated with the gauge generators, the Pauli matrices for $SU(2)_L$ and the identity for $U(1)_Y$. The strength of the coupling of each fermion doublet or singlet to the bosons depends on g, the gauge coupling constant and θ_W the weak angle, in addition to the gauge quantum number, isospin and hypercharge [10].

The Higgs particle is a scalar boson necessary in the theory since it introduces mass terms for the other particles without spoiling the invariance and renormalizability of the theory [10, 11, 12, 13, 14].

1.2 Beyond the standard model

In spite of the excellent agreement of the SM with many precision strong and electroweak measurements and although it is a mathematically consistent renormalizable field theory, theoretical and experimental considerations make clear that it is incomplete. Therefore the SM is not believed to be an exhaustive theory of elementary particles but, rather, an effective low energy approximation of some more general theory.
The commonly agreed choice of fermion representation under a certain group (such as organizing left fermions into doublets) is due only to fit experimental observations. Moreover, it is not clear why exactly three quark families exist and if there could be more of them.
In the SM, the parameters of the Higgs potential are arbitrary and unrelated to other energy scales, yet quantum corrections to the Higgs mass m_H, induced by loop diagrams, give contributions of order $\delta m_H^2 \sim \Lambda$, where Λ is the cut-off energy of the theory, making Λ as the natural scale for the Higgs boson mass. This creates the problem of naturalness and stability of the Fermi scale because an extreme fine-tuning of the parameters to every order in perturbation theory is necessary to keep m_H at the Fermi scale [15].
The force of gravity is not described by the SM, because general relativity was non conceived to be a renormalizable theory.
The SM can not explain the Dark Matter (DM) of non-baryonic nature and the barion (matter-antimatter) asymmetry in the universe.
Possible answers to these questions are usually found in the alternative theories like SUperSYmmetric Models (SUSY) [16, 17, 18], Grand Unified Theory (GUT) [19, 20, 21], Extra–Dimensions [22] and String Theories [23], which included the SM as a low–energy limit.

1.3 Flavor physics

Flavor physics represents one of the most interesting and, at the same time, less understood sector of the Standard Theory. On the one hand, the peculiar pattern of quarks and lepton masses, and their mixing angles, may be the clue to some new dynamics occurring at high-energy scales. On the other hand, the strong suppression of flavour-changing neutral-current processes, predicted by the Standard Theory and confirmed by experiments, represents a serious challenge to extend the theory.
The term flavour is used to characterize the different copies of fields with the same spin and gauge quantum numbers, and flavour physics refers to the study of the interactions that distinguish between these copies.
In the SM lepton flavour violation is forbidden, but the presence of a lepton-flavour violating signal, other than neutrino oscillation, can really indicate the existence of new physics beyond the Standard Model. In Table 1.1 the upper limits of various lepton-flavour violating processes are listed.

Reaction	Present limits	C.L.	Year	Reference
$\mu^+ \longrightarrow e^+\gamma$	$< 4.2 \times 10^-13$	90%	2016	[24]
$\mu^+ \longrightarrow eee$	$< 1.0 \times 10^-12$	90%	1988	[25]
$\mu^- Ti \longrightarrow e^- Ti$	$< 6.1 \times 10^-13$	90%	1998	[26]
$\mu^+ e^- \longrightarrow \mu^- e^+$	$< 8.3 \times 10^-11$	90%	1999	[27]
$\tau \longrightarrow e\gamma$	$< 3.3 \times 10^-8$	90%	2010	[28]
$\tau \longrightarrow \mu\gamma$	$< 4.4 \times 10^-8$	90%	2010	[28]
$\tau \longrightarrow \mu\mu\mu$	$< 2.1 \times 10^-8$	90%	2010	[29]
$\tau \longrightarrow eee$	$< 2.7 \times 10^-8$	90%	2010	[29]
$\pi^0 \longrightarrow \mu e$	$< 3.6 \times 10^-10$	90%	2008	[30]
$K_L^0 \longrightarrow \mu e$	4.7×10^-12	90%	1998	[31]
$K^+ \longrightarrow \pi^+\mu^+e^-$	$< 1.3 \times 10^{-11}$	90%	2005	[32]
$K_L^0 \longrightarrow \pi^0\mu^+e^-$	$< 7.6 \times 10^{-11}$	90%	2008	[30]
$Z^0 \longrightarrow \mu e$	$< 7.5 \times 10^{-7}$	95%	2014	[33]
$Z^0 \longrightarrow \tau e$	$< 9.8 \times 10^{-6}$	95%	1995	[34]
$Z^0 \longrightarrow \tau\mu$	$< 1.2 \times 10^{-5}$	95%	1997	[35]

Table 1.1: Limits for the branching ratio of the lepton-flavour violating processes involving muons, taus, pions, kaons and Z bosons. For the muon capture processes the limit of the relative probability with respect to the SM predicted processes is given [36].

1.4 The lepton flavour violation

The flavour sector of the Standard Model, which means the fermion masses and the mixing among different generations, takes origin from the Yukawa couplings of the fermion field with the Higgs field ϕ, which is:

$$\mathcal{L}_{Yukawa} = -(Y_u)_{ij}\bar{Q}_{Li}u_{Rj}\tilde{\phi} + (Y_d)_{ij}\bar{Q}_{Li}d_{Rj}\phi + (Y_e)_{ij}\bar{L}_{Li}e_{Rj}\phi + h.c. \tag{1.1}$$

where i,j run over all the three families and Y_f are 3×3 complex matrices.
The fields are defined as: the left-handed (LH) quark doublets $Q_L^T = (u_l\ d_l)$; the right-handed (RH) up and down quarks u_R, d_R; the LH lepton doublets $L_L^T = (\nu_l\ e_L)$; the RH lepton e_R; the Higgs field ϕ_R. Fermion mass terms arises from the breaking electroweak symmetry $SU(2)_L \otimes U(1)_Y$ by the vacuum expectation value of the Higgs field, such that:

$$m_f = \frac{v}{\sqrt{2}}Y_f \tag{1.2}$$

In the original formulation of the Standard Model, the Lagrangian of Eq. 1.1 does not give rise to mass terms for the neutrinos, which are thus exactly massless. The Yukawa matrices and thus the fermion mass matrices can be diagonalised by unitary rotations of the fields, as follows:

$$Y_f = V_f\hat{Y}_f W_f^+ \tag{1.3}$$

where $\hat{Y}_f$ are the diagonal Yukawa matrices and $f = u, d, e$. The matrices V_f and W_f are unitary, so that, by applying these transformation, the kinetic terms and the neutral current interactions are not modified, such as the fermion couplings to the photon and the Z bosons, which then result flavour conserving. In the same way, the fermion couplings to the physical

Higgs are proportional to the mass matrix, so that they can be diagonalized in the same basis and no flavour violation is induced in the interactions with the Higgs either [36]:

$$\mathcal{L}_{h\bar{f}f} = -\frac{m_f}{v}\bar{f}_L f_R h + h.c. \tag{1.4}$$

On the other hand, the rotations in the Eq. (1.3) do induce flavour violation in the charged-current interactions with the W bosons:

$$\mathcal{L}_{cc} = \frac{g}{\sqrt{(2)}}(\bar{u}_L\gamma^\mu(V_u^+V_d)d_L + \bar{\nu}_L\gamma^\mu(V_\nu^+V_e)e_L)W_\mu^+ + h.c. \tag{1.5}$$

Flavor violation in quark sector comes from the fact that the diagonalization of Y_u and Y_d requires that $V_u \neq V_d$. This misalignment gives rise to the flavour-changing transitions controlled by the Cabibbo-Kobayashi-Maskawa (CKM) matrix [37, 38]: $V_{CKM} \equiv V_u^+V_d$, whose elements represent how likely a quark from a specific family is expected to turn into a different quark of a possibly different family.

In the lepton sector, since SM neutrinos are massless, the mass matrix is fully diagonalized by an unitary transformation for L_L and e_R. In the lepton sector of the original Standard Model with massless neutrinos, since no other term in the Lagrangian involves the lepton doublets, $V_\nu = V_e$ can be chosen and the leptonic flavour is exactly conserved [36].

The Lagrangian in Eq. (1.1) is invariant under three independent global $U(1)$ rotations associated to each lepton family implying three conserved charged: the lepton family numbers L_e, L_μ, L_τ.

In other words, in the SM the lepton numbers are conserved because of the minimality of the construction, which also implies that neutrinos are massless. In fact, the matrix of the lepton Yukawa couplings Y_e defines a single direction in the space of leptonic flavour. Hence, by using the freedom of rotating LH and RH lepton fields, the matrix can be made diagonal without inducing flavour-changing effects in other sectors of the theory. This is in contrast to the quark sector where there are two different Yukawa matrices, Y_u and Y_d, both involving Q_L, such that they can not be simultaneously diagonalised in the same basis [36].

However, flavour transitions between neutral leptons have been observed in the phenomenon of neutrino oscillations by several experiments! Lepton flavour oscillations on neutrino side implies that neutrinos have mass, which brings to a non diagonal unitary mixing matrix U_{PNMS} Pontecorvo-Maki-Nakagawa-Sakata [39, 40], between mass eigenstates and flavour eigenstates:

$$\nu_l = \sum_{i=1}^{3}(U_{PMNS})_{l_i}\nu_i \tag{1.6}$$

where $l = e, \mu, \tau$ are the flavour eigenstates and $i = 1, 2, 3$ are the mass eigenstates.

The neutrino oscillations imply the non conservation of the lepton flavour number, due to the presence in the SM Lagrangian of other terms to include ν mass which involves the lepton fields. So that it can be assumed also that lepton flavour is not conserved also in transitions involving charged leptons, even though the SM contribution due to neutrino mixing is negligible.

1.5 Charged lepton flavour violation

The Charged Lepton Flavour Violation (cLFV) searches are extremely tempting because of the possibility to carry out clean measurements which are at the same time free of theoretical

background. Indeed, in the case of direct observation they could prove the existence of physics beyond the standard model, but even in the case of non observation they establish strong limits for the development of new theories. On the other hand, such searches are difficult to be carried out at general-purpose machines and detectors, thus dedicated detectors and even dedicated accelerators or storage rings have to be exploited or designed for the future.
A lot of experiments have been performed in search of hints of new Physics, by exploring the evidence of cLFV. Here some examples:

- the MEG and its upgrade, MEGII, experiment at PSI;
- Mu3e experiment at PSI;
- Mu2e at Fermilab, COMET at J-PARC, for muon to electron conversion;
- SuperKEKB for the τ decays.

1.5.1 LFV at high energy colliders

The cLFV signature could be observed at LHC if supersymmetric particle were discovered. Indeed, according to SUSY model, they generate LFV coupling in slepton mass matrix. So if sleptons are light enough to be produced in pairs, then different lepton flavours will show up in decay chains like $l^+l^- \longrightarrow l^+l^-\chi^0\chi^0$.
New particles could be also reconstructed from resonance peaks if they have lepton-violating tree couplings ($H \longrightarrow ll'$ or $Z \longrightarrow ll'$). Due to the existing bounds on flavour changing processes, these LFV decays are small and difficult to detect above the large background from WW-production with subsequent leptonic decays. However, with high enough luminosity LHC can go beyond the LEP bounds on LFV Z decays.
Finally, future e^+e^- colliders could give an important improve to this research, as it will be discussed in section 1.6.

1.5.2 Tau sector

Search for charged lepton flavour violation in decays involving taus is very promising. Indeed, thanks to its large mass (around 1777 MeV [41]), many flavour violating channels are open: besides $\tau \longrightarrow \mu\gamma$, $\tau \longrightarrow e\gamma$, $\tau \longrightarrow 3l$ ($l = e, \mu,$), there is a number of channels involving hadrons in the final state, like $\tau \longrightarrow l\pi^0$ or $\tau \longrightarrow l\pi^+\pi-$, which are characterized by the presence of an energetic lepton and other charged or neutral particles with a topology which is more or less easy to identify.
The BR for LFV in the τ channel is predicted to be larger than the one in μ channel by a power p, which depends on the model used to describes the LFV process, of the lepton mass ratio: $(\frac{m_\tau}{m_\mu})^p$ [42, 43].
In Figure 1.2 the limits on cLFV tau decays set by CLEO, BaBar and Belle are reported, together with some recent limits posed by ATLAS and LHCb on selected decay channels.

1.5.3 Muon sector

The starting point for LFV decays searching and the first limit in the muon sector was set by Pontecorvo and Hincks in 1948 [45]: $BR(\mu \longrightarrow e\gamma) \leq 10\%$.
The ordinary muon decays are well known and described in [41, 46, 47], so the rare ones will

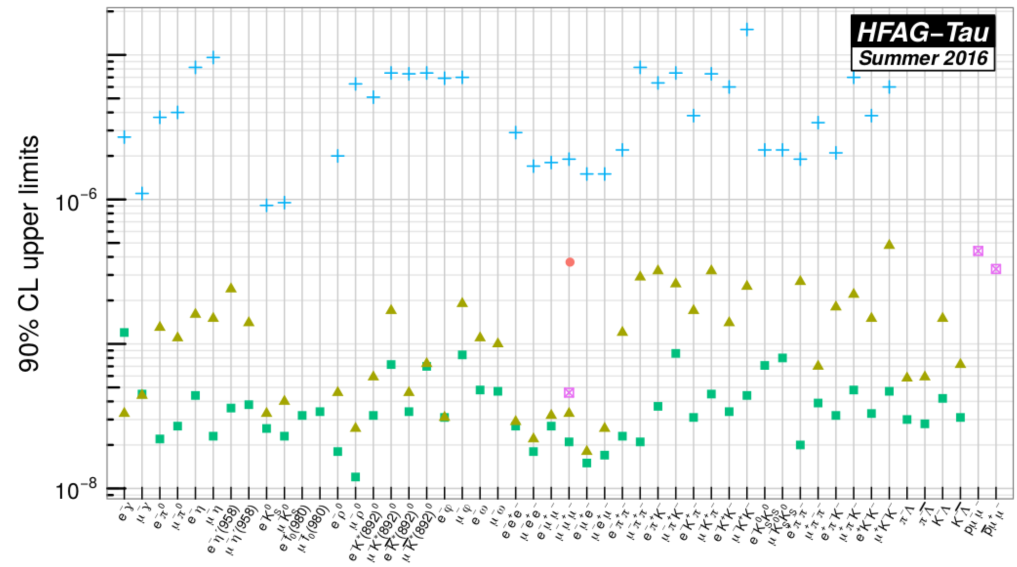

Figure 1.2: Limits on CLFV tau decays [44].

be discussed, by starting with cLFV. cLFV explorations in muon sector play a key role in the Physics beyond the Standard Model. Several experiments have taken place over the years, summarized in Figure 1.3.

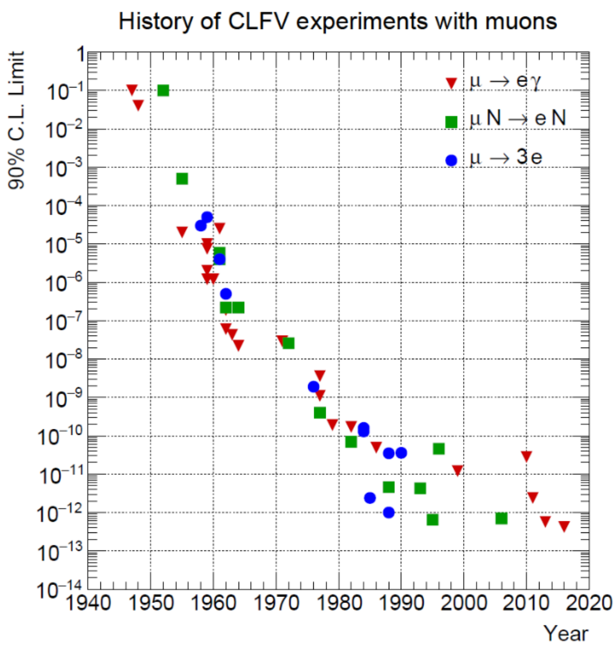

Figure 1.3: CLFV searches improvements in the μ decay [48]

The discovery of the LFV in muon decays $\mu^+ \longrightarrow e^+\gamma$, $\mu^+ \longrightarrow e^+e^-e^+$, $\mu^-N \longrightarrow e^-N$ conversion in nuclei, would be an indisputable proof of the existence of new dynamics BSM. cLFV transitions are related to new lepton-lepton couplings and effective operators, some examples of these processes are in Figure 1.4:

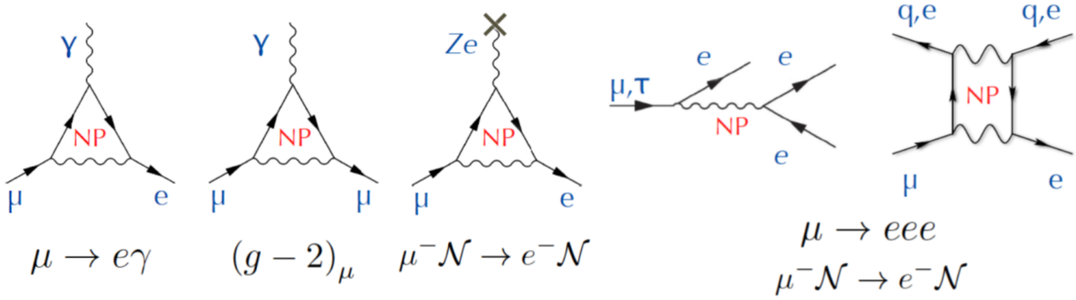

Figure 1.4: Schematic representation of vertices and interactions of some of CLFV processes in which NP contribution could be measurable.

The processes in Figure 1.4 can be divided in dipole amplitude, the first three Feynman diagrams (from the left) and 4-fermion amplitudes, the last two diagrams. The interplay between the two type of diagrams could be parameterized by means of two parameters, Λ and K, in the effective Lagrangian for leptons interaction [49, 42, 43]:

$$\mathcal{L}_{cLFV}\frac{m_\mu}{(k+1)\Lambda^2}\bar{\mu_R}\sigma\mu\nu e_L F^{\mu\nu} + \frac{k}{(k+1)\Lambda^2}\bar{\mu}_L\gamma^\mu e_L(\bar{e}\gamma^\mu e) + h.c. \tag{1.7}$$

where L and R indicate the chirality of the fermions field and $F^{\mu\nu}$ is the photon field strength. The dipole-like or 4-fermion interaction is determined by the dimensionless parameter k. The Eq. (1.7) is used to plot the new physics scale Λ versus the parameter k: for $k << 1$ the dipole interaction dominates the cLFV processes, while for $k >> 1$ the four fermion interaction dominates. Figure 1.5 summarizes the power of different searches to explore this parameters space.

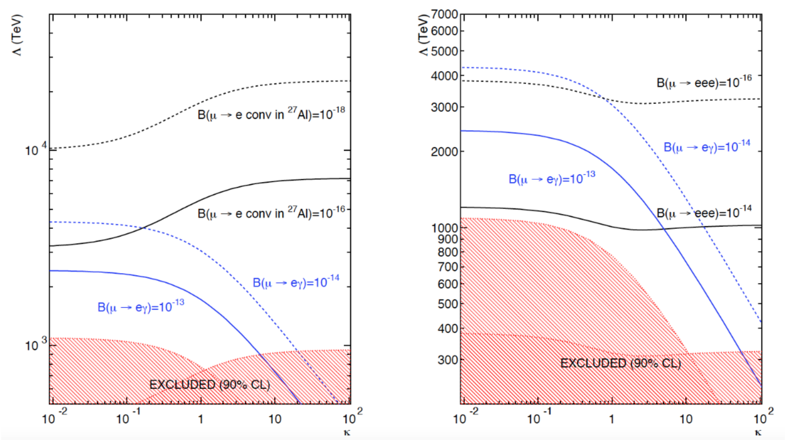

Figure 1.5: Left: Sensitivity of a $\mu \longrightarrow e$ conversion in ^{27}Al experiment that can probe a normalized capture rate of 10^{-16} and 10^{-18}, and of a $\mu \longrightarrow e\gamma$ search that is sensitive to a branching ratio of 10^{-13} and 10^{-14} , to the New Physics scale Λ as a function of k. Right: Sensitivity of $\mu \longrightarrow eee$ experiments that is sensitive to a branching ratios of 10^{-14} and 10^{-16} and of a $\mu \longrightarrow e\gamma$ search that is sensitive to a branching ratio of 10^{-13} and 10^{-14}, to the New Physics scale Λ as a function of k. In both plots are also depicted the currently excluded region of this parameter space [43].

As Figure 1.5 shows, for $\Lambda < 10^3 TeV$ present limits posed constraints on Standard Model extensions. The $\mu \longrightarrow e\gamma$ process is sensitive only in the dipole-dominating region, instead the $\mu \longrightarrow e$ conversion and the $\mu \longrightarrow eee$ decay take contributions from the 4-fermion interactions. In any case, Λ is an effective scale and it is not directly comparable with the mass M of new particles accessible by direct search. The dependence between Λ and M is parameterized by the following relation:

$$\begin{aligned} \frac{1}{\Lambda^2} &\sim \left(\frac{g_{BSM}\alpha}{M}\right)^2 \\ \frac{1}{\Lambda^2} &\sim \left(\frac{g_{BSM}}{M}\right)^2 \end{aligned} \tag{1.8}$$

with α the fine-structure constant and g_{BSM} the new BSM coupling [43].

1.5.4 $\mu \longrightarrow e\gamma$

According to the Minimal Supersymmetric Standard Model extension, which include the neutrino oscillations, the $\mu \longrightarrow e\gamma$ decay has a $BR \neq 0$. In Figure 1.6, the Feynman diagrams of this process are depicted. The Feynman diagrams show that the amplitude of this decay

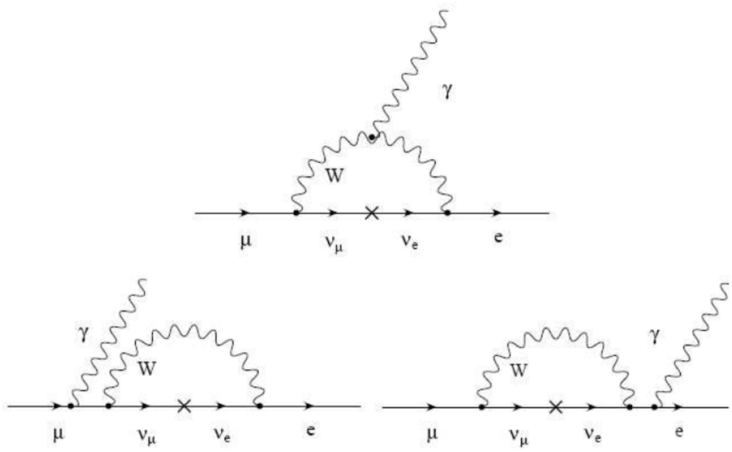

Figure 1.6: Feynman diagrams of the $\mu \longrightarrow e\gamma$ decay in the Minimal Standard Model extensions [50].

is extremely tiny, since the muon neutrino has to oscillate into an electron neutrino within a W vector boson lifetime [49, 42, 43]:

$$\Gamma(\mu \longrightarrow e\gamma) = \frac{\alpha G_F^2 m_\mu^5}{2048\pi^4}\left(\frac{\Delta m_{12}^2}{m_W^2}\right)\sin^2\theta_{12}\cos^2\theta_{12} \tag{1.9}$$

where the identity relation $\sum_{i=1}^{3}\left(|V_{ei}^2 V_{\mu i}^2|^2\right)$ is used and m_W is the W boson mass. Considering the 2-state approximations, θ_{12} is the mixing angle and $\Delta m_{12} = m_1^2 - m_2^2$ is the difference between the two ν mass eigenstates.
The muon total decay width is:

$$\Gamma_{TOT} = \frac{G_F^2 m_\mu^5}{192\pi^3} \tag{1.10}$$

so that the branching ratio is:

$$BR(\mu \longrightarrow e\gamma) = 5 \times 10^{-48}(\Delta m_{12}^2 eV^2)^2 \sin^2\theta_{12}\cos^2\theta_{12} \tag{1.11}$$

Taking the measurements of Δm^2_{12} and θ_{12} from KamLAND [51]:

$$\Delta m^2_{12} = 7.5 \times 10^{-5} eV^2 \quad \tan^2\theta_{12} = 0.44 \Longrightarrow BR < 10^{-50} \tag{1.12}$$

Such a tiny value is impossible to be experimentally measured! To give a more clear idea of what the value in the relation (1.12) means, it is useful to think at a high intensity muon beams at level of 10^8 muons per second. Taking this high intensity muon beam, the observation of a single $\mu \longrightarrow e\gamma$ decay would require $\sim 10^{35}$ years.
This means, without any doubts, that the cLFV processes in SM are forbidden in practice, even if they are in principle possible. The conclusion is that if such effects are experimentally observed, they must originate outside the SM [50]. BSM theories predict additional particles and interactions that can enhance such process up to a measurable level, like SUSY model.
Several studies have been performed, giving different BRs for the cLFV process, using various symmetry groups.
In general, different SUSY models predict different BRs, since the mixing mechanisms involve different SUSY particles and different members of slepton doublets. As example, Figure 1.7 shows that in the SUSY-GUT SU(5) model only right-handed components of sleptons are subject to mixing. On the contrary, in the SO(10) mixing is effective also for the left-handed

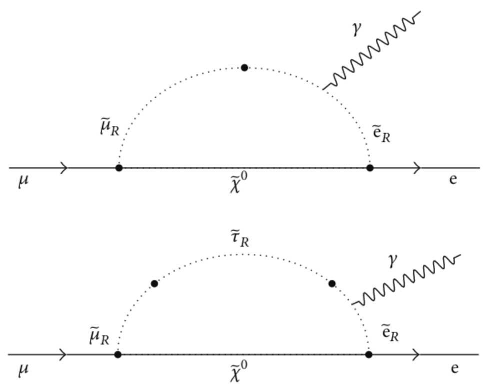

Figure 1.7: Loop diagrams according to the SUSY-GUT model [50].

components, as shown in Figure 1.8. The presence of an heavy particle in the loop enhances the expected BR, usually proportional to the square of the particle mass. In SUSY-GUT the the $\mu \longrightarrow e\gamma$ decay BR ranges from 10^{-15} to 10^{-13} in SU(5) models [52, 53], and from 10^{-13} to 10^{-11} in SU(10) models [52, 54].

1.6 Physics after LHC (FCC & CEPC) and the open question: route for BSM

LHC provides a conspicuous legacy of a rich and incredible physics landscape:

- the discovery of the Higgs boson and the detailed studies of its properties;
- the indication that signals of new physics around the TeV scale are, at best, elusive;

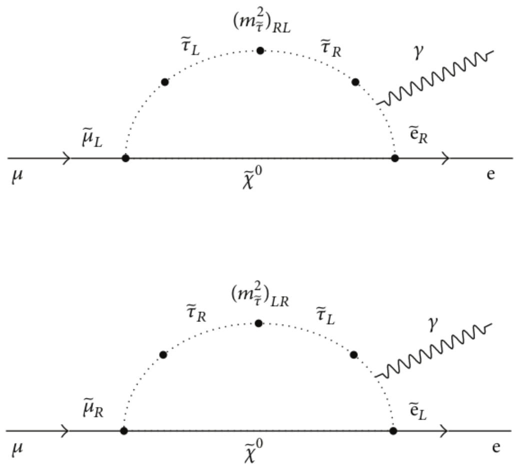

Figure 1.8: Loop diagrams according to the SUSY-GUT model [50].

- the rapid advance of theoretical calculations, whose constant progress and reliability inspire confidence in the key role of ever improving precision measurements, from the Higgs to the flavour sectors
- the extraordinary achievements of the accelerator and of the detectors, whose performance is exceeding all expectations

Thanks to the excellent performances of LHC, the international scientific community started the development of a new powerful tools to scan the unknown world of nature. Indeed two high performative colliders are in project: FCC at Cern [55, 56], and CEPC in China [57, 58]. The Future Circular Collider (FCC) study is developing designs for a new research infrastructure to host the next generation of higher performance particle colliders to extend the research currently being conducted at the LHC, once the High-Luminosity phase (HL-LHC) reaches its conclusion in around 2040. The goal of the FCC is to push the energy and intensity frontiers of particle colliders, with the aim of reaching collision energies of 100 TeV, in the search for new physics. The FCC examines scenarios for three different types of particle collisions: hadron (proton–proton and heavy ion) collisions (FCC-hh), electron–positron collisions (FCC-ee), as in the former LEP. Other options include proton–electron collisions or proton-heavy ion collisions (FCC-eh). The **FCC-ee**, e^+e^--collider would operate at multiple center of mass energies $\sqrt{s}$, producing 10^{13} Z bosons, 10^8 WW pairs, over 10^6 Higges and over 10^6 $t\bar{t}$ pairs; it will improve the precision of Higgs and other SM measurements by orders of magnitude.
The **FCC-hh**, 100 TeV pp collider, is designed to collect a total luminosity of 20 ab^{-1} corresponding e.g. to more than 10^{10} Higgs bosons produced. FCC-hh would also enable heavy-ion collisions, and its 50 TeV proton beams, with 60 GeV electrons from an energy-recovery linac, would generate $\sim 2ab^{-1}$ of 3.5 TeV ep collisions at the **FCC-eh** [55]; it will have a direct discovery potential over five times greater than the LHC.
The FCC-eh, in addition to contributing to Higgs studies and searches, will measure the proton's substructure with unique precision.
In addition to this extremely promising future, the Institute of High Energy Physics (IHEP) in Beijing, in collaboration with a number of other institutes in China as well as in many

different countries, started a study of the Circular Electron Positron Collider (CEPC), whose research is the same as the one planned for FCC-ee [59, 58]
The structure of the two future circular colliders are depicted in Figure 1.9.

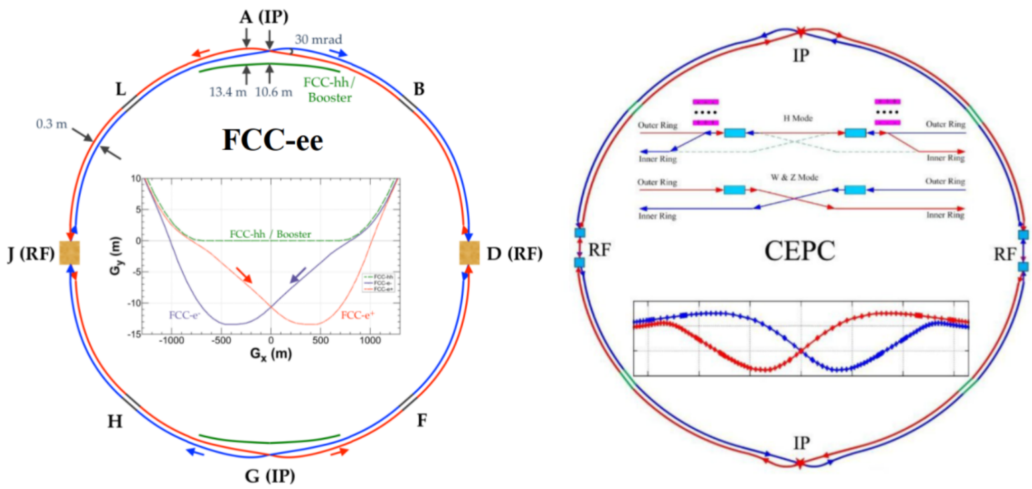

Figure 1.9: The two future circular colliders of FCC-ee (left) and CEPC (right).

1.7 Physics discoveries at FCC-ee

Since the main focus of this thesis involves FCC-ee, this section is dedicated to summarize the possible physics improvements attainable thanks to the FCC-ee collider, which are the same as CEPC.

1.7.1 Electroweak measurements

Precision Electroweak measurements at FCC-ee will be an important part of the physics program, with a sensitivity to new physics that is very broad and largely complementary to that offered by measurements of the Higgs boson properties. Starting from the LEP experience and thanks to the huge statistics and to the improved prospects for beam energy calibration, a very significant jump in precision can be achieved, like shown in Table 1.2, which summarizes the main quantities and experimental errors at FCC-ee, compared to the present ones. Table 1.2 presents a first sample of the main accessible observable. Other important contributions are expected from the b,c and τ physics at the Z pole, like forward-backward polarization asymmetries.

1.7.2 Higgs measurements

The FCC-ee offers powerful opportunities to determine the Higgs boson parameters, exploiting over 10^6 $e^+e^- \longrightarrow ZH$ events and almost 10^5 $WW \longrightarrow H$ events at center-of-mass energies around 240 and 365 GeV. The measurement of the total ZH cross section is an essential input to the absolute determination of the HZZ coupling – a "standard candle" that can be used by all other measurements, including those made at hadron colliders – at the per-mille level. A combination of the measured cross sections at the two different center-of-mass energies

Observable	Present value ± error	FCC-ee Stat.	FCC-ee Syst.	Comment and dominant exp. error
m_Z (keV)	$91{,}186{,}700 \pm 2200$	5	100	From Z line shape scan Beam energy calibration
Γ_Z (keV)	$2{,}495{,}200 \pm 2300$	8	100	From Z line shape scan Beam energy calibration
R_ℓ^Z ($\times 10^3$)	$20{,}767 \pm 25$	0.06	0.2–1.0	Ratio of hadrons to leptons acceptance for leptons
α_s (m_Z) ($\times 10^4$)	1196 ± 30	0.1	0.4–1.6	From R_ℓ^Z above [43]
R_b ($\times 10^6$)	$216{,}290 \pm 660$	0.3	< 60	Ratio of $b\bar{b}$ to hadrons stat. extrapol. from SLD [44]
σ^0_{had} ($\times 10^3$) (nb)	$41{,}541 \pm 37$	0.1	4	Peak hadronic cross-section luminosity measurement
N_ν ($\times 10^3$)	2991 ± 7	0.005	1	Z peak cross sections Luminosity measurement
$\sin^2\theta_W^{\text{eff}}$ ($\times 10^6$)	$231{,}480 \pm 160$	3	2–5	From $A_{FB}^{\mu\mu}$ at Z peak Beam energy calibration
$1/\alpha_{\text{QED}}$ (m_Z) ($\times 10^3$)	$128{,}952 \pm 14$	4	Small	From $A_{FB}^{\mu\mu}$ off peak [34]
$A_{FB}^{b,0}$ ($\times 10^4$)	992 ± 16	0.02	1–3	b-quark asymmetry at Z pole from jet charge
$A_{FB}^{\text{pol},\tau}$ ($\times 10^4$)	1498 ± 49	0.15	< 2	τ Polarisation and charge asymmetry τ decay physics
m_W (MeV)	$80{,}350 \pm 15$	0.5	0.3	From WW threshold scan Beam energy calibration
Γ_W (MeV)	2085 ± 42	1.2	0.3	From WW threshold scan Beam energy calibration
α_s (m_W) ($\times 10^4$)	1170 ± 420	3	Small	From R_ℓ^W [45]
N_ν ($\times 10^3$)	2920 ± 50	0.8	Small	Ratio of invis. to leptonic in radiative Z returns
m_{top} (MeV)	$172{,}740 \pm 500$	17	Small	From $t\bar{t}$ threshold scan QCD errors dominate
Γ_{top} (MeV)	1410 ± 190	45	Small	From $t\bar{t}$ threshold scan QCD errors dominate
$\lambda_{\text{top}}/\lambda_{\text{top}}^{\text{SM}}$	1.2 ± 0.3	0.1	Small	From $t\bar{t}$ threshold scan QCD errors dominate
ttZ couplings	$\pm 30\%$	0.5–1.5%	Small	From $E_{CM} = 365$ GeV run

Table 1.2: Measurement of selected electroweak quantities at the FCC-ee, compared with the present precisions [55].

provides the first evidence for the trilinear Higgs self-coupling, and possibly its first observation if the cross-section measurement can be made accurate enough. The determination of the Higgs boson mass with a precision significantly better than the Higgs boson width (4.1 MeV in the Standard Model) is a prerequisite to either constrain or measure the electron Yukawa coupling via $e^+e^- \longrightarrow H$ production at $\sqrt{s} = 125GeV$ [60, 55].

1.7.3 QCD measurements

High-luminosity e^+e^- collisions at the FCC-ee provide an extremely clean environment, with a fully-controlled QED initial-state with known kinematics, to probe quark and gluon dynamics with very large statistical samples. At variance with pp collisions, QCD phenomena appear only in the final state and are amenable to perturbative calculations over most of the accessible phase space, free from complications due to initial-state parton distribution functions, multiparton interactions, beam-remnants, etc. FCC-ee provides the best conditions possible to carry out very precise extractions of the strong coupling, to study parton radiation and fragmentation, with cleanly-tagged light quarks, gluons, and heavy quarks [55],[61].
The main QCD physics goals of FCC-ee, are:

- per mille extraction of the QCD coupling α_s;
- High-precision analyses of perturbative parton radiation including high-order leading corrections and logarithmic resummations for jet substructure, quark/gluon/heavy-quark discrimination, and q,g,c,b parton-to-hadron;
- High-precision non-perturbative QCD studies including color reconnection, parton hadronisation, final-state multiparticle correlations, and very rare hadron production and decays.

1.7.4 Top quark measurements

The top quark is the massive one among the other quarks, it influences the Higgs boson and its potential, leading to important puzzles about the origin of EW symmetry breaking. FCC-ee will operate at and above the $e^+e^- \longrightarrow t\bar{t}t$ threshold, dominating the precision in the measurement of the top mass and of its EW neutral couplings [55].
Flavour changing neutral current are forbidden at tree level and highly suppressed in the Standard Model, with BR at the level of $10^{-12} - 10^{-15}$. These transitions could be enhanced in the BSM models, increasing the branching ratio to $10^{-6} - 10^{-8}$. These processes could be studied at the FCC-ee in the top decay and in the top pair production at $\sqrt{s} = 365GeV$ or in the anomalous production $e^+e^- \longrightarrow tq$ (q=u,c) at $\sqrt{s} = 240GeV$ [62].

1.7.5 Flovour physics measurements

A total of 7×10^{11} $b\bar{b}$ available with a sample of 5×10^{12} Z decays obtainable at FCC-ee, provides great opportunity in flavour physics. The research for unobserved phenomena will be pushed forward, such as CP-symmetry breaking in the mixing of beauty neutral mesons.
Moreover, searches for rare decays make FCC-ee a direct discovery machine. The phenomena of lepton flavour violating Z decays, LFV *tau* decays searches for heavy neutral leptons and rare b-hadron decays will be the flagship of FCC-ee [55, 63, 64].
A list of interesting processes to be studies is here reported:

- flavour anomalies and electroweak penguins in $b \longrightarrow s$ quark transitions,
- lepton flavour violation in Z-boson decays: $Z \longrightarrow e\mu,\ \mu\tau,\ e\tau$,
- cLFV in τ decays: $\tau \longrightarrow \mu/e\gamma$, $\tau \longrightarrow \mu/el^+l^-$, $\tau \longrightarrow 3\mu$
- FCNC-mediated leptonic decays $B_{d,s} \longrightarrow ee, \mu\mu, \tau\tau$,
- search for BSM physics in $\Delta F = 2$ quark transitions.

Other possible fields of researches are available at FCC-ee, like the FCNC-mediated leptonic decays $B_{d,s} \longrightarrow ee,\ \mu\mu,\ \tau\tau$ as well as the EW penguin dominated $b \longrightarrow s\nu\nu$, which are sensitive to several realisations of BSM Physics. The cleanliness of the e^+e^- environment will be useful to study the decay modes involving the B_s, B_c or b-baryons with neutral final state particles, as well as many-body fully hadronic b-hadron decays. The data collected for the study of the CP-eigenstates in several b-hadron decays will allow comprehensive measurements of the CP-violating weak phases. Rare exclusive Z decays might probe both new physics and perturbative QCD factorization [55].

Chapter 2

Principles of operation of the gaseous detectors

The tracker of the MEGII experiment and the one for the future detector IDEA at the future colliders of FCC and CEPC consists of an ultralight drift chamber, a new generation of drift chambers which provide competitive tracking and particle identification performances.
This chapter has the goal of providing the basic notions about the gaseous detector operation, to better appreciate the innovative solutions applied to the new generation of ultralight drift chamber, which will be used for the double function of:

- particle identification
- reconstruction of the particle trajectory

The innovations involve the **mechanical design** of the detector, by implementing new technological solution on the construction of the drift chamber and the **data analysis**, by introducing the cluster counting/timing technique.

2.1 Passage of particle through matter

Starting from the basis process, it is well known that there are two types of interactions for charged particle detection: electromagnetic and nuclear interactions. In gaseous detectors, the electromagnetic interaction is more relevant in terms of energy loss.
A fast charged particle[1] traversing a medium interacts with the electromagnetic field generated by the atomic electrons and the nuclei located along its trajectory, producing [65]:

- multiple scattering, consisting of the deflections of the particle trajectory;
- *bremsstrahlung*, which is the emission of photons in the electromagnetic field of the nuclei and of the atomic electrons. The energy loss in this process depends on the ratio of the particle energy to its squared mass. So that, this process dominates the ionization loss for electrons at energies as low as 10 MeV. For muons and pions, this dominance occurs at several hundreds of GeV;
- inelastic collisions with the atomic electrons resulting in both excitation and/or ionization of the atoms of the medium.

[1] Fast particles are particles with a velocity that is large compared to the velocities of the atomic electrons, corresponding to the domain of validity of the first-order Born approximation.

2.1.1 Energy loss due to electromagnetic interactions

When a charged particle enters any absorbing medium, it interacts simultaneously with many electron and in anyone such encounters, the electron feels an impulse from the Coulomb force as the particle passes its vicinity. Depending on the proximity of the encounter, this impulse could raise the electron to a higher-lying shell within the absorber atom, generating an excitation, or could remove completely the electron from the atom, generating an ionization [66]. The products of these encounters in the absorber are either excited atoms or ion pairs, consisting of a free electron and the positive ion of an absorber atom. The ion pairs have a natural tendency to recombine to form neutral atoms, but in some types of detectors, this recombination is suppressed and the ion pairs are used as the basis of the detector response. Sometimes, an electron may undergo a large impulse that after having left its parent atom, it still has sufficient kinetic energy to create further ions. These energetic electrons are sometimes called *delta rays*. Their range is small compared with the range of the incident energetic particle, so that the ionization is still formed close to the primary track, which means that the ion pairs do not appear as randomly spaced single ionization, but there is a tendency to form many cluster of multiple ion pairs distributed along the track of the particle [66]. The quantum expression of the mean energy loss per unit length of traveled material, normalized to the medium density, is given by the Bethe-Bloch equation [41]:

$$-\frac{dE}{dx} = Kz^2 \frac{Z}{A} \varrho \frac{1}{\beta^2} \left[\frac{1}{2} \ln \frac{2m_e c^2 \beta^2 \gamma^2 T_{max}}{I^2} - \beta^2 - \frac{\delta}{2} - \frac{C}{Z} \right] \tag{2.1}$$

where A, Z, and I are respectively the atomic weight, the atomic number and the mean excitation potential of the traversed material; z is the particle charge, expressed in unit of the elementary charge e and βc is its velocity. δ is a factor describing the density effect and C is a factor describing the shell effects. T_{max} represents the maximum kinetic energy which can be imparted to a free electron in a single collision, like a head-on or knock-on collision [41]:

$$T_{max} = \frac{2m_e c^2 \beta^2 \gamma^2}{1 + 2\gamma m_e/M + (me/M)^2} \tag{2.2}$$

where M indicates the particle mass.

The equation (2.1) indicates the *mass stopping power* $[MeV/g^{-1}cm^2]$, it is almost the same for most material, decreasing slowly with Z. The linear stopping power is expressed as $\rho \frac{dE}{dx}$ [MeV/cm], where ρ is the material density in g/cm^3.

The Bethe and Bloch formula remains valid for $0.1 < \beta\gamma < 1000$: as $\beta\gamma$ approaches at 0.1, the projectile velocity is comparable to atomic electron velocity, on the other side, when $\beta\gamma$ approaches a 1000 radiative effects begin to be important [41].

The stopping power falls as $1/\beta^\alpha$, where $\alpha \simeq 1.4 - 1.7$, depending slightly on the incident particle's mass and decreasing with Z, and reaches a broad minimum at $\beta\gamma \simeq 3.5 - 3.0$, as Z goes from 7 to 100. Then, it rises as the argument of the logarithmic term increases. At this point, two mechanisms are in play. Two thirds of the rise is produced by the explicit $\beta^2\gamma^2$ dependence through the relativistic flattening and extension of the particle's electric field. Rather than producing ionization at greater and greater distances, the field polarizes the medium, canceling the increase in the logarithmic term at high energies. This phenomenon is taken into account by the density effect correction $\delta(\beta\gamma)$. The other third is introduced by the $\beta^2\gamma$ dependence of T_{max}. "Hard collision" events increasingly extend the tail of the energy loss distribution, increasing the mean but with little effect on the position of the maximum,

the most probable energy loss [41].
The stopping power in copper for positive muons in copper as a function of $\beta\gamma = p/Mc$ is shown in Figure 2.1.

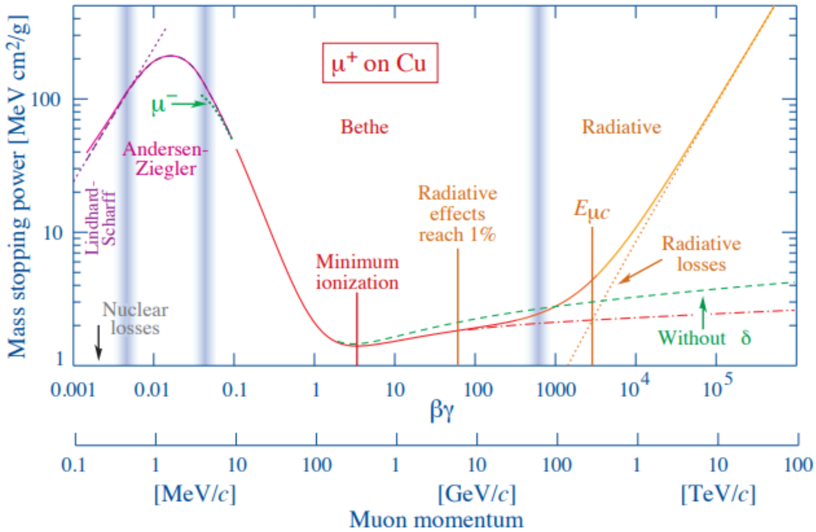

Figure 2.1: Mass stopping power for positive muons in copper as a function of $\beta\gamma$ over nine orders of magnitude in momentum. The short dotted lines labeled "μ^-" illustrate the "Barkas effect", the dependence of stopping power on projectile charge at very low energies [41]

2.1.2 Restricted energy loss rates for relativistic ionizing particles: the Fermi plateau

The mean energy deposit by an ionizing particle when the energy transfers are restricted to $T < T_{max} < T_{cut}$ is:

$$-\frac{dE}{dx}|_{T<T_{cut}} = Kz^2\frac{Z}{A}\varrho\frac{1}{\beta^2}\left[\frac{1}{2}\ln\frac{2m_ec^2\beta^2\gamma^2T_{cut}}{I^2} - \beta^2 - \frac{\delta}{2}\left(1+\frac{T_{cut}}{T_{max}}\right) - \frac{C}{Z}\right] \tag{2.3}$$

Since T_{cut} replaces T_{max} in the argument of the logaritmic term of the equation (2.1), the $\beta\gamma$ term producing the relativistic rise in the close-collision part of dE/dx is replaced by a constant and the $\frac{dE}{dx}|_{T<T_{cut}}$ approaches the constant "Fermi plateau." The density effect correction δ eliminates the explicit $\beta\gamma$ dependence produced by the distant-collision contribution [41].
Figure 2.2 shows the restricted loss rates for two examples of T_{cut}, shown in comparison with the full Bethe dE/dx and the Landau-Vavilov most probable energy loss [41].

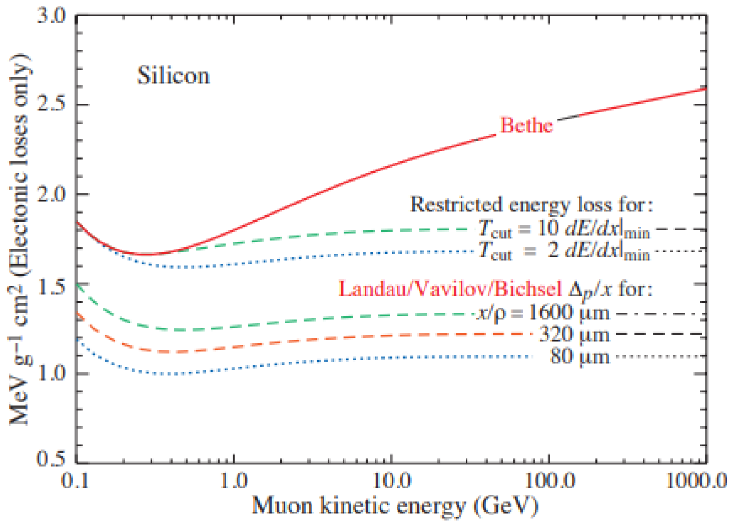

Figure 2.2: Two examples of restricted energy loss and the Landau most probable energy per unit thickness in silicon. The incident particles are muons [41].

2.2 Gaseous detectors

All gaseous detectors give the signal of the passage of charged particles by gathering the electrons from the ion pairs produced in the gas, usually after some amplification.
The passage of charged particles through a gas is signaled by the production of electron/ion pairs along its path. The electrons are attracted by electrodes on positive potential, in the vicinity of which they are usually amplified in a avalanche process. Some details about the aspects of the ionization process will be provide in this section.

2.2.1 Primary ionization: clusters

The ionizing collisions of the particle occur randomly with a mean distance λ, related to the ionization cross-section per electron σ_I and the electron density N_e of the gas [66, 67]:

$$1/\lambda = N_e\sigma_I \tag{2.4}$$

The number K of ionizing collisions on a path length L thus follows a Poisson distribution with mean L/λ:

$$P(k|L,\lambda) = \frac{(L/\lambda)^k}{k!}e^{-\lambda/L} \tag{2.5}$$

So that, the probability to have no ionization in L (k=0) is:

$$P(0|L,\lambda) = e^{-\lambda/L} \tag{2.6}$$

This relation is used to determine λ and defines the inefficiency of a counter measuring a track length L, if it is sensitive to a single primary electron [65].
An electron ejected in a primary collision may have enough energy to ionize one or more other atoms. Thus clusters of two or more electrons are formed by secondary ionization. These clusters are mostly rather localized, as the ejection energy is usually low and results in a short range. High ejection energies for so-called $\delta-$electrons are rare, their average number

per cm is approximately inversely proportional to energy [66].
The table 2.1 summarizes the properties of several gases commonly used in gaseous detectors. It includes the gas density, the excitation and ionization energy, the average energy dissipated per ion pair, the energy deposit per centimeter and the mean primary and total number of electron-ion pairs per centimeter.

Gas	Density, $mg\,cm^{-3}$	E_x eV	E_I eV	W_I eV	$dE/dx\|_{min}$ $keV\,cm^{-1}$	N_P cm^{-1}	N_T cm^{-1}
He	0.179	19.8	24.6	41.3	0.32	3.5	8
Ne	0.839	16.7	21.6	37	1.45	13	40
Ar	1.66	11.6	15.7	26	2.53	25	97
Xe	5.495	8.4	12.1	22	6.87	41	312
CH_4	0.667	8.8	12.6	30	1.61	28	54
C_2H_6	1.26	8.2	11.5	26	2.91	48	112
iC_4H_{10}	2.49	6.5	10.6	26	5.67	90	220
CO_2	1.84	7.0	13.8	34	3.35	35	100
CF_4	3.78	10.0	16.0	54	6.38	63	120

Table 2.1: N_p, N_T mean primary and total number of electron-ion pairs per cm; W_I: average energy dissipated per ion pair; E_I,E_x : ionization and excitation energy [41]

2.2.2 Total Number of Ion Pairs

The average energy lost by ionizing particle for the creation of one ion pair is:

$$W = E_I/n_E \tag{2.7}$$

where E_i is the initial kinetic energy and n_T the average total number of ion pairs. Measurements of W by total absorption of low energy particles show that it is practically independent of energy above a few keV for electrons and above a few MeV for α-particles, which means that the differential value $w = x\langle dE/dx\rangle/\langle n_T\rangle$ could be use to relate the average total number of ion pairs n_T, created in the track segment of length x, to the average energy lost by the ionizing particle.
The distribution of n_T in small gas segments is very broad, as shown in Figure 2.3. To describe the measurement result, it is thus appropriate to use the most probable value instead of the mean, since the mean of a small number of measurements will depend strongly on some events from the long tail of the distribution. The measured pulse height spectrum contains some additional broadening from the fluctuations of the avalanche process.

2.3 Transport of electron and ions

On the microscopic scale, electrons or ions drifting through a gas are scattered on the gas molecules. By adding a homogeneous electric field E, they acquire a constant drift velocity u in the electric field direction. In the presence of an additional magnetic field B, the drift velocity direction will be determined by both fields. Their drift velocities are much smaller than their

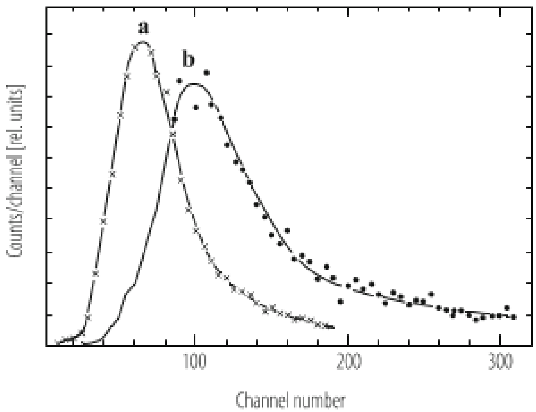

Figure 2.3: Measured pulse height distribution for 2.3 cm in Ar/CH 4 at 1 atm: (a) protons 3 GeV/c, (b) electrons 2 GeV/c [68].

instantaneous velocities c between collisions, moreover electrons and ions will behave quite differently because of their mass difference.
The equation describing the motion of free charges inside a medium under the influence of electric and magnetic fields, E and B, is [67]:

$$m\frac{du}{dt} = q\mathbf{E} + q[\mathbf{u} \times \mathbf{B}] - K\mathbf{u} \tag{2.8}$$

where m and q are the mass and the charge of the particle, $\mathbf{u}$ is its velocity and $K\mathbf{u}$ is a frictional force caused by collisions of the particle with the gas molecules. For large t, which means $t \gg \tau = m/k$, where k is a factor depending on the gas, the increasing friction force compensates the accelerating electromagnetic force leading to a constant drift velocity, v_d, solution of the steady state equation, $dv_d/dt = 0$ [67]:

$$\frac{\langle\mathbf{u}\rangle}{\tau} = \frac{q}{m}(\mathbf{E} + \mathbf{u} \times \mathbf{B}) \tag{2.9}$$

The right hand side of the equation (2.9) corresponds to the average acceleration of the electrons between consecutive collisions, due to the electromagnetic force, and therefore τ can be considered as the average time between collisions. In the absence of a magnetic field, equation (2.9) becomes:

$$v_d = \frac{q}{m}\mathbf{E}\tau = \mu_q\mathbf{E} \qquad\qquad \mu_q = \frac{q\tau}{m} \tag{2.10}$$

where μ_q is called charge mobility.
In absence of an electric field, the gas molecules undergo thermal agitation, as described by the classic kinetic theory and the charges released by an ionizing particle behave in a similar way. The classic kinetic theory attributes to each particle, with three degree of freedom, an average kinetic energy $\epsilon_T = 3/2KT$, where K is the Boltzmann's constant and T is the gas temperature. In absence of other forces, the charges locally distributed diffuse by multiple scattering following the Gauss law:

$$\frac{dN}{dx} = \frac{N_0}{\sqrt{4\pi Dt}}e^{-\frac{x^2}{4Dt}} \tag{2.11}$$

where N_0 is the total number of charges localized at $x = 0$ at $t = 0$, D is the diffusion coefficient and $dN(x)$ represents the fraction of charges located in the element dx at the distance x, at the time t [67].
The standard deviation of the distribution in one dimension is given by $\sigma_x = \sqrt{2Dt}$. The diffusion coefficient can be calculated from the kinetic theory:

$$D = \frac{2}{3}\frac{\epsilon}{m}\tau\epsilon = \frac{3}{2}KT \tag{2.12}$$

where τ is the average time between collisions. Since the diffusion coefficient depends on the particle mass m, its value for electrons is larger than the one for ions [67].
The table in figure 2.4 shows the mean free path, the velocity, the diffusion coefficients and the mobility for several gasses under normal condition. In the presence of an external force,

Gas	λ (cm)	u (cm/sec)	D^+ (cm^2/sec)	μ^+ ($cm^2\ sec^{-1}\ V^{-1}$)
H_2	1.8×10^{-5}	2×10^5	0.34	13.0
He	2.8×10^{-5}	1.4×10^5	0.26	10.2
Ar	1.0×10^{-5}	4.4×10^4	0.04	1.7
O_2	1.0×10^{-5}	5.0×10^4	0.06	2.2
H_2O	1.0×10^{-5}	7.1×10^4	0.02	0.7

Figure 2.4: λ the mean free path, u the velocity D is the diffusion coefficient and μ is the mobility for atoms and molecules at standard conditions [69]

like in an electric field, the electrons and the ions are accelerated along the field lines towards the anode and the cathode, respectively, so that the average kinetic energy becomes:

$$\epsilon = 1/2mv^2 = \epsilon_E + 3/2KT \tag{2.13}$$

where ϵ_E is the average energy acquired in the electric field. For the values of drifting field commonly used in gaseous detectors (few hundred of V/cm), ϵ_E amounts to a few electron-volts. Therefore the contribution of the thermal energy, which is around 0.04 eV in the normal condition of temperature and pressure, can be neglected and the value of the diffusion coefficient is affected by the presence of an external field.
It is been observed that the value of the electron diffusion in the direction of the electric field can be quite different from that in the transverse direction. Therefore two diffusion coefficients are introduced D_L and D_T , respectively, for the longitudinal and the transverse direction with respect to the electric field. Figure 2.5 shows the measured values of D_L/μ and D_T/μ as a function of field in argon [70].

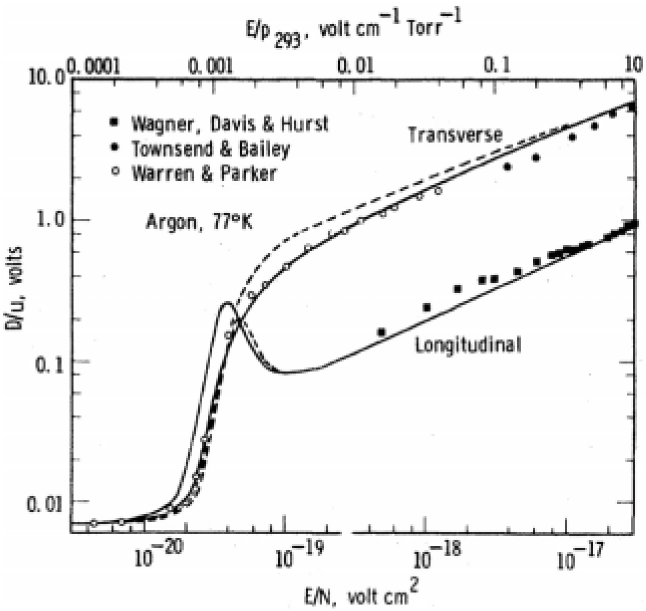

Figure 2.5: Longitudinal and transverse diffusion in argon [70]

2.4 Avalanche amplification

The gas multiplication is a consequence of increasing the electric field within the gas to high values. Indeed at low values of the field, the electrons and ions created by the incident particle drift to their respective collecting electrodes and during the migration, many collisions occur with neutral gas molecules. Because of their low mobility, positive or negative ions achieve very little average energy between collisions. Free electrons, on the other hand, are easily accelerated by the applied field and may have significant kinetic energy when undergoing such a collision. If this energy is greater than the ionization energy of the neutral gas molecule, it is possible for an additional ion pair to be created in the collision. Because the average energy of the electron between collisions increases with increasing electric field, there is a threshold value of the field above which this secondary ionization will occur. The threshold value is typically around $10^6 V/m$ [66].
The electron liberated by this secondary ionization process will also be accelerated by the electric field. During its subsequent drift, it undergoes collisions with other neutral gas molecules and thus can create additional ionization. The gas multiplication process takes the form of a cascade, known as *Townsend avalanche*, in which each free electron created in such a collision can potentially create more free electrons by the same process. The fractional increase in the number of electrons per unit path length is governed by the Townsend equation:

$$\frac{dn}{n} = \alpha dx \tag{2.14}$$

where α is the first Townsend's coefficient. For a spatially constant field, α is a constant and the density of electrons grows exponentially with distance as the avalanche progresses [71]:

$$n(x) = n(0)e^{\alpha x} \tag{2.15}$$

In non-uniform electric field, α is a function of x:

$$n(x) = n(0)e^{\int \alpha(x)dx} \tag{2.16}$$

2.5 The gas choice

Avalanche multiplication occurs in all gases; virtually any gas or gas mixture can be used in a proportional counter. However the experimental requirements, like low working voltage, high gain operation, good proportionality, high rate capabilities, long lifetime, restrict the choice to selected families of compounds.

The avalanche multiplication occurs in noble gases at much lower fields than in complex molecules because of the many non-ionizing energy dissipation modes available in polyatomic molecules, so that noble gases are using as main filling in proportional counter.

The excited noble gases return to the ground state only through a radiative process and the minimum energy of the emitted photon (11.6 eV for argon) is well above the ionization potential of any metal constituting the cathode (7.7 eV for copper, as example). Photoelectrons can therefore be extracted from the cathode and initiate a new avalanche very soon after the primary; an argon-operated counter generally does not allow gains in excess of a few hundred without entering into permanent discharge. Positive ions produced in the avalanche migrate to the cathode and are there neutralized by extracting an electron; the balance of energy is either radiated as a photon or by secondary emission of electrons from the metal surface. Both processes result in a delayed spurious avalanche: even for moderate gains, the probability of the processes discussed is high enough to induce a permanent regime of discharge [69, 67].

Polyatomic molecules have a different behavior, especially when they contain more than four atoms; the presence of non-radiative excited states, rotational and vibrational, allows the absorption of photons in a wide energy range. This phenomenon, known as "quenching", has an efficiency increasing with the number of atoms in the molecule; isobutane ($i - C_4H_{10}$) is often used for high-gain, stable operation.

Unfortunately, the use of polyatomic organic gases has a price, named "aging", a degenerative process which occur when high fluxes of radiation are detected [69]. Moreover, it is important to avoid the electronegative gas, like oxygen, which capture the electrons produced by the ionizing tracks. This phenomenon is known as *attachment* [69].

2.6 Multiwire proportional chambers

A multiwire proportional chamber consists of a set of thin parallel and equal spaced anode wires, symmetrically sandwiched between two cathode planes, as shown schematically in Figure 2.6.

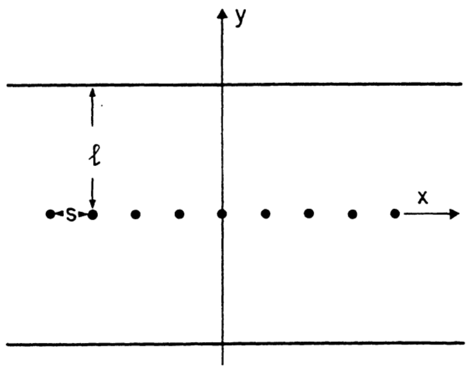

Figure 2.6: Cross-section of a multiwire proportional chamber [69].

The gap l, indicated in the Figure 2.6 is tipically three or four times larger than the wire spacing s.
When a negative potential is applied to the cathodes, the anodes being grounded, an electric field develops as indicated by the equipotentials and field lines in Figure 2.7.

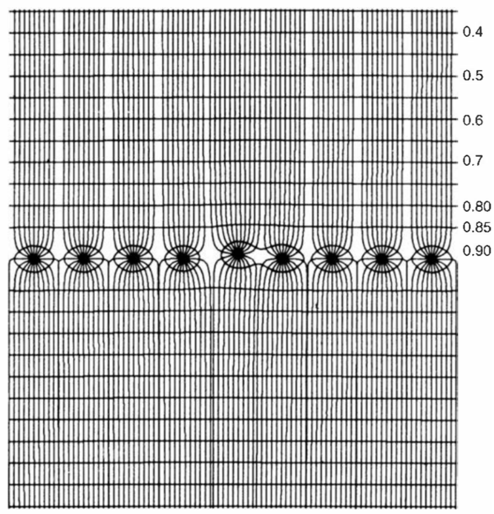

Figure 2.7: Electric field equipotentials and field lines in a multiwire proportional chamber. the effect of a small displacement of one wire is also shown [69].

When charges are generated in the gas volume by an ionizing particle, the electrons will drift along field lines until they approach the high field region, where avalanche multiplication occurs. A large negative-polarity-induced pulse appears on the anode wire on which the avalanche is collected, while the neighboring anodes show smaller positive amplitude pulses. The signals from preamplifiers connected to each wire can thus be used to localize the event to the nearest wire [66]. To reduce the number of preamplifiers, the anodes can be interconnected using resistors to form a charge-division chain, and the signals from preamplifiers at both ends can then be processed in the same type of scheme shown in Figure 2.8.

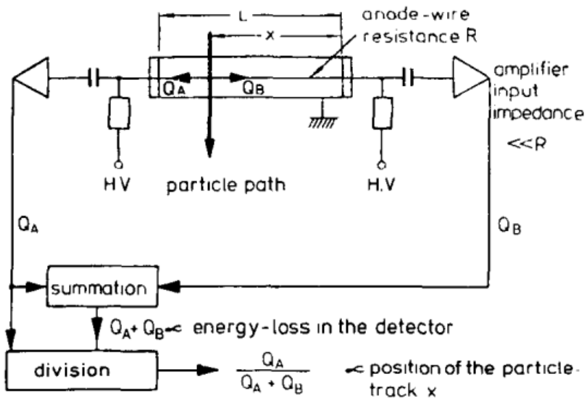

Figure 2.8: Position localization in proportional counters using the harge-division method [66].

The cathode planes also can be fabricated in the form of isolated strips or groups of wires, as shown, for example, in Figure 2.9. Positive signals are induced by the avalanches on the cathode strips, but since they are located some distance away, the induced charge is spread over a wider area. By using electronic center-of-gravity techniques, the centroid of the discharge can be located with reasonable precision. The strips on one cathode plane can be in the x direction while the strips on the opposite cathode are often made to be orthogonal to give an independent y coordinate.

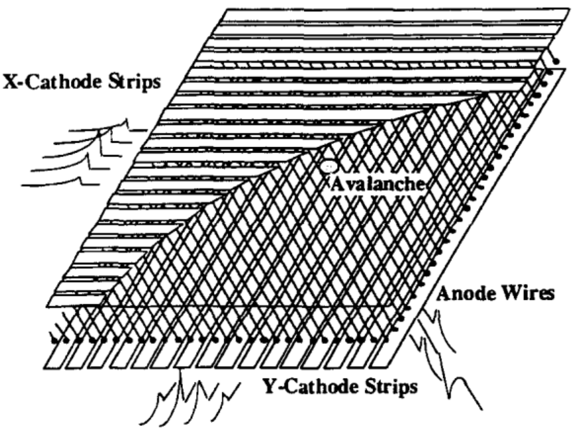

Figure 2.9: Sketch of a two-dimensional position-sensing multiwire proportional counter [66, 69].

2.7 Drift chamber

The intuition which brings to the development of the drift chambers was the possibility of measuring the electrons' drift time to get the information about the spatial coordinates of an ionizing event.
A single-cell drift chamber consists of a region of a constant electric field followed by a proportional chamber, like in Figure 2.10.

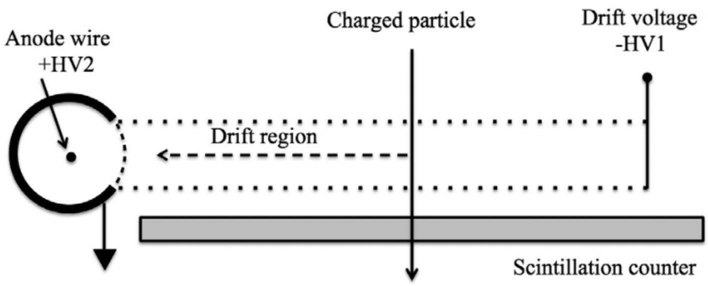

Figure 2.10: Schematic of a single-cell drift chamber [69].

The electrons produced by a charged particle at time t_0 migrate inside the drift region to one end of the cell with a drift velocity w, where avalanche multiplication occurs in a single wire proportional counter at time t_1. The coordinate of the track, in respect to the anode wire is:

$$x = \int_{t_0}^{t_1} w dt \tag{2.17}$$

which reduces for a constant drift velocity to $x = (t_1 - t_0)w$. For larger surfaces, a multi cell structure is preferable and a structure similar to the one of a multiwire proportional chamber can be used to realize a multiwire drift chamber [69]. As shown in Figure 2.11, anode wires are alternated with field wires, at suitable potentials, in order to eliminate low field region between anode wires which would result in a strong non linearity of the space-time relationship [69].

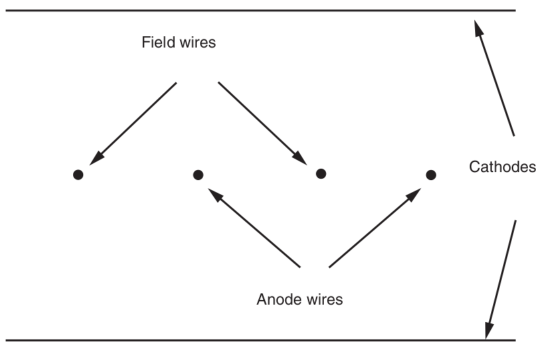

Figure 2.11: Schematic of a multiwire drift chamber [69].

Different geometry have been developed and largely used [69, 67].

2.8 Space-time correlation

The accuracy achievable by using a drift chamber depends on the good knowledge of the space-time relationship and on the diffusion properties of electrons in gases. Due to the chamber geometry with a non-uniform electric field, the correlation is generally not linear, although an appropriate choice of the gas and operating condition can reduce the variations. The correlation depends also on the angle of incidence of the tracks.
A simple way to measure the space-time relationship in a drift chamber is to record its time

spectrum on a uniformly distributed beam, since:

$$\frac{dN}{dt} = \frac{dN}{ds}\frac{ds}{dt} = kw(t) \tag{2.18}$$

so that,

$$N(t) = \int \frac{dN}{dt} dt = \int kw(t)dt = ks(t) \tag{2.19}$$

The time spectrum represents the drift velocity as a function of the time of drift and its integral the space-time relationship. The limitation of this method lies in the accuracy with which a uniform beam can be produce over a large surface. More accurate measurements exits, by using mechanical or electronic scanning [69]. Figure 2.12 shows the results obtained in a high-accuracy multiwire drift chamber, with quasi-uniform field [72].

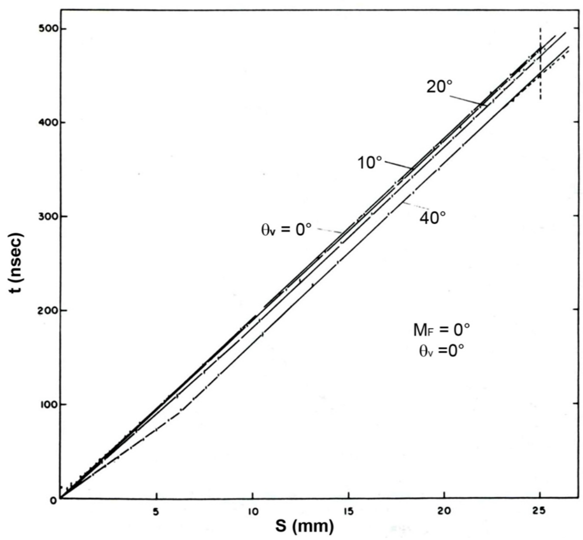

Figure 2.12: Measured and computed space-time relationship for a high-accuracy drift chamber as a function of the minimum ionizing beam angle of incidence [72].

The space-time correlation has been measured for several angles of incidence of the minimum ionizing beam and it is linear within the measurement errors of ± 50 μm over all the cell for the tracks perpendicular to the chamber plane, $\theta_V = 0°$ with a slope of 5.20 ± 0.02 $cm/\mu s$. For a beam inclined in the plane perpendicular to the wires, the correlation is slightly modified by the fact that the electrons having the shortest time of drift are not those produced in the middle plane of the drift cell [69]. In case of less uniform field, the space-time relationship deviates from the linearity.
Operation of the drift chambers at high pressures improves the localization accuracy, because of both the increase of ionization density and decrease in diffusion, as shown in Figure 2.13

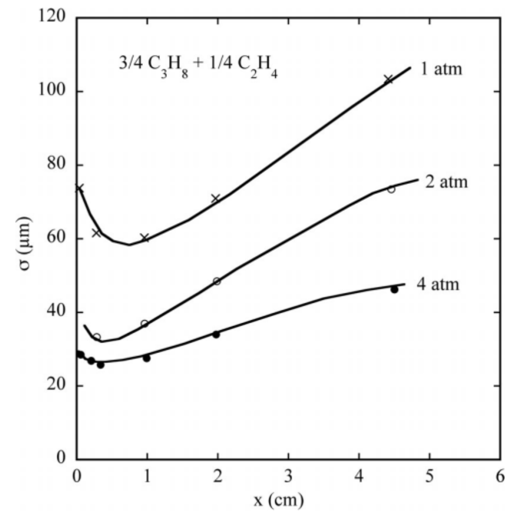

Figure 2.13: Position accuracy of a drift chamber at increasing pressures [73].

2.9 The intrinsic accuracy of a drift chamber

The traditional method used to measure the intrinsic accuracy of a drift chamber is to measure the same track in a set of equal chamber and computing the standard deviation of the difference, in a given chamber, between the measured and fitted coordinate. One of the most known results obtained is presented in Figure 2.14.

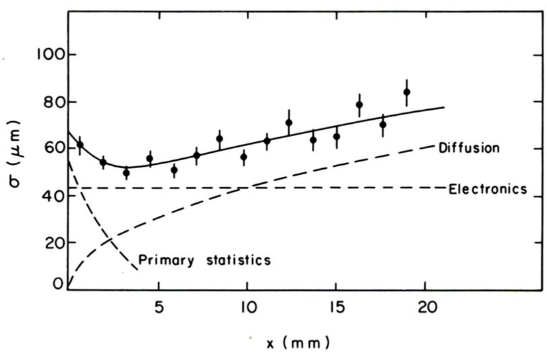

Figure 2.14: Measured intrinsic accuracy of the high accuracy drift chamber as a function of the drift space [72].

The result consists of three contributions: a square root dependence on the distance of drift, due to the electron diffusion, a constant electronics spread estimated to correspond to about $40\mu m$ and a contribution of the primary electrons production statistics.

Chapter 3

The MEG II experiment

Before describing the details the MEG apparatus and in particular its drift chamber, this chapter will provide a brief description of the experimental methodology applied by MEG to search the $\mu^+ \longmapsto e^+\gamma$ decay.

3.1 Signal and background: phenomenology of the rare decay

Apart from its rarity, the phenomenology of the $\mu^+ \longmapsto e^+\gamma$ decay is quite simple, as shown in Figure 3.1. Experimentally, a positive muon beam is stopped in a target and its decay

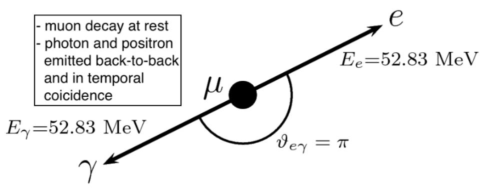

Figure 3.1: Kinematics of $\mu^+ \longmapsto e^+\gamma$ decay.

products are observed in the laboratory system. A negative muon cannot be used, since it is captured by a nucleus when it is stopped in a material. Positive muon decay at rest, so that the Center-of-Mass (CM) reference frame coincides with the laboratory. Since the process is a 2-body decay, apart from second-order corrections due to the fact that the electron mass is not zero, the outgoing particles have $E = \frac{m_\mu}{2}$ and are emitted simultaneously in a back-to-back direction. The signal consists in a photon and a positron of equal momentum emitted in collinear and temporal coincidence.
The physical observables that characterize the decay process are:

- ⋆ the energy of the positron and the photon, E_e and E_γ,
- ⋆ the relative angle between the emission directions of the outgoing positron and photon, $\vartheta_{e\gamma}$,
- ⋆ the relative time between the final state positron and photon, $t_{e\gamma}$.

3.1.1 Backgrounds

In order to identify the μ^+ decay as a signal candidate, the MEG detectors have to measure the key quantities involved in the process, rejecting all the events that can mimic the signal signature. This means that a good angular, timing and energy resolutions are required. There are two categories of background events which can mimic the signal signature: prompt background and accidental background.

Prompt background

The prompt background is due to the Radiative Muon Decay (RMD) $\mu^+ \longmapsto e^+\nu_e\bar{\nu}_\mu\gamma$ where γ and e^+ are emitted back-to-back and small energy is carried out by the two neutrinos. This process is characterized by four time-coincident particles and it can mimic the 2-body decay at the very end of the kinematic edge. The RMD rate is proportional to $R_\mu \times BR(\mu^+ \longmapsto e^+\nu_e\bar{\nu}_\mu\gamma)$, where R_μ indicates the muon beam intensity. The differential RMD width is usually expressed in terms of the reduced e^+ and γ energy, respectively $x = \frac{2E_e}{m\mu}$ and $y = \frac{2E_\gamma}{m\mu}$, and the relative emission angle $z = \pi - \theta e\gamma$. The variables x and y vary between 0 and 1 [74]. When $x = 1$ and $y = 1$, the width vanishes, but the finite experimental resolutions give background a possibility to mimic the signal, limiting the achievable sensitivity [49].
The probability of one background event to fall in the signal region is easily computed given the experimental resolutions δ_x, δ_y and δ_z and integrating the differential RMD width in the signal region smeared by the detectors resolutions. To keep the RMD rate at $\approx 10^{-15}$ level, resolutions of 1% for both γ and e^+ energy are required, as shown in Figure 3.2 [49].

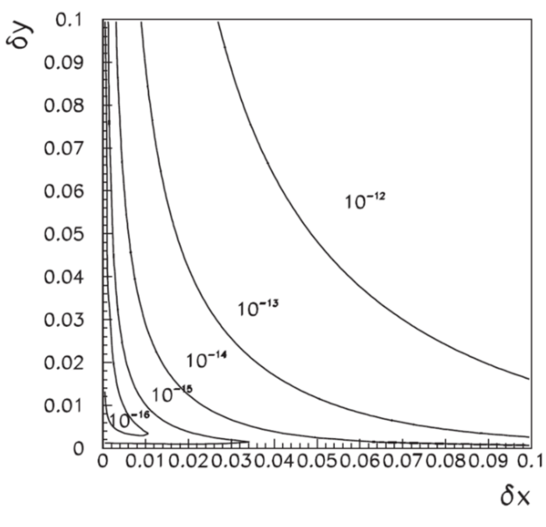

Figure 3.2: Effective branching ratio of the physics background from the $\mu^+ \longmapsto e^+\nu_e\bar{\nu}_\mu\gamma$ decay as a function of e^+ energy resolution δ_x and photon energy resolution δ_y [49].

Accidental background

An accidental background event occurs when a γ and an e^+ produced in two distinct processes are in accidental temporal coincidence and spatial collinearity. On one hand, the pure muon beam exploited by the MEG experiment ensures that the unique source of e^+ is the μ^+ decay (Michel positrons). On the other hand, there are many sources of high energy γ

which could pollute the experimental environment, like RMD, positrons interacting in the detector materials (e^+ Annihilation-In-Flight (AIF), bremsstrahlung), neutrons capture in the surrounding materials.
All the contributions are proportional to the beam μ^+ stopping rate in the target, $R\mu$. The probability that a background event is recognized as a signal B_{acc}, i.e. the ratio between the number of accidental events interpreted as $\mu^+ \longmapsto e^+\gamma$ to the total number of μ decays observed, is obtained by using the reduced variables for positron and photon energy, x and y, and by integrating over the corresponding energy spectra in the intervals $[1-\delta_x, 1]$, $[1-\delta_y, 1]$ [49]:

$$B_{acc} \approx \delta x \delta t_{e\gamma} (\delta\theta_{e\gamma})^2 [\alpha(\delta y)^2 ln(\delta y)] \longmapsto R_{acc} \approx B_{acc} \times R_\mu \tag{3.1}$$

where R_{acc} is the effective rate of accidental background events and $\delta t_{e\gamma}$ and $\delta\theta_{e\gamma}$ are the time and angular resolutions on the time-coincident back-to-back final state particles respectively. It is important to notice that the accidental background rate R_{acc} increases quadratically with the muon rate R_μ delivered on the target, becoming predominant for intense μ beam, which is the case of MEG experiment! For this reason the optimum muon beam for a $\mu^+ \longmapsto e^+\gamma$ decay search is a continuum beam which minimizes, for the same number of delivered μ, the number of accidental coincidence.
Figure 3.3 shows the AIF contribution to the total rate of accidental background photons as a function of the γ energy.

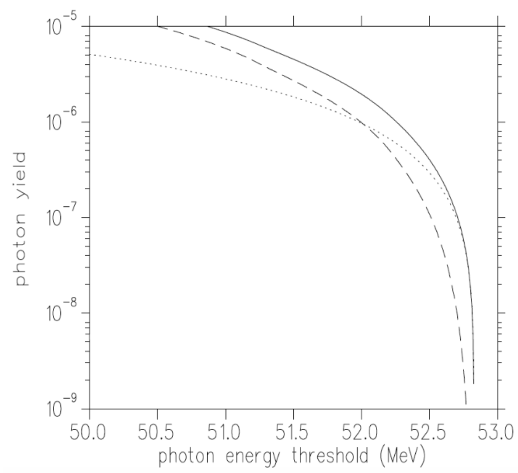

Figure 3.3: Integrated background rates as a function of the γ energy. Dotted line represents the e^+ annihilation in flight; dashed line represents the radiative muon decay and the solid line is the sum of the dotted and dashed line [49].

3.1.2 Single Event Sensitivity (SES)

Given the Branching Ratio for the $\mu^+ \longmapsto e^+\gamma$ decay process, $BR(\mu^+ \longmapsto e^+\gamma)$, the average number of expected signal events $N(\mu^+ \longmapsto e^+\gamma)$ in the case of a background-free experiment is:

$$N(\mu^+ \longmapsto e^+\gamma) = BR(\mu^+ \longmapsto e^+\gamma) \times k \tag{3.2}$$

where

$$k = R_\mu T \frac{\Omega}{4\pi} \epsilon_e \epsilon_\gamma \epsilon_{sel} \tag{3.3}$$

with R_μ the μ beam intensity, T the data taking live time, $\frac{\Omega}{4\pi}$ the solid angle covered by the apparatus, ϵ_e and ϵ_γ the the geometric efficiencies (related to the detector geometry and materials) of e^+ and γ, i.e. the probability that they reach the respective detectors and ϵ_{sel} is the signal selection efficiency (related to the experimental resolutions).
The Single Event Sensitivity (SES) is defined as the $BR(\mu^+ \longmapsto e^+\gamma)$ for which the average number of expected signal events is equal to 1 in absence of background. By imposing in equation (3.2) $N(\mu^+ \longmapsto e^+\gamma) = 1$:

$$SES = BR(\mu^+ \longmapsto e^+\gamma | N(\mu^+ \longmapsto e^+\gamma) = 1) = \frac{1}{k} = \frac{1}{R_\mu T \frac{\Omega}{4\pi} \epsilon_e \epsilon_\gamma \epsilon_{sel}} \tag{3.4}$$

The SES is the inverse of the normalization factor k. In principle the lowest SES, and therefore the largest possible R_μ , is experimentally desirable in order to be sensitive to the lowest possible branching ratio. However, due to the quadratic dependence on the muon stop rate, the accidental coincidences are largely dominant over the background coming from RMD (which is linearly dependent on R_μ). So that, for fixed experimental resolutions, the muon stop rate cannot be increased too much but it must be chosen in order to keep a reasonable signal over background ratio [75]. The first phase of MEG [76], [77] poses the most stringent constraint on the $\mu^+ \longrightarrow e^+\gamma$ decay, by setting, with the analysis of the data collected in the period from 2009 to 2013, the final upper limit at 90% Confidence Level (CL) on the branching ratio of [78]:

$$BR(\mu^+ \longrightarrow e^+\gamma) \leq 4.2 \times 10^{-13} \tag{3.5}$$

The goal of the second phase, named MEG II, is to improve this result of a factor of 10, reaching a BR of $\sim 6 \times 10^{-14}$ [75, 79]. The MEG upgrade makes us of a series of improvements, which include new detectors with better acceptances, efficiencies and performances to operate with a larger intensity muon beam and a new and optimized trigger and DAQ electronics.
In a nutshell, the MEG II upgrade consists of:

1. increasing the μ^+ flux and the stopping efficiency on the target;
2. reducing the stopping target thickness;
3. replacing the previous e^+ tracker (DCH) with a new single volume drift chamber;
4. using a new tracking procedure which follows e^+ until they hit the new timing detector;
5. replacing the previous TC with a new highly segmented system;
6. extending the LXe detector acceptance;
7. improving LXe detector efficiency and performances.

Figure 3.4 compares the main features of the previous MEG experiment (top) to the ones of the MEG II (bottom). The numbers refer to the items listed just above in the text.

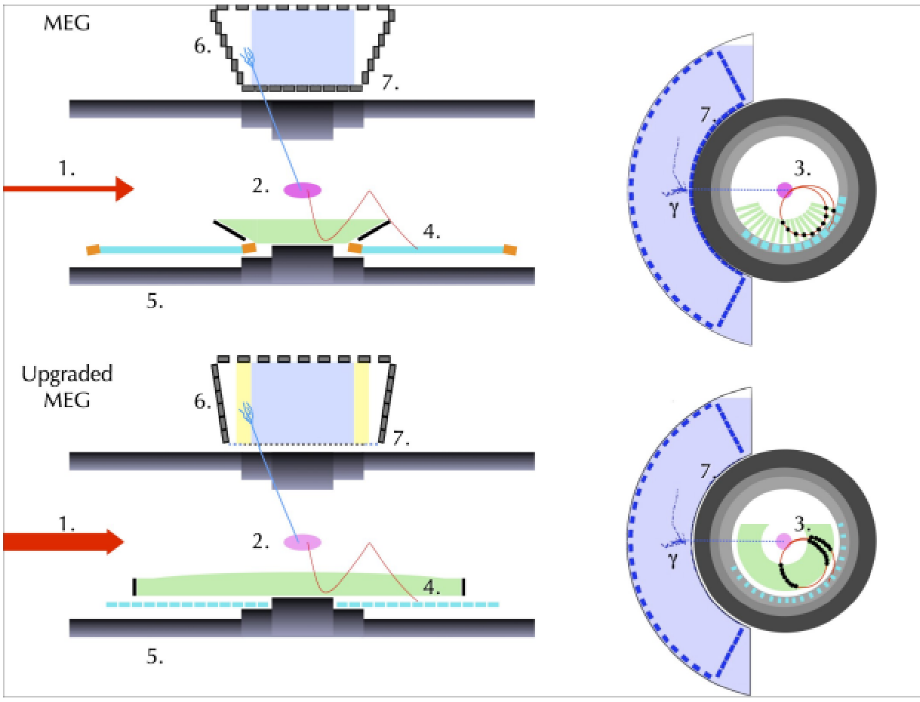

Figure 3.4: An overview of the MEG experiment compared to the MEG II. The numbers refer to the items listed in the text. [75]

3.2 The beam line and the target

The optimal signal sensitivity for MEG was achieved with a μ^+ stopping rate $R_\mu = 3 \times 10^7$, which is around 3 times lower than the maximum rate achievable (10^8 Hz) at PSI. This was due to the accidental background rate being proportional R_μ^2, while the signal dependence on R_μ is linear. Thanks to the higher rate capabilities of all the MEG II detectors joined with the improved efficiencies and resolutions, the muon stopping rate can be increased up to 7×10^7 Hz.
The beam line components and optics of MEG II is the same as for MEG, but new beam monitoring tools have been introduced.
The surface muons, which originate from a layer of thickness equivalent to a few hundred of microns in the production target surface, are transmitted and focused on the stopping target. To increase the R_μ, the $\pi E5$ beamline channel momentum slits are opened to their full extent, which means increasing the momentum-byte Δp. However, increasing the momentum-byte leads to an increased range straggling of the beam, ΔR_{TOT}, which has a direct impact on the target thickness, which in turn determines the intrinsic resolution on the determination of the relative angle between the photon and the positron. The goal of reducing the target thickness is minimizing the amount of material crossed by the decay products, γ and e^+ and consequently reducing the Multiple Coulomb Scattering (MCS) and the photon background production (Annihilation-In-Flight and bremsstrahlung) from the outgoing positrons. So that, the crucial requirement is to maximize the stopping density, i.e. the maximal stopping rate in the thinnest possible target.
The target thickness is related to the beam momentum p, since the total range straggling

ΔR_{TOT} is given by the empirical formula:

$$\Delta R_{TOT} = M\sqrt{\Delta E_s^2 + \left(3.5\frac{\Delta p}{p}\right)^2 p^{3.5}} \tag{3.6}$$

where M is a constant depending on the material and $\Delta E_s^2 \approx 9\%$ is the energy loss straggling of the traversed material. Due to the power-law dependence on p, the most efficient way to reduce ΔR_{TOT} and the target thickness is to reduce p. The central momentum for surface muons is $\approx$ 28 MeV/c, but the $piE5$ magnetic channel can be tuned to transmit muons with a momentum window centered at 25 MeV/c. These muons are called "sub-surface", because the muon acceptance layer in the production target lies below the surface.
During the R&D phase, several combinations of beam momentum and target options have been investigated [79]. Figure 3.5 shows the measured momentum spectrum for the muons provided by the $\pi E5$ beam line.

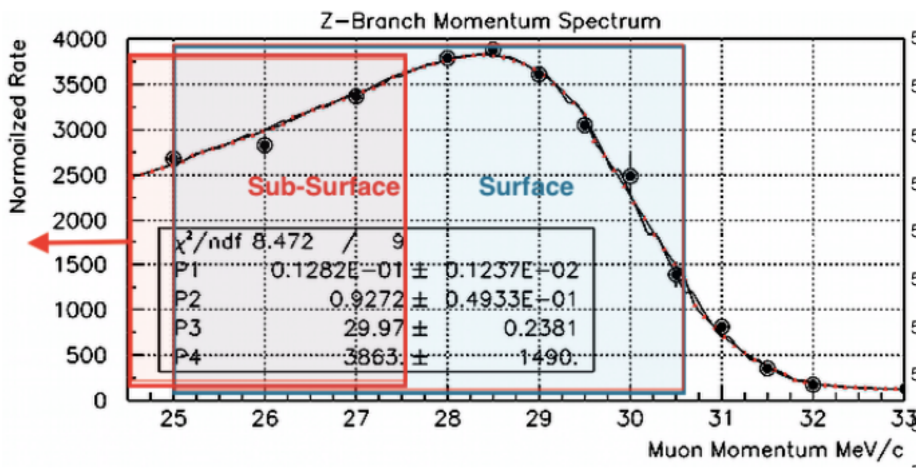

Figure 3.5: $\pi E5$ measured momentum spectrum with full momentum-byte[75]

The red curve represents the fit to the data with a $p^{3.5}$ power low folded with a Gaussian resolution function. The blue and red truncated boxes, centered at $\approx$28 and $\approx$25 MeV/c, show the full $\pm 3\sigma$ momentum spread for surface and sub-surface muons. Different studies have been conducted to investigate various combinations of the beam momentum and target parameter such as thickness (100μm -200 μm) and orientation angle (15°-20°) and in order to the highest intensity the optimal solution is: a surface muon beam of 28 MeV/c with a polyethylene target of 140 μm thickness, placed at an angle of 15° to the axis [79].
Figure 3.6 shows the MEG II target with its Carbon Fiber (CF) support structure.

Figure 3.6: The MEG II 140 μm thick polyethylene target with its CF support structure [75]

It is crucial to know with high accuracy the target positions, its planarity and its perpendicular distance from the nominal position, because any errors in this coordinate introduce a systematic error in the positron direction at the target due to the error in the path length of the curved positron trajectory projected on to the target plane. An offset of 1 mm in the target plane introduces a systematic error in the ϕ angle of 7-12 mrad, comparable to the *phi* angular resolution achieved by MEG. An automatic target monitoring method based on photographs taken by a CMOS photo-camera has been developed for the MEG II detector [80]. The method exploits imaging techniques to find displacements of patterns drawn on the target with respect to a reference picture taken at the beginning of a data-taking run. By combining this information with the results of an optical survey, it is possible to determine the position of the target during the run when the target is not accessible. The method described reaches the required resolution of less than 100 μm on the displacements along the axis normal to the target plane [80].

3.3 The new detectors

All the MEG II detectors have been optimized to achieve the fundamental requirements of high transparency for 50 MeV positrons, fast response and stable operation at high rates for precision measurements and background rejection.
The positron spectrometer consists of a new ultralight cylindrical drift chamber (CDCH) with high granularity and full stereo wires configuration, followed by a pixelated Timing Counter (pTC), based on scintillator tiles read out by SiPMs, for precise measurement off positron momentum vector and time respectively. The two detector are placed inside the COBRA superconducting gradient field magnet, retained from MEG. This optimized design increases the positron signal acceptance by more than a factor of 2 due to the reduction of the inactive materials between CDCH and pTC.
The photon energy, the interaction point and time are measured by an upgraded LXe detector. The energy and position resolutions improvement relies in a more uniform collection of the scintillation light achieved by replacing the PMTs on the γ entrance face with new Vacuum-UltraViolet (VUV) sensitive 12×12 mm^2 SiPMs.
A completely new device for an active background suppression has been introduced: the Radiative Decay Counter (RDC). It uses plastic scintillators for timing and scintillating crystals for energy measurement in order to identify low-momentum positrons associated to high-energy RMD γ detected in LXe.

The Trigger and Data-AcQuisition system (TDAQ) has been improved to meet the stringent requirements of an increased number of read-out channels and to cope with the required bandwidth by integrating into one condensed unit the various functions of analogue signal processing, biasing for SiPMs, high-speed waveform digitization and trigger capability.

3.3.1 The pixelated Timing Counter (pTC)

Precise measurement of the time coincidence of $e^+\gamma$ pairs is one of the decisive features of the MEG II experiment joined with the goal of suppressing the predominant accidental background. The positron time t_{e^+} must be precisely measured by the pixelated timing counter (pTC), with a resolution $\sigma_{t_e^+} \sim 30$ ps at a hit rate ~5 MHz. In addition, it also generates trigger signals by providing prompt timing and direction information on the positron [81].

During the running phase, the MEG timing counter [82] experienced a worsening of the intrinsic time resolution up to 70 ps compared to the excellent time resolution of 40 ps shown during the preliminary beam tests before the experiment. The main causes of the degradation are to be sought in the following items:

- the high intensity magnetic field provided by the COBRA magnet caused a gain lowering of the PMT amplification stage up to a factor 30 and an increase of ≈5 % in the Transit Time Spread (TTS), leading to a larger time-walk contribution on time resolution;
- a large variation of the optical photon paths originating from the large length of the scintillator (long longitudinal propagation and incident-angle dependence due to the not negligible thickness);
- the PMTs occupancy of ≈1 MHz/PMT is at the edge of their rate capability;
- sometimes positron could leave double hits in a single TC bar. The scintillator pulse width is increased by the large z projection of the tracks, which produced a tail component in the timing response function.

All these reasons bring the MEG collaboration to the development of a new high performing timing counter.

In the new configuration the scintillator bars have been replaced by 512 small scintillation tiles. In this way, the single counter can have a good time resolution due to the small dimensions, the hit rate of each counter is under control to keep the pile-up probability and the "double-hit" probability negligible. Moreover each particle's time is measured with many counters to significantly improve the total time resolution.

By combining the times measured by N_{HIT} counters, the total time resolution is expected to improve as:

$$\sigma_{t_e}(N_{HIT}) = \frac{\sigma_{t_e}^{single}}{\sqrt{N_{HIT}}} = \frac{\sigma_{t_e}^{counter} \oplus \sigma_{t_e}^{inter-single} \oplus \sigma_{t_e}^{electronics}}{\sqrt{N_{HIT}}} \tag{3.7}$$

where $\sigma_{t_e}^{single}$ is the total time resolution of a single counter, which includes the counter intrinsic resolution, the time alignment among counters and the electronic jitter. The contribution of the multiple Coulomb scattering, which does not scale linearly with $\sqrt{N_{HIT}}$, is negligible. Such a flexible pixelated design is made possible by the use of Silicon Photo-Multipliers (SiPMs), which have compact size, a sensitivity to a single γ, high internal gain, high photon

detection efficiency (PDE) peaked at ≈ 450 nm, good $\sigma_t < 100$ ps for a single γ, immunity to magnetic fields, low bias voltage, and low power consumption, no avalanche fluctuation, low cost [83].
The pTC consists of two semi-cylindrical (600 mm wide $\times$ 900 mm long) super-modules, mirror symmetric to each other, placed Up-Stream (US) and Down-Stream (DS) with respect to the μ^+ stopping target in the air space between CDCH and COBRA. The full e^+ angular acceptance coverage when photons point to LXe calorimeter is guaranteed: $27 < |z| < 116.7$ cm and $-165.8°|z| < 5.2°$. Each super-module hosts 256 counters: 16 counters with 5.5 cm interval in z and 16 counters with 10.3° interval in ϕ. Each counter is tilted by 45° to be roughly perpendicular to the positron trajectories and is wrapped with a 25 μm black foil for light tightness, above a 35 μm 3M Enhanced Specular Reflector (ESR) for internal reflections. The counters have a width (40-50 mm) which depends on the longitudinal position in the pTC region due to the radial spread of the signal positron trajectories, a length of 120 mm and a thickness of 5 mm. Each counter is read out by 6 AdvanSiD[1] SiPMs connected in series [75]. The e^+ impact time is obtained by averaging the times measured at both ends.
Figure 3.7 shows the DS pTC module inside COBRA.

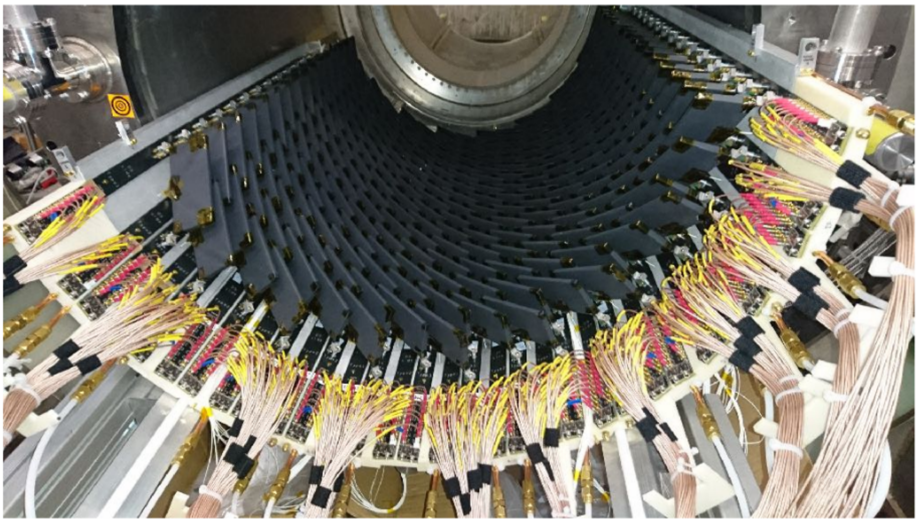

Figure 3.7: DS pTC module inside COBRA [75]

3.3.2 The Liquid Xenon Detector (LXe)

The liquid xenon (LXe) photon detector is a key ingredient to identifying the signal and suppressing the background in the $\mu^+ \longrightarrow e^+\gamma$ decay [84, 85]. In MEG, the energy resolution was dependent on the depth of the reconstruction capabilities which were worse for photons converting close to the inner face and at the edge of the acceptance. The non complete coverage of the entrance face by the 2" PMTs introduced a strong photo-detection non uniformity which deteriorated energy and position resolutions, due to event-by-event fluctuations of the shower shape, especially for shallow events.
The upgrade aims to reduce the non-uniform response and increase the granularity by replacing the PMTs on the inner face with with 4092 12×12 mm^2 Multi-Pixel Photon Counters (MPPCs), see Figure 3.8 top, which are insensitive to the COBRA magnetic field.

[1]http://advansid.com/home

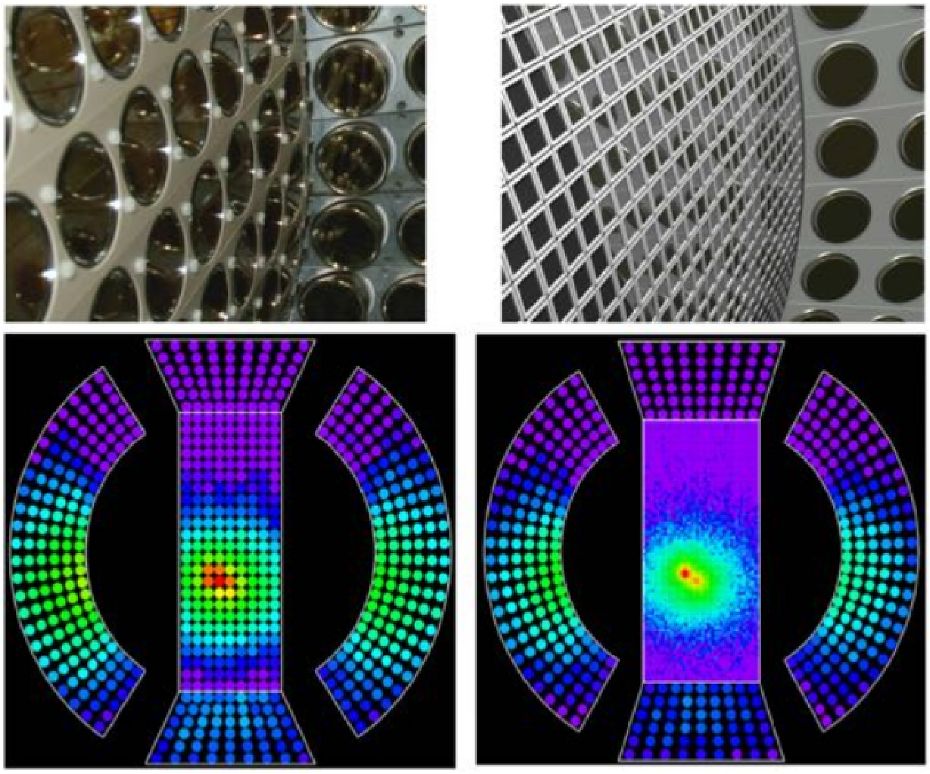

Figure 3.8: Above: LXe interior view before (left) and after (right) the MEG II upgrade. Below: example of scintillation light distribution as detected by PMTs (left) and smaller MPPC photosensors (right) [75].

Figure 3.8 bottom shows an example of event display for MEG and MEG II, highlighting the upgrade improvement: the same two photons event appears as a single cluster in the MEG configuration, while in the MEG II configuration two separate clusters are clearly visible. Moreover, the active volume has been increased, so that the photons shower leakage near lateral faces is better contained, as shown in Figure 3.9.

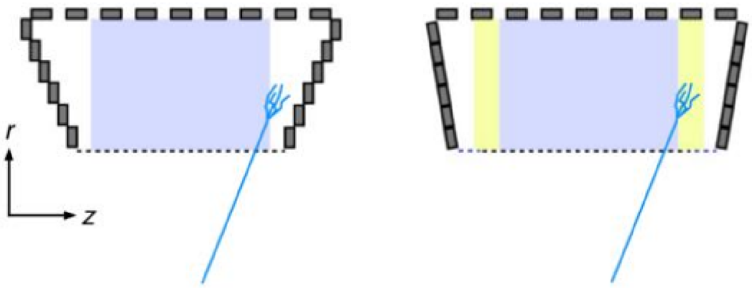

Figure 3.9: Section of the LXe photon detector in MEG (left) and MEG II (right). In yellow the increased acceptance after the new lateral PMTs arrangement for MEG II [75].

The MPPCs, developed by the MEG II collaboration together with Hamamatsu Photonics [2], has a photon detection efficiency (PDE) $> 10\%$ for LXe scintillation light and a decay time of ~ 50 ns.

[2]http://www.hamamatsu.com/eu/en/index.html.

Each MPPC consists of four independent 6 × 6 mm^2 sensor chips connected on a PCB in series to reduce the capacitance. Thus the signal can be read out by one channel per MPPC. The installation of these detectors improved the imaging of the LXe, increasing the separation power of two pileup photons.
Figure 3.10 shows the spatial resolution as a function of the conversion depth for 52.8 MeV signal photons.

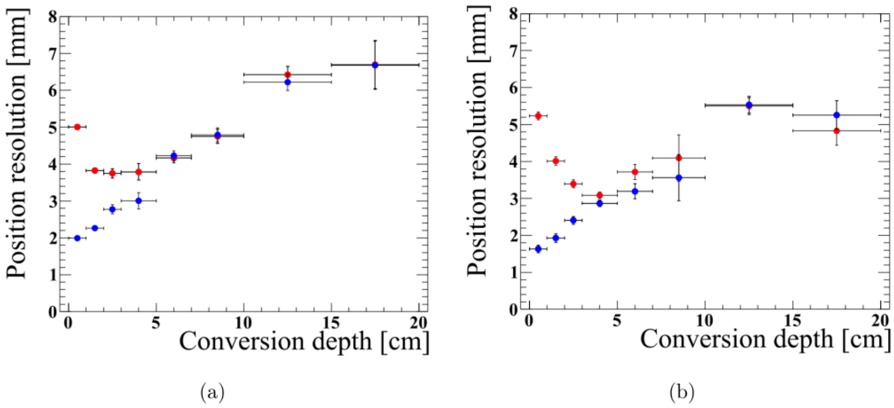

Figure 3.10: Spatial resolution as a function of the conversion depth for horizontal (a) and vertical (b) directions. MEG resolutions are reported in red, while MEG II resolutions are reported in blue [75].

It is evident the improvement from MEG in the shallow region of the detector because of the smaller size of the MPPC with respect to the PMTs.
Figure 3.11 shows the fit to the measured background photon spectrum obtained from muon decays.

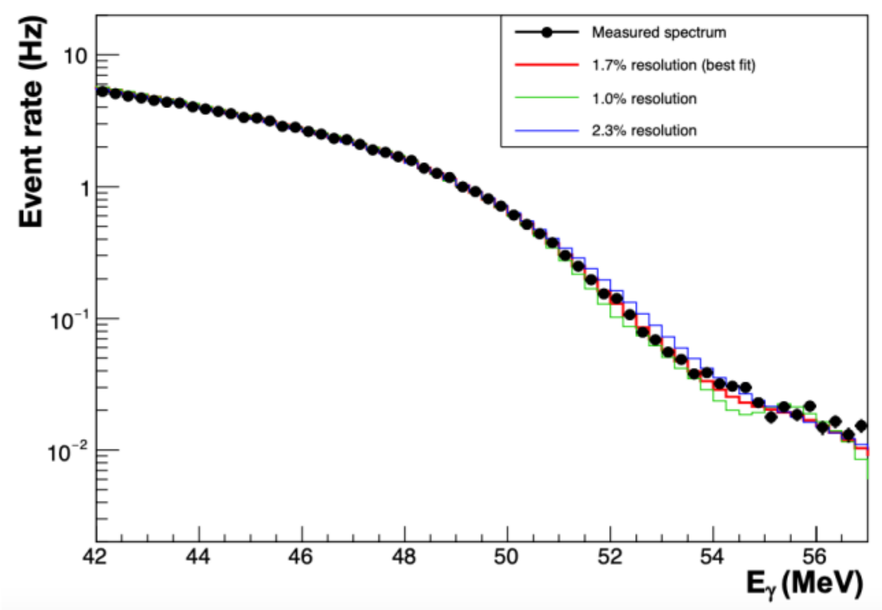

Figure 3.11: Measured and simulated background photon spectrum. The different colors represent the convolution of the spectrum with different energy resolution assumptions. The best fit is the red histogram, corresponding to 1.7% resolution [86].

3.3.3 The Radiative Decay Counter (RDC)

Photons contributing to accidental background come from either RMD, bremsstrahlung or positron AIF. The AIF background decreases in MEG II thanks to the reduced mass of the CDCH compared to the MEG drift chambers. The yield of the AIF background photons above 48 MeV per muon decay expected from Monte Carlo simulations is 1.4×10^{-6} (in MEG 2.3×10^{-6}). Anyway, on the other side, the RMD photon background remains unchanged.
The RDC is a new detector capable of identifying a fraction of low-energy positrons from RMD decays with photon energies close to the kinematic limit. It consists of 12 plastic scintillators BC-418 for time measurement and 76 LYSO crystals for energy measurement. It is placed 140 cm downstream of the muon stopping target and covers the region within 10 cm from the beam axis. It identifies low-energy positrons (1–5 MeV) in time coincidence with the detection of a high energy photon in the LXe detector [75].
Simulations results prove that it can detect about 40% of RMD γ background events and should lead to an improvement of the sensitivity of $\mu^+ \longrightarrow e^+\gamma$ search of about 15% [75], [86].

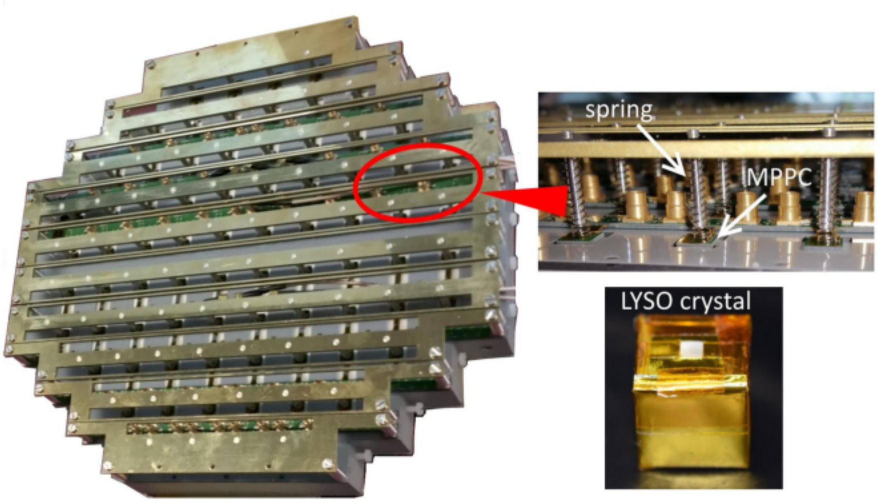

Figure 3.12: LYSO crystals with the SiPMs attached with springs [75].

3.3.4 The TDAQ system

The upgrade of the detectors lead to a huge increase in the number of readout channels which required a new TDAQ system able to fit all the electronics in the same physical space used in the first phase of MEG [24, 76].

DAQ

The new system integrates the basic Trigger and DAQ (TDAQ) functionalities in the same electronics board, the WaveDREAM Board (WDB) [87]. A simplified schematics of the WDB is shown in Figure 3.13. It contains 16 channels with variable gain amplification and flexible shaping through a programmable pole-zero cancellation. Switchable gain-10 amplifiers and programmable attenuators allow an overall input gain from 0.5 to 100 in steps of two.

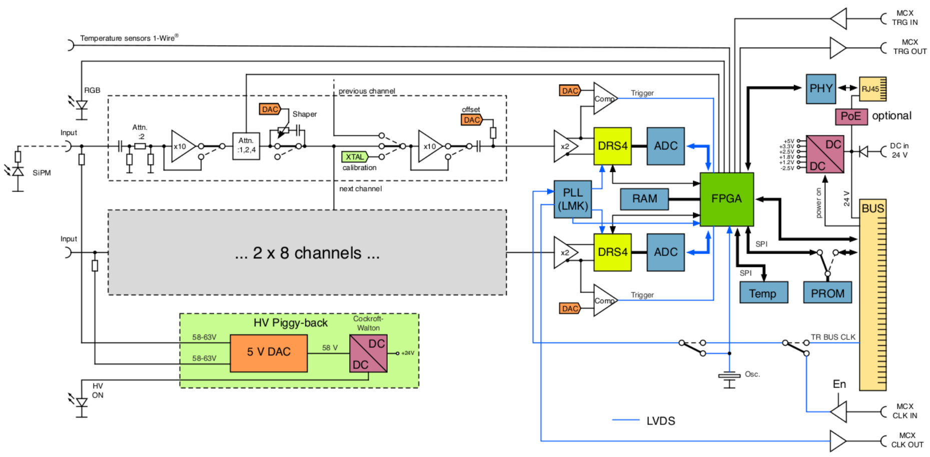

Figure 3.13: Simplified schematics of the WaveDREAM board. It contains 16 variable gain input amplifiers, two DRS4 chips, 16 ADC channels and a Spartan 6 FPGA. A optional high voltage generator for SiPM biasing can be mounted as a piggy-back board [75].

Two DRS4 chips [88] are connected to two 8-channel ADCs, which are read out by a

Field-Programmable Gate Array (FPGA). In normal operation, the DRS4 chips sample the input signals continuously at a speed up to 5 GSPS in an analogue ring buffer. At the same time, a copy of the input signal is sent to the DRS4 output, where it is digitized continuously by the ADCs at 80 MHz with a 12 bit resolution. The output stream of the ADCs is used in the FPGA to perform complex trigger algorithms. When a trigger occurs, the DRS4 chip is stopped and the internal 1024-cell analogue memory is digitized through the same ADCs. This technique allows to perform complex triggering and high speed waveform sampling on the same board. An ultra-low noise bias voltage generator (implemented as an optional PCB) can supply the voltage to SiPMs up to 240 V (six SiPMs in series) and 50 mA through the signal cables [75].
The WDB can be used in stand-alone mode, where it is read out through Gigabit Ethernet and powered through Power-over-Ethernetin. For MEG II, it has been decided to house 16 boards in a custom compact crate (Figure 3.14).

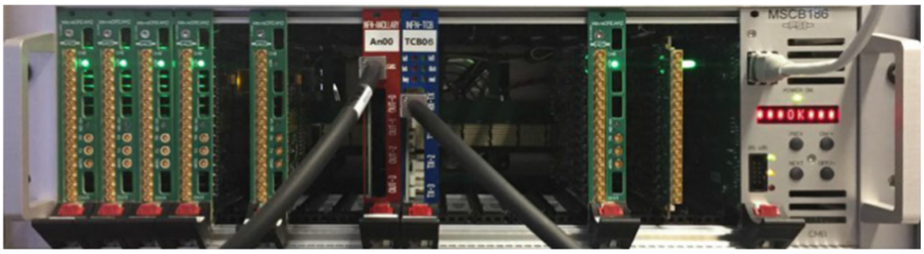

Figure 3.14: WaveDREAM crate shown with 7 WDB (green), one ancillary board (red), one TCB (blue) and the CMB (right) [75].

This crate requires Gbit links for the simultaneous read-out of waveforms and trigger data, a common high voltage for the SiPMs biasing, an integrated trigger distribution and an ultra-low jitter clock with a few picoseconds phase precision [75].
The Crate Management Board (CMB) contains the 220 V power supply together with a shelf management unit and is placed to the right side of the crate. The power supply generates a 24 V crate power of 350 W and a 5 V standby power for the shelf manager. Cooling is achieved by fans on the rear-side blowing air from the back to the front, where it exits through holes in the various boards.
The CMB contains an 8 bit micro-controller programmed in the C-language. It is connected to a dedicated Ethernet network for remote control and monitoring, and it has a LED display and buttons for local control. A Serial Peripheral Interface (SPI) bus allows communication with all WDBs [75].
The global trigger and clock distributions are also housed in WaveDAQ crates. In addition, the crate contains two slots for the Trigger Concentrator Board (TCB) and Data Concentrator Board (DCB). The DCB is responsible for the configuration of all boards, the distribution of the master clock and trigger signals, the read out of waveform data, the merging and formatting of the data and the interface to DAQ computers through Gbit Ethernet [75].

Trigger

The two fast response detectors which are entitled to perform trigger decision are the LXe and the pTC. The long ionization drift time in CDCH prevents the trigger system from using any information from the track reconstruction for trigger level 0.
The event selection relies on an online reconstruction of the decay product observables: momenta, relative timing and direction. Logic equations are mapped in FPGA cells and executed at 80 MHz, synchronous with the FADC data flow.
An estimate of the photon energy is obtained by the linear sum of pedestal subtracted signal amplitudes of LXe photo-sensors, which is implemented by using Digital Signal Processor (DSP) units.
The boards designed for the online data processing are called TCB, which gathers the information from a lower level trigger board, which could be a WDB or another TCB in the same or another crate. TCB features depend on the slot assignment within the crate (Figure 3.15): data-flow is set from the back-plane to the on-board FPGA for a Master TCB, while it is reversed for Slave TCBs hosted in the trigger crate.

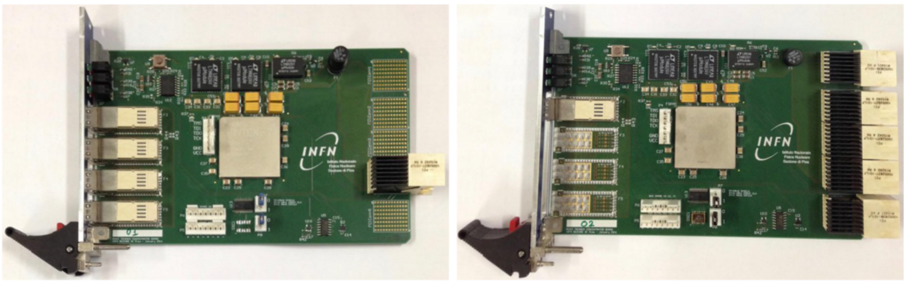

Figure 3.15: TCB configured as slave (left) and master (right); in case of a slave board the data-flow is from the left (front panel) to the right (back plane) and vice versa for a master [75].

An ultra-low jitter ($<$10 ps) clock signal at 80 MHz to be used as the experiment time reference is distributed by a dedicated board, named the "Ancillary board", which can be configured as Master, in this case it generates a clock signal and receives the control signals, such as the trigger and synchronisation pulses, from the master TCB and forwards them to all the other TDAQ modules through the Slave modules. The other way round the busy signal is distributed from the DAQ crates to the trigger crates and used as a veto for any trigger signals generation.
The read out scheme guarantees a data transfer dead time of about 1 ms leading to a possible trigger rate of about 100 Hz with irrelevant dead time.
The trigger processing includes zero suppression algorithms to reduce the background by almost 6 orders of magnitude.

3.4 The MEGII cylindrical drift chamber

A great number of innovative elements have been developed for the MEG II drift chamber, which is the detector with a complete new design respect to the one used with MEG [76].
The MEG II Cylindrical Drift Chamber (CDCH) [89], [90], [91] is a single volume detector,

whose design was optimized to satisfy the fundamental requirements of high transparency and low multiple Coulomb scattering contribution for 50 MeV positrons, sustainable occupancy (at $\sim 1 \times 10^7$ μ^+/s stopped on target) and fast electronics for cluster timing capabilities [92].

3.4.1 Detector design

The MEG II positron tracker was inspired by the one used in the KLOE experiment [93]. The chamber has a cylindrical symmetry along the z axis, parallel to the muon beam. It covers the whole azimuthal angle ϕ subdivided in 12 30°-sectors (numbered from 0 to 11). The wires have been arranged in a full stereo configuration, which gives a hyperbolic shape to the active volume, which extends radially from $\sim$ 174.500 mm to $\sim$ 234.260 mm at the detector center (z=0) and $\sim$ 201.490 mm to $\sim$ 270.500 mm at the endplates ($z = \pm 956mm$). Wires in the Up-Stream (US) endplate arrive in sector $s \pm 2$ in the the Down-Stream (DS) endplate ($\Delta\phi = 60°$). The entire length of the sensitive volume is about 1912 mm. The high granularity is ensured by the segmentation of the drift chamber volume in 9 layers of 192 drift cells each [75].
The stereo angle varies from 6° in the innermost layer to about to 8.5° in the outermost layer. The schematic view of the stereo wires configuration is depicted in Figure 3.16. The wire length for layer k is L_k and the corresponding stereo angle is ϵ_k. The wire radii at the endplates and at the chamber center are:

$$R_k \qquad R_{k_0} = R_k \cos\frac{\alpha_k}{2} \tag{3.8}$$

where α_k, which represents the azimuthal shift between the 2 wire ends (suspension points), is $\pm 60°$, depending on the layer.
The positive and negative stereo angles define two projective views, the and V-view and the U-view respectively. All the wires with the same sign of the stereo angle are parallel, this is the reason why the drift chamber takes the shape of a rotation hyperboloyd whose surface is given by the envelope of the wires planes.

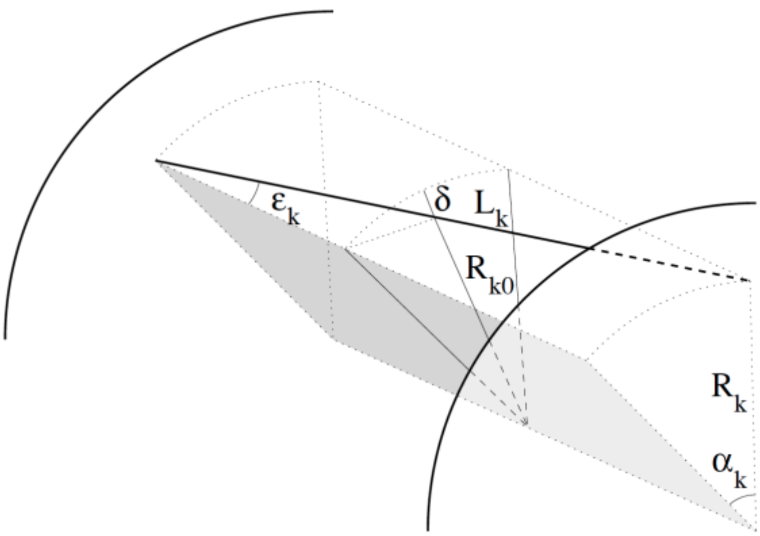

Figure 3.16: Schematic view of the stereo wires configuration

The external radius of the chamber is constrained by the available space inside the COBRA magnet, while its length is set by the necessity of tracking the particle trajectories up to pTC. This reduces any passive material along the positron trajectories, minimizing the contribution of uncertainty in the track length measurement to the total timing resolution and increasing the positron resolution efficiency, i.e. tracks reconstructed in the drift chamber with a corresponding hit on pTC.
The internal radius is large enough so that the low energy e^+ are swept away by the gradient magnetic field without crossing the sensitive volume. The e^+ with momentum larger than 45 MeV/c are tracked until they reached the pTC scintillation tiles, crossing a minimum amount of passive material. Read out preamplifiers, cables and wires supporting structures are placed in regions which are off the positron paths.
Three kinds of wires are used to build CDCH:

1. **guard wire** which have a shaping and closing function of the electric field lines near the radial edge of the active volume. By applying a proper HV, the gas gain in the border drift cells at the innermost and outermost radii is equalized despite the discontinuity. Guards are Silver-plated Aluminum wires with 50 μm diameter;

2. **cathode field wires** which create a ground mesh and define drift cells. Cathodes are Ag-plated Al wires with 40 and 50 μ**m** diameters;

3. **anode sense wires** which collect the charge induced by positrons crossing the chamber. Anodes are Gold-plated Tungsten wires with 20 μm diameter.

The innermost and outermost wires planes are made of guard wires which enclose the sensitive volume. Between the two guard planes, 10 cathode planes and 9 anode planes alternate. Cathodes are stringed in both U and V directions, creating a ground mesh between anode planes. Sense wires planes are stringed at alternating sign stereo angle in order to measure the z coordinate of the reconstructed hits along the beam axis by combining the information of adjacent planes. In one anode plane, sense and field wires alternate in order to form a drift cell together with the field wires of the upper and lower cathode planes. Each drift cell has an almost square shape with 8 field wires surrounding the central sense wire. A sector of the chamber at $z = 0$ is shown in Figure 3.17.

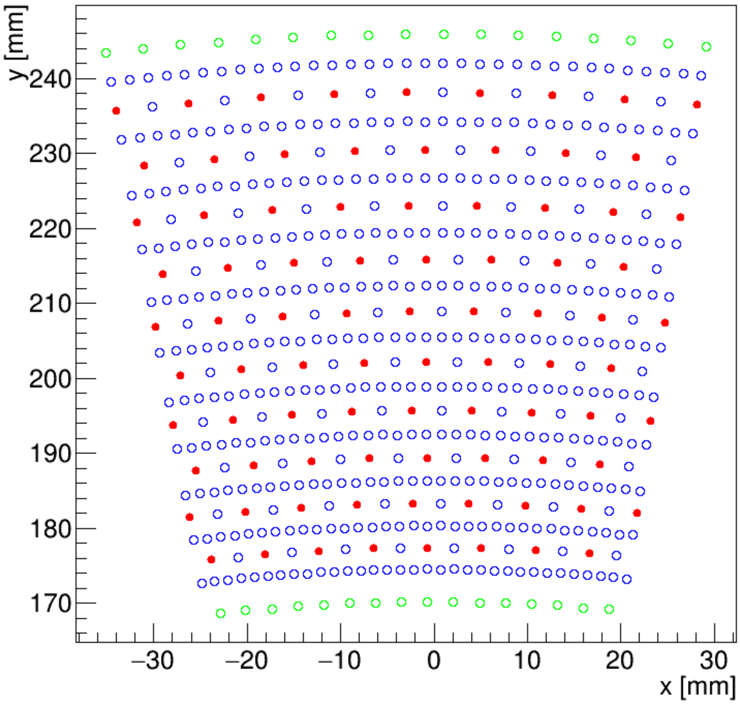

Figure 3.17: Sector of the chamber at z=0: the green dots represent the guard wires, the blue dots the field wire and the red dots the sense wires.

The diameter of the field wires within the cathode and anode planes is 40 μm and 50 μm respectively. Cathodes between anodes are in common between two consecutive cells of the same layer and must withstand a higher electric field avoiding ions multiplication near the wires and consequently the accelerated wires aging. The cells dimensions increase linearly with layer radius and, because of the stereo configuration, also slightly vary with the position along the z axis.

3.4.2 Gas mixture

A very important element for a drift chamber is the gas mixture chosen to filling the sensitive volume. Usually, the mixture consists of a noble gas and a quencher: noble gases are used because they require lower electric field intensity for the avalanches formation, on the other hand, the quencher is required to avoid self-sustained discharge.
The MEG II CDCH requires a highly transparent gas to minimize the MCS, for this reason the choice of a suitable gas mixture fell on a Helium based gas mixture, which has a long radiation length (for pure Helium the the radiation length is 5300 m at STP); moreover it has a high ionization potential respect other noble gas, causes small primary ionization density and a small drift velocity, so that the time separation between consecutive ionization clusters goes from a few ns to a few tens of ns. These features are especially suitable for cluster counting techniques.
Initially, the MEG II drift chamber used an ultra-low mass gas mixture with 85% Helium and 15% Isobutane, then the mixture has been changed to $90\% - 10\%$ and now, due to some aging effect, to this mixture a small content of alcohol (1%) and oxygen (0.5%) have been added [86].

3.4.3 Single-hit resolution measurements with prototypes

The geometry of the CDCH provides a good spatial resolution thanks to the high granularity and the stereo configuration of the wires, that allows a precise measurement of the z coordinate. Moreover the choice of a light gas and thin wires minimized the mass of the detector, reducing the multiple scattering contribution and improving the overall performance. The single-hit resolution was measured using three different prototypes operated with a Helium and Isobutane gas mixture similar to the one used in the MEG experiment. The measurements were performed with cosmic rays, electron beams and radioactive sources [94].
The different setups used for the single-resolution measurements are described.

Three-tubes prototype

A system of three parallel copper drift tubes, having 8 mm internal diameter, 30 cm length and 500 μm wall thickness, has been used for a first check of the performance of a drift cell similar to the one of the MEG II drift chamber. Anodes are 20 μ, gold-plated tungsten wires. The voltage has been set at 1500 V.
The middle tube has been staggered respect to the outer ones by $\Delta = 500\mu$m, as shown in the scheme reported in Figure 3.18 (Left).

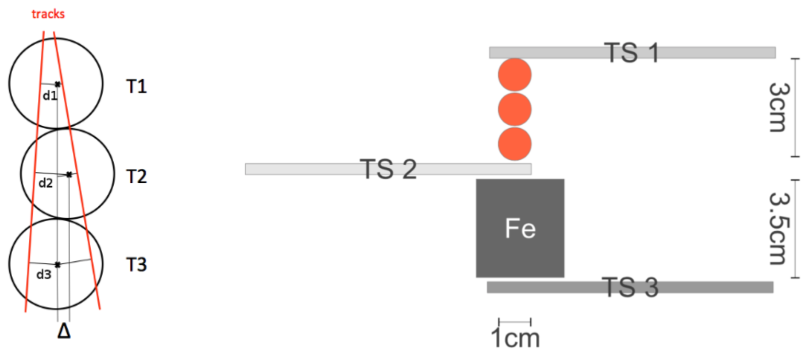

Figure 3.18: Left: distances between a normal-incident cosmic ray and the sense wires. Right: schematic view of the 3-tubes experimental setup. The 3 trigger scintillators (TS) and iron degrader are highlighted [94].

The cosmic rays trigger consists of the coincidence of three plastic scintillators (Figure 3.18 (Right)): two of them are placed above and below the tubes, the third one is placed under 3.5 cm thick iron slab in order to select tracks as vertical as possible and to remove the low-energy component of cosmic rays.

Three-cells prototype

The second prototype has a square cell geometry and it consists of three adjacent drift cells, to simulate, at a given z, shape and dimensions of the MEG II drift chamber cell (Figure 3.19 Left).

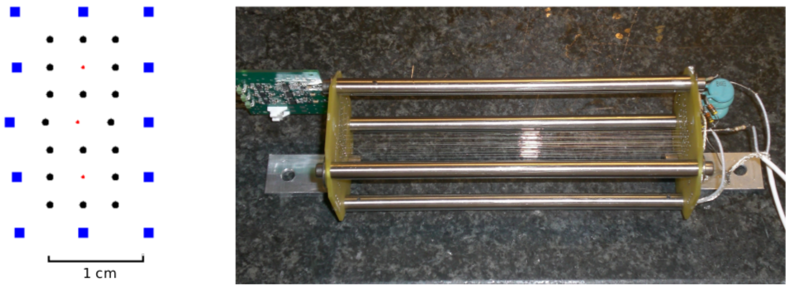

Figure 3.19: Left: Scale schematics of the three-cells configuration with anode wires (small red circles), cathode wires (big black circles) and guard wires (blue squares). Right: schematic view of the 3-tubes experimental setup. [94].

The central cell is staggered by 500 μm. The wires are 20 μm gold-plated tungsten anodes and 80 μm silver-plated aluminum cathodes and guard wires. Guard wires surrounding the three cells are included for a proper definition of the electric field inside the cells. The prototype, shown in Figure 3.19 (right), operated with helium-isobutane 85-15. Wire voltages are set at 1700 V on the anode wires and 375 V on the guard wires, with respect to the grounded field wires, resulting in a gain in excess of several times 10^5.
Measurements of time-to-distance relations and spatial resolution are performed by irradiating the prototype with a ruthenium source. A plastic scintillating counter is placed on the opposite side with respect to the radioactive source to provide a trigger signal. A 500 μm thick Cu foil is placed on the scintillator to select only the high energy component of the ruthenium spectrum, as shown in Figure 3.20.

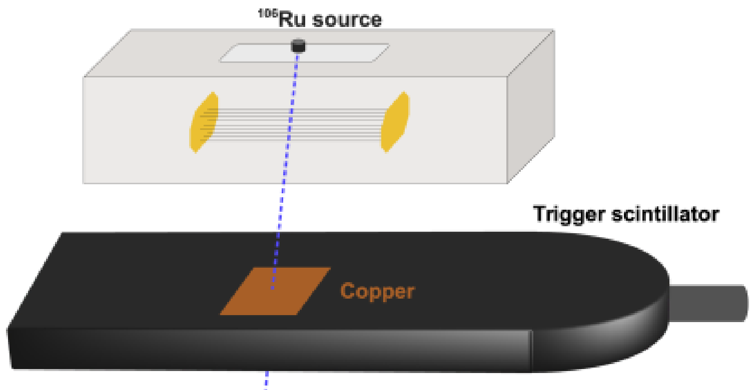

Figure 3.20: Schematic view of the three-cells prototype [94].

Multi-cells prototype

The third prototype is a multi-cells prototype enclosed in a $200 \times 200 \times 500\ mm^3$ Al structure, closed by two Al faces and two golden endplates. It has an 8×8 of 7 mm square cells with 25 μm Au-plated tungsten sense wires and 80 μm Au-plated tungsten cathode wires. The voltage on the sense wires is 1620 V. This prototype operates with a gas mixture of 89%He and 11 % iC_4H_{10}.
The multi-cells prototype was illuminated at the Beam Test Facility of the INFN Frascati National Laboratories, where an electron beam of 447 MeV/c momentum with an average

multiplicity of one particle per spill was used. The drift chamber prototype was placed perpendicularly to the beam axis, on a precision moving table. Upstream of the prototype a pixelated detector allowed the visualization of the beam spot while about 4 m downstream of the prototype a calorimeter was used to count the number of electrons per spill. A schematic view of the experimental set up is illustrated in Figure 3.21.

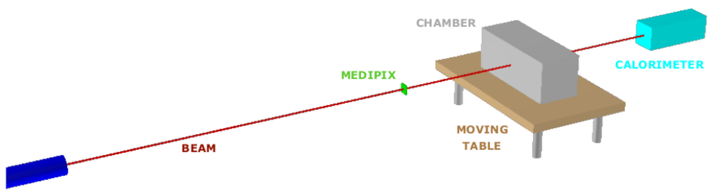

Figure 3.21: Schematic view of the experimental set-up for the multi-cells prototype [94].

The three-tubes and three-cells array prototypes allow to measure the average (over almost all the drift distance range) single cell resolution.
As shown in Figure 3.18 left, for almost vertical tracks traversing all three cells and not passing in between the sense wires, the displacement estimator S of the central sense wire is:

$$S \equiv \frac{d_1 + d_3}{2} - d_2 \backsimeq \pm\Delta \tag{3.9}$$

where Δ is the stagger of the central wire (500 μm) and d_1, d_2, d_3 are the impact parameters respectively on the first, second and third cell. The distribution of S, shown in Figure 3.22 left for the three-tubes prototype and in Figure 3.22 right for the three-cells prototype, is bimodal as expected from equation 3.9.

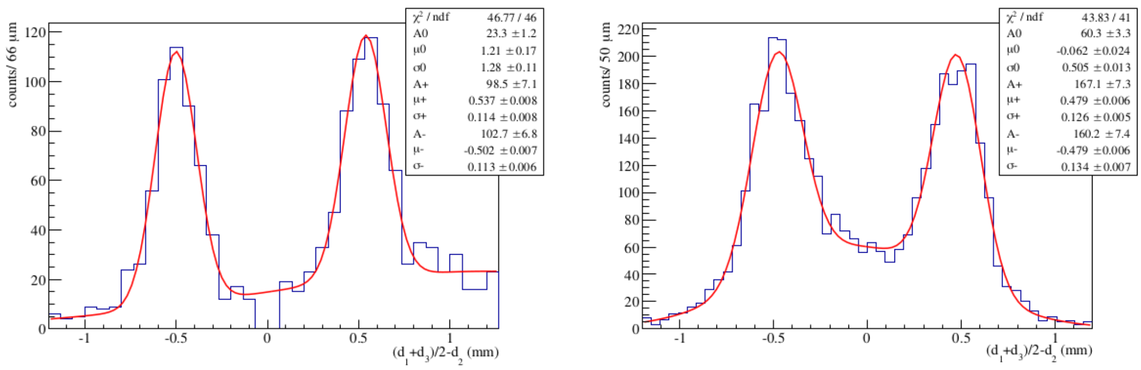

Figure 3.22: Three-tubes (a) and three-cells (b) measurement distribution with helium-isobutane 85%–15% superimposed with a 3-Gaussian fit [94].

The distribution is fitted with the sum of three Gaussian functions: two of them have a means of $\mu\pm = \pm\Delta$, the other takes into account the wrong track reconstructions or tracks for which equation 3.9 does not hold, in particular those which are crossing the zone between the sense wires. From the fitted value of the peaks position it is possible to measure the stagger value, approximately 520 μm for the three-tubes and 480 μm for the three-cells, in agreement with the expected stagger (500 μm) taking into account the uncertainties on the positioning of the anode wires. Assuming an equal average resolution for the three cell, $\sigma_{d1} = \sigma_{d2}\sigma_{d3}$ and taking the variance of S from Equation 3.9, by using the using the peak widths σ_S^+ and σ_S^-, an estimation of the σ_{HIT} is obtained:

$$\sigma_{HIT} \approx \sigma_d \approx \frac{2}{3}\left(\frac{\sigma_S^+ + \sigma_S^-}{2}\right) \tag{3.10}$$

The resolution is 93 ± 5 μm for the three-tubes prototype and 106 ± 4 μm for the three-cell prototype.
The measurement with the three-tubes prototype was repeated with different helium/isobutane content, from 50%–50% to 95%–5%, with the goal of studying the dependence of the single-hit resolution on the gas mixture. The results are summarize in Table 3.1.

Table 3.1: Measured spatial resolution with different Helium:Isobutane gas mixtures [94].

He:Isobutane	σ_{TOT} (μm)
50:50	71 ± 2
75:25	80 ± 4
80:20	90 ± 4
85:15	93 ± 5
90:10	107 ± 7
95:5	115 ± 15

The ionization contribution to the single cells resolution can be modeled as:

$$\sigma_d = \sigma_0 + \alpha N \tag{3.11}$$

where N is the average number of ionization clusters created in the gas volume, while σ_0 and α are free parameters. Taking a certain helium fraction f_{He}, the average number of ionization cluster is: $N = f_{He}N_{He}+(1-f_{He})N_{Ib}$, where $N_{He} = 7.4/cm$ and $N_{Ib} = 54/cm$ are the average cluster densities for helium and isobutane, respectively. The multiple scattering contribution is added in quadrature, so that:

$$\sigma_{tot} = \sqrt{\sigma_{SM}^2 + (\sigma_0 + \alpha N)^2} \tag{3.12}$$

The spatial resolution as a function of the He fraction is reported in Figure 3.23: the data are well fitted by the relation 3.12.

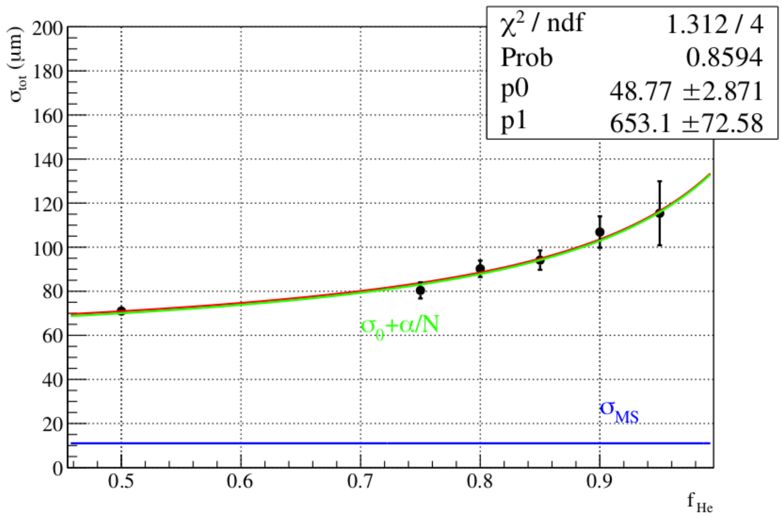

Figure 3.23: Spatial resolution as a function of the He fraction [94]

Measurements performed with the multi-cell prototype show that the resolution of the detector amounts to about 100 μm.
The combined results of these experiments lead to a single hit resolution less than 120 μm, but for these tests only the information from the first ionization cluster was used.

Cluster Timing (CT) technique

The use of a low-Z gas mixture such as 90% He-10% iC_4H_{10} is essential for minimizing the MCS. Moreover, the high He ionisation potential of 24.6 eV is such that a crossing particle produces only a small number of primary electron pairs (around 12 cluster/cm at m.i.p.). In combination with the small drift cells size (few mm), this enhances the contribution to σ_{HIT} coming from the statistical fluctuation of the primary ionization along the track. This brings to a bias in the measurement of the impact parameter, if only the first arrival electron is used for timing. Figure 3.24 shows the σ_{HIT} as a function of the impact parameter as measured by the KLOE experiment, for a gas mixture of 90% He-10% iC_4H_{10}

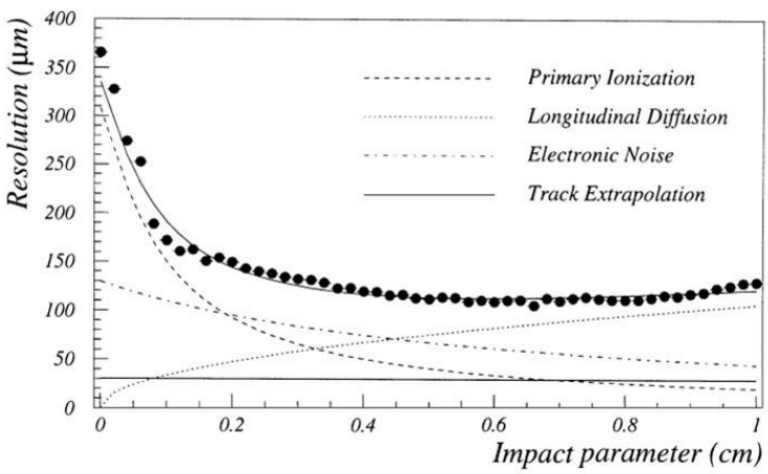

Figure 3.24: Measured σ_{HIT} versus impact parameter in Kloe [93].

In CDCH range of interest, less than 3.5 mm, the contribution of primary ionization dominates. As opposed to the traditional determination of the impact parameter, the goal of MEG II drift chamber is to implement the cluster timing technique [92], [95], which measures the arriving time of all the individual clusters, minimizing the bias and improving the σ_{HIT}.

3.4.4 Wiring procedure

The CDCH is the first cylindrical drift chamber built in a modular way [89], [91], [96].
The CDCH gas volume is delimited by a thin 20 μm Mylar foil at the innermost radius and a Carbon Fiber (CF) support structure at the outermost radius. The Mylar foil separates the active volume from the target volume, called COBRA volume, which is filled with He: the choice of the light gas in this volume and of the light separation foil minimizes the material crossed by the decay products.
The high wire density, 12 wires/cm^2, makes the use of the feed-through technique impossible and requires a completely new design. The innovative approach followed consists of separating the wire anchoring function by the mechanical and gas containing ones. This leads to create frames of multi-wires, by soldering the wires between on 400 μm thick ad hoc Printed Circuit Boards (PCBs).
The chamber is assembled by stacking on the wire support endplates alternatively a multi-wires frame and a spacer, as shown in Figure 3.25.

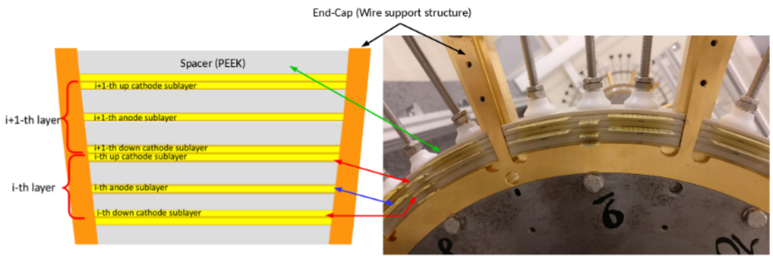

Figure 3.25: Schematic view (left) and real picture (right) of the stack [97].

Despite to the conceptual simplicity of the building strategies, to ensure the electrostatic stability of the drift cells, great precision is needed in the following aspects: the end-plates and the spacers have to be numerically machined to guarantee the mechanical precision in the wire PCBs positioning; the wires must be placed with a precision of 20 μm and stretched with an accuracy of 0.5 g. These means that a wiring robot must be used to produce the all the multi-wire frames with the right accuracy and homogeneity. More information can be found at [97, 98].

3.4.5 The assembly procedure

39 multi-wire layers were shipped, every three weeks, from INFN-Lecce to INFN-Pisa where the CDCH was assembled. The wire PCBs of the multi-wire planes were kept parallel in order to avoid stresses to the wires at the soldering points. For this reason the assembly procedure was performed with a DEA Ghibli coordinate measuring machine. The machine allows a position accuracy of about 20 μm in the horizontal plane and 40 μm on the vertical axis of the fiduciary markers on the wire PCBs. After passing a mechanical stress test (a repeated

cycle of elongation up to 25% over the nominal tension), and a check of the wire tension by measuring their resonant frequency [99], the multi-wire frame is mounted on the chamber wire support end-plates. The wire support end-plates (Figure 3.25 right) have a helm shape with 12 spokes at 30°, one per sector and are made of gold-plated aluminum with a thickness of 30 mm. They are loaded with a total force of about 3000 N due to the tension on the wires, which is 24.5 g for sense wires, 19.2 g and 29.6 g respectively for 40 μm and 50 μm field wires, and are designed to have a maximum deflection at the extremity of the helm spokes of about 200 μm, a tolerable value given the wire elongation [97, 91].
During the assembly phase, the end-plates have been moved to a shorter distance than the nominal one to avoid the stress on the wire in the procedure. The mounting procedure was performed by using an adjustable arm to release a multi-wire frame from the transport support and, by placing it next to the end-plates for the engagement procedure, to transfer the multi-wire frame on the end plates between two spokes.
The final positioning was driven by hand through dedicated nippers. The wire PCBs were glued on the peek spacer with a double-sided tape previously applied on the inner layer. This procedure was repeated for each of the 12 sectors and for the 9 layers.
After mounting the outermost layer, the end-plates were moved to the nominal distance and the CDCH was closed with the outer structural carbon fiber cylinder. Then the end-plates were sealed to prevent gas leakage by using the ThreeBond 1530 glue[3] and the Stycast 2850 resin[4]. After the sealing the CDCH was shipped to PSI. Before the insertion of the CDCH into the experiment it was equipped with the front end electronics, their supports and cooling pipes [91], [97]. Figure 3.26 shows the drift chamber fully wired on the assembly structure.

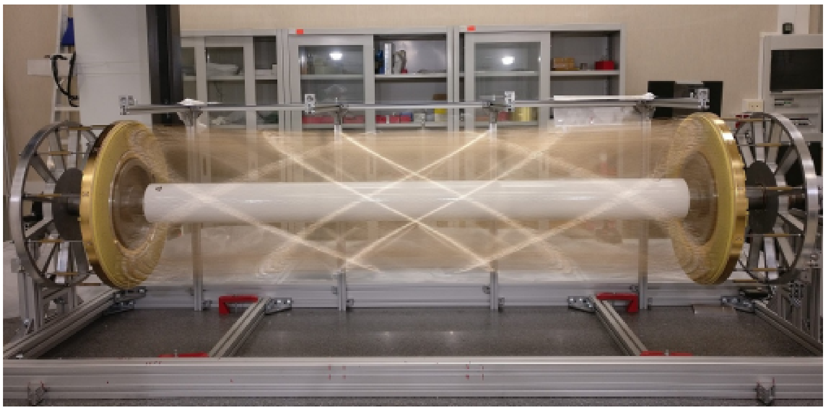

Figure 3.26: The MEG II CDCH fully wired on the assembly structure [91].

3.4.6 Front end electronics

Front-end electronics plays an essential role in drift chambers for time resolution and spatial resolution. So that, a high performance front-end electronics, characterized by low distortion, low noise and a wide bandwidth has been developed with the purpose to implement cluster timing techniques [100].
Figure 3.27 shows the schematics of a FE board.

[3]https://threebond-europe.com/it/products/tb1530/
[4]https://www.henkel-adhesives.com/it/en/product/ potting-compounds/loctite_stycast_2850ft.html

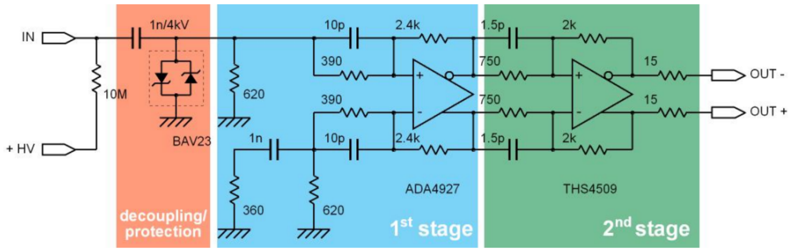

Figure 3.27: Schematics of a FE board [100]

According to the drift cell dimensions, the mean distributed resistance is 140 Ω/m, the mean distributed inductance is 1.2 μH/m and the mean distributed capacitance is 9.4 pF/m; the distributed conductance is negligible. Due to the significant resistance of the wires, the resulting characteristic impedance of the drift cell depends on the frequency, nevertheless its variation is less then 10 % from the mean value of 354 Ω, for frequencies greater then 200 MHz.
Typical signal waveform acquired from the CDCH is a pulses train (Figure 3.28): time separation between the different pulses goes from few nanoseconds to a few tens of nanoseconds. Main signal information is contained within a bandwidth in the order of 1 GHz.

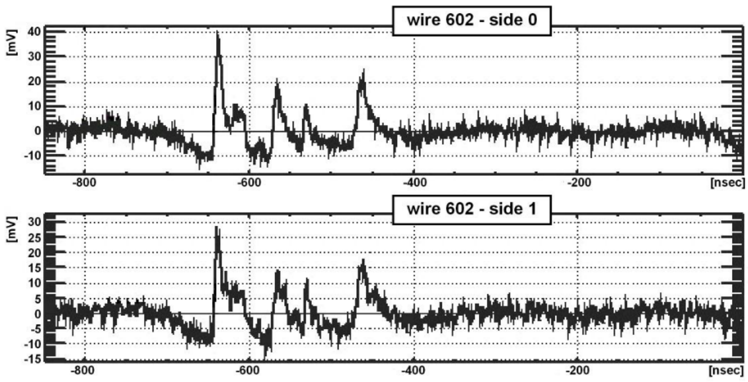

Figure 3.28: Typical signal waveforms measured at both the ends of a drift cell in the MEG II CDCH [100].

The board consists of three stages:

- input stage: decoupling and protection, matches the characteristic impedance of the drift cell;
- first gain stage: amplification with ADA4927 [5] wide bandwidth, low distortion, low noise, high speed differential amplifier with a current feedback;
- second gain stage: amplification with the fully differential operational amplifier THS4509[6] and handling of the output of the board.

[5]Analog Device ADA4927. https://www.analog.com/media/en/ technical-documentation/data-sheets/ADA4927-1_4927-2.pdf
[6]Texas Instruments THS4509. https://www.ti.com/product/THS4509

Figure 3.29 shows a picture of the top and bottom faces of a single board. Each board has 8 channels. Because of the high density of the channels, the boards are designed in three different variants to fit in the small space: type L, type C and type H, the only difference being the position of the output/Low Voltage (LV) connector position. The total number of FE boards needed to readout and power all CDCH wires both US and DS is 432 [100].

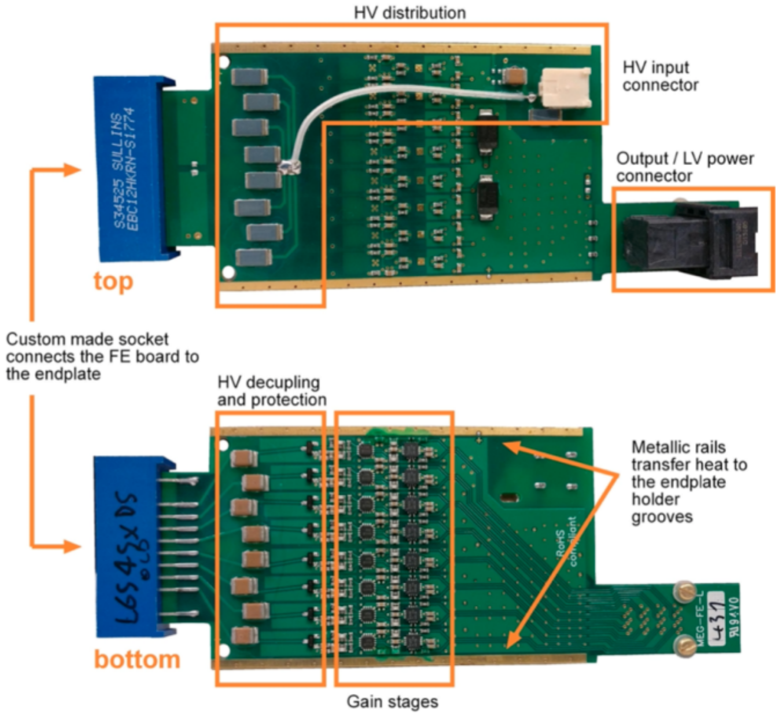

Figure 3.29: Top and bottom sides of the FE board [100]

3.4.7 High Voltage System

The 1728 drift cells of the CDCH are powered in group of 8, with each HV channel powering 1 FE board on one side, which is the US side for almost all the boards. The 216 channels needed are supplied by 9 modules installed in a crate. The modules are 16-channels ISEG EHS F430p[7] with SHV outputs. The SHV cables from the modules output are connected to 3 CAEN A648 SHV-to-Radiall adapters[8], and the 3 Radiall cables are connected to custom patch panels. The HV is supplied to the FE boards by the Draka coaxial cables[9] that are connected to the patch panels. Figure 3.30 shows a picture of the HV crate and of a patch panel [76].

[7]ISEG EHS F430p. https://iseg-hv.com/en/products/detail/EHS
[8]CAEN A648. https://www.caen.it/products/a648/
[9]Draka. https://www.drakauk.com/

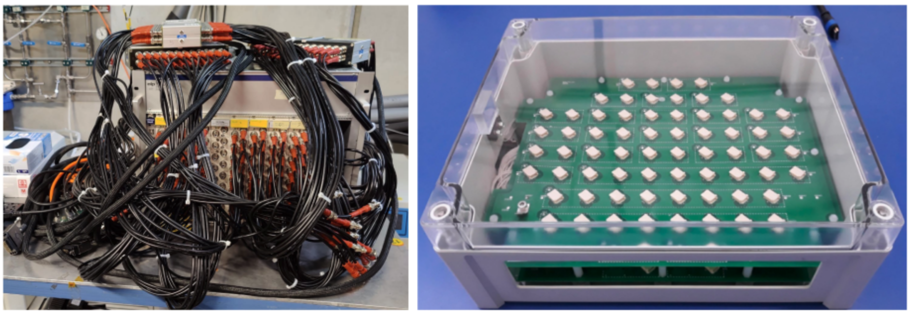

Figure 3.30: Left: Picture of the CDCH HV crate with the 3 CAEN SHV-to-Radiall converters on top of it. Right: Picture of the custom patch panel with the Draka cables connectors.

3.4.8 Gas System

The gas system mixes Helium and Isobutane with the desired percentage, with the possibility to add a other gasses to modify the mixture properties [101].
The final composition of the gas used in MEG II is 90:10 He:iC_4H_{10} with the addition of 0.5% O_2 and 1% isopropyl alcohol to suppress the discharges that were observed during the commissioning period. The system flows 600 ccm in the CDCH active volume and 600 ccm in the COBRA volume and since the two volumes are 360 and 180 liters respectively, one volume exchange takes around 10 hours and 5 hours.
The system allows also to keep the volumes at a pressure slightly over the atmospheric pressure to prevent air from entering the detector: the over-pressures are 10 Pa and 5 Pa in the COBRA and CDCH volumes respectively.
The contaminants and composition of the mixture are measured by three commercial gas analyzers, while a 16 drift tubes small drift chamber measures the gain and drift velocity.

3.4.9 The CDCH problems

Several problems affected the CDCH during its construction and commissioning. The first issue was the unexpected breaking of some wires during the construction, which required a detailed investigation and showed that the problems was traced back to the presence of humidity.
Furthermore, during the first complete HV test with the whole detector powered on, before the start of 2018 pre-engineering run, the detector showed electrostatic instability. This was due to the mechanical tension of the wires being too low, since it was discovered that the more the wires were tensioned, the more the corrosion speed up and was likely to cause their breaking.
The last problem was the presence of discharges inside the active volume, discovered at the end of the 2019 pre-engineering run. From an eye inspection the discharges were found to be correlated to the presence of white areas on the cathode wires.
A solution was found to all these problems and the chamber is under data taking mode now. Nevertheless, there is a chance that the life of the detector was shortened by these events, thus a backup CDCH2 is under construction, with the same conceptual design but slightly different cathode wires.

Wires breaking: a careful study on corrosion

The CDCH observed a drastic effect of the humidity. The reason was identified in some cracks present on the wires surface, probably generated in the last drawing phase of the wires, named ultra-finish. This conclusion is a result of a careful and extremely detailed analysis of the wires at the microscope. The 40 μm wires, which underwent a more stressful ultra-finish procedure, showed more cracks. Such cracks allowed the water molecules to start a corrosion process that ended in the breaking of the wire. This phenomenon happens only in presence of a silver coating: the galvanic coupling between Ag and Al, in fact, makes the localized corrosion possible [102]. Figure 3.31 shows a picture of two wires taken with the Scanning Electron Microscope (SEM): the first one on top highlights the presence of cracks on the surface of the wire, while the second at on bottom is an image of the breaking point.
An Energy-Dispersive X-ray Spectroscopy (EDS) analysis of this region showed the presence of several contaminants, not strictly related to the aluminum or silver alloys used for wire fabrication; traces of chlorine and other halogen elements are visible in some cases (Figure 3.31). Independent tests performed outside of the CDCH showed the same phenomenology when the wires where sprayed with water. Wires stored in a dry environment didn't show any sign of aging, while wires exposed to a humid atmosphere quickly started to deteriorate.

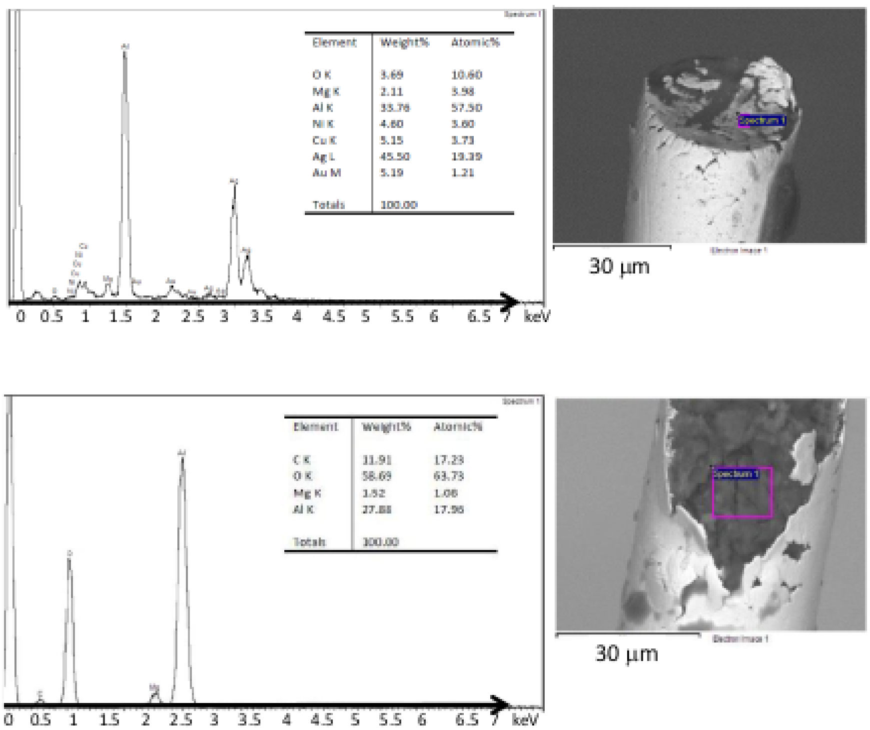

Figure 3.31: Examples of pictures of broken wires taken with a $\times 2500$ magnification SEM. The results of the X-ray spectroscopic analysis and the relative concentrations of the materials extracted from the spectral analysis are also reported. The energy scales are in keV.

Another interesting feature came up: the deterioration is sped up by stretching the wires, so that an extra stretching of the CDCH was performed after the first run to let all the weak wires break. Removing the broken wires and returning back to the original wire tensioning

prevents wire breaks due to corrosion during the CDCH operation.
A phenomenological model of the number of breakages as a function of exposure to relative humidity and mechanical tension was developed. The model matches very well the experimental observations and predicts the rate of broken wires. This allowed to calculate a safe amount of exposure to humidity and extra stretching without the risk to break more wires [102].

Electrostatic instability

Electrostatic instabilities came up in the CDCH during the first HV test, before the installation in the experiment in the second half of 2018. Above a bias voltage of 1000 V, the wires in the inner layers started to show high fast oscillating currents up to 150 μA, much higher than expected, which is explainable as the effect of the anodes and the cathodes in a drift cell approaching and finally touching each other. The cause of this phenomenon is the insufficient mechanical tensioning of the wires, adopted after the wire breaks to slow down the corrosion process. This effect disappeared by lowering the HV below a certain value, which was variable according to the layer and consequently to the cell size. The inner cells, the smallest ones, were the most problematic. The outer cells were brought, without critical issues, to the expected HV working point, which was estimated by simulations, to be 1400 V, outermost layer 1480 V, innermost layer, reducing/increasing by 10 V for each subsequent layer.
Sometimes the instabilities cause two wires to attach, creating a permanent short circuit; to avoid the severe damages that they can caused, a safety feedback in the HV system was implemented. This ramps down the HV of the whole detector when the current on a wire exceeds a threshold for a selected amount of time (order of 100 μA and 1 s). The permanent shorts found in the CDCH were isolated on the corresponding FE board. The issues related to the electrical instability have been solved by increasing the operating mechanical tension of the wires, operation performed during the re-opening of the detector happened after the pre-engineering runs to remove the broken wires. The over-stretching of the CDCH allowed also to remove most of the permanent shorts, making the wires detach from each other.

Discharged in the active volume

The CDCH suffered a problem of discharges on the sense wires when exposed to the full intensity muon beam.
For the first time, this phenomenon appeared at the end of the 2018 pre-engineering run: the discharges started when the beam was on and didn't disappear by blocking the beam, but only when the HV was lowered enough to stop the amplification of the internal avalanches started by the electrons, at values around 800 V. The HV threshold at which the currents appeared/disappeared varied in time and were also different for different sectors of the CDCH. The effect of these discharges was a large current readout on the sense wires: it reached values up to $\approx$ 350 μA on some wires, but the effect was not uniform, since there were areas completely unaffected. Figure 3.32 shows an example of the second layer current readout from the ISEG HV system connected to MIDAS, where the currents affected many sectors and reached values up to 350 μA, very high with respect to the expectations of $\approx$ 20-30μA and possibly dangerous for the detector.

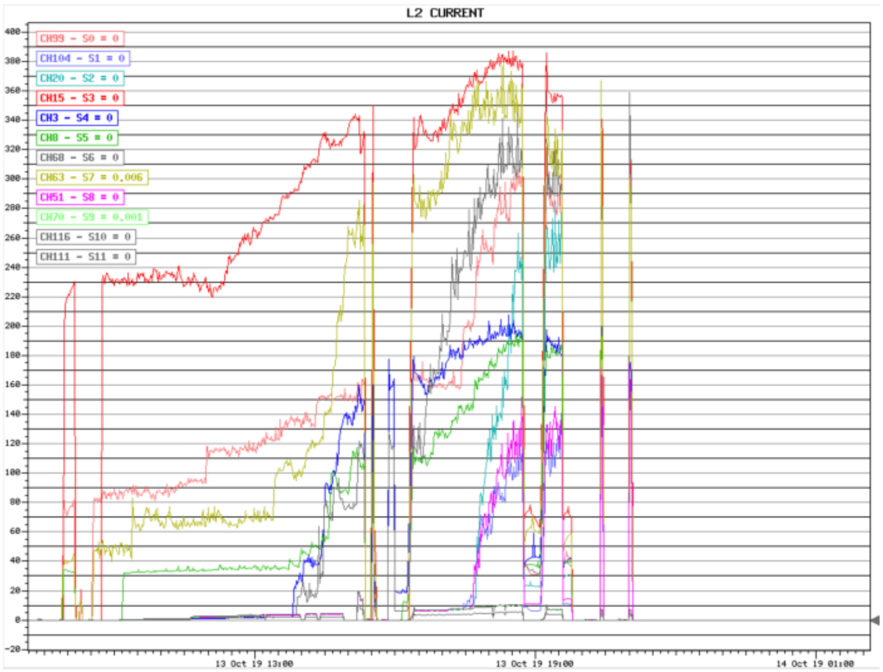

Figure 3.32: MIDAS history plot of the CDCH current on layer 2 during 2019 run. The vertical axis is the current in μA, the horizontal axis is the time.

The same problem persisted during the 2019 pre-engineering run, causing difficulties during the muon data taking. Indeed the high currents showed up erratically even without the exposure to the muon beam. After several investigations, it turned out that the cause of the currents was the presence of discharges in certain specific areas of the CDCH. The investigations consisted in the direct observation, thanks to a plexiglass shell temporarily installed instead of the usual CF shell, of some corona discharges visible by eye in several spots thanks to the Plexiglas' transparency. Upon closer inspection it was discovered that the discharges showed up in white areas, where the cathode wires presented this different color instead of the usual one. Ten areas were found, distributed almost flatly along the longitudinal z and azimuthal ϕ coordinate.
Figure 3.33 shows a picture of one of such areas, along with an example of the signals that generates the high currents, present on both endplates readout, which are larger and broader than the signals expected for positrons. This strange phenomenology can indicate that some areas of the detector have suffered from ageing more than it was expected for the time, maybe due to the other issues that affected the CDCH during the years.

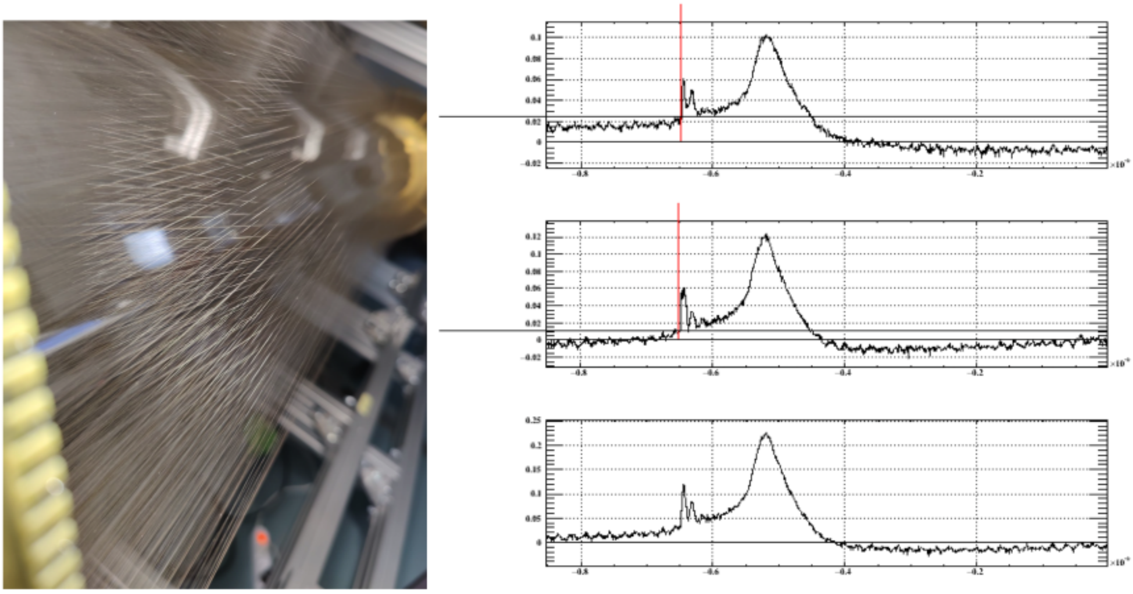

Figure 3.33: Left: White region where the discharges have been observed by eye. Right: CDCH signal corresponding to the discharges. The first two waveforms are readout respectively US and DS, while the third is the sum of the two. The vertical scale is the amplitude in [V], the horizontal scale is the time in [s].

A solution was found to solve this critical issue: modify the gas composition by adding oxygen and isopropylic alcohol to suppress the discharges. Thanks to this solution, the CDCH is currently operating with great success and it is in data taking mode.

3.4.10 CDCH2

Because of the fragile nature of this detector, the construction of a backup CDCH2 is under development. The new chamber has the same design of the predecessor, since it is compatible with the rest of the apparatus, its mechanical structure is highly stable and its performances complies with the experiment requirements.
The only innovation of the new chamber resides is the material of the cathode and guard wires. This is because of the discovery of the present wires weakness to humidity, caused by the cracks in the Ag coating from which a corrosion process may start. To avoid this problem several kind of wires have been considered, with both 40 and 50 μm diameters: pure Al (50 μm), Al/Ag (40 - 50 μm), Ti (50 μm), Al/Au (40 - 50 μm), Ti/Au(50 μm) and Cu (50 μm). The final choice is using 50 μm the pure aluminum wire (Al 5050), avoiding coating and the 40 μm diameter.

3.4.11 Commissioning

After its installation in the PSI experimental area in 2018, the CDCH was able to take data during four pre-engineering and engineering runs [103]. From 2018 to 2021 the CDCH operation was tested and several problems have been found and solved.

The pre-engineering phase: 2018

The pre-engineering run of 2018 was the first one with the CDCH installed in the experiment. The electrostatic instability didn't allow to reach the HV working point in the inner layers and since the readout electronics was not completely available yet it was only possible to readout a small portion of the detector. This run aimed to test the possibility to operate the CDCH inside the experiment and to take the first data both with cosmic rays and muon beam. Other important tasks were the estimation of the working point both for HV and gas mixture, the test of the stability of the detector under the muon beam, the preliminary estimation of the gain and the test of the wire-by-wire time calibration procedure.
Figure 3.34 shows the result of the HV scan with a 90:10 gas mixture (He:Isob) extrapolated from cosmic rays data: here the actual gain is not quoted because of the large uncertainty on the electronics gain, nonetheless it was interesting to see the behavior of the mean amplitude of the signal as a function of the HV. By confronting thess data with the Monte Carlo simulations, it was decided to use as a working point the 90:10 mixture and the HV from 1480 V to 1400 V from L1 to L9, decreasing at step of 10 V for each layer to compensate the smaller dimension of the drift cells.

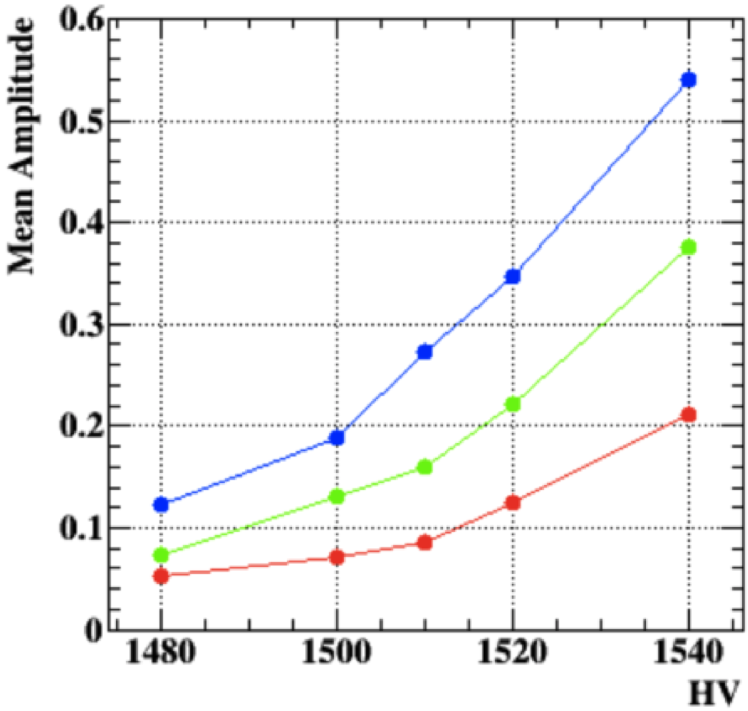

Figure 3.34: Mean amplitude as a function of the HV for L1 (red), L2 (green) and L3 (blue).

The behavior of the detector with the muon beam was also studied during this run. The positrons that produced the signal in the detector were originated in the Michel decay of the muon. The Michel events were triggered by a hit on a tile of the pTC. Three different muon beam intensity were tested: low intensity 6×10^6, MEG intensity 3×10^7 and MEG II intensity 7×10^7. Figure 3.35 shows an example of a signal from a Michel positron, where the different signals are highlighted by pink arrows.

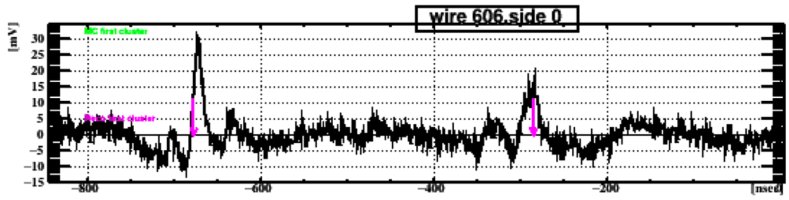

Figure 3.35: Signal from a Michel positron with a pileup event. The arrows indicate the different signals.

The signal shows a low frequency noise problem, which was cured during the pre-engineering run of 2019. The pre-engineering run of 2018 allowed to set a starting point for the next years' run, with an estimate of the working points of the HV and gas mixture and the knowledge of the critical issues in the detector operation.

The pre-engineering phase: 2019

After removal of the broken wires and the extra stretching of the chamber during the first half of 2019, the CDCH was installed again in the experimental area for another pre-engineering run. This run was divided into two phases: the first one with the old 12 WDBs and the second one with 12 additional WDB with a differential input, the WD2A-diff.
The new HV map, in Figure 3.36, shows that the instability issues were solved, indeed the HV working point was reached for all the layers, with the exception of only few drift cells. It was therefore possible to look at signals in the inner and outer part of the CDCH. However, the discharges issue was even worse than the previous year, therefore it was impossible to take any Michel data for the analysis. Nonetheless a good set of cosmic rays data were taken to be analyzed and compared to the previous year's set. The introduction of the new WDB was crucial for the data analysis thanks to the noise reduction. In fact the low frequency noise disappeared after removing the differential to single-ended conversion boards needed with the old WDB, as shown in Figure 3.37.

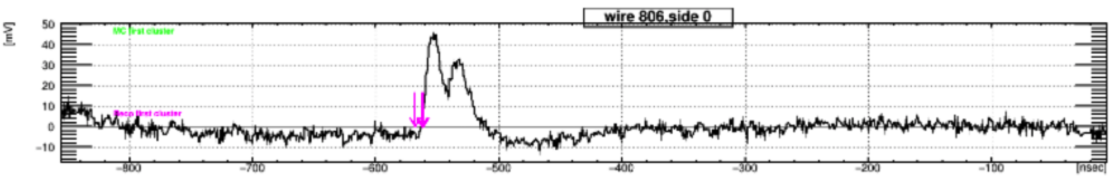

Figure 3.37: Example of a cosmic ray signal with a WD2A-diff without software noise reduction.

Though it wasn't possible to collect Michel data due to the discharges issue, the cosmic rays data collected were used to better understand the CDCH behavior.
Moreover the comparison of the data with those of the previous year at least for L1, L2 and L3 at 1480 V, showed the impact of the electric field unbalance of 2018. The mean amplitude showed in Figure 3.38 is slightly different from the one calculated the previous year, mostly for L3. The expectations from the MC simulations and the results obtained from actual data were in disagreement, indicating that the electronics gain estimate still had to be improved.

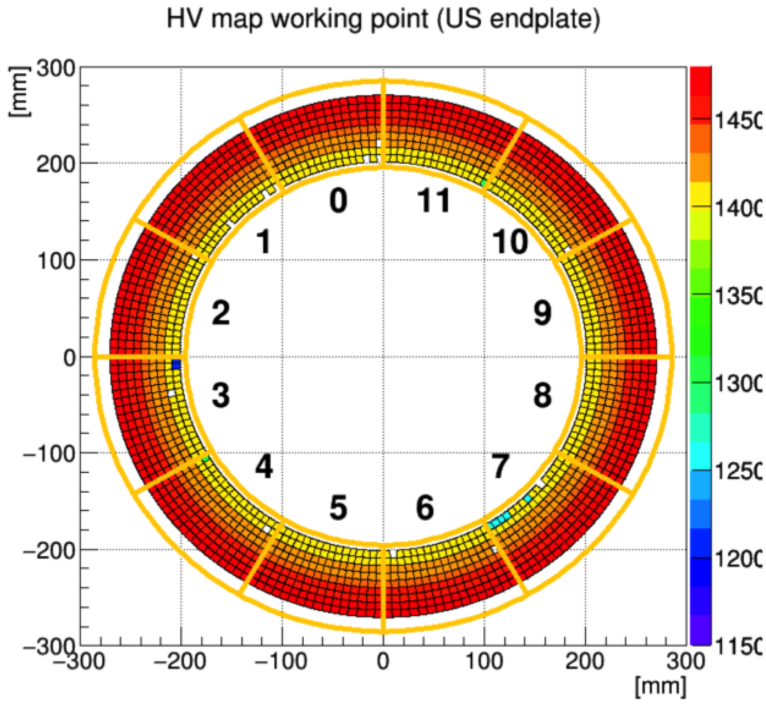

Figure 3.36: CDCH HV map during 2019 pre-engineering run

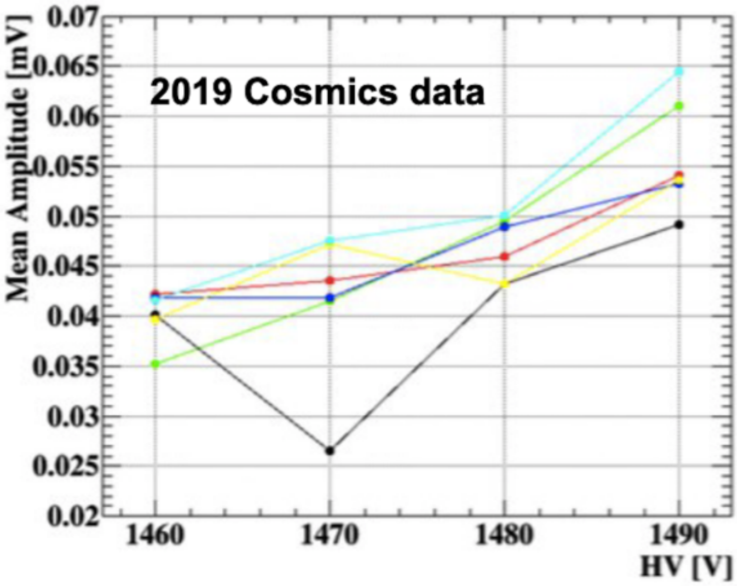

Figure 3.38: Mean amplitude as a function of HV from 2019 CR data. Each curve represents a layer: L1 (red), L2 (green), L3 (blue), L4 (black), L5 (yellow), L6 (cyan)

The pre-engineering phase: 2020

The CDCH was opened in 2020 to remove the residual broken wires and install the Plexiglas shell to investigate the detected discharges. After inspection, the detector was installed in the

experiment.
The main goal to be achieved in this run was the improvement of the stability of the detector under the muon beam thanks to the use of small percentages of additives to the gas mixture. Different additives were tried in the gas mixture to mitigate the discharges: dry air, oxygen, water and isopropyl alcohol. The electron attachment that happens in the presence of the additives molecules prevents the creation of discharges that generates high current on the wires.
After some tests with water and different percentages of oxygen, the additive chosen were oxygen (0.5 %) and isopropyl alcohol (1 %): the first gas was flowed in the extra line of the gas system, while the alcohol was brought to the CDCH active volume by flowing a small percentage of the He flux inside a bubbler containing the liquid. Figure 3.39 shows the effect of the oxygen on the signal amplitude.

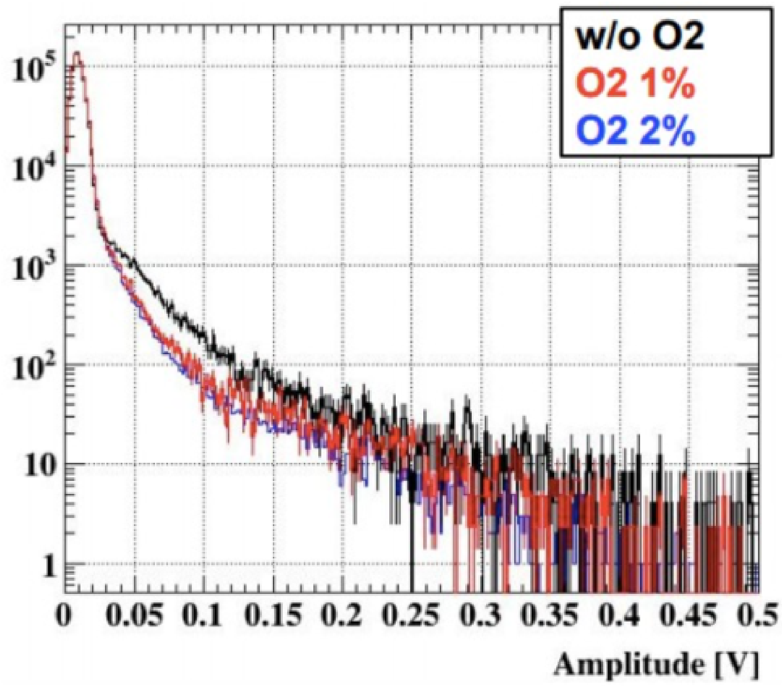

Figure 3.39: Example of amplitude distributions from cosmic rays data with H_2O and different concentration.

The relative gain drop from the 0% case is evident, and ranges from 20% to 30% for 1% and 2% O_2 concentration respectively.
Figure 3.40 shows the number of hits per track as a function of the drift distance in the same dataset: there is a 7%-9% relative drop in the number of hits on track when the O_2 concentration is set 1%-2%.

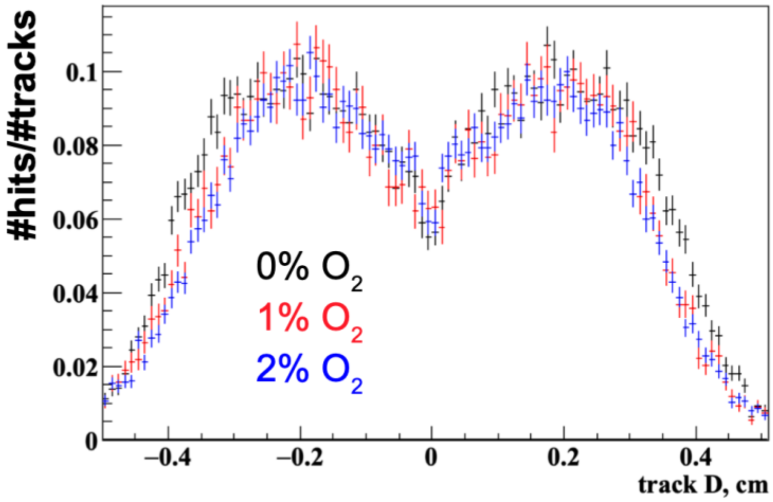

Figure 3.40: Number of hits per track vs drift distance calculated from cosmic rays data with H_2O and O_2.

During 2020, new FE boards with increased gain were tested, in this way the overall gain has been increased without increasing the gas gain, which would speed up ageing of the chamber.
Figure 3.41 shows a schematic of the readout, optimized to reconstruct some positron tracks. The three different colors used in the image are for the three different FE boards used: one with the standard gain as in 2018 and 2019, one with x2 gain and one with x4 gain.

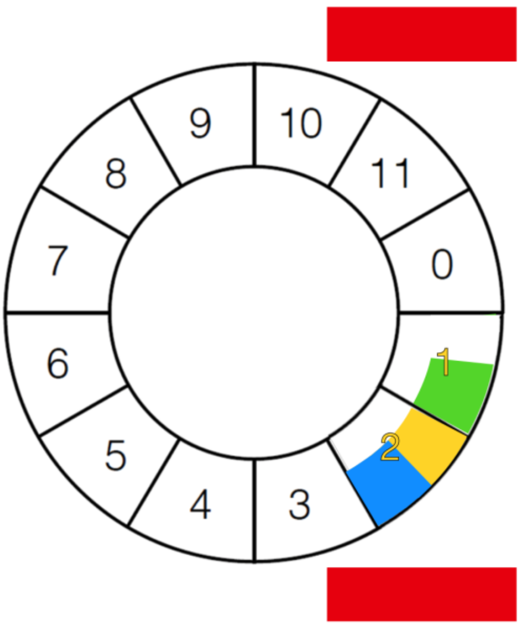

Figure 3.41: Schematic view of the CDCH readout configuration used during 2020 pre-engineering run. The three colors represent the different FE board gain: standard gain (green), x2 gain (yellow) and x4 gain (blue).

Monte Carlo simulations were improved to include a proper simulation of the electronic chain, allowing the estimation of the overall gain, which is the product of the gas gain and the FE gain. In Figure 3.42 an example of waveforms from simulation and data with a distribution of the maximum amplitude for a cosmic rays dataset with the 90:10 mixture with the addition of water is shown. The amplitude is measured for L3, a sector with standard FE gain and no noise reduction filters are applied.

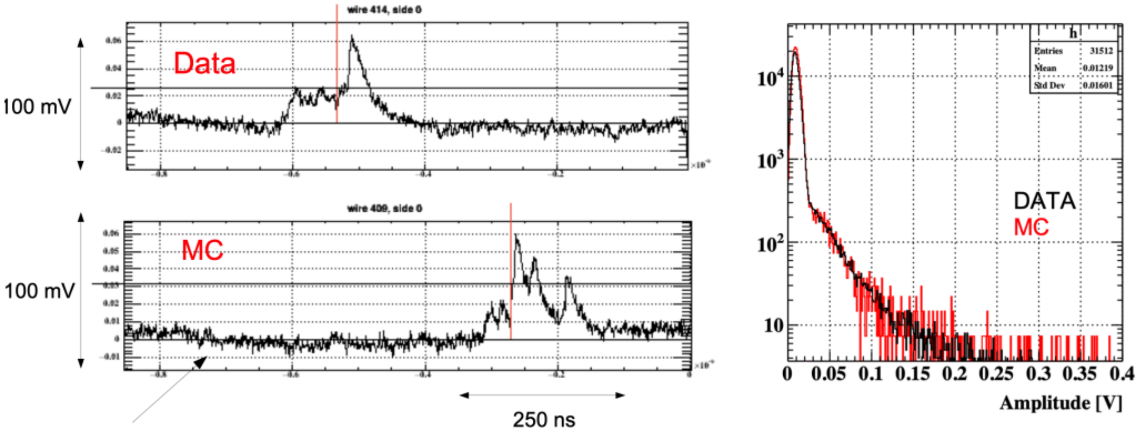

Figure 3.42: Left: Comparison between a waveform from data and a waveform from MC. The time offset can be adjusted in the simulation and will be aligned to the data. Right: Comparison between the amplitude distribution of a dataset with the corresponding MC simulation

The overall gain has been estimated in the standard FE gain configuration, and ranges from 4 to 7 $\times$ 10^5, in good agreement with the design value of 5 $\times$ 10^5.
Finally, detailed study were made about noise reduction, which was improved thanks to the implementation of several software filters: the Median Filter, which is a low-pass filter, the Moving Average, which is a high-pass filter; the Burst noise suppression. Figure 3.43 shows the effect of three of these algorithms and the result of the filter to the time distribution obtained from a dataset of cosmic rays collected with air and water as additives in the gas. It is evident that the filters remove the noise hits, leaving only real hits with good hit times.

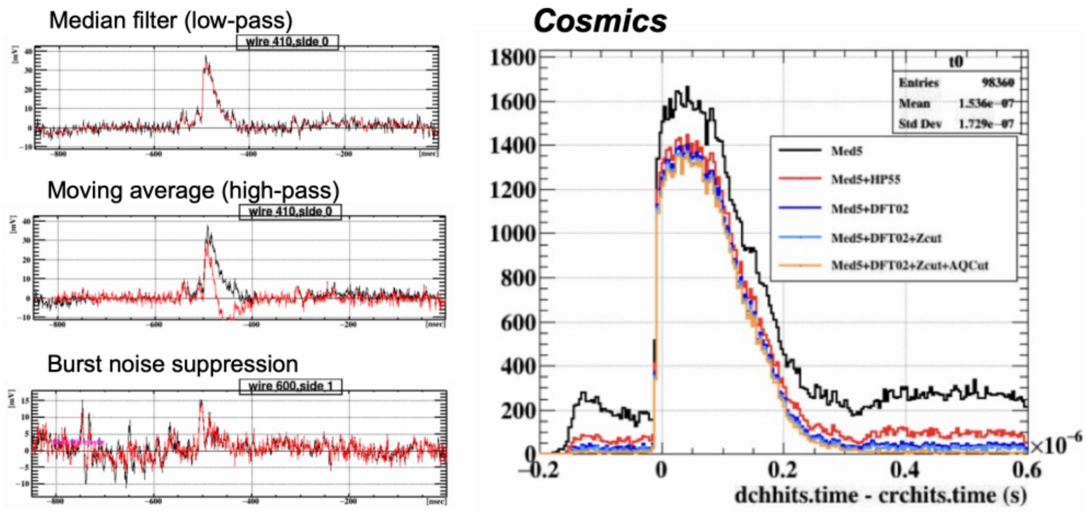

Figure 3.43: Left: Example of filtered waveforms. The original waveform is in black, while the filtered one is in red. Right: Time distribution from a CR dataset. The different colors represent a different combination of the filters applied to the waveforms. Even the application of the high-pass filter alone (in red) drastically improves the shape of the distribution.

The pre-engineering phase: 2021

After the last opening of the drift chamber for broken wires removal, the detector was installed in the experiment. For the first time it was possible to test all the detectors in the final configuration of the physics run. The beam time granted from the PSI to the MEG II experiment in 2021 consists of two parts: the engineering run and the physics run.
The engineering run has the goal to study the long term stability of the detector with the final gas mixture of 90:10 He and iC_4H_10 with 0.5 % O2 and 1% of isopropyl alcohol. The CDCH was equipped with the new FE boards with modified gain and read out with WD2A-diff on 8 sectors of each layers. The Figure 3.44 shows the readout scheme and the map of the short circuits at the beginning of the run.

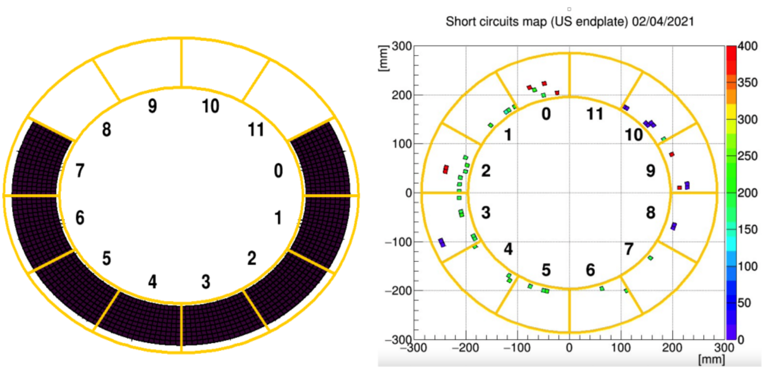

Figure 3.44: Left: CDCH readout channels during 2021 run (SW notation from the DS view). Right: CDCH maps of the short circuits at the beginning of the 2021 run (HW notation from the US view)

The new mixture was sufficient to suppress the discharges without affecting the detector performances, but any small drop in the isopropyl alcohol concentration caused the reappearance of the discharges. Since this concentration depends on the capability of the He flow to capture the alcohol molecules in the bubbler and since this depends on the temperature, a new thermostated bubbler was installed before the physics run. The concentration of the alcohol in the mixture was maintained constant over time and independent from the environmental changes.

During the engineering run, Michel data with pTC trigger were collected. Instead during the physics run it was possible to collect physics data with all the detectors using the $\mu^+ \longrightarrow e^+\gamma$ coincidence trigger. These data allowed to preliminary estimate the resolution and efficiency of the detectors.

Several software improvements were implemented to the analysis code thanks to the data collected during the run. The results of the optical survey performed right after the installation of the CDCH in the experimental area were included for the first time in the code, so to improve the precision on the knowledge of the position of the wires, which is crucial in the evaluation of the tracking performance. The drift time to distance relations (txy tables) were also computed from scratch to take into consideration the new gas mixture with the additives (more details in the next sections).

The gain was estimated in 2021 for all the layers, by using MC simulations: a set of data was simulated with different gain values and then a χ^2 test between the simulated gains and the cosmic rays data collected during the run was performed. The χ^2 trend with the gain was then fitted with a parabola and the position of the minimum of the fit was identified as the best gain estimate. The procedure was repeated for each layer and for each wire end, including the sum of the two ends. The results are shown in Figure 3.45: the gain looks lower on average with respect to 2020, most likely due to the use of isopropyl alcohol instead of water.

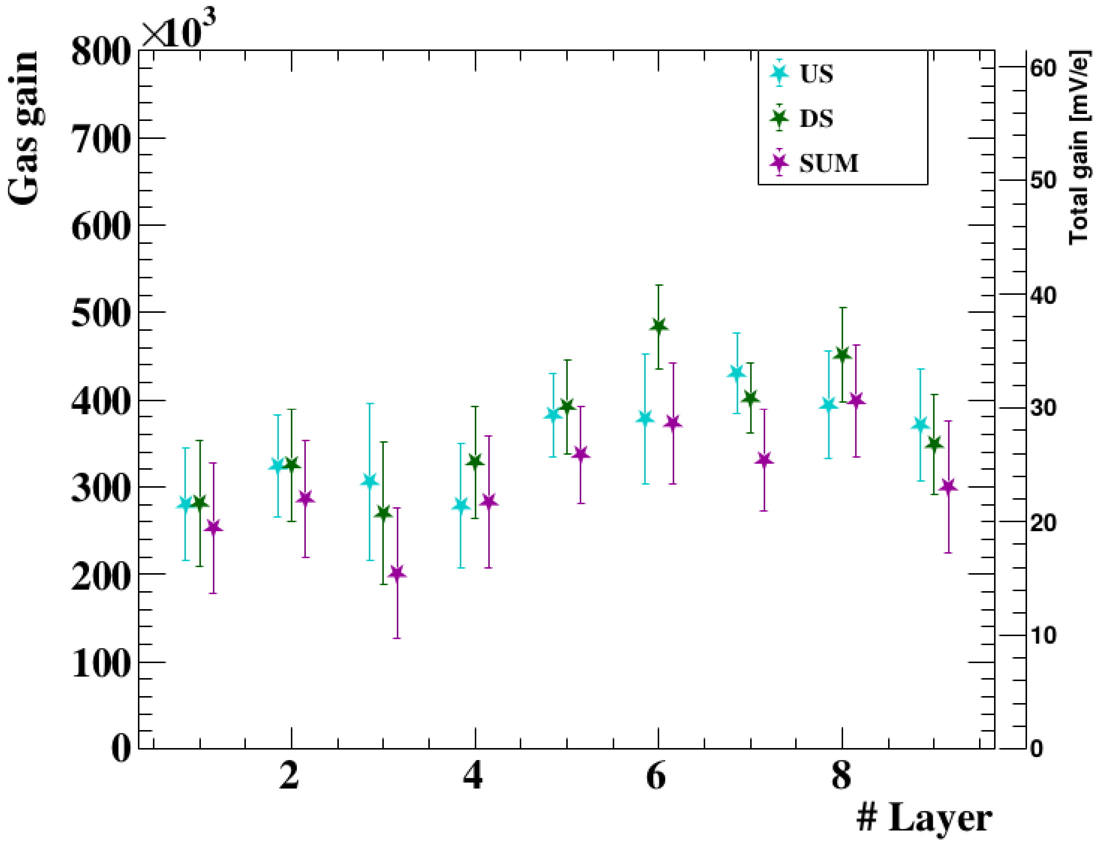

Figure 3.45: Estimated gas gain for each layer and each end. The total gain, that includes also the electronics gain, is reported as well.

Figure 3.46 shows a preliminary estimate of the drift distance resolution, obtained as the width of the distribution of the track residuals and resulted to be 230 μm with the new TXY tables, with a core/tail ratio of 4.2 using a 2σ cutoff.
Unfortunately, the result is a factor 1.6 worse than the MC expectation, which is around 145 μm, mainly due to the non perfect alignment of the CDCH wire of the software.

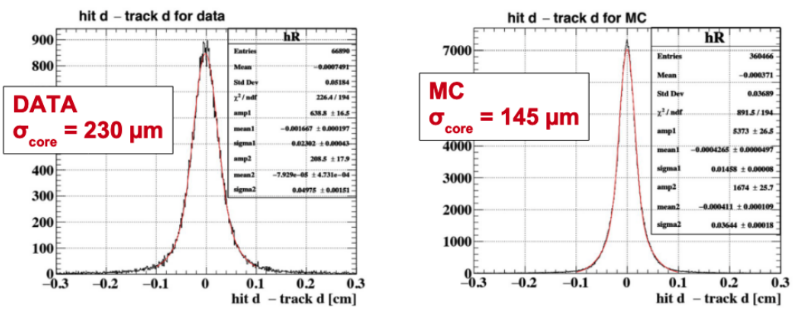

Figure 3.46: Track residuals distribution from data (left) and MC (right).

The physics run: 2022

The long term stability during the 2021 run proved that the drift chamber could be used during the MEG II physics data taking in 2022. Indeed the chamber took data in 20222, without any particular issues and a lot of studies were performed to improve the software analysis.
The detector underwent a maintenance work at the beginning of this year to recover some bad channel and improve the noise status. More in details, a series of 3D-printed plastic wedges were installed in between the endplate sectors to slightly increase the spacing between the FE boards and the metallic holders, responsible for cooling them thanks to an embedded cold water circuit. Accidental contacts between a lateral feedback resistor and the holders could cause an increase in the noise level, propagating to the neighboring boards. This is now solved. Furthermore, a general check of the High Voltage and signal cabling and connections was successfully performed. A damaged cold water inlet tube on the Up-Stream side was also repaired. The HV was immediately set at the working point with a muon beam stopping rate of $3 \times 10^7 \mu^+/s$, currently used.
A great analysis effort is currently ongoing to tune the reconstruction algorithms with continuous developments and improvements. The analysis of 2022 data is ongoing to evaluate the detector performances.

Chapter 4

The MEGII drift chamber constants

4.1 The drift velocity and the velocity monitoring chamber

The cylindrical drift chamber of MEG II has the task o fprecisely reconstructing the trajectory of the positron coming from the muon decay: $\mu^+ \longrightarrow e^+\gamma$.
So that, it is of crucial importance to provide a stable performance of the detector in terms of its electron transport parameters, avalanche multiplication, composition and purity of the gas mixture. In order to have a continuous monitoring of the quality of gas, a small drift chamber, with a simple geometry that allows to measure very precisely the electron drift velocity in a prompt way will be installed in the experiment. The monitoring chamber will be supplied with gas coming from the inlet and the outlet of the detector to determine if any gas contamination originates inside the main chamber or in the gas supply system [104].
The chamber can be described as a small box with cathode walls, that determine a highly uniform electric field inside two adjacent drift cells. Along the axis separating the two drift cells, four staggered sense wires alternated with five guard wires collect the drifting electrons. The trigger is provided by two ^{90}Sr weak calibration radioactive sources placed on top of a two thin scintillator tiles telescope. The whole system is designed to give a prompt response (within few minutes) about drift velocity variations at the ‰level.

4.1.1 Motivations for a drift velocity monitoring chamber

The choice of a gas mixture in a drift chamber is of utmost importance (as discussed in chapter 2), in particular for the experiments, like MEG-II, in which the trajectories of low momentum particles need to be reconstructed with high accuracy. Moreover, it is crucial to control the purity of gas injected in the drift chamber because uncontrolled fluctuations of the gas composition and contamination by impurities would make the drift velocity unstable and could deteriorate spatial and momentum resolution of candidate signal tracks.
Several studies about the behavior of drift velocity as a function of the reduced electric field in a mixture of He and iC_4H_{10} have been performed (two examples are shown in Figure 4.1), which prove that the drift velocity is the most sensitive parameter for the operation of a drift chamber with respect to tiny variations ($\sim$‰) of the gas mixture and so it is the most favorable "target" to be used in order to control the gas purity.

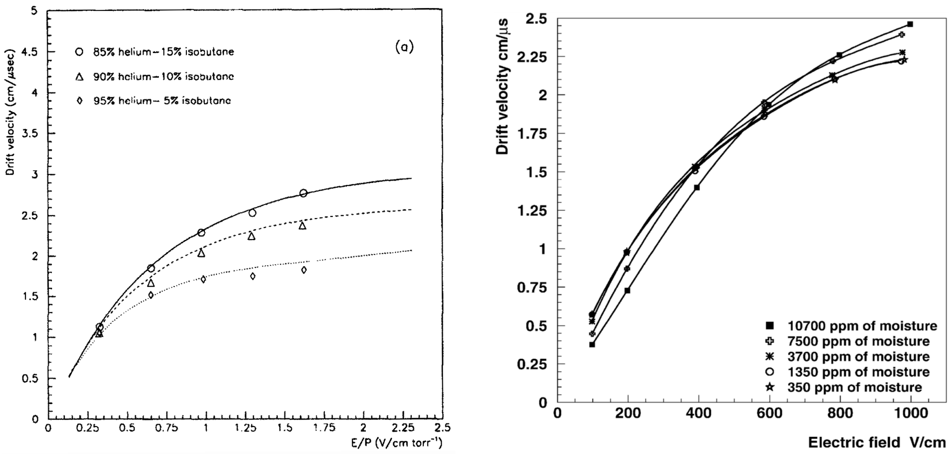

Figure 4.1: Left: drift velocity as a function of the reduced electric field for different percentages of helium-isobutane mixtures [105]. Right: drift velocity as a function of the applied electric field for different concentration of water vapors [106].

As an example, the left graph in Figure 4.1 shows that for a mixture of $He - iC_4H_{10}$ at normal pressure, the variations of the electric field around the operating value of 1 $\frac{V}{cm\,torr}$, of about 2 V/cm induce drift velocity variations of about ‰.
Moreover, to mitigate the aging effect, it is useful to introduce small quantities of water vapors in the gas mixtures, but it is mandatory to control the consequent variations of drift velocity. As an example, the right graph of Figure 4.1 shows that at the operating value of the electric field of about 1 $\frac{V}{cm\,torr}$, variations of ≈ 150 ppm lead to an increase up to 1×10^{-3} in drift velocity.

4.1.2 The monitoring drift chamber

The main goal of the monitoring chamber is to provide a fast response about drift velocity variations at 10^{-3} level.
This purpose can be obtained with a conceptually very simple structure, illustrated on the left side of the Figure 4.2.

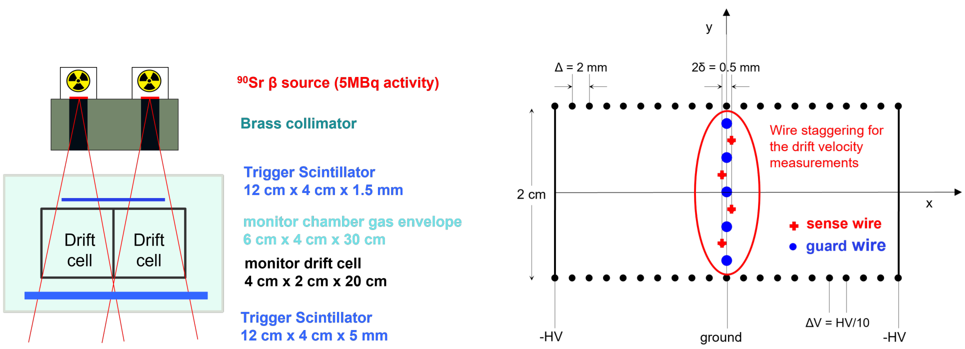

Figure 4.2: Left: schematic of the experimental set up of the monitoring drift chamber. Right: the transverse view of the monitoring drift chamber.

Two ^{90}Sr radioactive sources are placed on top of two thin scintillator tiles telescope. The sources will be collimated to select the tracks crossing the drift cells. The chamber is placed

inside a box and it will be supplied with the gas coming from the inlet and the outlet of the MEG II drift chamber.
The right side of the Figure 4.2 shows the transverse view of the chamber. Along the plane separating the two drift cells, four sense wires (20 μm diameter gold plated tungsten) alternated to five guard wires (80 μm diameter silver plated aluminum) collect the drifting electrons. The drift electric field is defined by two high voltage cathode walls and graded by two wires planes down to 0 V on the symmetry plane, containing the sense and guard wires. The mechanical design is presented in Figure 4.3, with a focus on the central part of the chamber which hosts the custom PCB for the wires staggering (details in section 4.1.6).

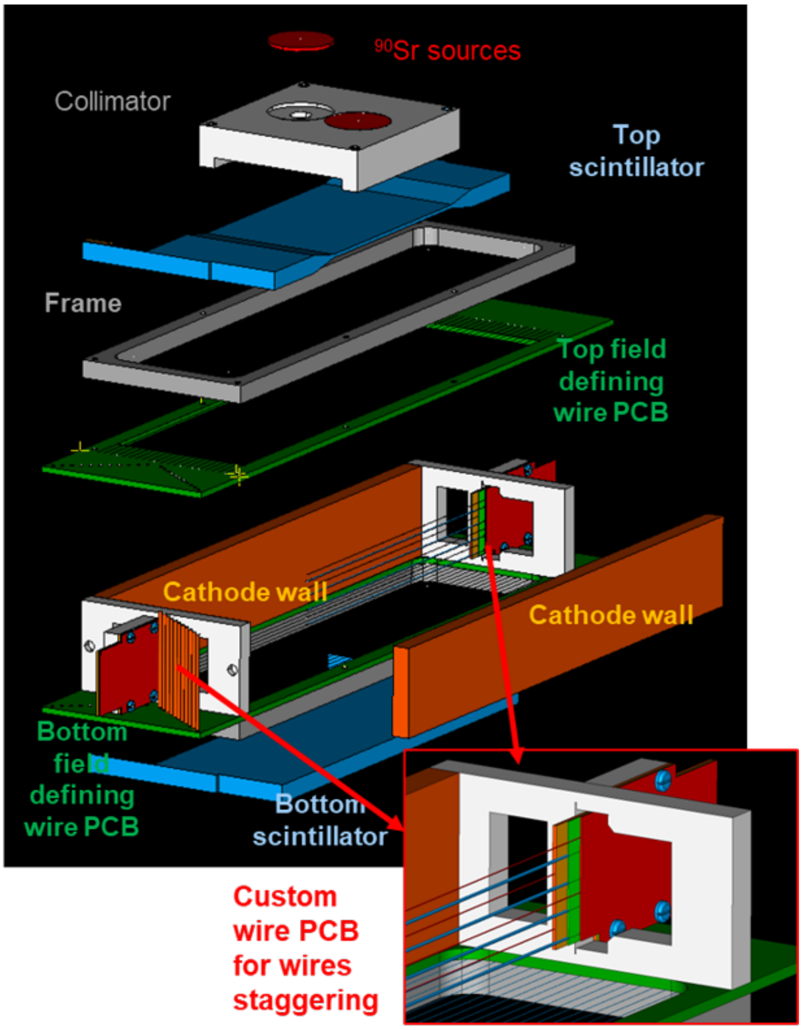

Figure 4.3: Mechanical design of the monitoring drift chamber.

4.1.3 Simulation of electric field configuration

The operation of the chamber has been studying by using the Garfield++ toolkit.
As a first step, the geometry of the chamber and the gas mixture has been defined. Then the simulation of the electric field configuration has been studied, by means of the following procedure:

- the voltage on the guard wires has been varied from -800 V to 0 V, with a step of 25 V,

- the voltage on the sense wires has been varied from 0 V to 1200 V, with a step of 25 V,
- the voltage on the field wires has been fixed at -2000 V.

The analysis of the operational parameters has been performed, for symmetry reason, for the left upper quadrant of the drift cell (-2 cm<x<0 and 0<y<1 cm).
The electric field has been scanned for each Oxy-plane along the Oy-axis from 0.9 cm to 0 cm with a step of 0.1 cm. To evaluate the electric field uniformity, the mean values, the rms and the skewness have been estimated. Figure 4.4 shows an example of this scan referred to the first sense wires ($y = 0.6$ cm).

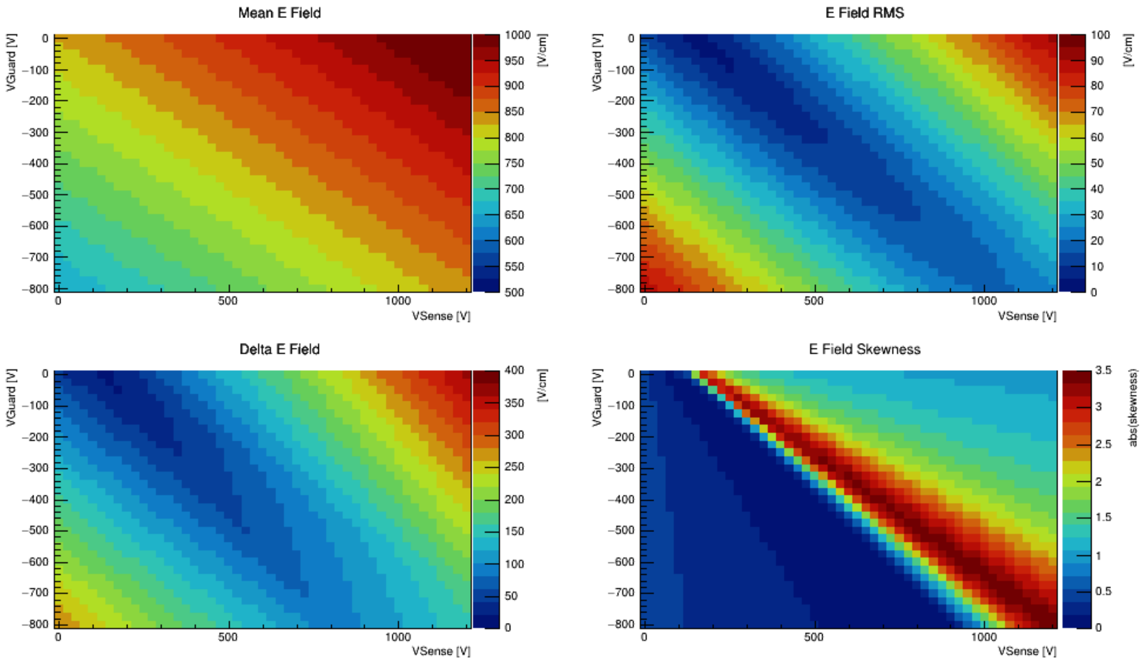

Figure 4.4: Scan of the electric field mean value, electric field variation, electric field rms and electric field skewness on the first sense wire ($y = 0.6cm$).

For the first and second sense wire the electric field, the number of collected electrons and the gain value has been observed, as shown in Figure 4.5.

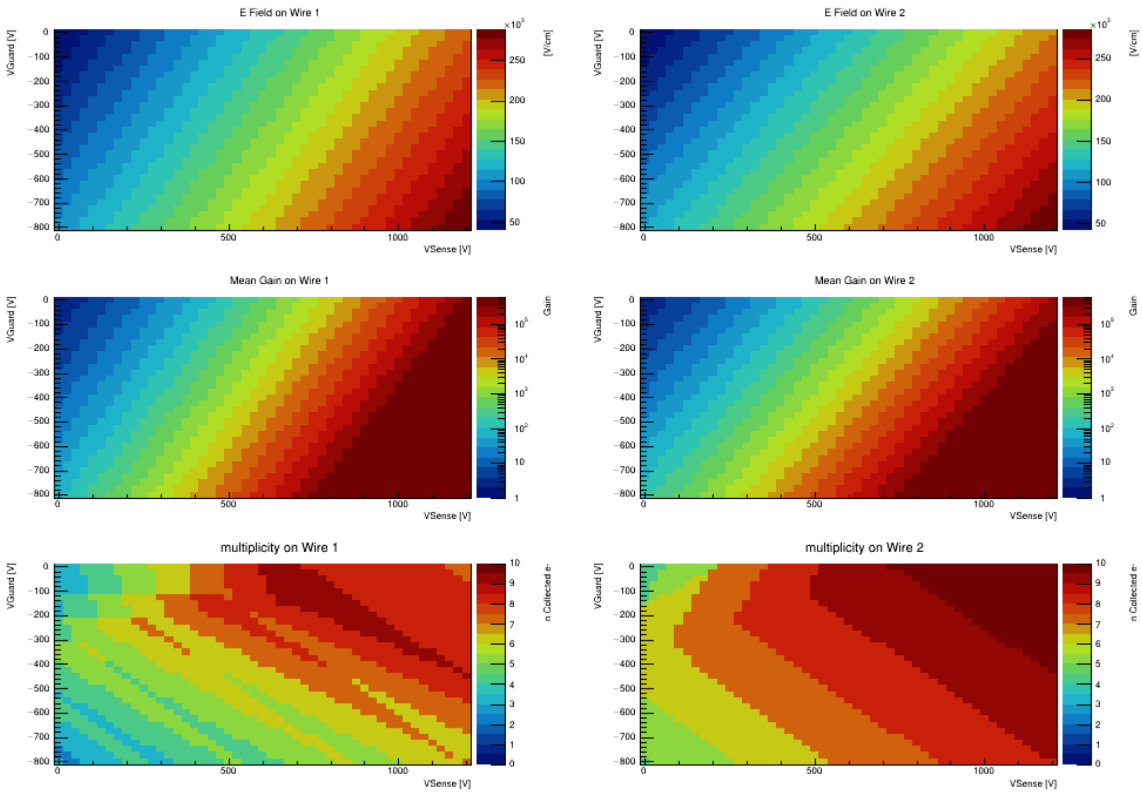

Figure 4.5: Scan of the electric field mean value, gain and number of collected electrons for the first two sense wires.

Next step of the procedure consists of finding the optimal voltage values for the sense and guard wires, by maximizing the figure of merit built on the base of the single information simulated. The weights for the RMS, skewness and the variation of the electric field ΔE have been calculated by following the procedure below:

- a weight value between 0-1 to each bin of the histograms has been assigned, by normalizing the Oz-axis, which means that every bin has been divided by a *reference value*;
- the *reference value* has been chosen as the mean value of the relative distributions with a confidence value of 3σ;
- if the weight value is higher 1, then the given weight value is set to 1;
- since the goal of the procedure is to append a bigger weight to the minimal variation of the field, RMS and skweness, the complementary of each weight has been evaluated $(1 - weight)$.

Figure 4.6 shows an example of the results obtained, referred to the first sense wire.

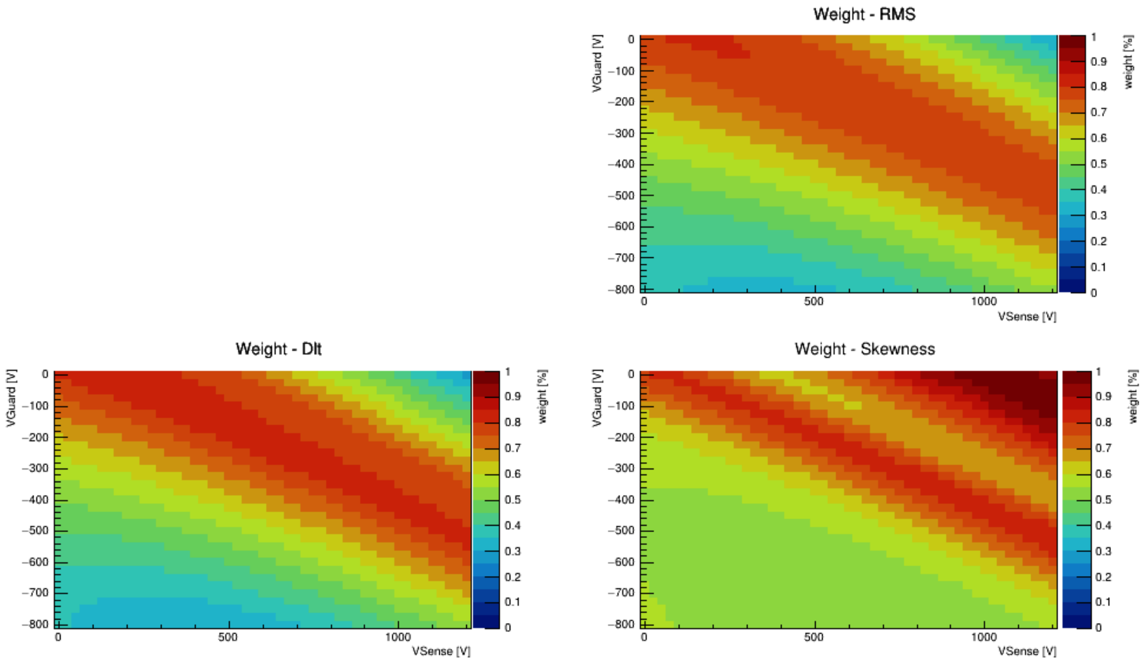

Figure 4.6: Scan of the weighted electric field variation, rms and skewness for the first sense wires.

The information provided by each scan along the Oy-axis has been analyzed, by means of three histograms related to the RMS, skewness ad ΔE , where each bin is filled with the mean values of all the scans, as shown in Figure 4.7.

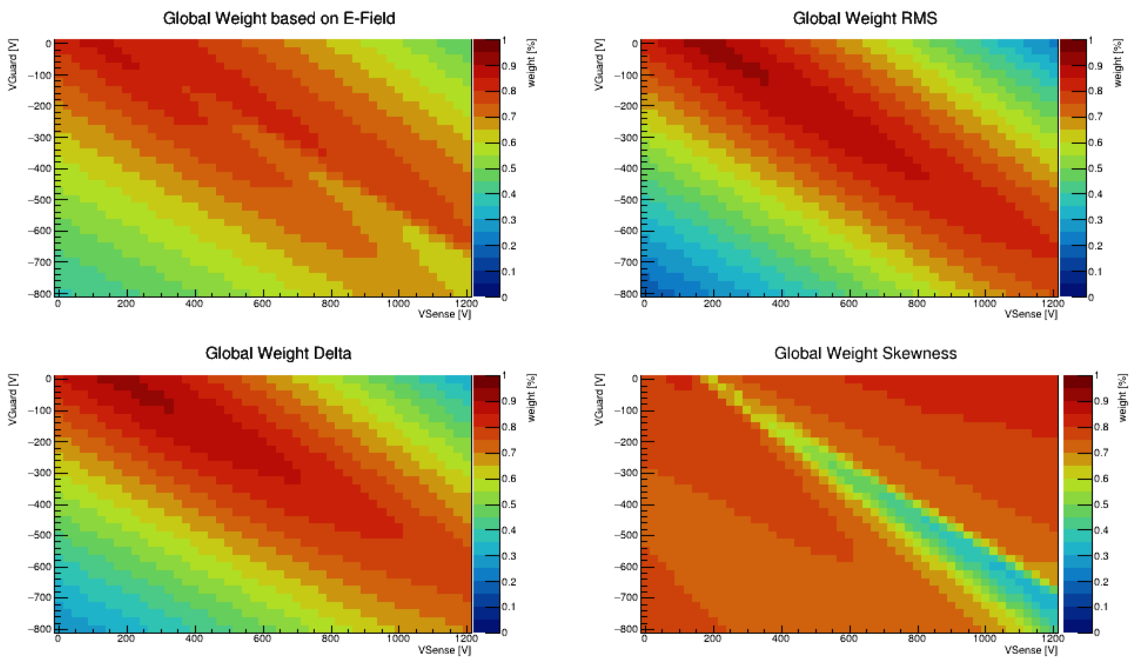

Figure 4.7: Top left: the global histogram that contains the average of the other three histograms. Top right: Δ average for all the plane scans. Bottom left: average RMS for all the plane scans. Bottom right: average Skewness for all the plane scans.

The same procedure has been followed for the studies on the gain and the number of collected electrons of the two sense wires in analysis: a weight has been assigned in the same way for the ΔE, skewness and rms. In this case, the value of each bin has been divided by the number of the simulated tracks.
For the gain evaluation, the weights per each bin of the gain histogram has been assigned in logarithmic scale, where each bin has been divided by a value of 10^5 (the reference value for the proportional operation). Since the highest gain value need to be avoided, if the weights are between 1 or 2, then the new weights are reassigned as $2 - previousweight$. If the weights are higher than 2, the weights are set to zero. The weighted histograms for gain and number of collected electron of the two sense wires in analysis are illustrated in Figure 4.8.

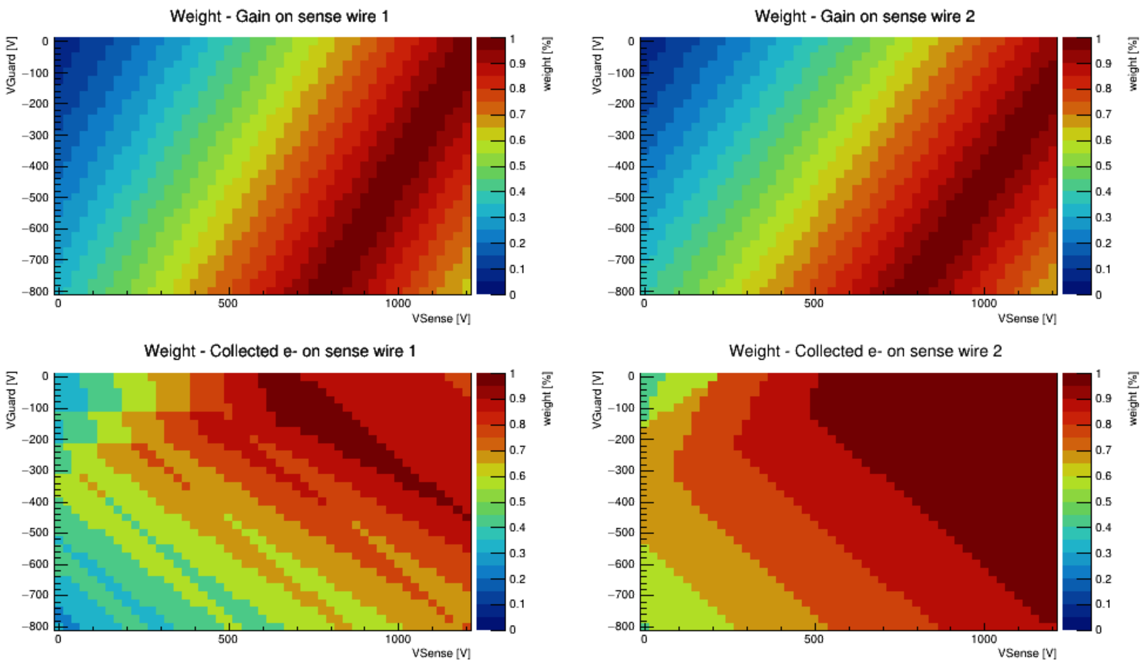

Figure 4.8: The weighted histograms for gain and number of collected electron of the first two sense wires.

At last, a global histogram, where each bin contains the average value of the weights from the histograms of electric field uniformity, gain, collected electrons of each sense wire has been built.
The global histogram, shown in Figure 4.9, suggests that the optimized voltage values for sense and guard wires are:

- $V_{sense} = 950V$
- $V_{guard} = -350V$

These values need to be considered as reference values: they will be tested with the experimental measurements.

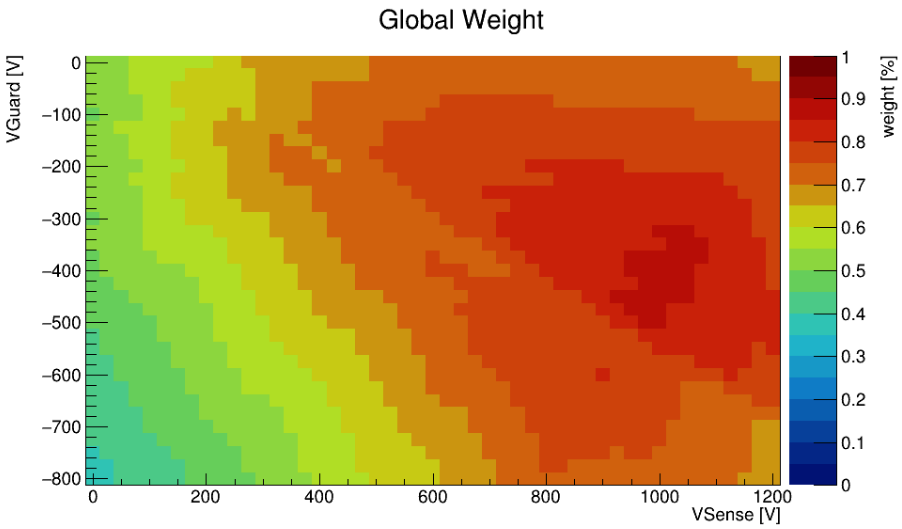

Figure 4.9: The global weight histogram for the optimized electric field configuration inside the two drift cells: the hot spot with the dark red shows the optimized region for the best possible voltages value of the sense and guard wires.

Figure 4.10 shows the electron drifting lines to the sense wires in the optimized electrostatic configuration. The asymmetry introduced by the sense wire staggering is confined to a very limited region around the wires (i.e. for very short drift times) and, as it will become clear in the next paragraph, its effects will be systematically subtracted in the calculation of the drift velocity.

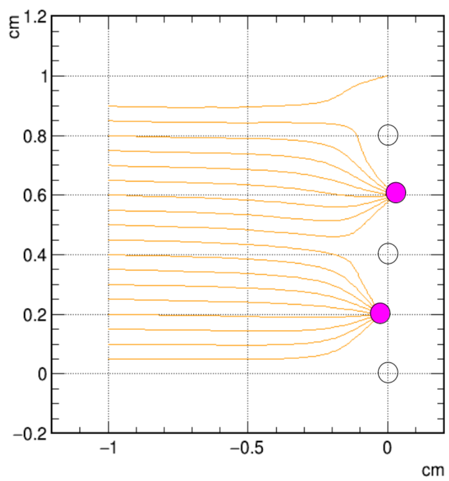

Figure 4.10: The figure shows the drift lines converging on the sense wires, marked with the pink dots.

Figure 4.11 shows the electric field and the potential in the optimized configuration.

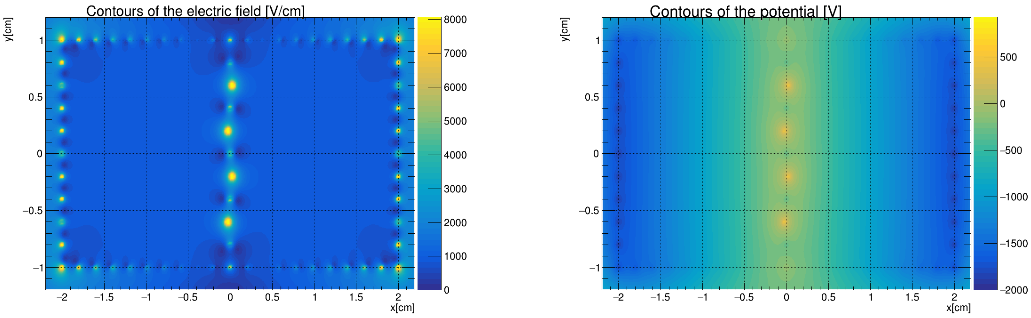

Figure 4.11: Electric field configuration (left) and potential configuration (right) of the monitoring chamber drift cells

4.1.4 Sensitivity of drift velocity measurement

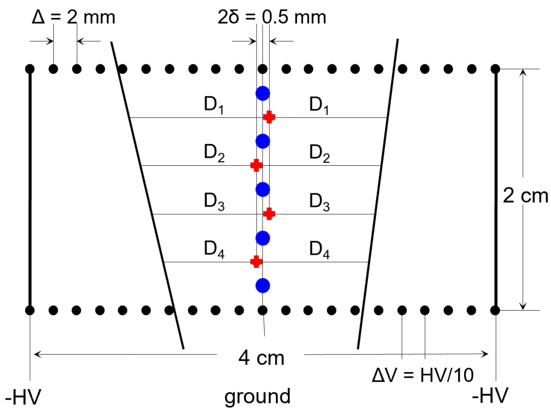

Figure 4.12: The figure shows drift cells structure and two tracks passing inside them. D_i indicate the drift distance from the crossing track to the sense wire i.

Considering the two triplets of the wires (*123*) and (*234*), as shown in Figure 4.12, indicating with v_d the constant drift velocity in the uniform electric field region, simple geometrical considerations lead to the following relations:

$$t_2 = \frac{t_1 + t_3}{2} \mp \frac{2\delta}{v_d} \tag{4.1}$$

$$t_3 = \frac{t_2 + t_4}{2} \pm \frac{2\delta}{v_d}, \tag{4.2}$$

where the first (second) choice of the signs refers to a track crossing the right (left) side drift cell.
The variable Θ can be defined as:

$$\Theta = (t_1 + t_3 - 2t_2) - (t_2 + t_4 - 2t_3), \tag{4.3}$$

which, according to the track crossing side, assumes one of the two values:

$$\begin{cases} \Theta_+ = +\frac{8\delta}{v_d} & left \\ \Theta_- = -\frac{8\delta}{v_d} & right \end{cases} \tag{4.4}$$

The estimation of v_d and of its variance as a function of $\Delta\Theta = |\Theta_+ - \Theta_-|$ is then obtained as:

$$\begin{aligned} v_d &= \frac{16\delta}{\Delta\Theta} \\ \sigma_{v_d} &= \sqrt{\left(\frac{16}{\Delta\Theta}\right)^2 \sigma_\delta^2 + \left(-\frac{16\delta}{\Delta\Theta^2}\right)^2 \sigma_{\Delta\Theta}^2}, \end{aligned} \tag{4.5}$$

where σ_δ represents the error on the wire positioning and $\sigma_{\Delta\Theta}$ depends statistically on the number of events collected. Since one is interested only in the variations of the drift velocity, the first contribution cancels out and the precision will scale with the collected statistics.

4.1.5 Simulation of the procedure

For the measurement of the drift velocity, 2×10^5 tracks passing through the chamber have been simulated. The gas mixture consists of $90\% He - 10\% iC_4H_{10}$ at pressure of 760 torr and temperature of 300 K. The tracks are generated with a uniform angular distribution within $\pm 12°$.
For every track, the four drift times are collected and the value of the variable Θ is plotted in the histogram of Figure 4.13. The two peaks, corresponding to Θ_+ and Θ_-, are highlighted by a fit to the distribution.

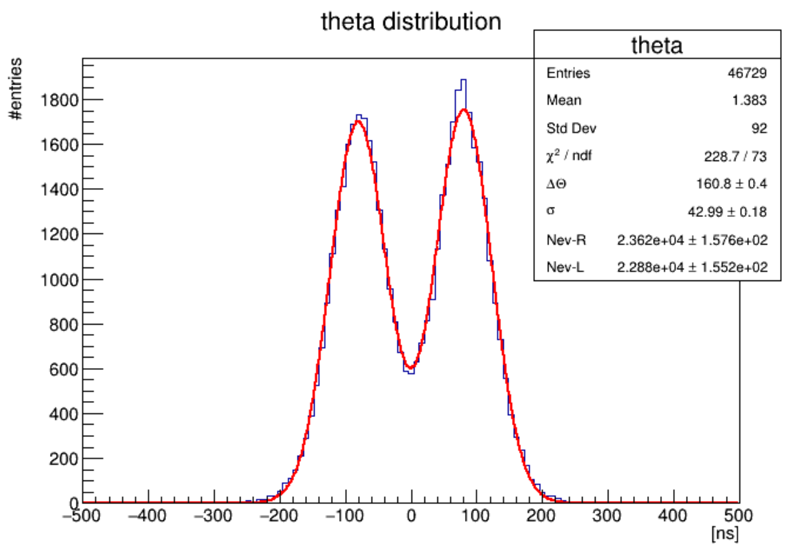

Figure 4.13: The double peak distribution for a mixture of $90\% He - 10\% iC_4H_{10}$ at pressure of 760 torr and temperature of 300 K.

The drift velocity calculated from this distribution is 2.488 ± 0.006 $cm/\mu s$, according to the relation (4.5).

4.1.6 The construction of the monitoring drift chamber

After a campaign of simulations aimed at studying the electric field configuration and the measurement procedure of the chamber [104], the construction of its components has been

started and despite being conceptually simple, the constraint on the 10^{-3} precision has made its construction quite challenging.
The accomplishment of the central wire staggering has been implemented, by using a custom PCB, shown in Figure 4.14, consisting of subsequent layers of resin and silver pad for wires soldering, performed with a 3D printing device [107].

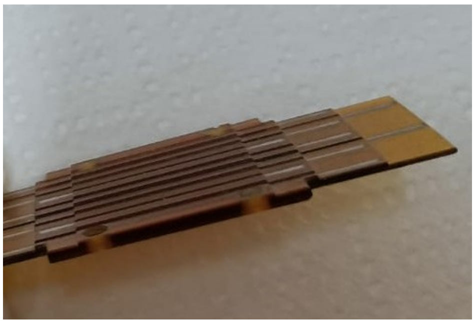

Figure 4.14: Custom PCB for wires staggering.

Figure 4.15 shows the drift velocity monitoring chamber complete in all its parts.

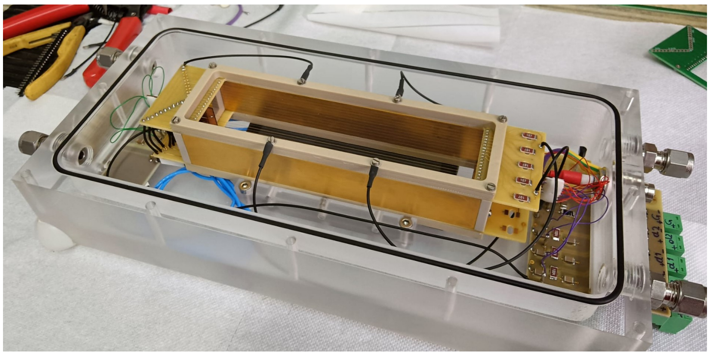

Figure 4.15: The monitoring drift chamber inside the gas box containment.

The cathode walls are made of gold plated brass. Two peek supports define the position of the upper and lower potential grading wire planes. The bottom trigger scintillator is kept in place by plastic supports anchored to the external gas container. The top scintillator, thinned down to 1.5 mm to minimize the β rays absorption, lays on top of the upper voltage grading plane, as shown in Figure 4.16.

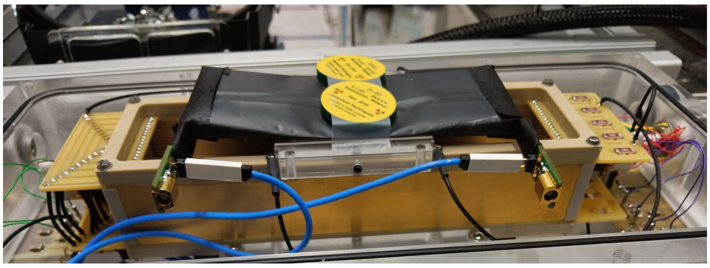

Figure 4.16: The two ${}^{90}Sr$ sources placed on top of the tapered scintillator.

Two feed-thorugh PCBs connect the drift chamber to the HV supply and to the data acquisition system.

4.1.7 The status of the monitoring drift chamber

The construction of the chamber has been completed. The chamber is under dedicated tests, before its installation at PSI.
Figure 4.17 shows the picture of the first signals collected.

Figure 4.17: The first signals collected by the monitoring drift chamber.

4.2 The TXY tables and the tracking system of MEG II positron tracker

For particle tracking, the drift time-space relations play a key role: in a drift cell the difference between the arrival time of the signal on the anode wire and the time of the trigger can be measured. Then the drift distance from the drift time measurement has to be obtained: any uncertainty (or misknowledge) of the drift space-time relations is reflected in the results.
A lot of effort has been spent on defining new drift distance-time relations (txy tables) for the MEG II drift chamber, which have to replace the old ones used by the MEG II tracking framework.

4.2.1 Positron reconstruction

To better appreciate the role of the txy tables for the tracking performances of the MEG II positron tracker, it is useful to have knowledge of the tracking framework.
The positron reconstruction is performed in 3 main steps:

1. hit reconstruction, where the information extracted from the waveforms is used for determining the coordinates of a hit;
2. track finding, where the hits are grouped in candidate tracks;
3. track fitting, where the particle trajectory is determined and the kinematic variables of the positron are measured.

4.2.2 Hit reconstruction

The fundamental track information relies in a hit in a drift cell: by means of the knowledge of the x, y, z coordinates of the hits, the track is reconstructed.

The raw observables of a hit are the z coordinate and the drift time, which is then converted to a distance in a drift cell. Once the "local" coordinates x_{loc}, y_{loc}, z_{loc} of the track hit in the drift cell are determined, they are converted into the global coordinates x, y, z by means of the alignment parameters of the drift chamber modules in the MEG reference frame.

Impact parameter

By definition, a hit is a coincidence between the signals at the two ends of a wire with the (negative) signal amplitude passing a fixed threshold of -5 mV below the baseline. The baseline with its standard deviation σ_B is determined in each waveform in the first nanoseconds of the sampled signals.The hit time is given by the first sample with amplitude below -3 σ_B from the baseline.
The drift time is computed subtracting the calibrated time offset to the measured signal time. The time offset is extracted for each channel from the distribution of the drift times as the edge that corresponds to particles passing close to the sense wire. Drift time is then converted to spatial coordinates by means of the txy tables, depending on the track local angle ϕ_{loc}:

$$t, \phi_{loc} \longrightarrow x_{loc}, y_{loc} \tag{4.6}$$

z coordinate

For the local z reconstruction, two methods have been developed.
The first method is the conventional **charge division method**: by measuring the charge asymmetry between the two ends, the local z can be measured as:

$$z = \frac{G\frac{Q_{up}}{Q_{down}} - 1}{G\frac{Q_{up}}{Q_{down}} + 1}(\frac{Z}{\rho} + \frac{L}{2}) \tag{4.7}$$

where the first factor is the charge asymmetry calculated from the charges at both ends, the latter factor correspond to the effective wire length. The input impedance of the readout preamplifier circuit is typically 360 Ω and the wire resistivity is 175 Ω/m. G is the gain ratio between the two ends, which need to be calibrated with the data.
The other method used is the **arrival timing difference** between the two ends:

$$z = \frac{(t_{up} - t_{up-offset}) - (t_{down} - t_{down-offset})}{2} v_{eff} \tag{4.8}$$

where the t_{up}, t_{down} are the reconstructed timing at the two ends, v_{eff} is the effective velocity of the signal propagation on a wire. $t_{up-offset}$, $t_{down-offset}$ are the timing offset of the two ends.

4.2.3 Track finding

The nearby reconstructed hits are then clustered to reconstruct the positron track. This process is often called *pattern recognition* or track finding. For the track finding algorithm, there are two major categories: one is the local following method and the other is the global following method:

- *Local Following*: starting from a reliable track seed, nearby hits are added step by step (**Kalman Filter technique**, local clustering are two main examples of this technique).

- *Global Following*: all hits are treated equally and simultaneously at the process of clustering (typical examples are neural Net and circle fits).

In MEG II track finding, the local following algorithm based on the *Kalman Filter* technique is adopted. A detailed description of the Kalman Filter is reported in Appendix B.
The procedure applied by the MEG II track finding consists of:

- calculation of the drift time for CDCH hits from the pTC clusters,
- construction of the possible *seed tracks* from the outer layers,
- extrapolation of the seed tracks,
- computation of the track qualities.

Figure 4.18 explains the seeding procedure. To calculate the drift time and the impact parameter, the timing from the pTC cluster is used as reference timing, T_0. The starting drift time is calculated as $t_{hit} - T_0$. At the seeding level, the averaged drift velocity of ≈2.7 cm/μm is used for the calculation.

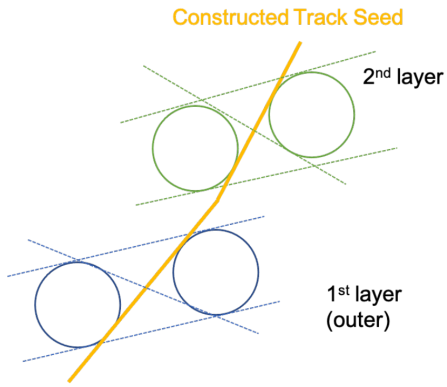

Figure 4.18: The CDCH seeding procedure. The blue and green circles show the drift time circle, and the dashed lines are the candidates of the track (left-right for each circle). The yellow line shows the constructed track seed.

The output of the pattern recognition consists of a set of candidate tracks.

4.2.4 Track fitting

In the final step of CDCH analysis, the positron tracks are reconstructed by using the fitting algorithms and the best estimate of the state vector at the vertex is obtained. This task is divided in three steps: the DAF (Deterministic Annealing Filter) fitting, the turn merge and the extrapolation.
The DAF algorithm, implemented in GENFIT, is an extension of the Kalman Filter technique (more details in Appendix B). The probabilities of the measurements, which are the "left" measurement and the "right" measurement on a wire measurement case, are assigned in this task. Those measurements compete with each other during the iteration process of the KF technique.
The higher assignment measurement will survive the fitting iteration and the lower assignment measurement will be frozen out. The sum of probabilities on a detector plane can be < 1,

which means that the inconsistent measurement will have the smallest probability and can be removed. Then the fitted tracks from different turns are merged. The typical positron trajectory has 1.5 turns before entering pTC and crosses the CDCH active volume three times (leaves three track segments). To achieve the target resolution, all the segments must be merged for fitting. This turn merge is based on the consistency of position and timing between the state vectors extrapolated to the plane defined at the center of the two segments. The turn merge criteria should be wider than the resolution since the number of hits and the path length is not large enough with the only single segment. If multiple tracks become the candidates for one segment, the χ^2 values, which are calculated from the DAF fittings, are compared and the best pair is accepted. After fitting again with full segments, the track state vector is extrapolated by the Runge-Kutta algorithm [108] to the stopping target to find the vertex position. The flight time from the vertex to the pTC (i.e. inside the CDCH region) is calculated from the path length of the reconstructed track divided by the speed of light.

4.2.5 The txy tables

Drift relations are necessary in two different steps. At simulation level it is required to assign a correct drift time to each ionization cluster generated by a track. Therefore the so-called "direct table" that associates a drift time to a pair of local coordinates are necessary: $(x_{loc}, y_{loc}) \longrightarrow t$.
During the hit reconstruction, the measured drift time and the local impinging angle from the track candidate are known. To reconstruct the impact parameter, with a sign required for solving the left-right ambiguity, the "inverse table" are used: $(t, \phi_{loc}) \longrightarrow \pm b$.
The two formats of tables are available for all layers and for each z coordinates spanning from 0 cm to 90 cm, with a step of 10 cm.
The tracking framework of MEG II uses a set of txy tables, which were developed for a gas mixture of 85% He-15% iC_4H_{10}. So that, it is necessary to replace these sets with new ones for the new gas mixtures currently used.

4.2.6 The first implementation of the txy tables

To reproduce correctly a new sets of tables, the starting point consists in a detailed study of the old ones, to respect their format and store all the needed information for the tracking framework of MEG II. An example of direct and the corresponding inverse tables for the outermost cells is shown in Figure 4.19.

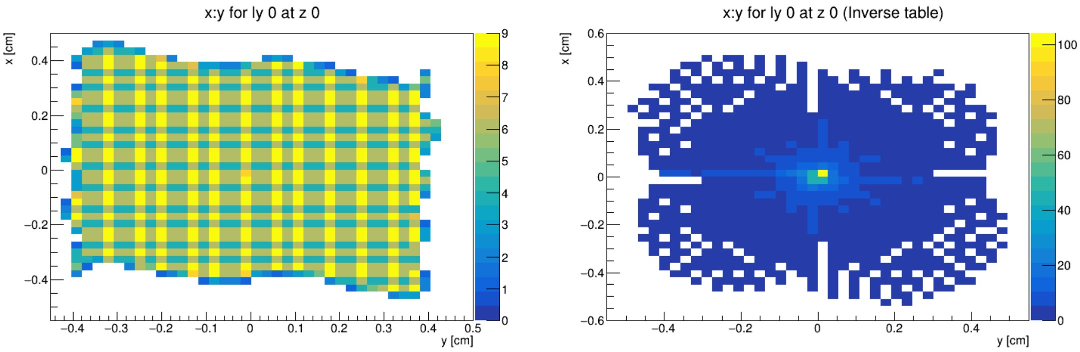

Figure 4.19: Distribution of the drift starting points corresponding to the direct (left) and inverse (right) drift tables for the outermost cells at z = 0 cm.

The direct tables store the information about x, y, z coordinates in cm and the drift time in ns. The scan in x and y coordinates is performed with step of 0.01 cm.
The inverse tables store the information of drift time in ns, *phi* (track angle with a scan of 6°) in radian, z coordinate in cm and impact parameter in cm.
Together with these sets of 100 tables, 2 average tables are provided: an average table layers per layers (over ϕ ans z) and a total average table (over layers) which are useful for a first estimation of the time-to-distance relation in pattern recognition.
These tables contain the information about the average impact parameter, the average drift time and the average σ over the impact parameter.

Chapter 5

The new drift-to-time relations

5.1 The new tables: the geometry reconstruction of a sector of the chamber

A fundamental step for the correct development of the new txy tables is the reconstruction of the drift cell geometry per each layer and z, since the geometry of each cell is the framework in which Garfield++ simulates the time-to-distance relations.
The needed information to reconstruct the drift chamber geometry are stored in dedicated geometry tables, divided in two formats:

- **NOMINAL TABLES**
  The tables contain plane, number of wire per plane, wire radius, x,y,z in the center, half length per wire, direction cosines.
- **MEASURED TABLES**
  The tables are created combining measurements performed at PSI with the measurements performed during the construction of the chamber. Those tables are formulated in two different formats:
  - **First format**
    The tables contain plane, sector, absolute number and relative number of wire, x,y,z at the endplates and in the center, endplate and center radius, stereo angle, wire length.
  - **Second format**
    The tables are arranged like the nominal table.

By using the nominal tables, a sector of the chamber has been reconstructed. To simulate properly the time-distance relation, the sector has been modeled by referring all the geometry to the plane orthogonal to a chosen wire, named "reference wire", instead of the plane orthogonal to the z-axis, like the old version of the tables [1]. Then for convenience, all the geometry has been centered on the reference wire.
Figure 5.1 shows the reconstructed sector of the chamber in the different configurations: plane orthogonal to z, plane orthogonal to the reference wire, geometry centered on the reference

[1] The electric field and the drift lines stay on the orthogonal plane to the wire direction.

wire.

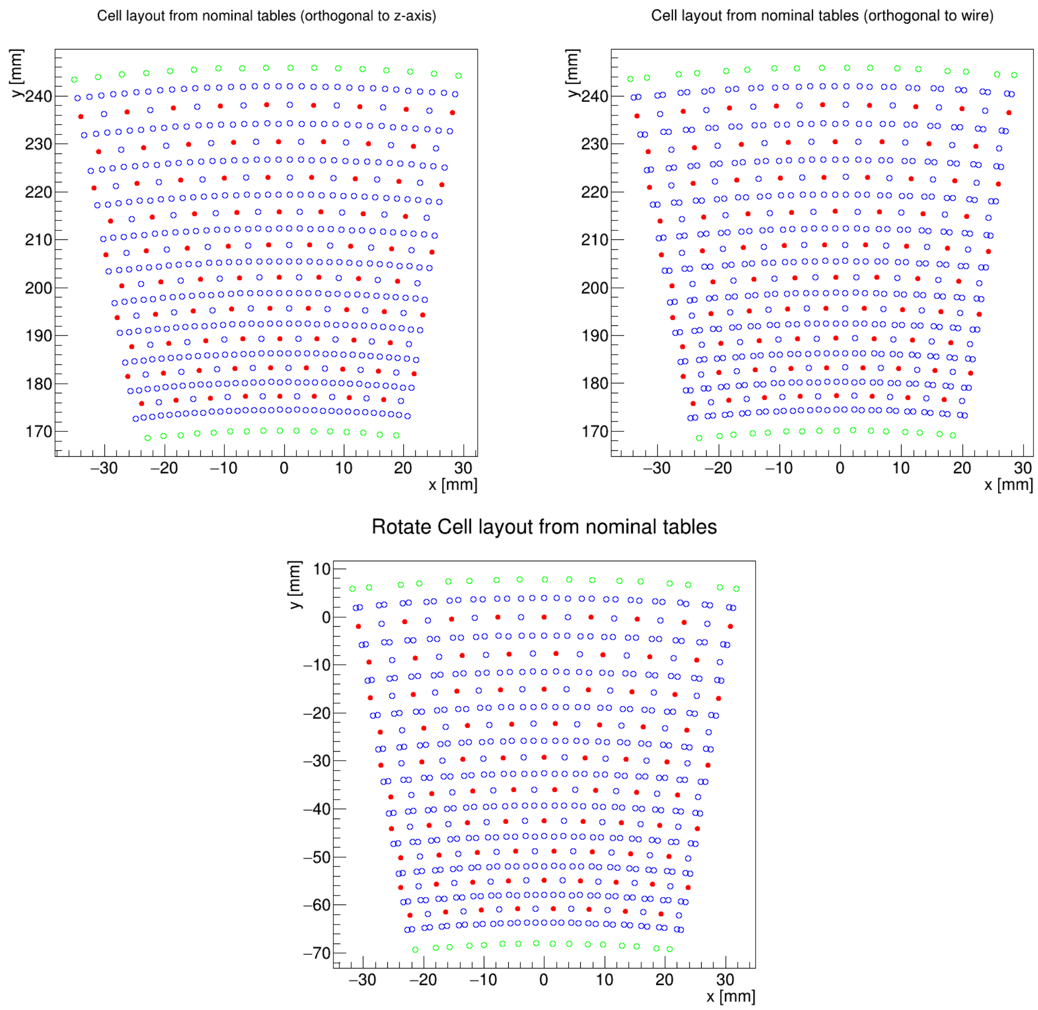

Figure 5.1: Geometry reconstruction of a sector of the drift chamber. The red dots represent the sense wires, the blue ones the field wires, the green ones the guard wire. Top left: the view orthogonal to the z axis. Top right: the view orthogonal the wire. Bottom: rotate layout.

5.2 The magnetic field

Magnetic field plays a key role in the development of the txy tables.
The effect of the magnetic field on the drift of electrons has been evaluated by means of simulations with Garfield++. The analytical calculation of the COBRA magnetic field has been used and a constant magnetic field is assumed in the drift cell and is calculated from the projections of the COBRA magnetic field on the local coordinates of the cell. The largest component of the magnetic field is parallel to the wire $B_{||} = B_z \cos\epsilon$, where ϵ in the stereo angle. Since this is orthogonal to the electric field its main effect is a twist of the drift lines, as shown in Figure 5.2. A component of the magnetic field perpendicular to the anode wire comes from the other projection of B_z and from the radial component of the magnetic field. In this case, when the magnetic field is perpendicular to the electric field, electrons drift also

along the wire direction. Because of the small size of the drift cells, the drift distance along the wire is less than 100 μm.

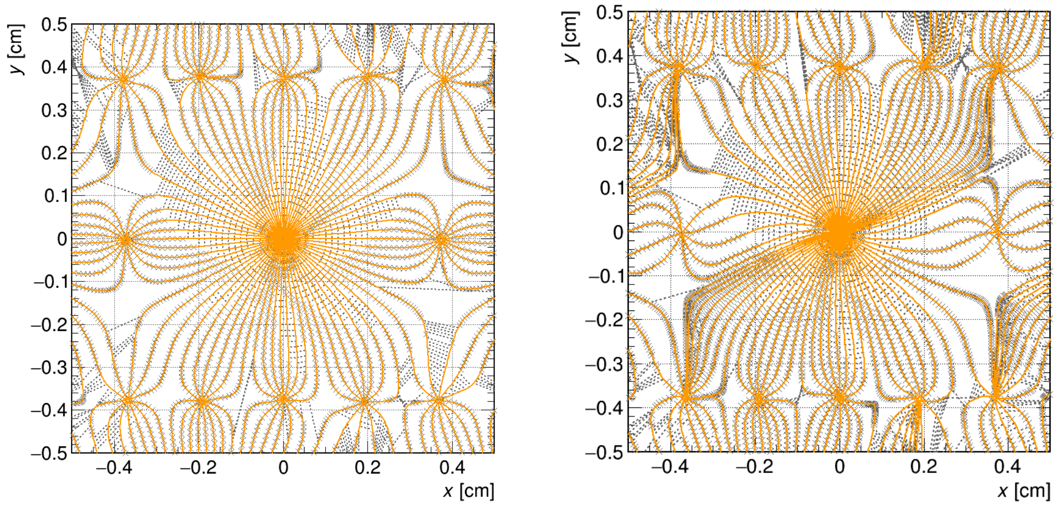

Figure 5.2: Left: drift lines in a cell without magnetic field. Right: drift lines in a cell with magnetic field.

Studies about the trend of the magnetic field with respect to the radial coordinate and z coordinate have been performed and are summarized in Figure 5.3.

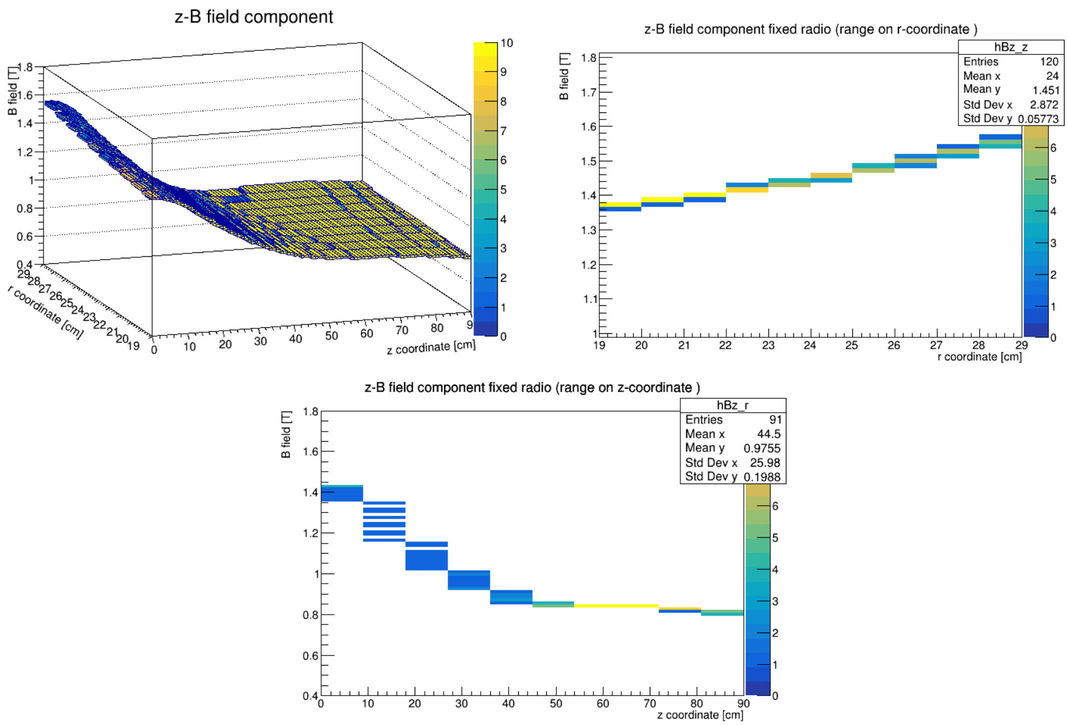

Figure 5.3: Top left: B_z vs the z and radial coordinate (r). Top right: B_z vs r at fixed arbitrary z coordinate. Bottom: B_z vs z at fixed arbitrary r coordinate

5.3 The new txy tables: version 1.0

Once completed the analysis about the geometry reconstruction and the magnetic field, a first preliminary set of tables have been produced, by means of the following procedure:

- For the direct tables:
  - the simulation uses the *DriftLineRKF* method provided by Garfield++.
  - starting from the external limit of the drift cell, the drifting electron starting position is generated following a step in x and y coordinates of 0.01 cm, as the old tables.
  - the electrons which drift toward the anode wire belonging to the selected drift cell and with a drift time less than 500 ns have been selected
- For the inverse tables, following the same generation method of the direct tables, the simulation:
  - performs a scan in angle and distance, with a step of 6 degree and 0.01 cm respectively

$$x = dist\cos(\phi - \frac{\pi}{2}) \tag{5.1}$$

$$y = dist\sin(\phi - \frac{\pi}{2}) \tag{5.2}$$

    where ϕ is the track angle.
  - applies the same cuts on anode wire and maximum drift time.

The tables have been generated with a mixture of 90%He-10% iC_4H_10 + 0.5% O_2 and 1.2% isopropanol, a temperature of 360 K, a pressure of 760 Torr.
The drift cells reconstructed by means of the new sets of tables are illustrated in Figure 5.4.

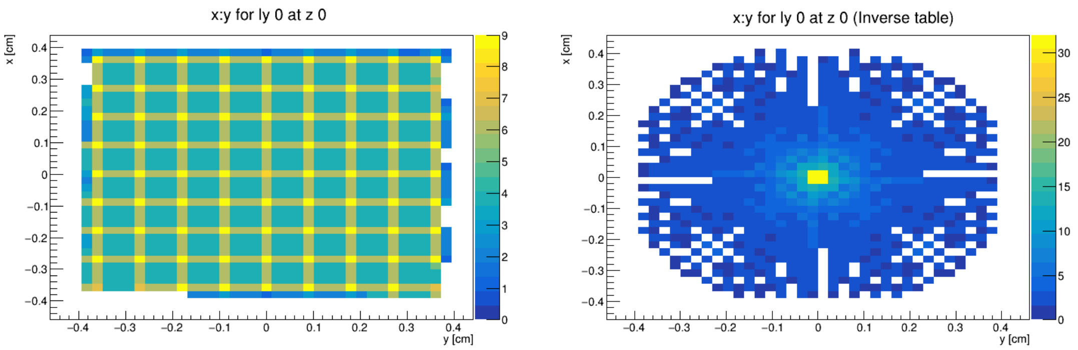

Figure 5.4: Distribution of the drift starting points for direct (left) and inverse (right) drift tables for the outermost cells at z = 0 cm obtained with the first version of the new txy tables.

5.4 The new txy tables: version 2.0

The first version of the new txy tables represents a preliminary phase to test the potential and the possibilities provided by Garfield++ to reproduce the electron drifting process inside the MEG II drift cell. So that, a second version has been developed to taking into account the diffusion process. The generation of the direct tables remains the same, all the changes rely in the inverse tables:

- the simulation uses the DriftLineRKF method provided by Garfield++,
- 500 tracks passing through the drift cell in each layers have been generated
- the arrival spread time has been saved and the time distribution of the first cluster has been smeared according to a Gaussian distribution, whose mean is set to zero and σ corresponds to the electronics time resolution.

The drift time distributions obtained have been fitted with a Crystall Ball function (Figure 5.5-Left), for the radii coordinate around the sense wire and a Gaussian function (Figure 5.5-Right) for the radii coordinate far from the sense wire.

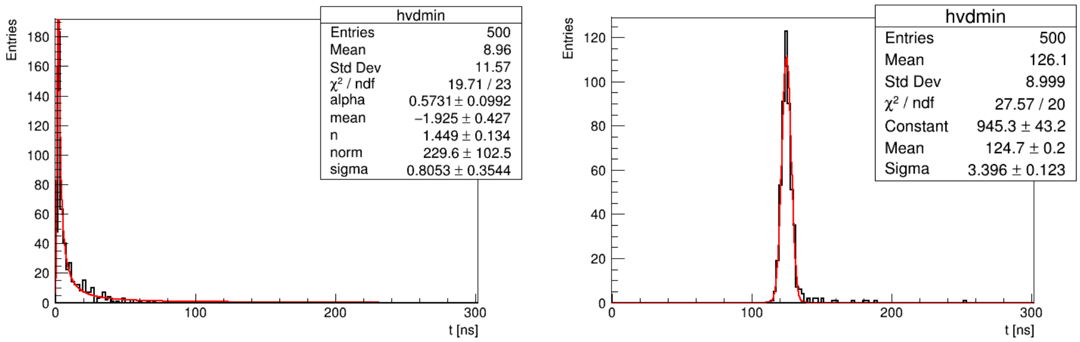

Figure 5.5: Left: first cluster drift time distribution for z=0 at layer 0 fitted with a Crystall Ball function. Right: first cluster drift time distribution for z=0 at layer 0 fitted with a Gaussian Ball function.

5.5 The new txy tables: version 3.0

An optimization of the second version of the tables has been implemented, by using an exponential+Gaussian function to fit the drift time distribution:

$$f(t) = Norm \begin{cases} f1\frac{1}{\sigma\sqrt{2\pi}}e^{-\frac{(t-\mu)^2}{2\sigma^2}} & t < t_c \\ f2\frac{1}{\lambda}e^{\frac{t-t_c}{\lambda}} & t > t_c \end{cases} \tag{5.3}$$

by imposing the continuity:

$$f2 = \frac{\lambda f1}{\sigma\sqrt{2\pi}}e^{-\frac{(t_c-\mu)^2}{2\sigma^2}} = \lambda f1 G(t_c) \tag{5.4}$$

An example of the fitted distribution is shown in Figure 5.6.

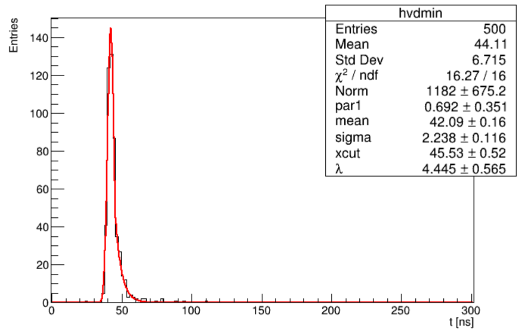

Figure 5.6: First cluster drift time distribution for z=0 at layer 0 fitted with the exponential+Gaussian function.

5.6 The average tables

Along with these sets of tables, direct and inverse, two other tables, named "average tables" are necessary for the MEG tracking dataframe. The average tables store the average impact parameter, the average drift time and the average sigma over the impact parameter.
To obtain the average sigma, the rms and the rms over the 80% of the integral of the first cluster time distribution (an example in Figure 5.6) have been evaluated. To convert this sigma on the drift time in a sigma on the impact parameter, a polynomial plus an exponential function has been used, whose parameters have been obtained by fitting the averaged relation distance-time, as shown in Figure 5.7.

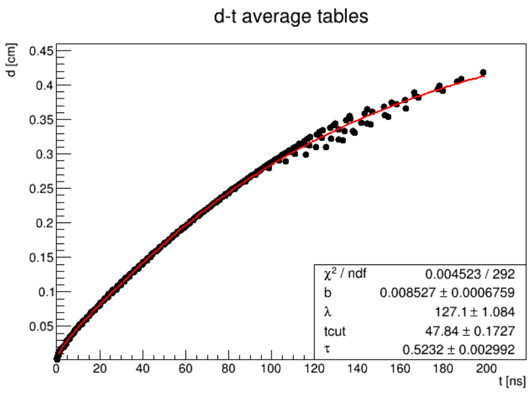

Figure 5.7: Average time to distance relation. The fit function consists of a polynomial plus an exponential function.

The mathematical formula of the fit function is:

$$f(t) = \begin{cases} a + b\sqrt{t} + ct & t < t_c \\ \tau(1 - e^{\frac{t}{\lambda}}) & t > t_c \end{cases} \tag{5.5}$$

The old average tables and the new ones have been compared, taking into account the two different possible choices for the rms, as shown in Figure 5.8.

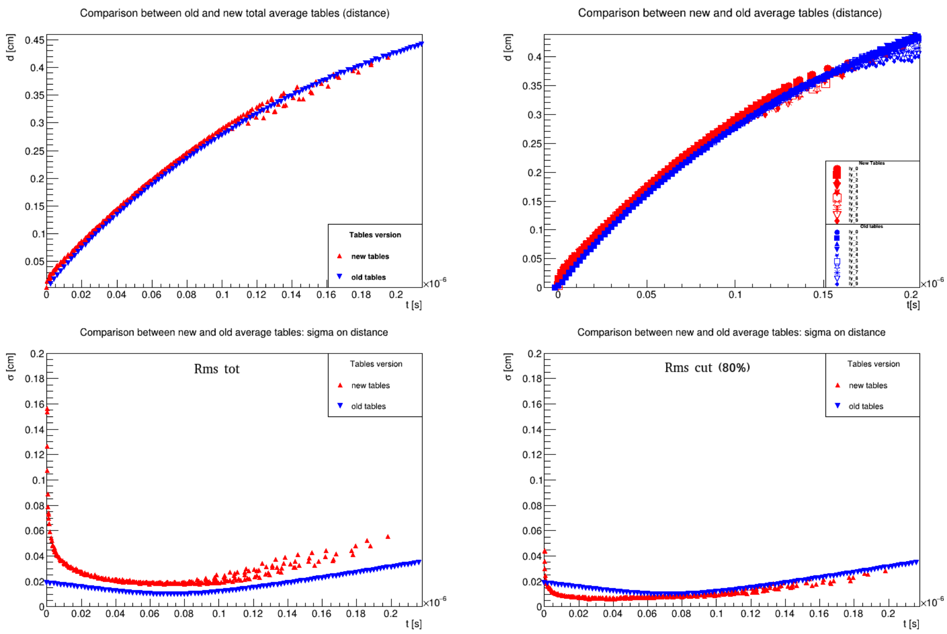

Figure 5.8: Top left: average distance-time from the total average table. Top right: average distance-time from the average table layer per layer. Bottom left: average sigma-time from the total average table, by using the rms cut at 80 %. Bottom right: sigma-time from the total average table, by using the total rms.

The subsequent steps for the txy tables analysis consists of the evaluation of the tables impact on the MEG II tracking performances.

5.7 The impact of the new txy tables on MEG II tracking performances

The third version of the txy tables have been studied, by investigating the impact of the txy tables on the tracking performances of MEGII. Three different sensitive variables have been checked: the χ^2 distributions of the reconstructed track, the number of good reconstructed hits and the distance of closest approach (DOCA) between the track and the cell's sense wire, since this is the primary CDCH track position measurement used in the positron track fitting. These features have been compared with the ones obtain by applying the old version of the txy tables. Moreover, the results obtained by using the total rms and the cut rms[2] in the average tables have been studied.
As first step, a rough estimation have been performed to check the main differences between the old and the new version of the tables (with total and cut rms) without imposing strict quality cuts on the reconstructed tracks.
Four different run data collected during 2022 run have been selected to test the performances of the tables. The distribution of the features taken as target of our analysis are reported in Figure 5.9 for the old tables, in Figure 5.10 for the new tables with the cut rms and in Figure 5.11 for the total rms.

[2]The cut rms is the one evaluated by considering the 80 % of the integral of the first cluster time distribution.

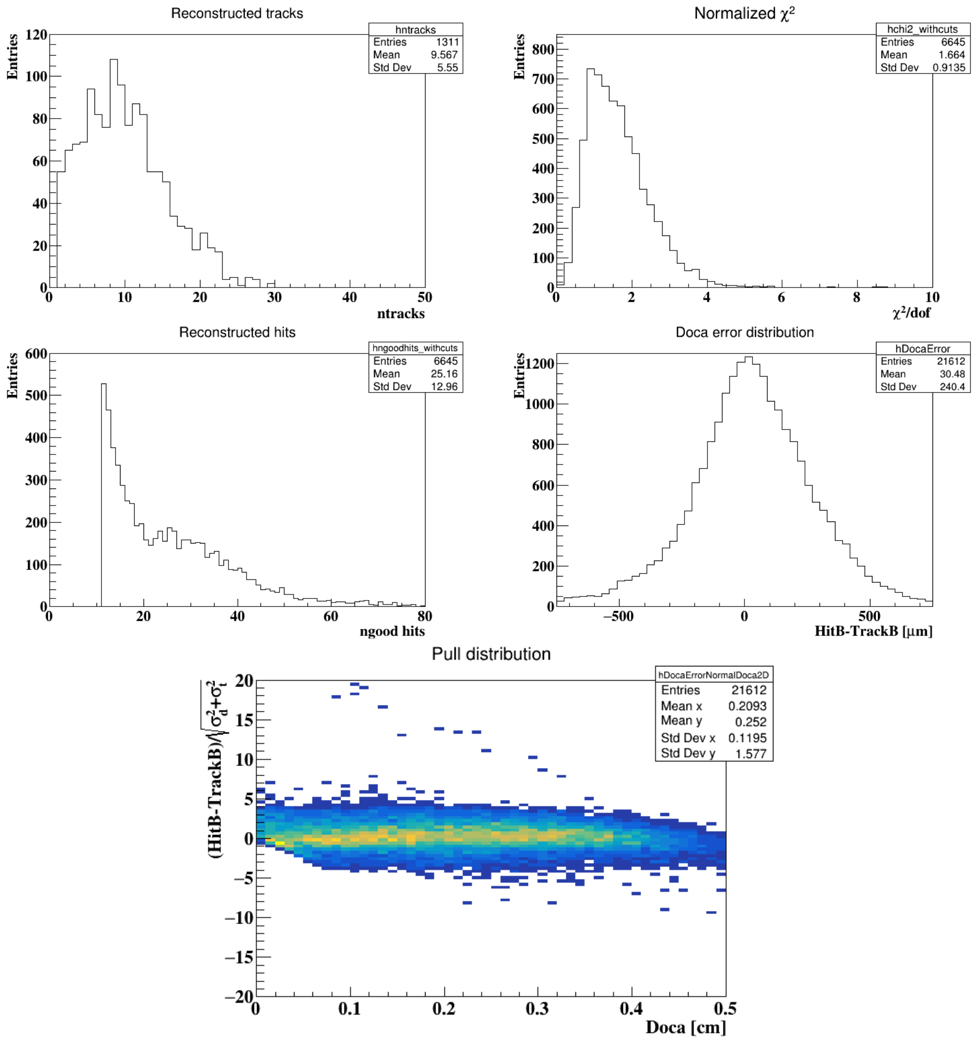

Figure 5.9: Analysis of target features obtained with the old version of the txy tables. Top Left: reconstructed tracks distribution. Top Right: Normalized χ^2 distribution. Bottom Left: reconstructed hits distribution. Bottom Right: Doca error distribution. Bottom Center: pull distribution.

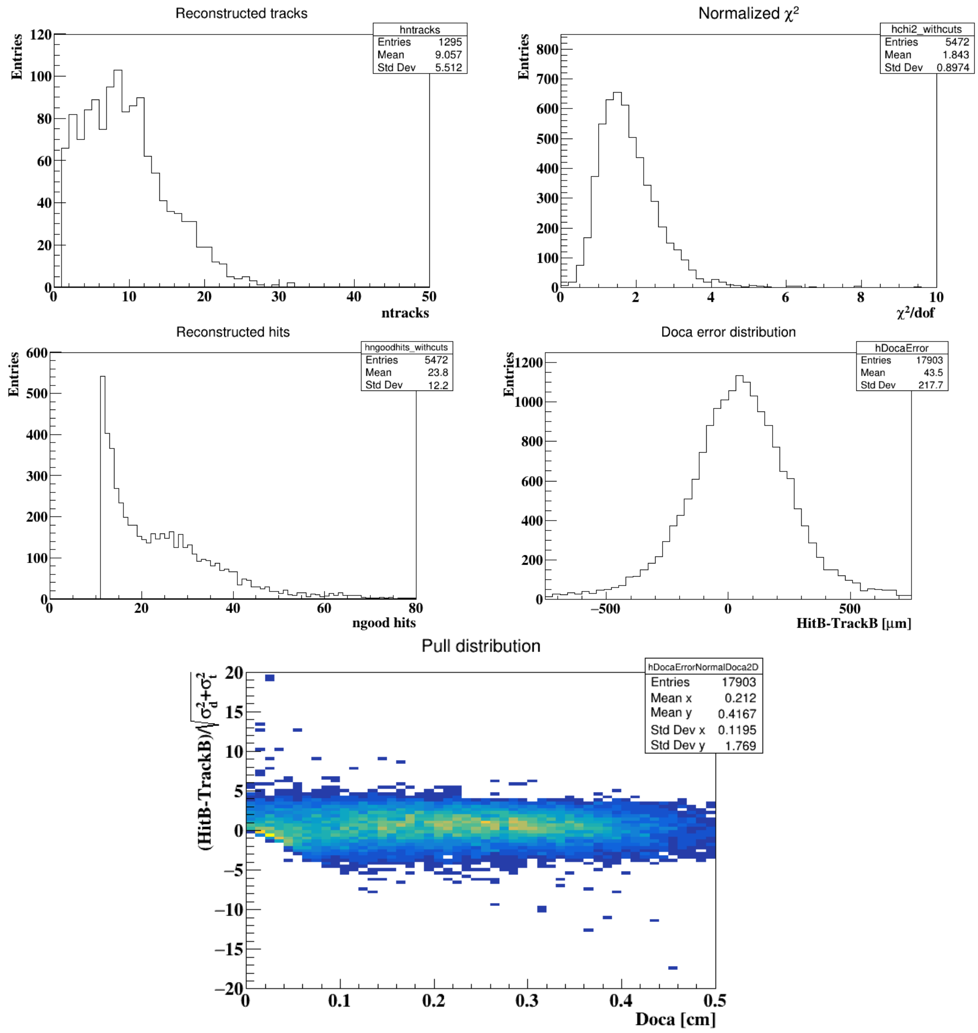

Figure 5.10: Analysis of target features obtained by applying the new version of the txy tables with the cut rms. Top Left: reconstructed tracks distribution. Top Right: Normalized χ^2 distribution. Bottom Left: reconstructed hits distribution. Bottom Right: Doca error distribution. Bottom Center: pull distribution.

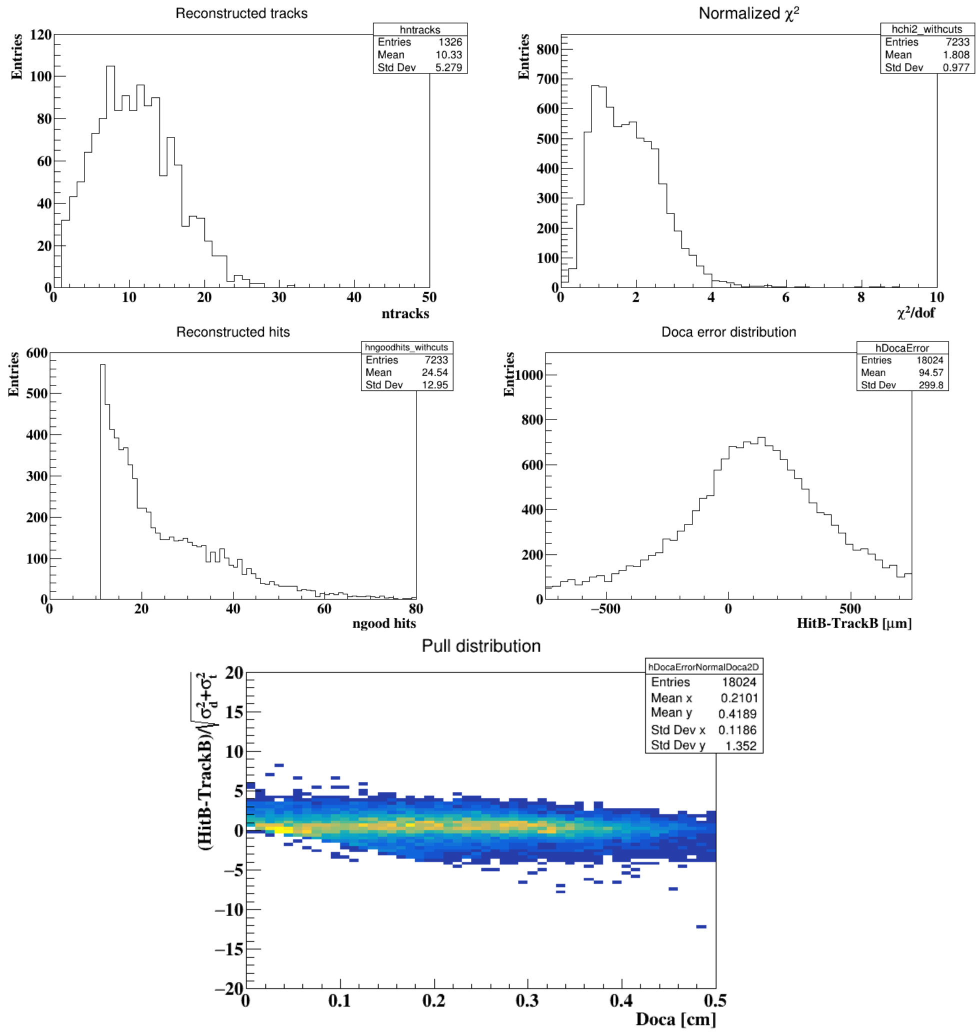

Figure 5.11: Analysis of target features obtained by applying the new version of the txy tables with the total rms. Top Left: reconstructed tracks distribution. Top Right: Normalized χ^2 distribution. Bottom Left: reconstructed hits distribution. Bottom Right: Doca error distribution. Bottom Center: pull distribution.

5.7.1 Doca error per range

It is useful to compare the doca error distribution for different impact parameter ranges:

- TrackB $<$ 0.1 cm,
- 0.1 cm $<$ TrackB $<$ 0.35 cm
- TrackB $>$ 0.35 cm

The results for the three different configuration are reported in Figure 5.12.

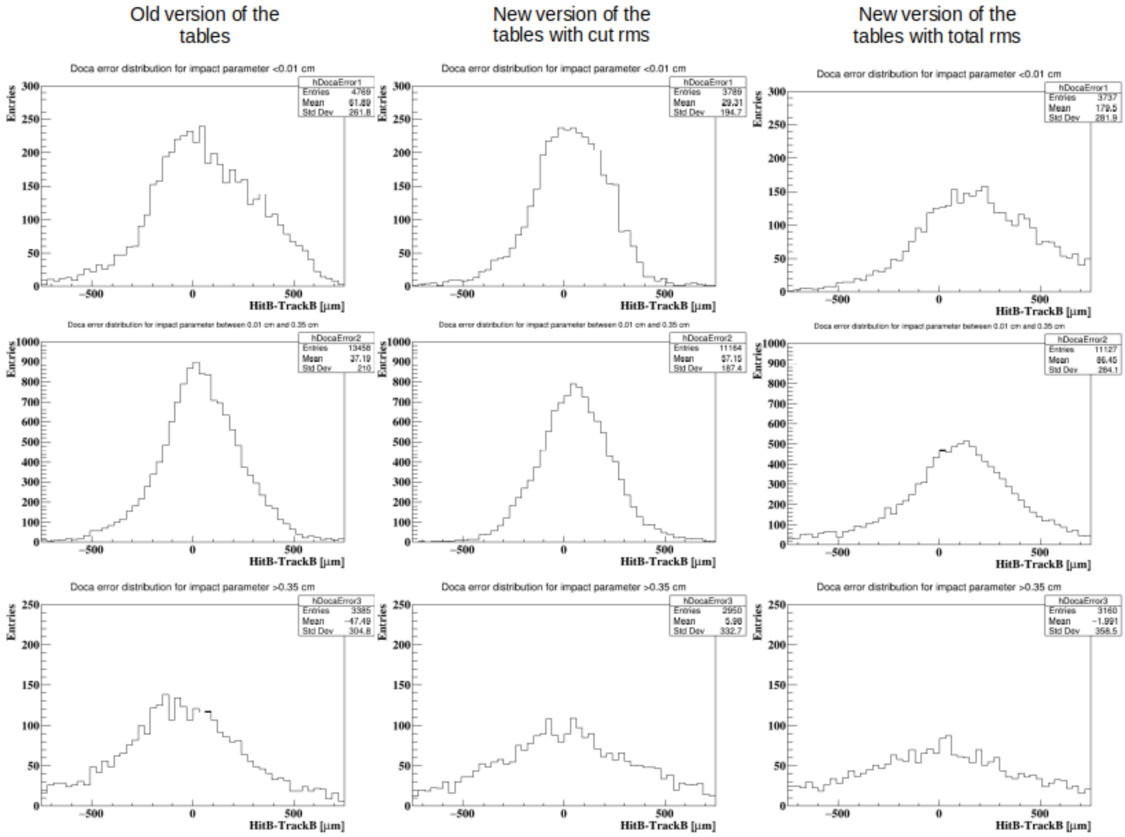

Figure 5.12: Doca error per range. First column is referred to the old version of the txy tables. Second column is referred to the new version of the txy table with the cut rms. Third column is referred to the new version of the txy table with the total rms

5.7.2 Summary table for the first rough estimations

The table 5.1 shows at glance the results obtained.

Table 5.1: Summary table of the performances obtained with the three different versions of the txy tables.

		Old version of the tables	New version of the tables with cut RMS	New version of the tables with total RMS
Number of tracks	#	1311	1295	1326
	Mean	9.567	9.045	10.33
	stdDev	5.55	5.512	5.279
χ^2	#	6645	5472	7233
	Mean	1.664	1.843	1.808
	stdDev	0.9135	0.8974	0.977
Number of reconstructed hits	#	6645	5472	7233
	Mean	25.16	23.8	24.54
	stdDev	12.96	12.2	12.95
Doca error	#	21612	17903	18024
	Mean	30.48	43.5	94.57
	stdDev	240.4	217.7	299.8
Pull	#	21612	17903	18024
	Mean x	0.2093	0.212	0.2101
	Mean y	0.252	0.4167	0.4189
	Std Dev x	0.1195	0.1195	0.1186
	Std Dev y	1.577	1.769	1.362

It is quite evident that the number of tracks reconstructed by using the cut rms is less than the one obtained with the old version of the tables. On the other hand, by using the total rms, the number of reconstructed tracks can be raised, but the doca performances have been deteriorated.
So that, we tried to improve the performances obtained with the txy tables using the cut rms by comparing the results reached with the experimental data and the ones with the Garfield++ simulation.

5.8 A time shift

The way followed to comprehend the different results between the new and the old version of the tables consists of comparing the experimental data with the simulations.
In particular the distributions of the doca error as a function of doca have been compared, as shown in Figure 5.13.

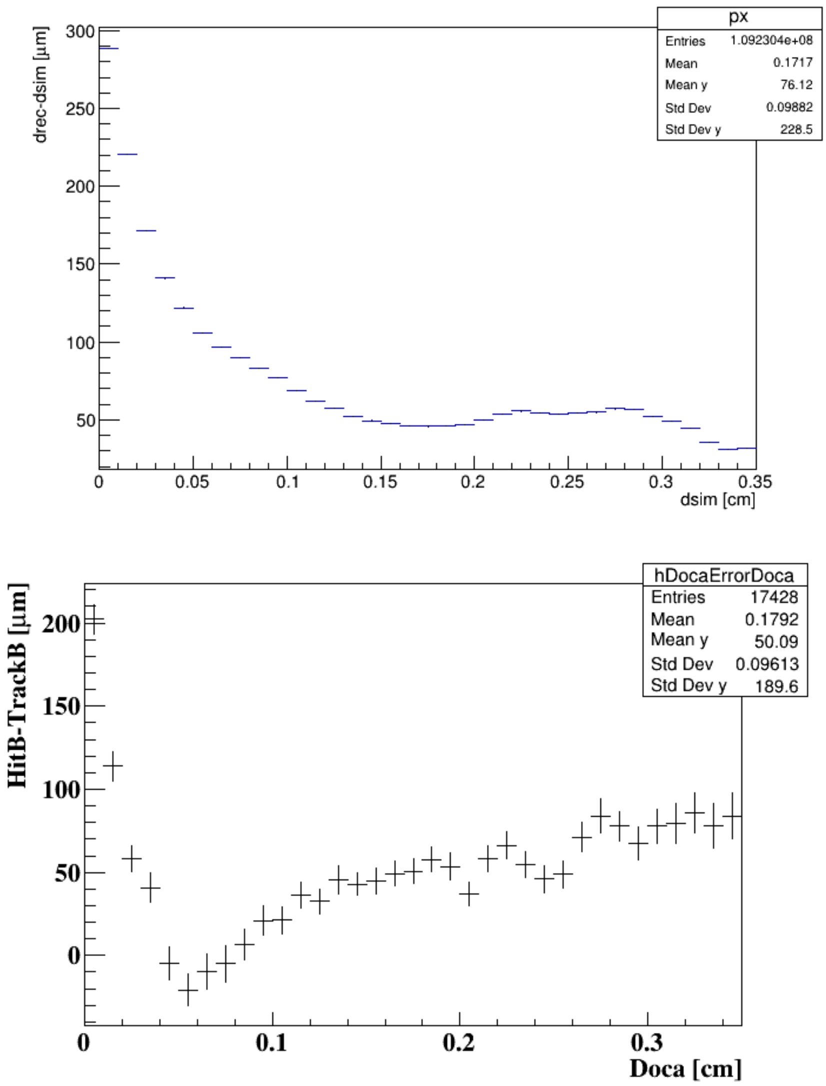

Figure 5.13: Top: doca evaluation from Garfield++ simulation. Bottom: Doca evaluation from experimental data.

The plot on the top of Figure 5.13 shows the trend of the difference between the impact parameter simulated by Garfield++ and the one reconstructed with the txy table vs the simulated impact parameter in a range from 0 to 0.35 cm.
On the bottom, the doca error (HitB-TrackB [3]) vs doca is shown as result of the experimental data analysis.
An offset in Figure **??** bottom is evident and in order to correct it, 1 ns has been added in the time values stored in the txy tables. The result is shown in Figure 5.14.

[3]HitB is the impact parameter from the reconstructed hit, instead TrackB correspond to the impact parameter from the reconstructed track

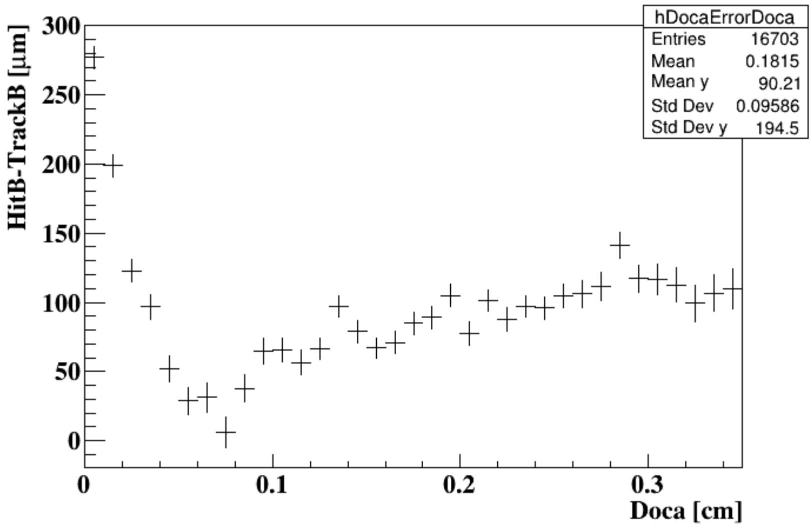

Figure 5.14: Doca error distribution vs doca after the time correction after the time shift correction.

Once restored the time shift, we investigated the difference between the reconstructed impact parameter and the simulated one. In order to correct this to reduced the separation between them a calibration procedure has been implemented.

5.9 The calibration procedure

To reduce the difference between the simulated and the reconstructed impact parameter, a calibration procedure has been performed, by writing a set of tables where the needed correction factors as a function of the drift time have been stored.
Indeed on the left side of Figure 5.15 it is evident that the reconstructed impact parameters by applying the txy tables and the simulated ones by garfield differ by a factor of around ten μm (at least up to 200 ns). This mismatch is restored after the calibration procedure, as shown on the right of the figure.

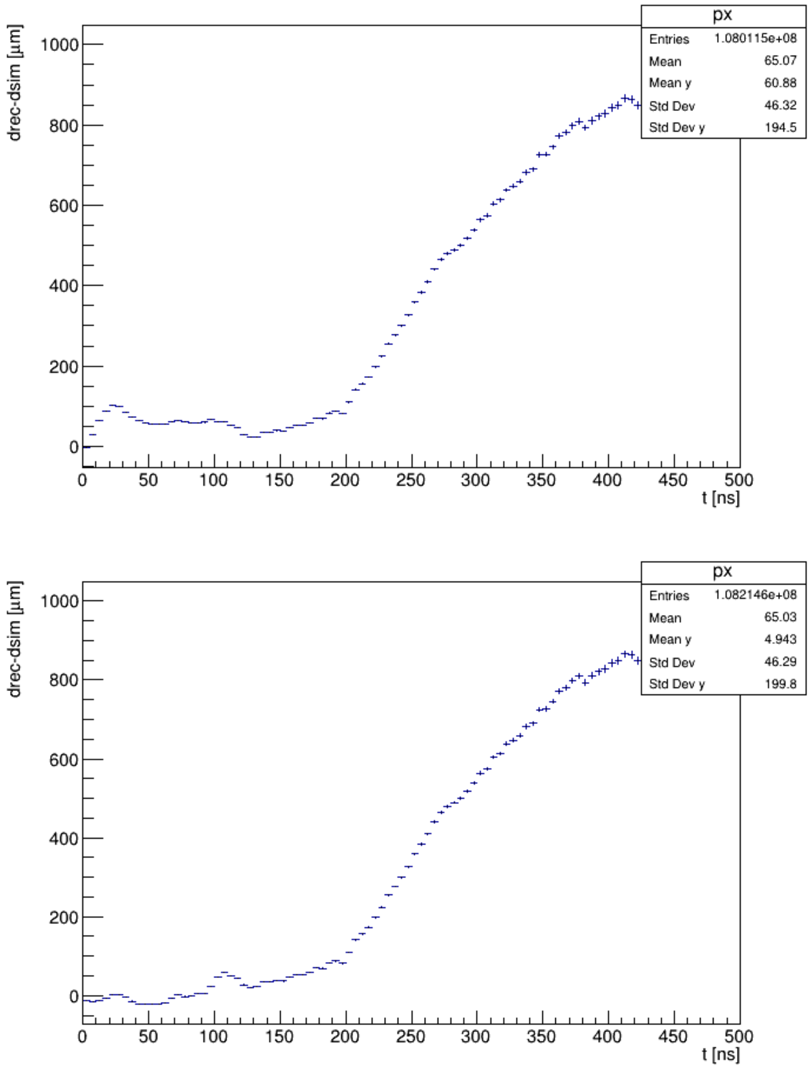

Figure 5.15: Top: Simulated doca distribution without the calibration procedure. Bottom: Simulated doca distribuiton after the calibration procedure.

The calibration has been performed up to 200 ns, neglecting higher drift times which correspond to larger impact parameter.
This procedure has been applied to the experimental data. The impact of the calibration has been studied by analyzing the same 3 features mentioned at the begin of this chapter. Their distributions are reported in Figure 5.16.

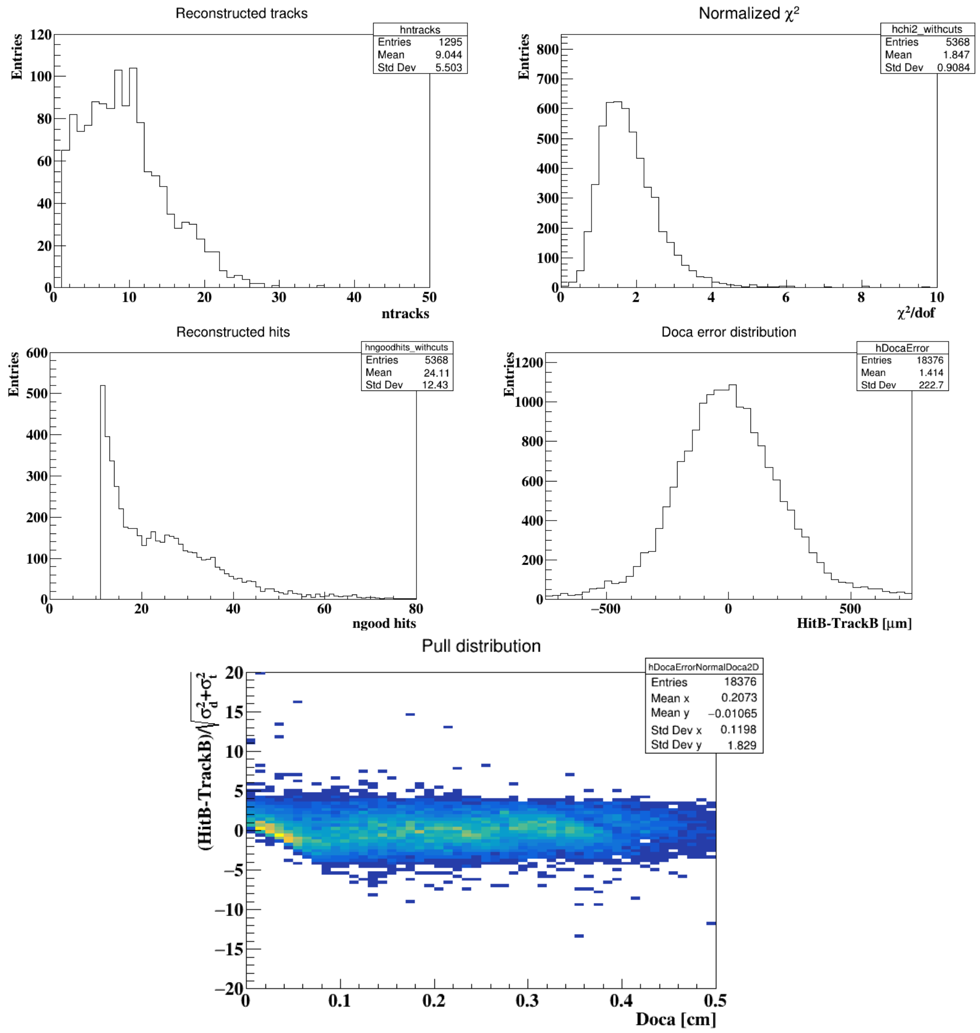

Figure 5.16: Analysis of target features obtained by applying the new version of the txy tables with the calibration procedure. Top Left: reconstructed tracks distribution. Top Right: Normalized χ^2 distribution. Bottom Left: reconstructed hits distribution. Bottom Right: Doca error distribution. Bottom Center: Pull distribution.

5.10 Sigma correction

At this point, the pull distributions have been studied to check the impact of the sigma stored in the average tables to the tracking performances.

In details, the 2D simulated pull distributions as a function of the impact parameter have been divided in slices; the core of each of them have been fitted with a Gaussian function. An example is reported in Figure 5.17.

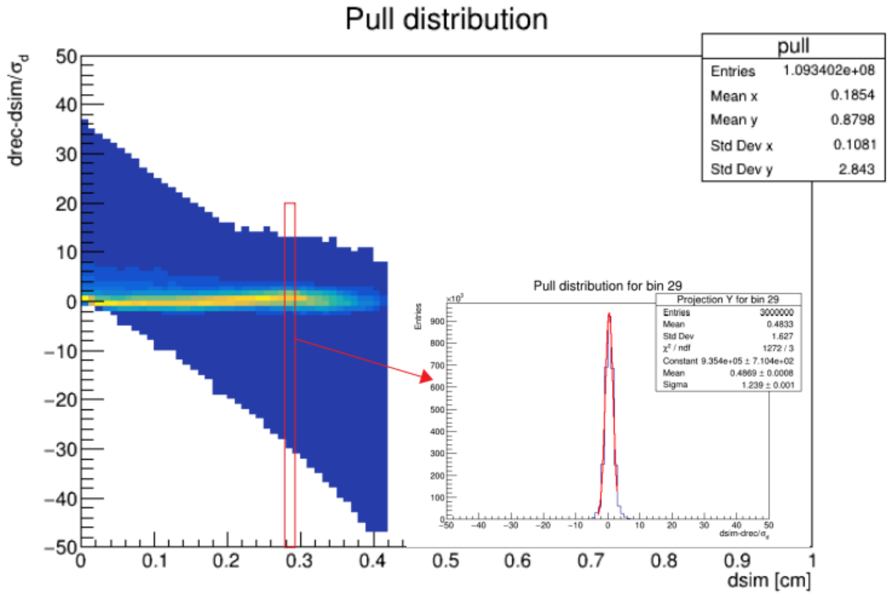

Figure 5.17: Simulated pull distribution with a slice corresponding to the 29^{th} bin of the histogram.

Each Gaussian sigma value has been stored and multiplied by the sigma of the txy average tables. Figure 5.18 shows the results obtain without (Left) and with (Right) the correction on simulations.

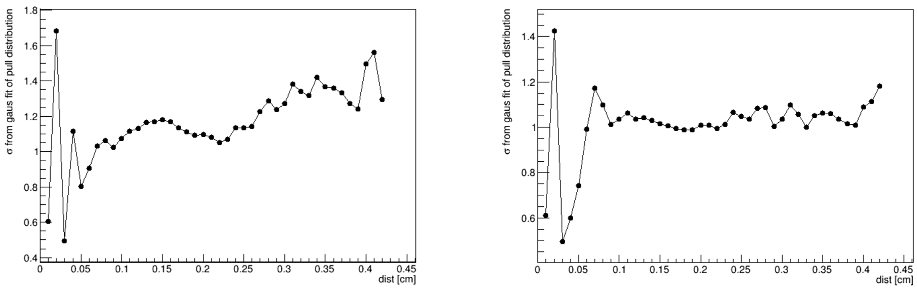

Figure 5.18: Sigma distribution vs impact parameter before (Left) and after (Right) the correction.

The same 3 features have been studied and reported in Figure 5.19.

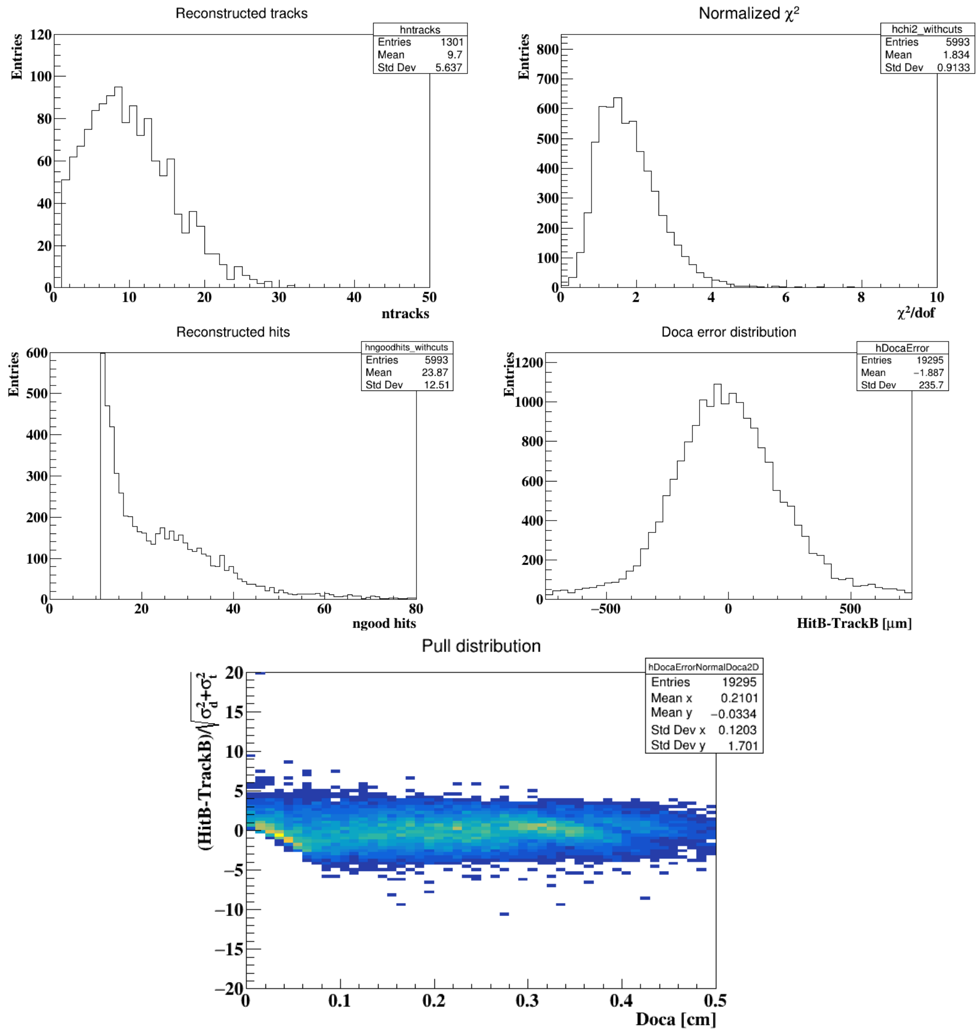

Figure 5.19: Analysis of target features obtained by applying the new version of the txy tables with the calibration procedure and the correction on sigma values. Top Left: reconstructed tracks distribution. Top Right: Normalized χ^2 distribution. Bottom Left: reconstructed hits distribution. Bottom Right: Doca error distribution. Bottom Center: Pull distribution.

5.11 A sigma multiplication factor

In the end, by studying the pull distribution for the chosen set of data, it is evident an almost constant multiplication factor for the sigma value, as shown in Figure 5.20.

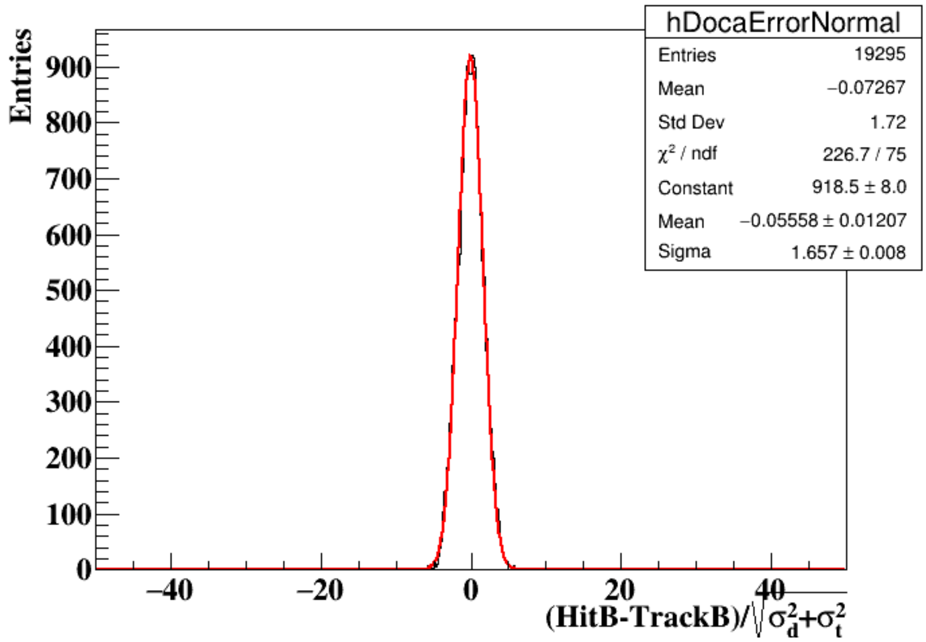

Figure 5.20: Pull distribution from experimental data fitted with a Gaussian function.

This is due to the fact that, besides we cut the tail of the distribution by choosing the cut rms, during the fitting procedure a bunch of hits which do not belong to the core play a certain role. So that, the sigma value is underestimated and to correct this effect, the sigma values stored in the average tables have been multiplied by this constant factor of 1.657. The result is shown in Figure 5.21.

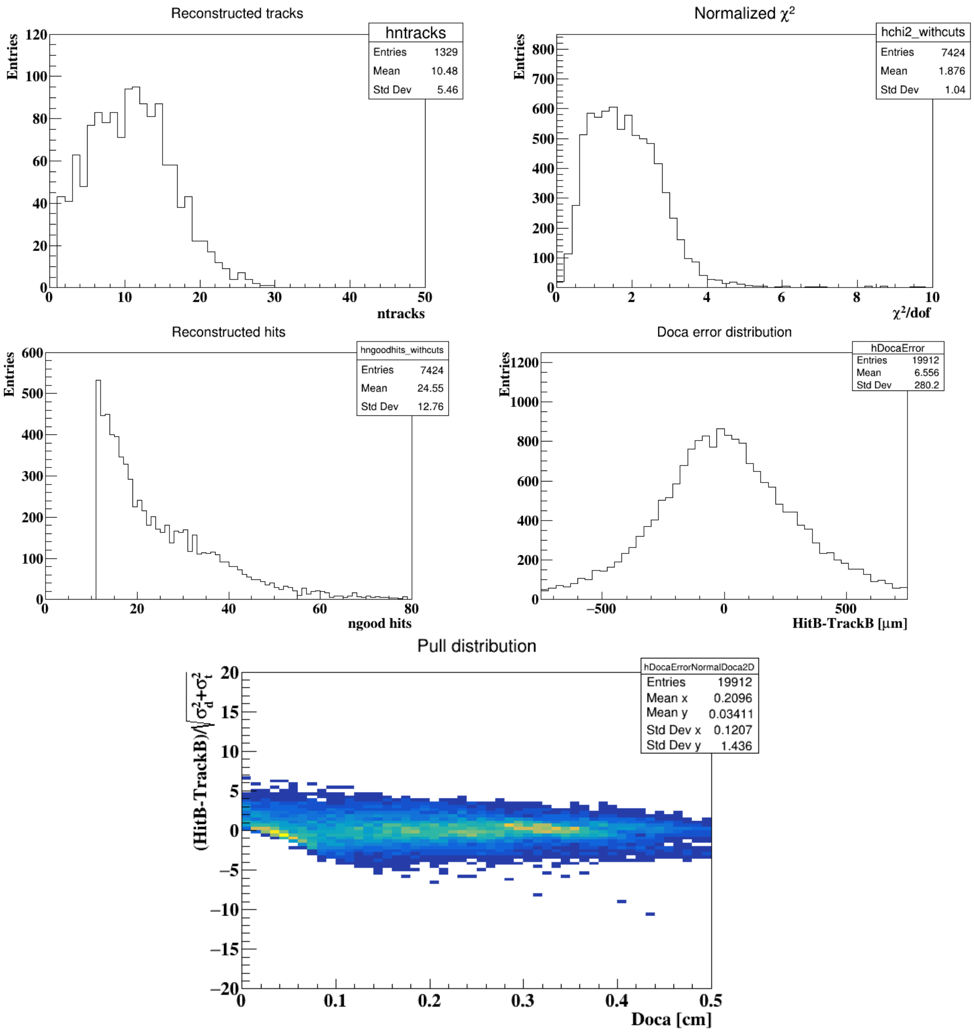

Figure 5.21: Analysis of target features obtained by applying the new version of the txy tables with the calibration procedure, the correction on sigma values and the constant multiplication factor. Top Left: reconstructed tracks distribution. Top Right: Normalized χ^2 distribution. Bottom Left: reconstructed hits distribution. Bottom Right: Doca error distribution. Bottom Center: Pull distribution.

5.12 The "mixed strategy"

Among all the differences between the followed step to improve the tracking performances by using the new set of txy tables, the most characteristic feature relies in the fact that by using the calibration procedure better resolutions have been obtained at the cost of less reconstructed tracks with respect to the old txy tables. By applying the correction on the sigma, the number of reconstructed tracks can be raised, with the cost of poor resolution. The strategy to find a compromise consists in applying all the corrections (calibration, sigma correction and sigma factor) at the pattern recognition stage, while maintaining only the calibration procedure during the fit stages.
The results are shown in Figure 5.22.

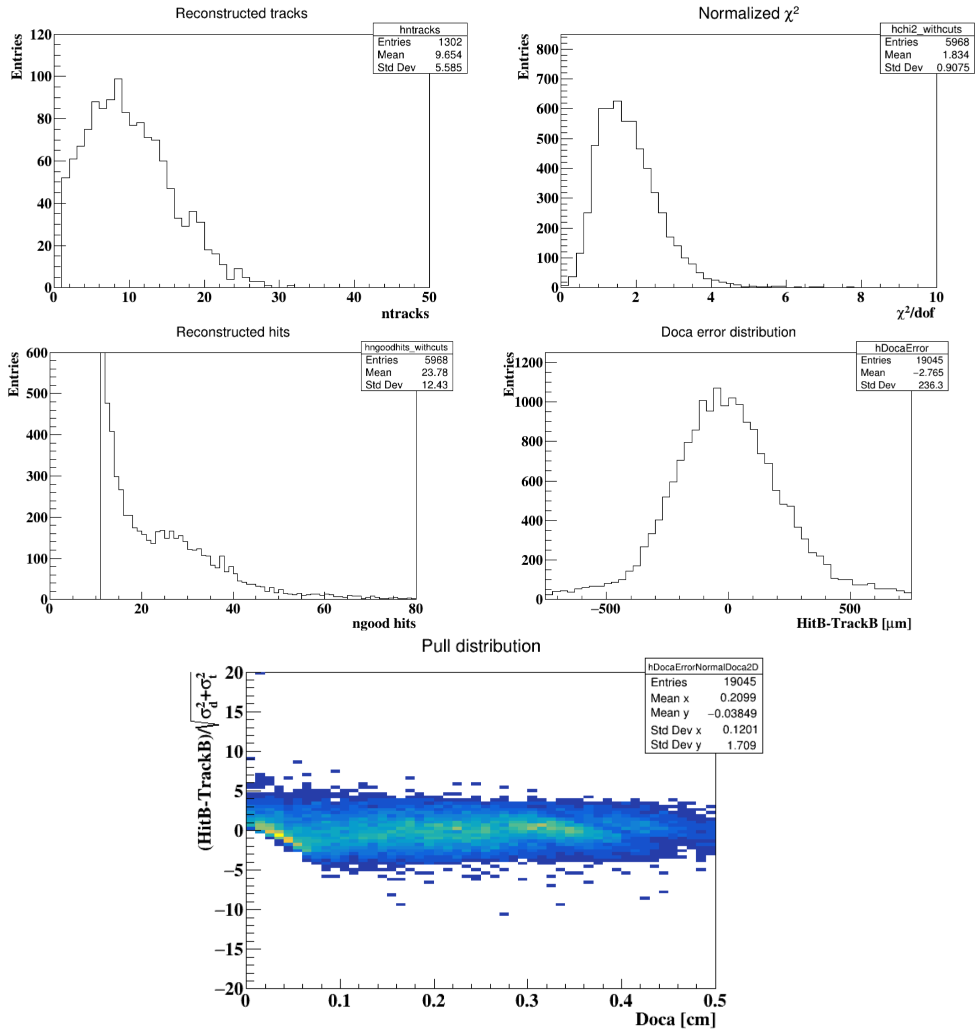

Figure 5.22: Analysis of target features obtained by applying the new version of the txy tables with the "mixed strategy". Top Left: reconstructed tracks distribution. Top Right: Normalized χ^2 distribution. Bottom Left: reconstructed hits distribution. Bottom Right: Doca error distribution. Bottom Center: Pull distribution.

5.12.1 Doca error in range

Once again, as mentioned in paragraph 5.7.1, it is useful to compare the doca error for three different range of the impact parameter between the results obtained with the calibration procedure, the ones obtained by adding the correction and the multiplication factor of the sigma and the mixed strategy. The distributions are reported in Figure 5.23.

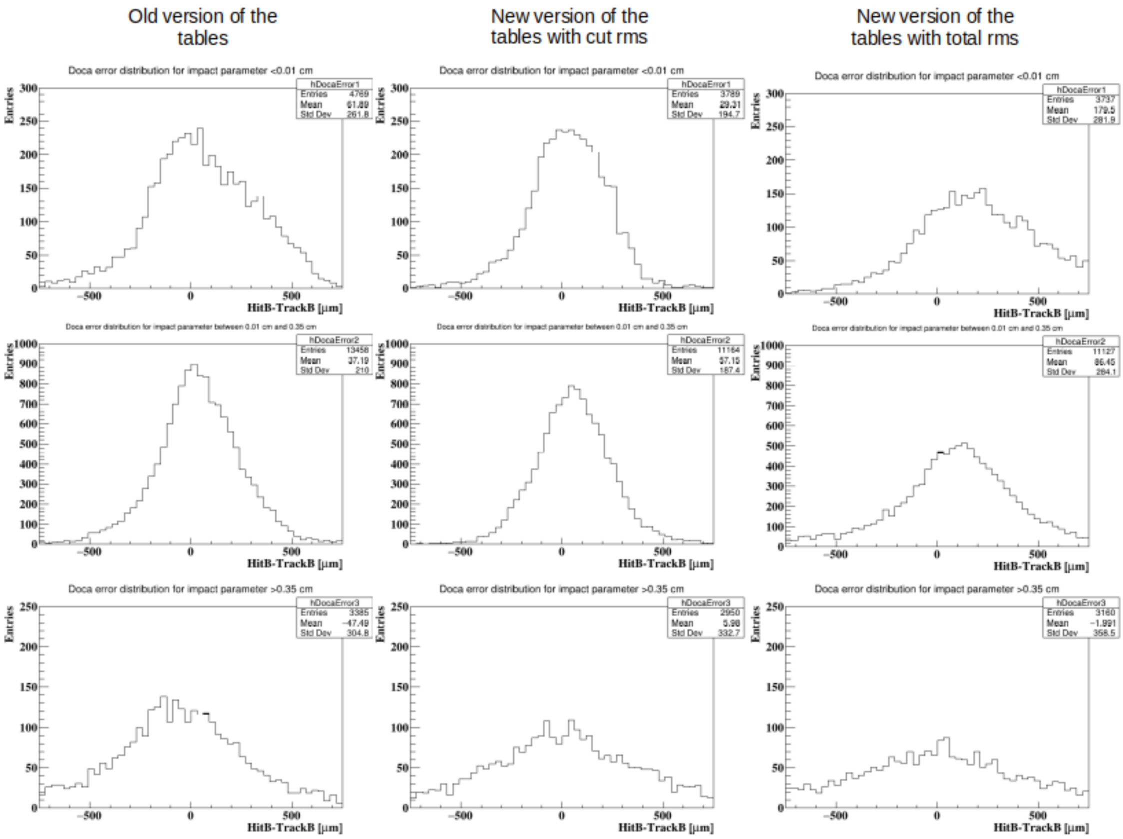

Figure 5.23: Doca error per range. First column is referred to the new version of the tables with cut rms and calibration procedure. Second column is referred to the new version of the tables with cut rms and all the correction chain. Third column is referred to the new version of the txy table with the cut rms and the mixed strategy.

5.12.2 Summary table

Table 5.2 shows at glance the performances obtained at each stage of the improvement procedure of txy tables.

Table 5.2: Summary table of the performances obtained with the different configuration tested.

		Old version of the tables	New version of the tables with cut RMS	New version of the tables with total RMS	New version of the tables with cut RMS with: • Calibration	New version of the tables with cut RMS with: • Calibration • Sigma correction	New version of the tables with cut RMS with: • Calibration • Sigma correction • Sigma factor	New version of the tables with cut RMS: • Mixed strategy
Number of tracks	#	1311	1295	1326	1295	1301	1329	1302
	Mean	9.567	9.045	10.33	9.044	9.7	10.48	9.654
	stdDev	5.55	5.512	5.279	5.503	5.637	5.46	5.585
χ^2	#	6645	5472	7233	5368	5993	7424	5968
	Mean	1.664	1.843	1.808	1.847	23.87	1.876	1.834
	stdDev	0.9135	0.8974	0.977	0.9084	12.51	1.04	0.9075
Number of reconstructed hits	#	6645	5472	7233	5368	5993	7424	5968
	Mean	25.16	23.8	24.54	24.11	23.87	24.55	23.78
	stdDev	12.96	12.2	12.95	12.43	12.51	12.76	12.43
Doca error	#	21612	17903	18024	18376	19295	19912	19045
	Mean	30.48	43.5	94.57	1.414	-1.887	6.556	-2.765
	stdDev	240.4	217.7	299.8	222.7	235.7	280.2	236.4
Pull	#	21612	17903	18024	18376	19295	19912	19045
	Mean x	0.2093	0.212	0.2101	0.2073	0.2101	0.2096	0.2099
	Mean y	0.252	0.4167	0.4189	-0.01065	-0.0334	0.03411	-0.2099
	Std Dev x	0.1195	0.1195	0.1186	0.1198	0.1203	0.1207	0.1201
	Std Dev y	1.577	1.769	1.362	1.829	1.701	1.436	1.709

5.13 Positron momentum resolution: Michel Fit

The resolutions and efficiency of the positron reconstruction are evaluated with the Michel fit method for a set of data collected during the 2022 run at beam intensity of 3×10^7. The theoretical energy spectrum from Michel decay is well known [109]. The positron energy resolution can be measured with a fit to the energy distribution of the Michel spectrum multiplied by an acceptance function and convoluted with a resolution function [76].

$$Probabilitydensity(E_e^{measured}) = (Michel \times Acceptance)(E_e^{true}) \otimes Resolution \qquad (5.6)$$

Functional forms for the acceptance and the resolution functions are based MonteCarlo simulation analysis. The acceptance function is:

$$Acceptance(E_e^{true}) = \frac{1 + Erf(\frac{E_e^{true} - \mu_{acc}}{\sqrt{2}\sigma_{acc}})}{2} \qquad (5.7)$$

and the resolution function is taken to be a double Gaussian function.

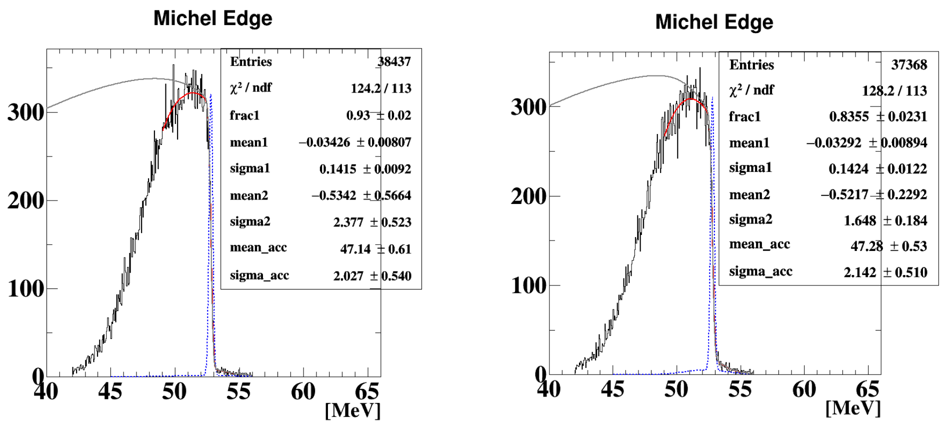

Figure 5.24: Michel-Fit with the reconstructed energy spectrum obtained with the old version of the table. The gray line shows the theoretical Michel spectrum, the blue dashed line resolution and the red line is the fitting result.

mean1 and sigma1 are referred to $\mu core$ $\sigma core$, while mean2 and sigma2 are referred to $\mu tail$ $\sigma tail$.
The table 5.3 compares the Michel fit performances between the 2013 data, the MC expectation and the old and new txy tables.

Table 5.3: Summary table of the Michel fit parameters.

	Michel Fit with 2013 data	Michel Fit with MEGII expected (MC)	Michel fit with MEG II 2022 data and the old version of the tables	Michel fit with MEG II 2022 data and the new version of the tables with cut rms: • Mixed strategy
σ_{core} (keV)	325	110	142	142
σ_{tail} (MeV)	1.91	2.28	2.38	1.6
f_{core}	0.852	0.911	0.93	0.83
μ_{acc} (MeV)	49	46.9	47.14	47.28
σ_{acc} (MeV)	2.5	2.4	2.1	2.1

Two of the applied selection cuts have been scaled by the average number of reconstructed hits, in order to taking into account the differences between the new and the old txy tables. In any case, other cuts should be checked and optimized with the new configuration, since the number of tracks reconstructed by the new txy tables are less than the ones reconstructed by the old version of the tables. Indeed the ratio between the number of positron tracks reconstructed and the tracks processed is 0.16 for the old txy tables and 0.14 for the new ones. Further investigations by experts need to be performed.

5.14 Further possible improvements

The "mixed strategy" gives promising results for the MEGII tracking performances, but of course, there is always room for improvement.
The first key relies on the calibration procedure: we developed a new set of calibration tables, which store calibration factor per each layer, but it could be more appropriate to perform this calibration at different z coordinate and at different ϕ.
The same observation can be made about the sigma correction, which is perform over all the layer and all the z coordinates, instead of considering separately each layer.
In the end, the evaluation of the multiplication factor should be refined considering once again each layer separately.

Chapter 6

The IDEA detector for FCC and CEPC

The Higgs boson discovery at the Large Hadron Collider of CERN was a turning point for high energy physics. Thanks to its relatively low mass, the Higgs boson can be copiously produced at a future high-luminosity e^+e^- collider in a very clean environment. Precise measurements of its properties, together with those of the Z and W bosons, will provide important tests for the Standard Model and for the physics Beyond the Standard Model (BSM). The high statistics measurement plan expects to study other important physics aspects: for instance, the observation of lepton flavour violating decays, or the precise measurements of the H and Z invisible decay widths, or the direct observation of particles with extremely weak couplings, are expected to provide signals of new physics.
For the FCC-ee and CEPC, the Innovative Detector for Electron-positron Accelerators (IDEA) [110], [111] has been proposed to investigate electron-positron annihilations in a wide range of center of mass energies.

6.1 The IDEA layout

The IDEA conceptual experiment is based on innovative technologies developed in recent years. It is equipped with a Silicon Inner Tracker, surrounded by a very light Drift Chamber and by a Silicon wrapper. The Inner detector is immersed in a 2T magnetic field, generated by a very thin superconducting solenoid. A dual readout calorimeter is positioned outside the magnet, and within the return joke of the magnet. A muon tracker, based on μ-RWELL technology, is interleaved with the return joke material. This same technology also provides a layer of preshower in front of the calorimeter [110, 112].
The structure of the IDEA detector is depicted in Figure 6.1 and its key parameters are listed in Table 6.1.

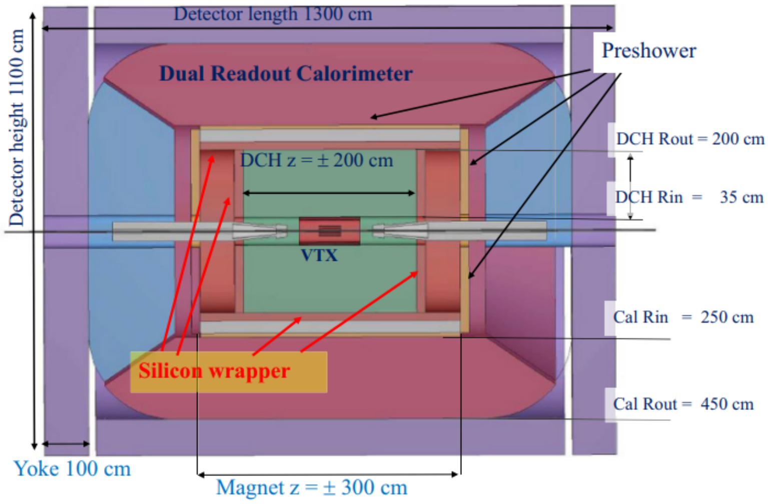

Figure 6.1: Schematic layout of the IDEA detector [56].

Table 6.1: Key parameters of the IDEA detector [56].

Vertex technology	Silicon
Vertex inner/outer radius	1.7 cm/34 cm
Tracker technology	Drift chamber + silicon wrapper
Tracker half length/outer radius	2.0 m/2.0 m
Solenoid bore radius/half length	2.1 m/3.0 m
Preshower/calorimeter absorber	Lead/lead
Preshower inner/outer radius	2.4 m/2.5 m
DR calorimeter inner/outer radius	2.5 m/4.5 m
Overall height/length	11 m/13 m

6.1.1 The vertex detector

The innermost detector, surrounding the 1.5 cm beam pipe, is a silicon pixel detector, based on monolithic active pixel sensors, for the precise determination of the impact parameter of charged particle tracks. A lot of effort is spent trying to reach resolutions at a few μm level, thickness in the 0.15-0.30 % X_0 range per layer and power dissipation not exceeding $20mW/cm^2$ [110].
Beam test results on the detectors developed for ALICE inner tracker upgrade (ITS) indicate a resolution of $\approx 5\mu m$ [113, 114], and a high efficiency at low power and dark noise rate [115]. This constitutes the state-of-art starting point for the IDEA vertex detector.

6.1.2 The preshower

The preshower detector uses the micro-Resistive WELL (μ-RWELL) technology, which is a compact Micro-Pattern Gaseous Detector (MPGD), with a single, intrinsically spark protected, amplification stage [116].
In the barrel region, the magnet coil works like an absorber of 0.7 X_0 and it is followed by a layer of μ-RWELL chambers. In the forward region, a 1 X_0 lead absorber is placed in front of a layer of μ-RWELL chambers, located immediately before the endcap calorimeter. This allows to tag $\approx 30\%$ of the π^0 by having both γ from their decay identified by the preshower and provides a good acceptance determination for photons given the high mechanical stability

of the chambers.
The μ-RWELL chambers together with the silicon detector provide a precise acceptance determination for charged particles.

6.1.3 The magnet system

A solenoidal magnet, 5 m long and with an inner diameter of 4.2 m, surrounds the tracking system. The 2 T and the small dimensions proposed can keep the overall magnet package thickness at 30 cm level. With the given dimensions, a yoke thickness of less than 100 cm of iron is enough to completely contain the magnetic flux and provide adequate shielding and support for the muon chambers [110].

6.1.4 Dual readout calorimeter

A copper-based dual-readout fiber calorimeter surrounds the preshower. The total calorimeter depth is 2 m, which corresponds to $\approx 8\lambda_{int}$. The expected energy resolutions will be around $11\%/\sqrt{E}$ for electrons and around $33\%/\sqrt{E}$ for isolated pions with negligible constant terms, as estimated from GEANT4 simulations [56].
The dual-readout calorimeter provides an excellent intrinsic discrimination between muons, electrons/photons and hadrons for isolated particles [117]. In addition to the intrinsic particle identification capabilities, the fine transverse granularity allows close showers to be separated and provides good matching to tracks in the inner, preshower signals, and also to muon tracks, making this calorimeter a good candidate for efficient particle-flow reconstruction. A longitudinal segmentation is required to disentangle signals produced by overlapping electromagnetic and hadronic showers. Different solution are under study with simulations and dedicated beam test [118, 119].

6.1.5 The muon detector system

The IDEA muon system uses the μ-RWELL technology, which provides good tracking efficiency, precise space resolution on the coordinates of a muon track (200-300 μm) and good time resolution. Moreover, this choice allows a significant reduction of the cost to equip extremely large surfaces with tracking chambers outside the calorimeter volume. The best option is using tiles of μ-RWELL detectors of $50 \times 50 cm^2$ assembled into 3 detector stations, each one equipped with a layer of μ-RWELL detectors with bi-dimensional readout [120].

6.2 The drift chamber of IDEA detector

The IDEA Central Drift Chamber (DCH) exploits the expertise earned from the previous chamber of KLOE experiment and MEG II experiment.
It is a unique-volume, high granularity, fully stereo, low-mass cylindrical drift chamber, co-axial with the 2 T solenoid field, operating with an helium based gas mixture. It extends from an inner radius $R_{in} = 0.35$ m to an outer radius $R_{out} = 2$ m, for a length $L = 4$ m and consists of 112 co-axial layers, at alternating-sign stereo angles (see Figure 6.2), arranged in 24 identical azimuthal sectors, a layout similar to the one used in MEG II drift chamber. The stereo angles range from 50 mrad to 250 mrad. The square cell size varies between 12.0 mm

and 14.5 mm for a total of 56,448 drift cells. Each cell is designed with a ratio of field to sense wires equal to 5:1 to ensure the proper electrostatic configuration, and is composed by one anode and two cathode sub-layers, as outlined in Figure 6.2 [121]. The anodes are 20 μm

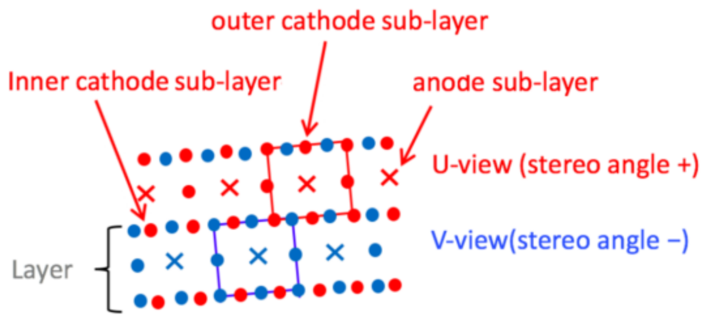

Figure 6.2: A sketch of the drift cells within two alternating sign stereo layers.

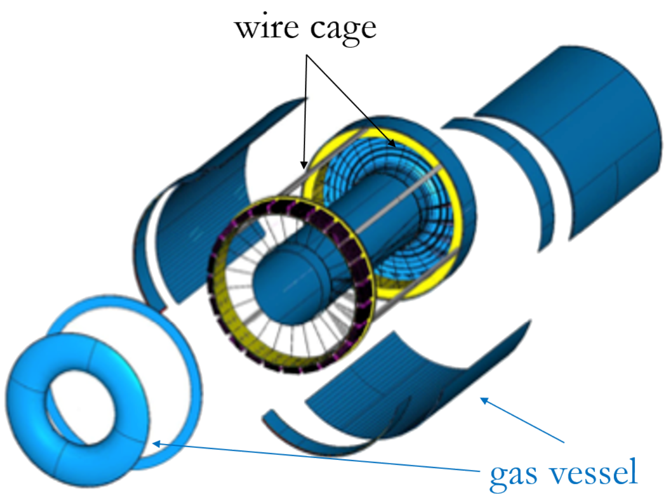

Figure 6.3: Schematic layout of the CDCH mechanical structure.

diameter tungsten wires, while the cathodes are 40 and 50 μm light aluminum alloy wires. In total, the CDCH is made with 56,448 sense wires, 285,504 cathode wires and 2,016 guard wires to equalize the gain of the innermost and outermost layers.
As for MEG II drift chamber, the high wire number requires a new wiring procedure and a feed-through-less wiring system, so its novel wiring procedure will be used [91].
To ensure the transparency, the gas containment function and the wire sustained function are separated: the wires are anchored to a self-sustained light structure (wire cage), which is surrounded by a thin skin of a suitable profile (gas vessel) to contain the gas mixture (see Figure 6.3). A system of tie-rods which directs the wire tension stress to the outer endplate rim, where a cylindrical carbon fiber support structure, bearing the total load, is attached. Two thin carbon fiber domes enclose the gas volume, as shown in Figure 6.3. Their profile is suitably shaped in order to minimize the stress on the inner cylindrical wall, and they are

free to deform under gas pressure variations, without affecting the wire tension [121].

6.2.1 Tracking performance and fast simulations studies

A Geant4 simulation has been performed to estimate the performance of the IDEA tracking system. Assuming a single cell resolution of 100 μm for the chamber (as expected for the average single cell resolution [94]) and a conservative spatial resolution (pitch/ $\sqrt{12}$) for Si detectors, the IDEA tracking system meets the expected great performances, shown in Figure 6.4. The lightness of the drift chamber allows to the IDEA tracking system to gain almost a factor $\sim$ 3 in momentum resolution respect to a full Si tracker system up to $\sim$50 GeV/c, as shown in Figure 6.4 [122]. Moreover the IDEA DCH will exploit the cluster timing technique

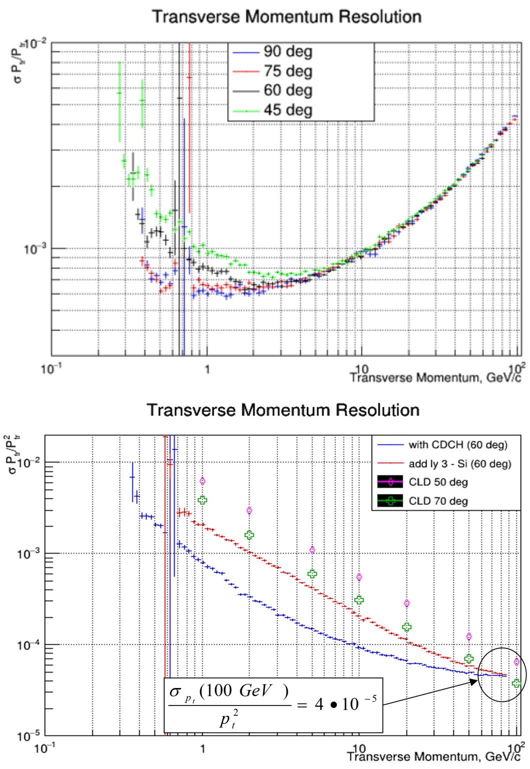

Figure 6.4: Top: Transverse momentum resolutions of the IDEA tracking system, evaluated for tracks with θ of 45° , 60° , 75° and 90°. Bottom: Transverse momentum resolutions of the IDEA tracking system respect to a full Si based tracking system like the CLD detector one [122].

[92], which will improve the tracking performances.
Cluster timing techniques use the information provided by the later clusters to form a weighted average of the impact parameter estimates, provided by the different clusters. Figure 6.5 shows the cluster counting improvement with respect to the other techniques.

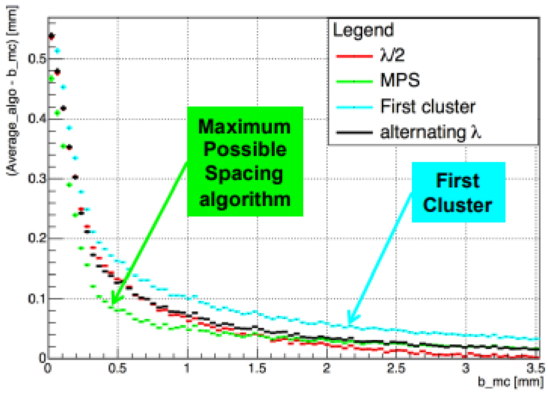

Figure 6.5: Cluster timing allows to reduce the average spatial resolution from 100 μm down to 85 μm in a 8 mm cell. For any given first cluster drift time t_1, the cluster timing technique exploits the drift time distribution of all the successive clusters to statistically determine, hit by hit, the most probable impact parameter. In this way, the bias is reduced and the average spatial resolution is improved with respect to that obtained from with the first cluster method alone [92].

6.2.2 Particle identification with cluster counting technique

By using the cluster counting technique instead of the traditional method of dE/dx, the particle separation capabilities could be improved of a factor of 2 [123].
From Walenta's parameterization:

$$\frac{\sigma_{\frac{dE}{dx}}}{dE/dx} = 0.41n^{-0.43}(L_{track}[m]P[atm])^{-0.32} \tag{6.1}$$

From the Poisson distribution:

$$\frac{\sigma_{\frac{dN_{cl}}{dx}}}{dN_{cl}/dx} = (\delta_{cl}L_{track})^{-1/2} \tag{6.2}$$

The cluster counting technique could improve the particle separation capabilities with respect to the traditional method of the dE/dx.
The techniques takes advantages of the *Poissonian* nature of the primary ionization and offers a more statistically significant way to infer mass information. For more details, refer to chapter 7.

6.3 Development of the mechanical design for the IDEA ultra-light drift chamber in the contest of the CMD3 and SCTF experiment

The CMD3 experiment [124] has been operating at the VEPP-2000 electron-positron collider, at the Budker Institute of Nuclear Physics, since December 2010. Its main goal is to measure the hadronic cross sections necessary to evaluate the anomalous magnetic moment of the muon. The discrepancy between the theoretical calculations [125] and the experimental results obtained at the Brookhaven experiments is approximately 3.7 σ [126]. The comparison

between the results of the new "g-2" experiment at Fermilab and the theoretical calculation with the new experimental contributions from CMD3 could confirm the discrepancy, which is a new important hint of New Physics. A key element for the success the CMD3 experiment is the tracking detector, which is a drift chamber built in the year 2009 at INFN of Lecce [124]. Due to aging effects, its replacement is necessary, so that an innovative tracking detector, named **TraPId** (Tracking and Particle Identification) [127], has been designed: an ultra-light drift chamber equipped with cluster counting/timing readout techniques, which exploits the expertise gained with the successful construction of the MEG II drift chamber. The drift chamber proposed for CMD3 will be also the prototype for the tracking system of the future Super Charm-Tau Factory detector (SCTF) [128].
TraPId represents a valid case of study for the development of the ultra-light drift chamber for IDEA, besides the constraints will be quite different.

6.3.1 The mechanical design

The construction of CMD3 drift chamber is driven by two main purposes:

- Maximize the transparency in terms of radiation length.
- Maximize the mechanical stability by reducing to acceptable limits the deformations of the endplates under the total load of the wires.

A significant reduction in the amount of material at the end plates is obtained by separating the gas containment function from the wire tension support function. The wires are anchored to a self-sustaining light structure ("wire-cage") surrounded by a thin skin ("gas vessel") of suitable shape to compensate for the gas differential pressure with respect to the outside, as shown in Figure 6.6 [127, 129]. The wire-cage consists of a set of radial spokes, constrained at

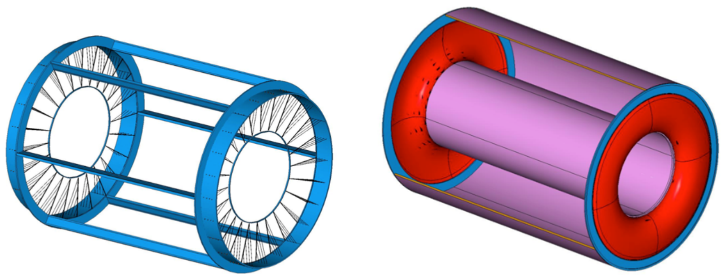

Figure 6.6: Left: the wire-cage. Right: the gas-vessel [127].

their inner ends into a tiny cylinder and extended to the outer endplate rim, thus subdividing the chamber in identical sectors. The chamber layout is obtained by stacking up radially, between adjacent spokes in each sector, printed circuit boards (PCB), where the wires ends are soldered with a well defined pitch, alternated with spacers to set the proper cell width. In order to minimize the deformations due to the wire load, it is necessary to create a system of adjustable tie-rods that steers the wire tension to the outer end plate rim, where a rigid cylindrical carbon fiber support structure, bearing the total wire load, is attached [127, 129].

6.3.2 Layout of the CMD3 drift chamber

The CMD3 drift chamber layout has to fit within the dimensions of the current CMD-2 drift chamber: 484 mm length, 609 mm outer diameter and 41 mm inner diameter. Optimization of the BGO endcap calorimeter electronics might allow extending the length of the drift chamber by about 10 mm. Figure 6.7 shows the schematic layout of the CMD3 drift chamber, which is divided in 4 concentric super-layers A, B, C and D and 24 identical sectors. Marked with black circles, from the inner to the outer radius, the inner, the middle and the outer cylinders are indicated. The red circles mark the separations between the different super-layers.

Super-layer A consists of open jet-cells with wires arranged axially. As illustrated in Figure 6.8, each cell defines one of the 24 sectors and includes 12 sense wires (red dots), azimuthally staggered with respect to field wires plane (black dots), the green dots represent two guard wire layers, at the two ends of the super-layer. As shown in Figure 6.8, the cell width increases from the inner to the outer radius up to the value of 28.4 mm. The middle cylinder at 120 mm radius divides the axial super-layer A from the next one, so that one could insert a thin mylar foil to separate the two volumes and use two different gas mixtures, to compensate the much longer drift times of the super-layer A. The mechanical design is being developed including this possibility [127].

Super-layers B, C and D are made of single-wire cells with the wires arranged in an appropriate stereo angle configuration (similar to the MEGII one) with 4 layers of 4 (5) cells per each sector B (C) and 8 layers of 6 cells per each sector D, as shown in Figure 6.9. The square cell size increases from 8.7 mm at the innermost radius to 12.4 mm at the outermost radius.

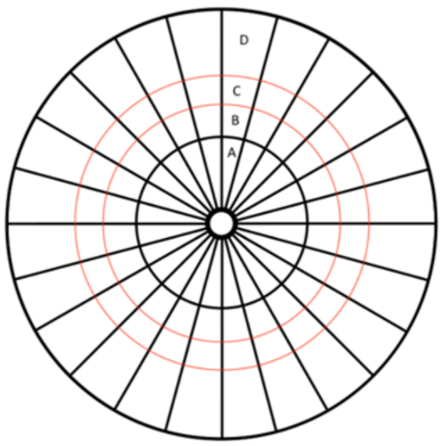

Figure 6.7: Schematic layout of the CMD3 drift chamber. The inner radius (20.5 mm), the outer radius (304.5 mm) and the separation region between axial and stereo super-layers (120 mm radius) are indicated with black circles. The outer cylinder is also shown. The red circles mark the separations between the different super-layers.

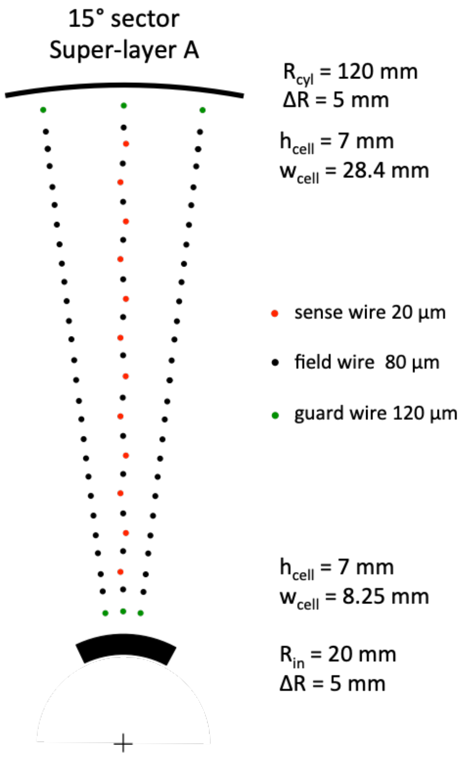

Figure 6.8: Cell structure in super-layer A: red dots represent sense wires, green dots represent guard wires and black dots represent field wires.

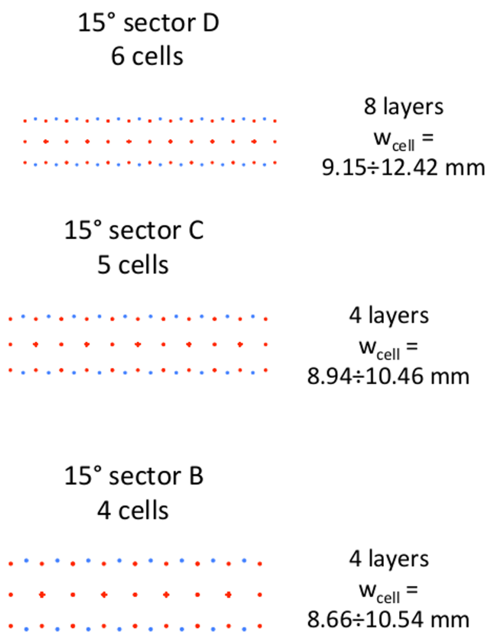

Figure 6.9: Cell layout in one layer of super-layers B, C, D. Red crosses represent sense wires, red and blue dots represent field wires. Red and blue wires are arranged at opposite stereo angles. Contiguous layers have stereo angles reversed.

6.3.3 The "wire cage"

The structural parts of the CMD3 drift chamber mechanics will be built in carbon fiber. Basic elements of the structure are: the "spokes", the "inner ring", the "intermediate ring", the "outer ring" and the "outer cylinder", all depicted in Figure 6.10.

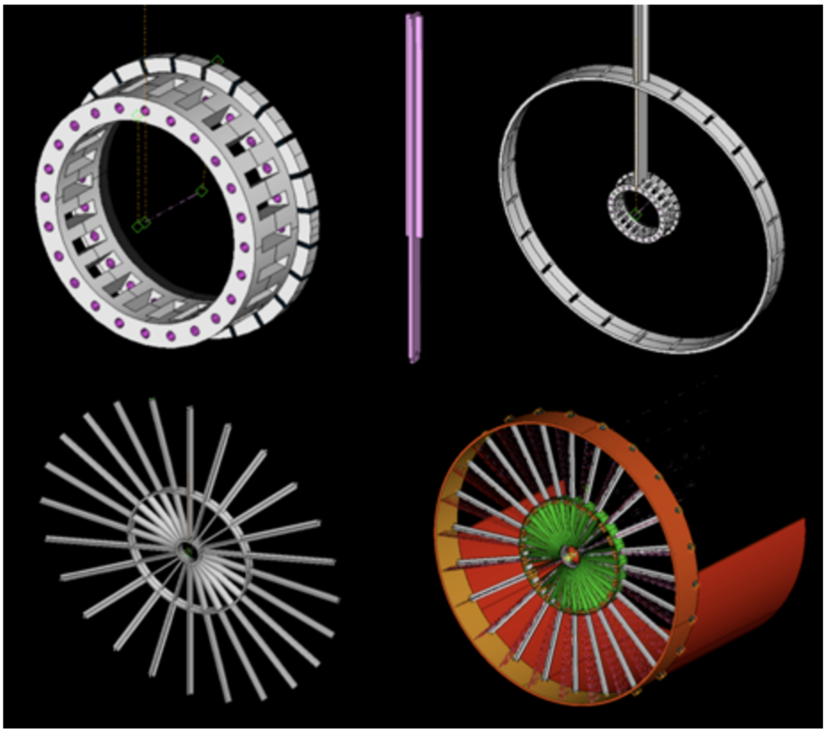

Figure 6.10: Top left: the inner ring. Top center: the spoke. Top right: assembly of the spoke with the inner and intermediate rings. Bottom left: assembly of the 24 spokes with the inner and intermediate rings. Bottom right: the outer ring and half of the outer cylinder; the wire holding PCB's in super-layer A and the first PCB's of super-layer B are visible [127].

The endplate assembly can be schematically summarized in the following steps.
Each spoke is inserted through a slit in the intermediate ring and is fixed with a dowel pin to the inner ring, as shown in the top right part of Figure 6.10. The operation is repeated for all 24 spokes, to form the structure shown in the bottom left part of Figure 6.10. The structural outer ring (bottom right of Figure6.10) is then placed around the spokes, which are bolted in with a proper tension (the bolts are visible in the bottom right part of Figure 6.10). The two identical endplates are then constrained at the nominal distance by means of external adjustable supports, capable of shifting longitudinally one endplate with respect to the other one.
With the endplates moved closer than the nominal chamber length, to facilitate the wiring operations, one can start the wiring procedures, which proceeds as follows for layer A. The wire holding PCB (two per sector, see Figure 6.11-a), to which the wires are soldered, are inserted on both ends of the chamber, from inside, through the slots of the inner ring (see Figure 6.11-b) and are fixed in position with properly shaped locking blocks (Figure 6.11-d and Figure 6.11-e). This complete the wiring of one sector (see Figure 6.11-c) and the entire procedure is repeated for all 24 sectors to complete the wiring of layer A.

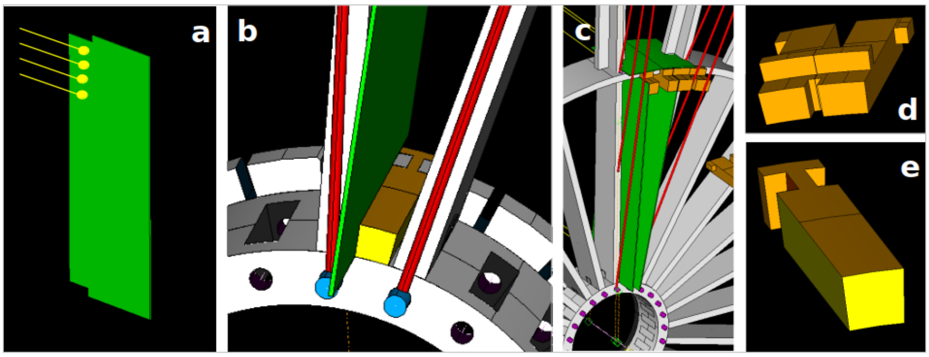

Figure 6.11: a: the wire holding PCB; b: detail of the inner ring with the slots allowing for the passage of the wire holding PCB from the inside of the chamber and of the wedge shaped inner locking block (e); c: one assembled sector of layer A with the two wire holding PCB and the corresponding support blocks at the intermediate ring (d).

Layers B, C and D are all wired in analogy to the MEG2 drift chamber. At the boundary between A and B a stereo layer of guard wires is placed to define a hyperboloid equipotential surface in order to avoid longitudinal gas gain variations for the stereo layers. The cell structure in each sub-layer is obtained by overlapping, in the order, inner field wires PCB, spacers, sense wire PCB, spacers and outer field wires PCB, all with the same stereo orientation. The spacer thickness sets the half-cell width. The stereo angle is obtained by jumping one sector from one endplate to the other. Successive sub-layers have alternating signs stereo angles. Both spacers and wire PCB are lowered from the outer radius and are engaged around the wings of the spokes, which take the whole load from the wires mechanical tension.
In order to limit the spokes deformation, a set of stays, the tension of which can be adjusted, are strung between the spokes and the structural outer ring. The whole system, shown in Figure 6.12, acts like a "harp cable stayed bridge" structure, with the outer ring acting like the tower (the pylon) and with the spoke representing the bridge deck [127].

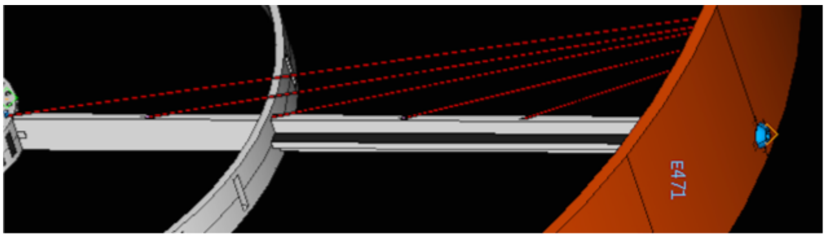

Figure 6.12: The arrangement of the system outer ring (pylon), spoke (bridge deck) and stays as in a "harp cable stayed bridge" structure [127, 129].

Preliminary Finite Element Analysis The mechanical design is completely innovative, thus requires accurate calculations to guarantee mechanical stability of the system. Preliminary investigations, by using Finite Element Analysis (FEA), have been performed under much simpler conditions, to establish the feasibility of the concept [129].
The total load due to the wire tension is of the order of 500 Kg (assuming 20 μm tungsten wires for sense, 40 and 80 μm aluminum field wires and 120 μm aluminum guard wires) or, approximately, 20 kg per spoke, considered for simplicity as uniformly distributed along the

spoke length, with the spoke fixed at both ends and free to translating along the symmetry axis. Using a 133 GPa low modulus carbon fiber with the spoke solidly constrained on one end to the non-deformable outer ring and free to flex at the other end. Using a 133 GPa low modulus carbon fiber, one get a spoke deflection of 4.8 mm, as shown in Figure 6.13.

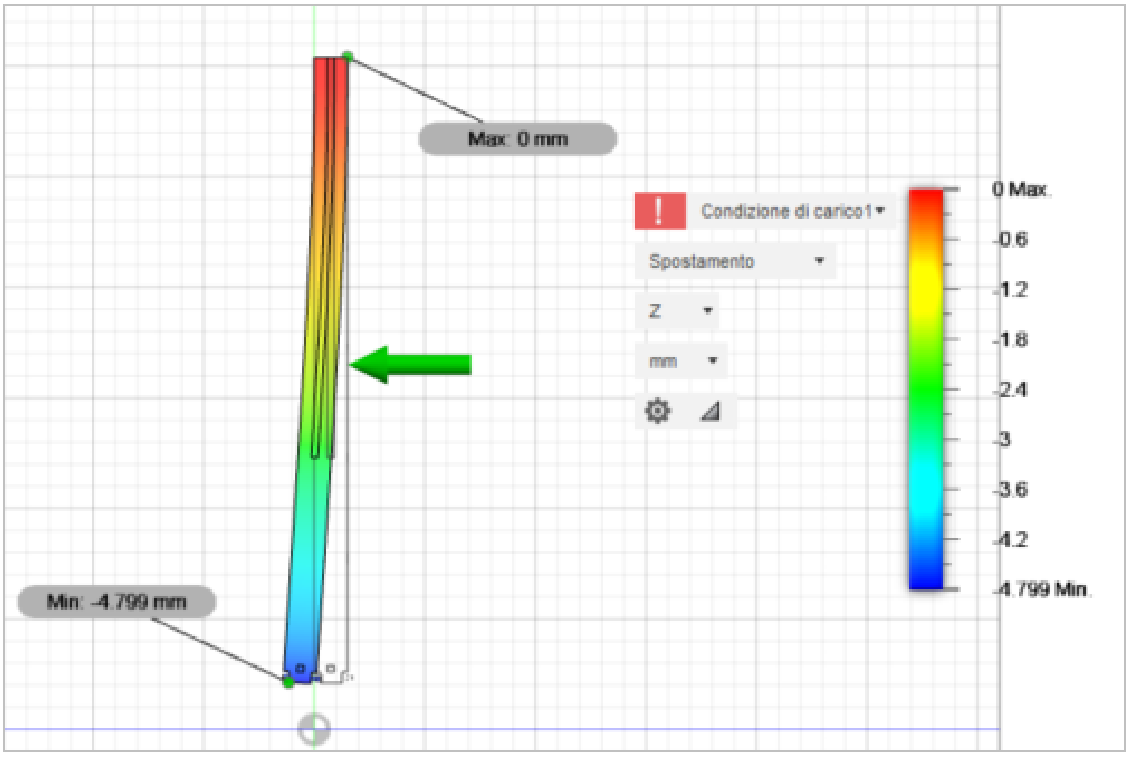

Figure 6.13: Spoke deflection under a load of 20 Kg uniformly distributed. Spoke constrained at one end and free to flex at the other end.

By adding the symmetry conditions of back-to-back spokes fixed to the inner ring and free of translating along the symmetry axis, the deflection is reduced to 2.2 mm, as shown in Figure 6.14-a. Tensioning with 45 Kg one stay per spoke, placed at the inner ring at an angle of 10° with respect to the spoke direction, further reduces the maximum deflection to 300 μm (Figure 6.14-b). Lastly, three stays per spoke, loaded with 14 Kg placed at 10° at the inner ring, 24 Kg at 14° at the intermediate ring and 20 Kg at 21° midway between the intermediate and the outer rings, reduce the maximum deflection within $\pm$25 μm (Figure 6.14-c).

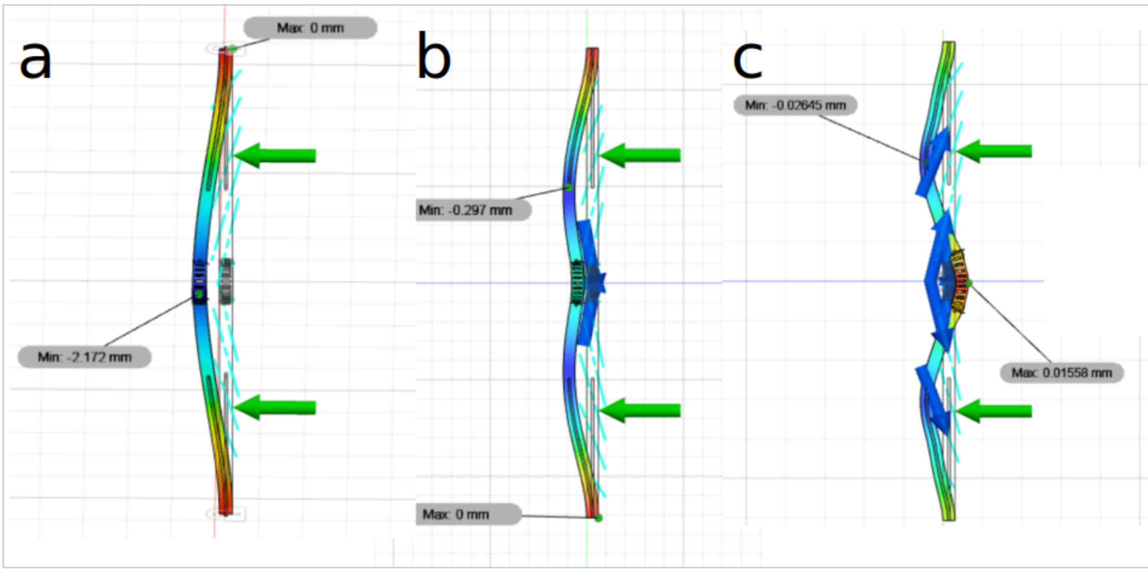

Figure 6.14: Spoke deflection under a load of 20 Kg uniformly distributed. a: symmetry condition added. b: one stay applied at the inner ring. c: three stays per spoke applied at the inner ring and at the intermediate ring and midway between the intermediate and the outer rings [129].

The preliminary FEA confirms that the concept is applicable to the drift chamber of CMD3. Obviously, a long campaign of finite elements calculations is needed to reproduce the correct constraint configurations, using the final version of the materials and shapes for the different components. Also, the reduction of the amount of material used in the endplates is the goal of the optimization of all parameters with the constraint of maximizing the stability of the entire structure.

Chapter 7

Particle identification with drift chamber: the cluster counting technique

Particle identification is one of the most important task for the experiments of high energy physics. There are two main ways to identify particles: the first is by analyzing the way in which they interact with the detector, i.e. by studying the signature that they leave. As an example, if a particle is detected only in a electromagnetic calorimeter, it can be concluded that it is a photon. The other way is by determining their mass and charge. In particular, the mass is derived by the simultaneous measurements of the momentum, measured thanks to the curvature of the track, in a suitable magnetic field and the velocity, obtained, among the other methods, by the measurement of the energy deposit by ionization. The charge sign is obtained from the curvature of the particle's track [130].
The ionization of matter by charged particles is the primary mechanism exploited for particle identification (dE/dx), but the large uncertainties in the total energy deposition represent a limit to the particle separation capabilities.
Even in the most favorable momentum region, i.e. the *relativistic rise*, the typical separation between the energy loss curves related to different particles is smaller than the spread around the relative mean values.
The cluster counting technique (dN/dx) takes advantage from the primary ionization *Poissonian* nature and offers a more statistically significant way to infer the mass information [95]. The method consists in singling out, in ever recorded detector signal, the isolated structures related to the arrival on the anode wire of the electrons belonging to a single ionization act. This technique will be widely explored with the **IDEA** drift chamber.
This chapter illustrates the procedure performed to investigate the potentials of the cluster counting technique, which consist of three different part: some theoretical calculation as a starting point, detailed simulations with Garfield ++ and the implementation of reasonable and fast algorithms to reproduce the clusters number distribution and the cluster size distribution in *Geant4*[1], and in the end, two beam tests performed at CERN to validate the simulations results and ascertain some questions arisen during the simulations phase.
Before entering in the details of the three parts of the procedure, a general description of the cluster counting technique and its main differences respect to the traditional dE/dx method

[1] Geant4, a simulation toolkit, `https://geant4.web.cern.ch/node/1`

are provided.

7.1 Particle identification: differences between dE/dx and dN/dx

A particle passing through a material undergoes a series of inelastic collisions with the atomic electrons of the material. As a result, each atom could be excited or ionized, while the particle loses a small fraction of its kinetic energy [66].
Measurements of the deposited energy are widely used for particle identification. Gaseous counters (as well as solid state counters) provide signals whose pulse height is proportional to the number of electrons produced in the ionization process along the track length inside the detector and thus proportional to the deposit energy.
The distribution of the deposit energy follows the *Landau* function (as shown in Figure 7.1), since it allows the possibility of large energy transfers in single collisions that add a long tail, named *Landau* tail, to the high energy side, resulting in a asymmetric shape whose mean value is significantly higher than the most probable value [130].

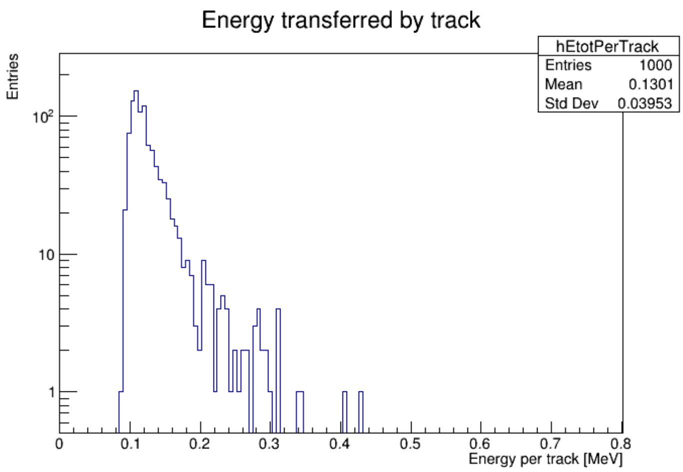

Figure 7.1: Energy loss distribution of a muon traversing 200 cells, 1 cm per side, filled with 90% He and 10% iC_4H_{10} simulated by *Garfield++*.

This implies that the mean value cannot be considered as a good estimator for the energy deposition and commonly a truncated mean, typically from 40 % up to 80 %, is used.
The separation power for two particles, labeled for simplicity p_1 and p_2, with different masses and same momentum, is evaluated with the relation (7.1) [130]:

$$n_{\sigma_E} = \frac{\Delta_{p_1} - \Delta_{p_2}}{< \sigma_{p_1,p_2} >} \tag{7.1}$$

where Δ_{p_1} and Δ_{p_2} are the measurements of the deposited energy, σ_E is the resolution in the ionization measurement (*energy resolution*) given by the variance of *Gaussian* distribution of the truncated mean values and $< \sigma_{p1,p2} >$ is the average of the two resolutions:

$$< \sigma_{p1,p2} >= \frac{\sigma_{E,p1} + \sigma_{E,p2}}{2} \tag{7.2}$$

A typical separation power achievable with ionization measurements in a gaseous detector with energy resolution of 5% is shown in Figure 7.2.

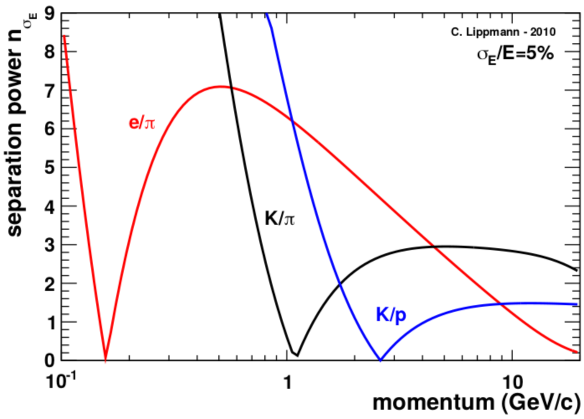

Figure 7.2: Typical separation power obtained with dE/dx method in a gaseous detector [130].

Another way to perform the particle identification can be explored, by studying the clusters distribution generated by a charged particle in a gas detector: the cluster counting technique. The process of energy loss of a charged particle crossing a medium is a discrete process: a particle traversing a gas leaves a track of ionization consisting of a sequence of clusters with one or more electrons which are all released in a single act of **primary ionization**. This is a typical *Poissonian* process, i.e. a result of a number of the order of the Avogadro number of independent random events, whose sum gives the mean specific ionization [95].
The main advantage of the *Poissonian* distribution is that its *Gaussian* limit is achieved when the mean value reaches 20, that is of the order of 1 cm track length for the most commonly used gas mixtures. Instead, the energy distribution follows a *Gaussian* shape just in thick and dense material (because of *central limit theorem*), but this situation is not helpful for the drift chambers [95].
The cluster counting technique is conceptually quite simple and practically consists in singling out, in ever recorded detector signal, the isolated structures related to the arrival on the anode wire of the electrons belonging to a single ionization act (see Figure 7.3) [95], [123].

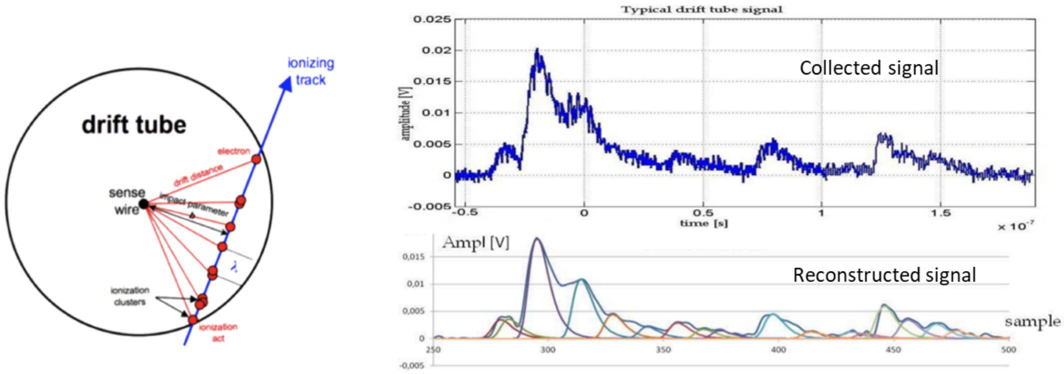

Figure 7.3: Left: The section of a drift tube, with an ionizing track (blu arrow) and some ionization clusters (red dots). Right: A typical signal with the identified peaks.

7.1.1 The analytical calculation

The starting point which brings to the belief that the cluster counting technique will strongly improve the particle identification capabilities relies in the analytical calculations shown in Figure 7.4, where the particle separation power in terms of the numbers of standard deviation (sigma) as a function of the momentum in a mixture of 90 % He and 10 % iC_4H_{10} is illustrated.

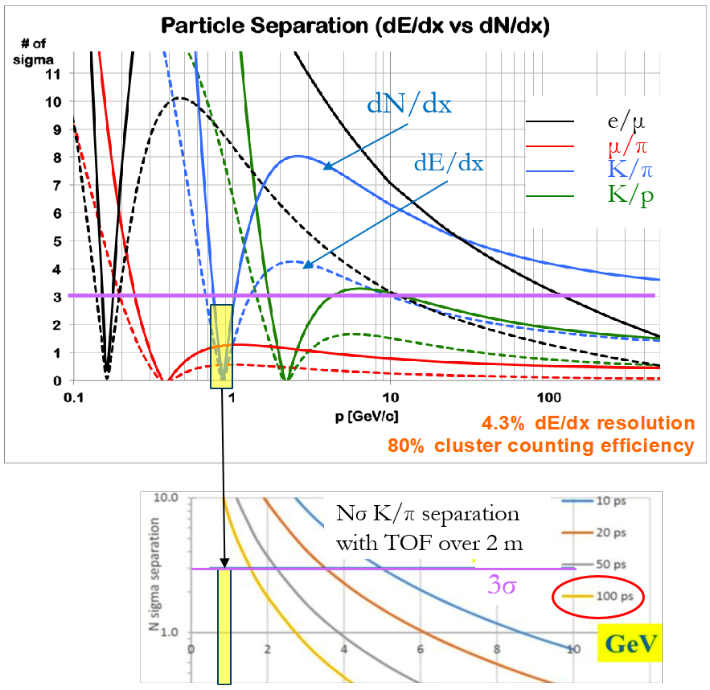

Figure 7.4: Top: Analytic evaluation of particle separation capabilities achievable with dE/dx (dashed curves) and dN/dx (solid curves). The region between 0.85 GeV/c and 1.05 GeV/c where a different technique is needed is highlighted in yellow. Bottom: PID performance as function of the time resolution by using a time of flight technique over 2 m to recover the particle identification in the range 0.85 GeV/c and 1.05 GeV/c [123, 131, 132].

Solid curves in Figure 7.4 refer to the separation power obtained with the cluster counting

technique and dashed curves refer to the optimal energy loss truncated mean technique. A cluster counting efficiency of 80 % is assumed in the calculations.
It is evident that a relative gain of a factor 2 of the cluster counting technique with respect to the dE/dx method is reached. The technique failed only in small gaps along the momentum range analyzed. For example, in the kaon-pion separation (blue curves), the technique failed around 1 GeV, but this gap could be easily recovered with a time of flight technique with a detector having a time resolution around 100 ps.
Another interesting feature that proves the great expectations placed on the cluster counting technique is illustrated in Figure 7.5, which shows that even if the cluster counting efficiency is lowered down to 40%, better resolutions than the traditional dE/dx method will be still achieved.

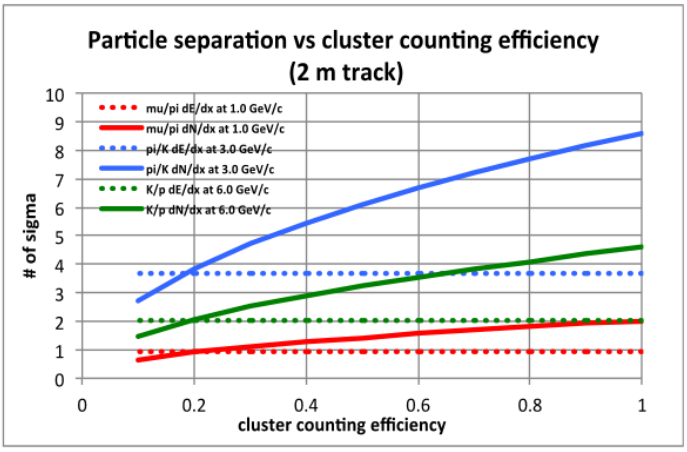

Figure 7.5: Separation power in terms of sigma versus cluster counting efficiency.

7.2 Cluster counting simulation in Garfield++ and Geant4

The results coming from the analytical calculation push to deep analysis. So that, to investigate the potential of the cluster counting techniques (for He based drift chamber) on physics events a reasonable simulation of the ionization clusters generation is needed [123].
Garfield++[2] and *Geant4* are two valid software tools for the drift chamber simulations.
Garfield++ is used to describe in details the properties and the performances of a single cell of drift chambers, but it is not suitable to simulate a large scale detector and to study colliders events. On the other side, *Geant4* can simulate elementary particle interactions with the material of a full scale detector and study collider events, but the fundamental properties and the performances of the sensible elements, like the drift cells, have to be parameterized or "ad-hoc" physics models have to be defined.
An algorithm, which can use the energy deposit information provided by *Geant4* to reproduce, in a fast and convenient way, the clusters distribution and the cluster size distribution has been developed.
In principle, a physics model, which, once integrated in *Geant4*, could reproduce in details the ionization process, could be developed, but this approach would cost a great space disk occupation and a long computational time. A simple algorithm which, by using the energy

[2] https://garfieldpp.web.cern.ch/garfieldpp/

deposit simulated by the software, provides all the necessary information seems to be a better solution, with a view to simulate in full scale the IDEA drift chamber.
For this purpose, tracks crossing 200 cells, 1 cm per side, filled with a mixture of 90 % He and 10% iC_4H_{10}, have been simulated by using *Garfield++* to implement an algorithm which can reproduce the clusters distribution and cluster size distribution in *Geant4* [123].

7.2.1 Garfield++ simulation analysis

The first step for the algorithm development consists of a detailed study of the ionization process by using the Garfield++ toolkit.
In particular, the cluster distribution and the energy loss distribution have been studied for muons, pions, electrons, protons and kaons in a range of momentum from 200 MeV up to 1 TeV, as reported in Figure 7.6.

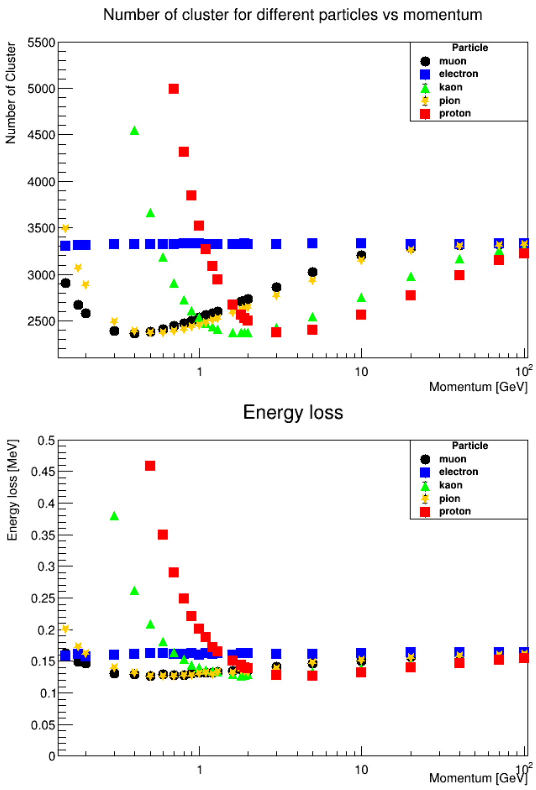

Figure 7.6: Top: Clusters distribution vs momentum. Bottom: Energy loss distribution vs momentum [123].

The subsequent step is the evaluation of the particle separation power achievable with dE/dx and dN/dx, as simulated by Garfield++. For the dE/dx evaluation a truncated mean of 70% has been chosen. The results are reported in Figure 7.7.

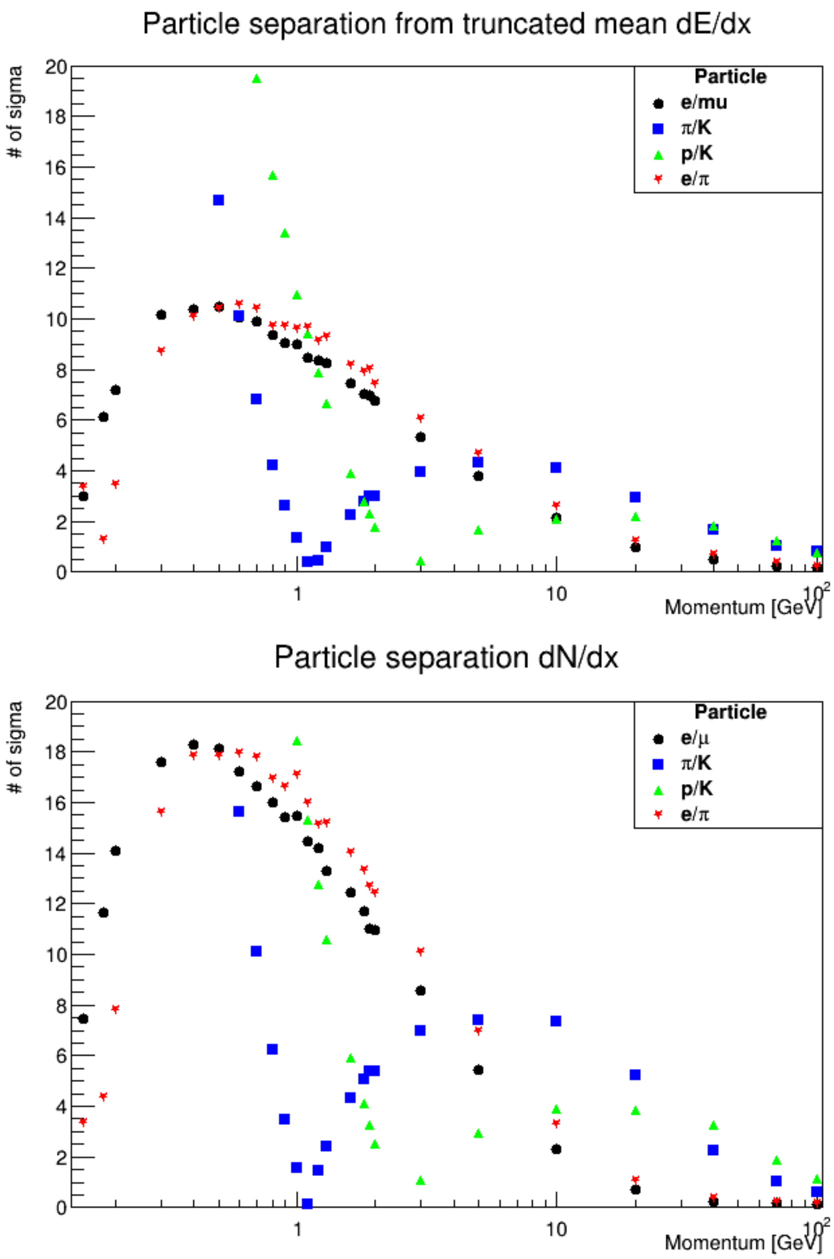

Figure 7.7: Top: Particle separation power with dE/dx (truncated mean at 70 %). Bottom: Particle separation power with dN/dx [123].

The two plots in Figure 7.7 show clearly that the cluster counting technique improves particle separation capabilities of a factor of ∼2 compared to the traditional method, as the analytical calculations predict.
As an example, around 5 GeV, the power separation of a pion from kaon (blu squared) obtained with the traditional method is around 4 sigma while the one obtained with the cluster counting technique is around 8 sigma.
The final goal is to obtain the same results by using *Geant4*. For this purpose, three different versions of an algorithm which reconstructs the clusters distribution and the cluster size distribution using the information given by *Geant4* have been implemented.

7.2.2 Algorithm implementation

The algorithm implementation starts from *Garfield++* simulations.
Firstly, the distribution of the kinetic energy for clusters that have a cluster size equal to 1 (left side of Figure 7.8) and clusters that have cluster size higher than 1 (right side of Figure 7.8) have been analyzed.

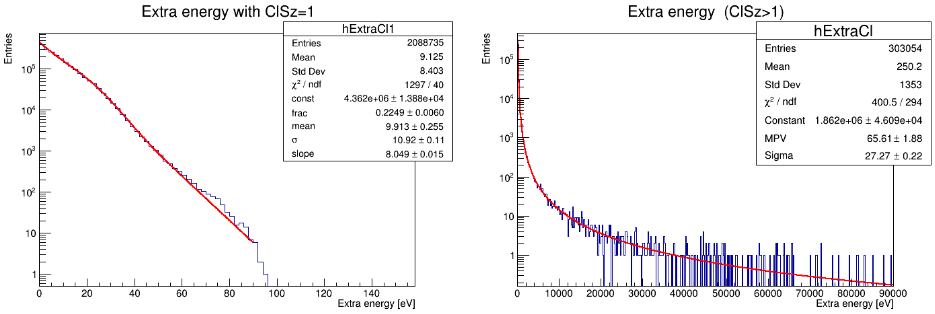

Figure 7.8: Left: Kinetic energy distribution for a muon at 300 MeV for cluster with cluster size equal to 1, fitted with an exponential function plus a *Gaussian* function. Right: Kinetic energy distribution for a muon at 300 MeV for cluster with cluster size higher than 1, fitted with a *Landau* function [123].

Moreover, the distribution of clusters with a cluster size higher than 1 up to a 1 keV has been studied: the cut at 1 keV is a cut equivalent to the single interactions range cut set by default in *Geant4*.
The distribution is shown in Figure 7.9.

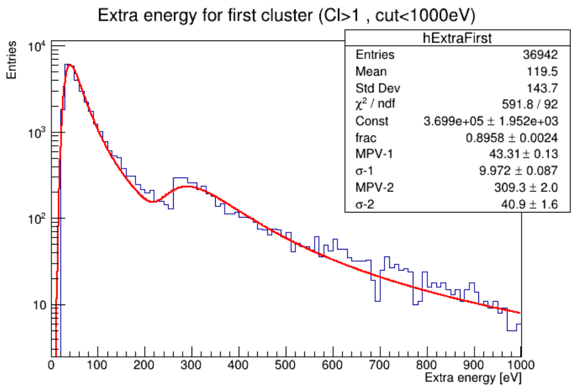

Figure 7.9: Kinetic energy distribution for clusters with cluster size higher than one for a muon at 300 MeV, up to 1 keV, fitted with a double *Landau* function [123].

The distribution on the left side in Figure 7.8 is fitted with an exponential function plus a *Gaussian* function, the distribution on the right side of the same figure with a *Landau* function and the one in the Figure 7.9 with a double *Landau* function.
The goal is to create two different models for kinetic energy of clusters with cluster size equal to 1 and higher than 1, with the purpose of interpreting correctly the total energy loss by different particles in a single cell. The analysis illustrated in Figure 7.8 and Figure 7.9 has been repeated for the 5 different particles at different momenta: the fit parameters have been

stored and analyzed separately to be used during the algorithm implementation.
The distribution obtained by collecting the fit parameters extrapolated from the distribution in Figure 7.8 at different $\beta\gamma$ have been fitted with custom functions.
To handle the fit parameters from the double Gaussian fit in Figure 7.9, an interpolation procedure has been used instead of the fit procedure.
Figure 7.10 shows the distribution of the mean values from the *Gaussian* fit of the kinetic energy for clusters with cluster size equal to 1. The distribution is fitted with an exponential function plus a plateau function.

$$f = const \quad \frac{1}{\tau} e^{-\frac{x - str\,Point}{\tau}} + \frac{\mu_{Plateau}}{1 + 81^{\frac{mid_{Plateau} - x}{\Delta_{Plateau}}}} + shift\,level \tag{7.3}$$

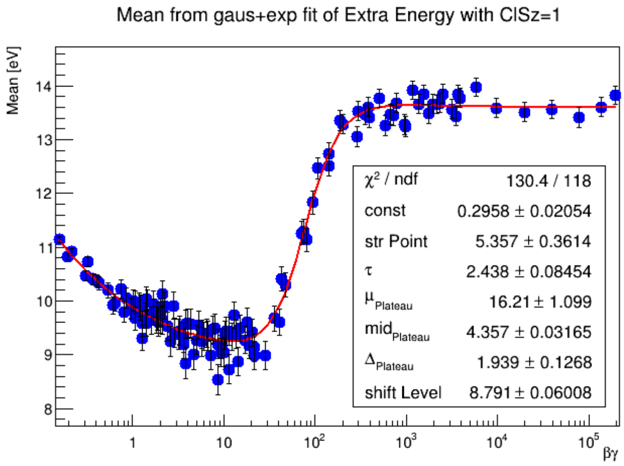

Figure 7.10: Mean value distribution of *Gaussian* fit of the kinetic energy distribution for clusters with cluster size equal to 1, fitted with the function in (7.3) [123].

Figure 7.11 shows the distribution of the sigma fit value from the *Gaussian* fit of the kinetic energy for clusters with cluster size equal to 1. The fit function is:

$$f = -const \quad \frac{1}{\tau} e^{-\frac{x - str\,Point}{\tau}} + \frac{\mu_{Plateau}}{1 + 81^{\frac{mid_{Plateau} - x}{\Delta_{Plateau}}}} + shift\,level \tag{7.4}$$

where $str\,Point$ indicates the starting point of the exponential function, $\mu_{Plateau}$ is the maximum plateau height, $mid_{Plateau}$ is the x value which corresponds to the half of the plateau, $\Delta_{Plateau}$ is the length of the plateau, the $shiftlevel$ is a shift in the y-direction.

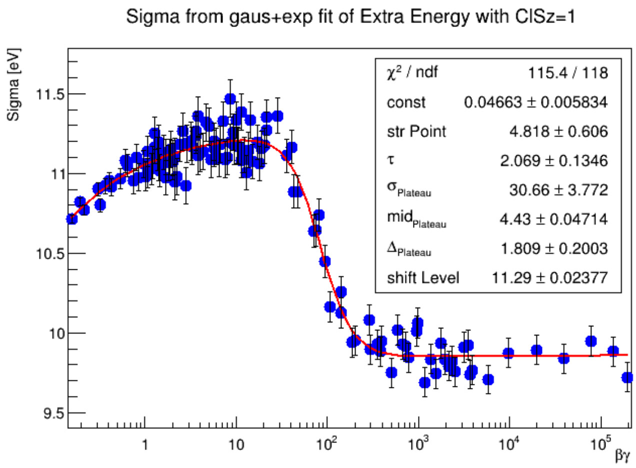

Figure 7.11: Sigma value distribution of *Gaussian* fit of the kinetic energy distribution for clusters with cluster size equal to 1, fitted with the function in (7.4).

The distribution of the fraction value (top Figure 7.12) is fitted with the fit function in (7.4). The slope value (bottom Figure 7.12) is fitted with the function:

$$f = const(1 - \frac{1}{\tau} e^{-\dfrac{x - str\,Point}{\tau}}) + \frac{\mu_{Plateau}}{1 + 81^{\frac{mid_{Plateau} - x}{\Delta_{Plateau}}}} \tag{7.5}$$

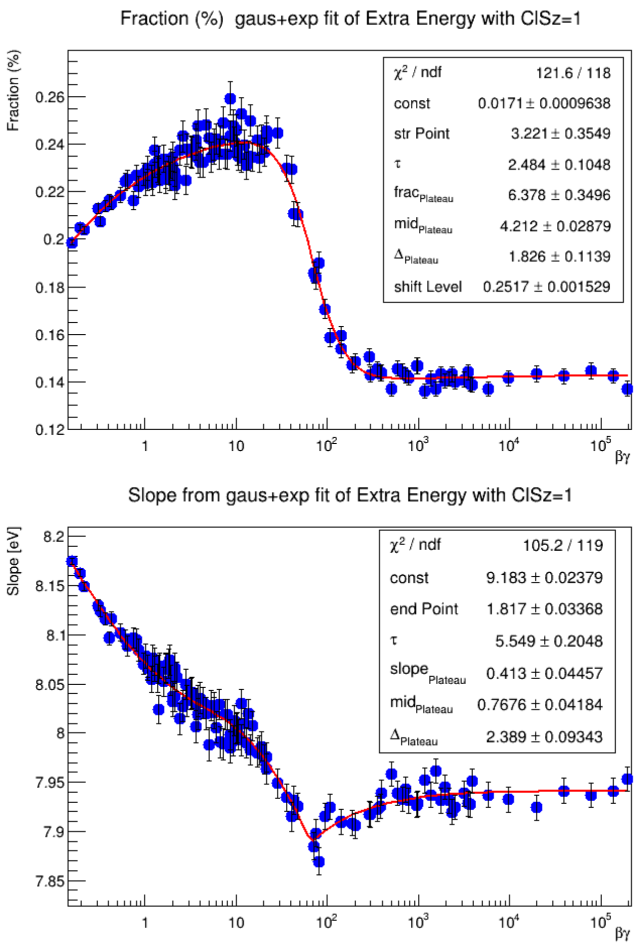

Figure 7.12: Fraction value (top) and sigma value (bottom) distribution of *Gaussian* fit of the kinetic energy distribution for clusters with cluster size equal to 1.

On top of Figure 7.13 the distribution of the most probable value from the fit of the cluster size higher than one distribution is illustrated. The distribution is fitted with the function (7.5). On bottom of the same figure, the distribution of the sigma value, fitted by the same function, is illustrated.

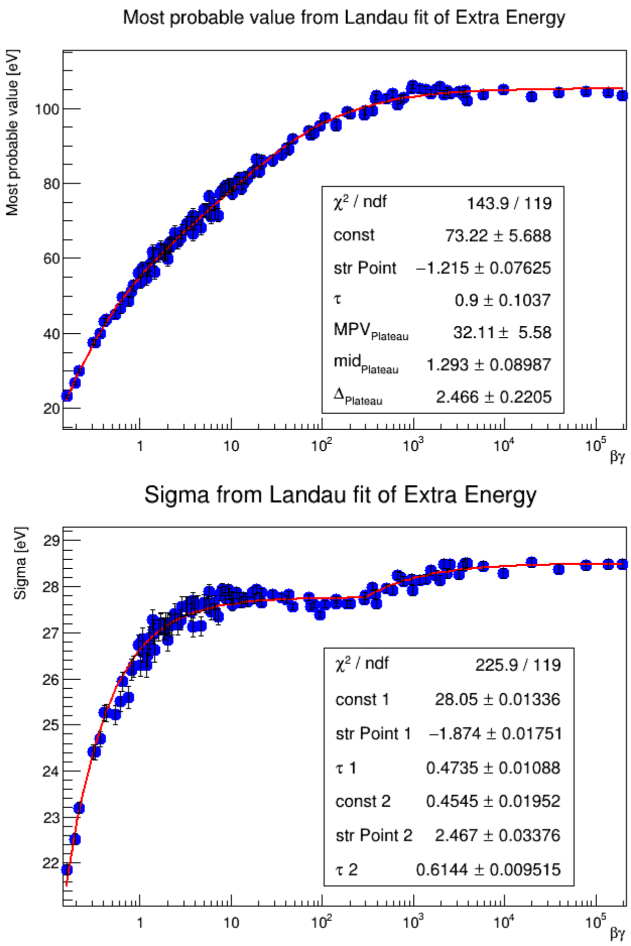

Figure 7.13: Most probable value (top) and sigma value (bottom) distribution of *Gaussian* fit of the kinetic energy distribution for clusters with cluster size higher than 1.

A key element for the algorithm implementation is the evaluation of the total kinetic energy spent to create clusters with cluster size higher than 1, by identifying the value named "maxExEcl".
To extract this parameter the correlation plots, (an example is shown in Figure 7.14), between the total energy loss by particles traversing the gas mixture and the total kinetic energy of clusters with cluster size higher than 1 has been studied.

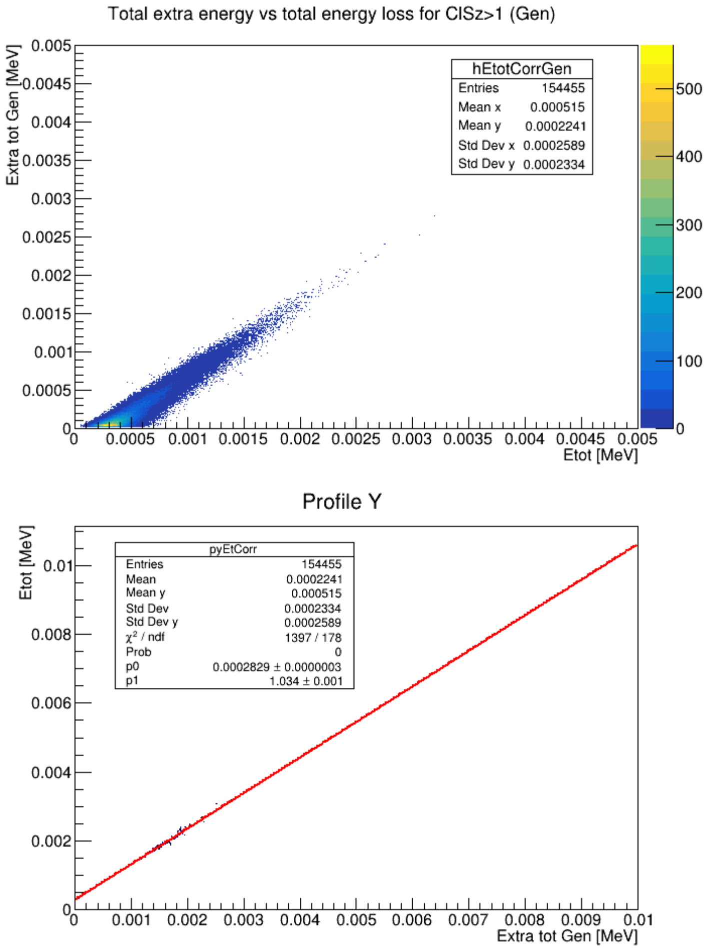

Figure 7.14: Correlation plot (top) and its profile plot (bottom) between the total energy loss by a muon at 300 MeV traversing gas and the total kinetic energy for clusters with cluster size higher than one [123].

A parameter, named *ExSgm*, to take into account the smearing around the mean value of the total energy loss has been evaluated, as the average of the sigma of each point in the correlation trend.
The profile plot in Figure 7.14 is fitted with a linear function and the relation used to the *maxExEcl* is:

$$maxExEcl = \frac{E_{tot} - p0 + Random(Gaus(0, ExSgm))}{p1} \tag{7.6}$$

where p0 and p1 are the fit parameters of the linear fit and E_{tot} is the total energy loss by the particles traversing the 200 cells of gas.
Once again the linear fit of the correlation plot has been performed for all the particles at the different $\beta\gamma$, the fit parameters have been saved and handled by means of an interpolation function.

7.2.3 Three different algorithms

Using the results from the *Garfield++* analysis described in the section above, three different algorithms which give results consistent with the ones expected from simulations have been

implemented.
The first algorithm, if the *maxExEcl* is higher than zero, generates the kinetic energy for clusters with cluster size higher than 1 by using its distribution and evaluates the cluster size. This procedure is repeated until the sum of primary ionization energy and the kinetic energy per cluster saturate the *maxExEcl* of the event. Then, by using the remaining energy, the algorithm creates clusters with cluster size equal to 1 by assigning their kinetic energy according to the proper distribution.
The second algorithm (similar to the previous one), during the generation of clusters with cluster size higher than 1, assigns the kinetic energy to them, choosing the best over five extractions that makes the total kinetic energy for cluster with cluster size higher than 1 better approximating the *maxExEcl*.
The last algorithm follows a different methodology, since it uses the total kinetic energy of the event to evaluate "a priori" the number of clusters, applying the most likelihood criterium.
The workflow of each algorithm is described in details in appendix A.
To verify the validity of the algorithms, their results have been compared with the ones simulated by *Garfield++*, taking as case of study a muon with a momentum of 300 MeV, whose clusters number and cluster size distributions are shown in Figure 7.15.

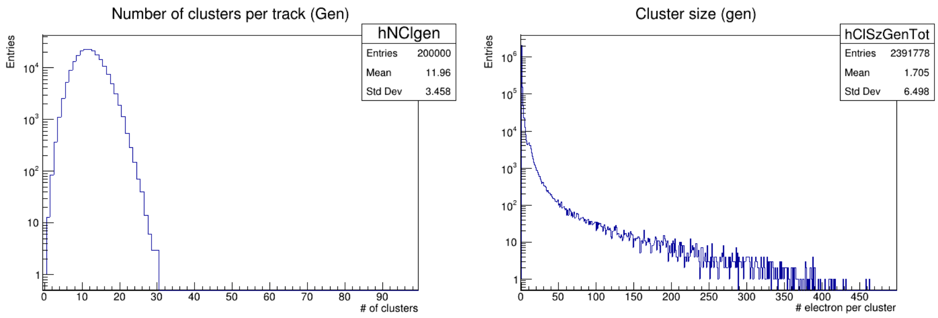

Figure 7.15: Clusters distribution (left) and cluster size distribution (right) for a muon at 300 MeV traversing 200 cells, 1 cm per side, filled with 10 % He and 90 % iC_4H_{10}

Results for first algorithm

Figure 7.16 shows the results obtained by applying the first algorithm.

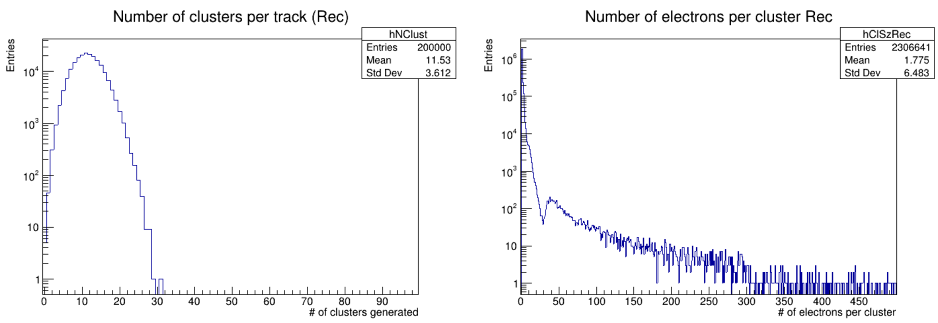

Figure 7.16: Clusters number distribution (left) and cluster size distribution (right) for a muon at 300 MeV traversing 200 cells, 1 cm per side, filled with 10% He and 90 % iC_4H_{10}, as reconstructed by the first algorithm [123].

The clusters distribution reconstructed by the algorithm reproduces the *Poissonian* shape expected. The cluster size distribution has a mean value compatible with the one expected but its shape presents a small dip before the value of 50 electrons.

Results for the second algorithm

Figure 7.17 shows the results obtained by applying the second algorithm.

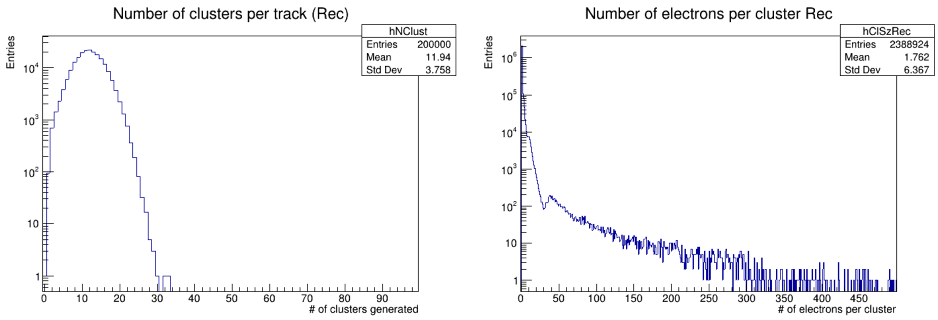

Figure 7.17: Clusters distribution (left) and cluster size distribution (right) for a muon at 300 MeV traversing 200 cells, 1 cm per side, filled with 10% He and 90 % iC_4H_{10}, as reconstructed by the second algorithm.

Once again, the cluster distribution follows the expected *Poissonian* shape. The cluster size distribution has a mean value consistent with the one expected but the shape has a small dip before 50 electrons.

Results for third algorithm

Figure 7.18 shows the results obtained by the third algorithm.

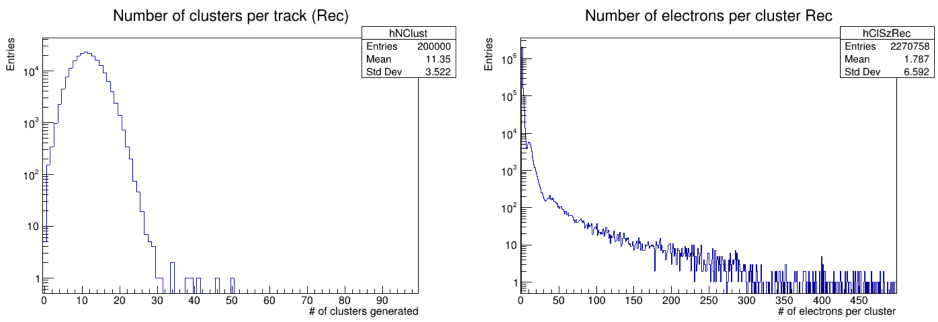

Figure 7.18: Clusters distribution (left) and cluster size distribution (right) for a muon at 300 MeV traversing 200 cells, 1 cm per side, filled with 10% He and 90% iC_4H_{10}, as reconstructed by the third algorithm.

The third algorithm reproduces the expected clusters distribution; moreover the cluster size shape is more similar to the one expected than the previous ones obtained from the other two algorithms.

The three algorithms are tested also for different particles at different momenta.

7.3 Cluster counting simulation in Geant4

The simulations performed in *Geant4* follow the same strategy of the one performed in *Garfield++*, i.e. 200 cells, 1 cm per side, filled with 10 % He and 90 % iC_4H_{10} traversed by the same five particles in the same momenta range have been simulated. The energy loss distribution for each particle reconstructed by Geant4 is shown in Figure 7.19.

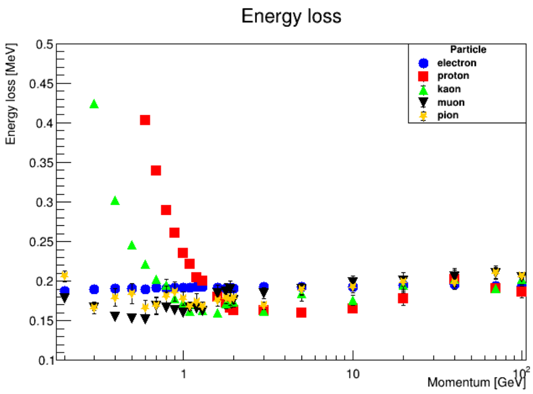

Figure 7.19: Energy loss distribution simulated by Geant4 [123].

The energy loss is the only necessary information to be provided to the algorithms, whose results (for the first and the second one), are shown respectively on top and bottom of Figure 7.20.
The two algorithms give consistent results. The particle separation power obtained by implementing the traditional method of dE/dx with a truncated mean of 70 % (Figure 7.21), and by implementing the cluster counting technique (Figure 7.21), has been compared.
The simulations confirm that the cluster counting technique improve the particle separation capabilities compared to the traditional method of dE/dx.

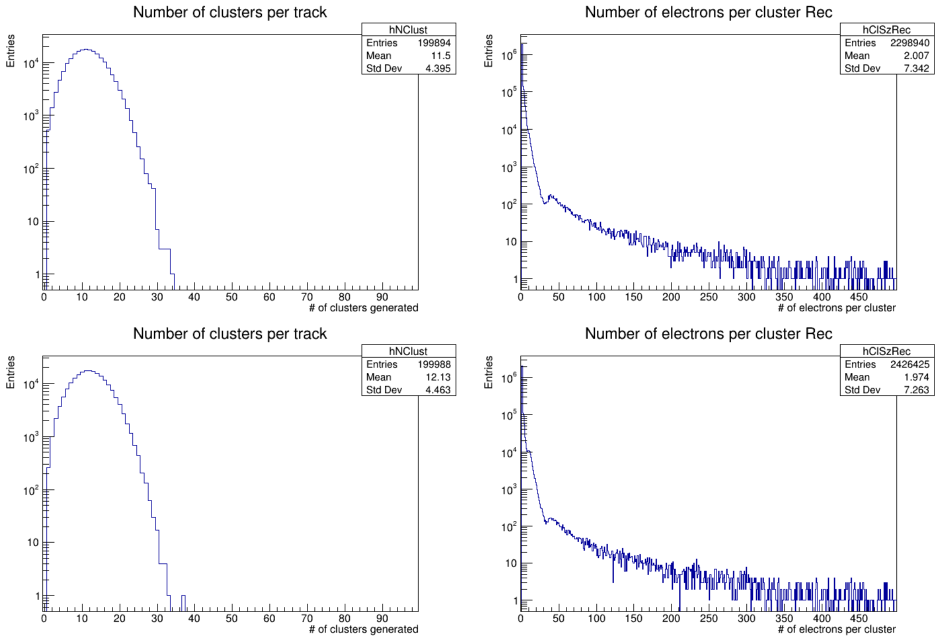

Figure 7.20: Clusters distribution (left) and cluster size distribution (right) for a muon at 300 MeV. On top the ones reconstructed by the first algorithm, on bottom the ones reconstructed by second algorithm.

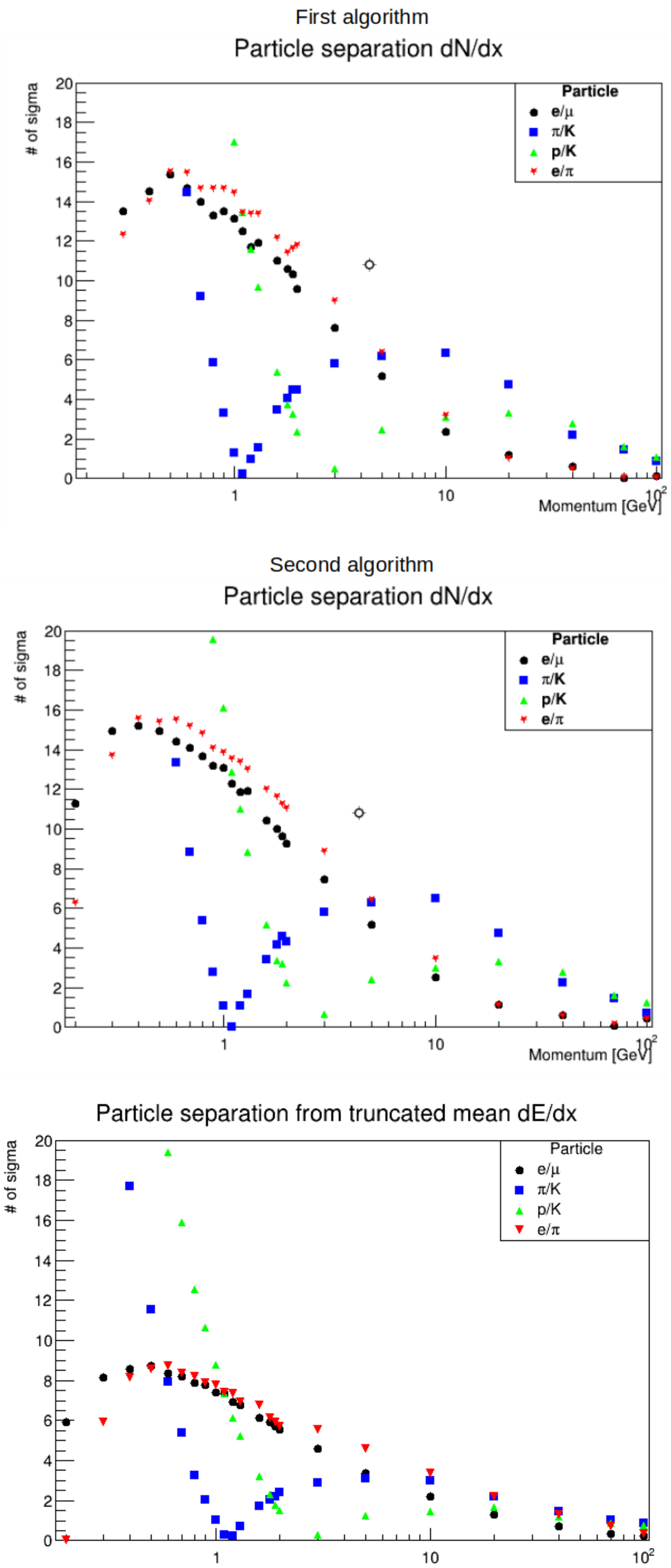

Figure 7.21: Top The particle separation power obtained with the cluster counting technique implementing the first algorithm. Center: The particle separation power obtained with the cluster counting technique implementing the second algorithm. Bottom: The particle separation power obtained with traditional dE/dx method.

The two algorithm shows similar performances for the particle separations capabilities with the cluster counting technique.

7.4 Beam Tests to validate the simulations' results

Besides the successful campaign of simulations' results, different questions come out. Firstly, the power separation capabilities in Geant4 are slightly different with respect to Garfield++, then the dN/dx Fermi plateau has higher value than the dE/dx one and it is reached at lower values of $\beta\gamma$ with a steeper slope, as shown in Figure 7.22. Unfortunately, the lack of

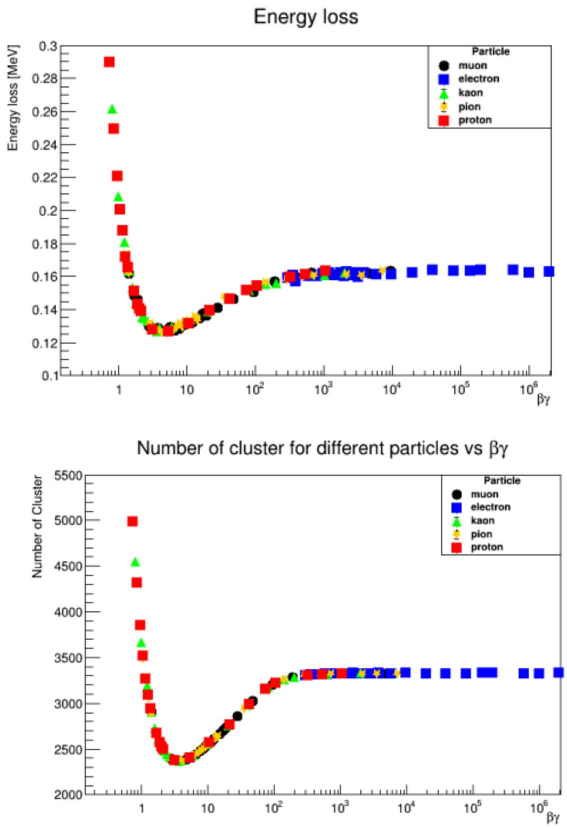

Figure 7.22: Top : dE/dx vs $\beta\gamma$. Bottom: dN/dx vs $\beta\gamma$.

experimental data on cluster density and cluster population for He based gas, particularly in the relativistic rise region does not allow for an answer to these questions. The only way to find a proper response is an experimental measurement. Two beam tests have been performed at CERN/H8 beam line to investigate the cluster counting technique potentials and the ionization process in helium based gas mixtures.

The beam tests have different goals, since they aim:

- to ascertain the Poisson nature of the cluster counting technique;
- to find efficient cluster counting and electrons clustering algorithms, as a function of the operative parameters like gas mixture, gas gain, geometrical configuration (drift cell size, sense wire diameter, angle between wire direction and ionizing track);

- to define the limiting effects for a fully efficient cluster counting, like the cluster dimensions, the space charge density around the sense wire and the dependence of the counting efficiency with respect of the impact parameter;
- to demonstrate the ability to count the number of electron clusters released by an ionizing track at a fixed $\beta\gamma$ as a function of the cell size, of the angle between the track and the normal to the wire direction (from 0° to 60°), of different percentage of helium and isobutane in the gas mixture (90 % He-10% iC_4H_{10}, 80 % He-20 % iC_4H_{10} and 85 % He-15 % iC_4H_{10});
- to establish the limiting parameters for an efficient cluster counting, like cluster density as a function of impact parameter, space charge as a function of the gas gain, of the sense wire diameter and of the track angle and gas gain stability.

The first beam test was performed in November 2021 and the second one in July 2022.

7.4.1 The first beam test

The first test has been conducted in parasitic mode, by using a muon beam at 165 GeV/c. The experimental setup consists of:

- a pack of drift tubes with different cell size, wire materials and wire diameters (Figure 7.23),
- two trigger scintillator tiles (Figure 7.25),
- a portable gas system (Figure 7.26),
- a Wave Dream Board, WDB, [88, 133] (Figure 7.27)

The drift tubes pack

The basic idea is to test different configurations of the drift cell, by exploring different materials and diameter size for the sense wires, as shown in Figure 7.23. The connecting scheme of the drift tubes pack is represented in Figure 7.24.

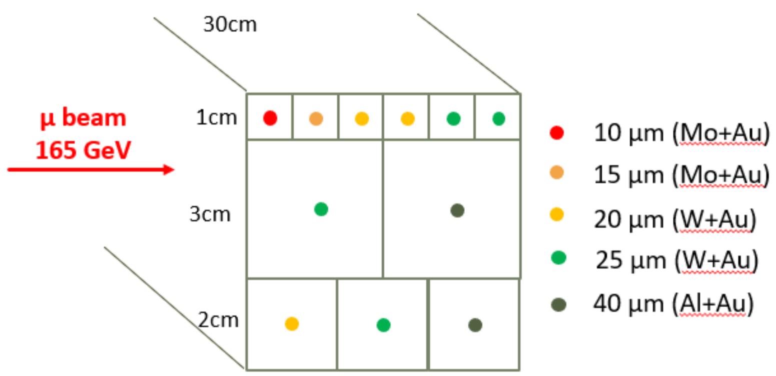

Figure 7.23: Pictorial representation of the drift tubes pack.

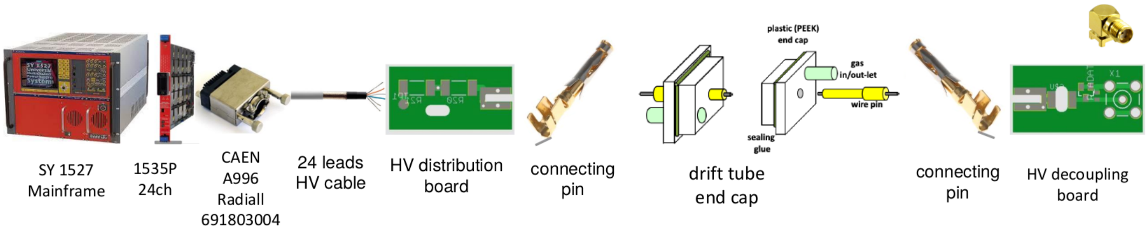

Figure 7.24: The connecting scheme of the drift tubes pack.

The trigger scintillator tiles

The two scintillator tiles (12 cm $\times$ 4 cm), instrumented with SiPMs, have been placed upstream and downstream of the drift tubes pack. These tiles are currently used in the MEG II pixelated timing counter.

Figure 7.25: Scintillator tile from MEG II timing counter.

The portable gas system

The gas system consists of two barometers for the measurement of the inlet and the outlet pressure, a flow control valve, a mixer, a flowmeter and a pump. The system is designed to keep constant pressure inside the system, but some technical problem did not allow the use of this feature. Anyway, the pressure variations have been monitored and the main pressure for the whole test was mainly constant around 725 Torr.

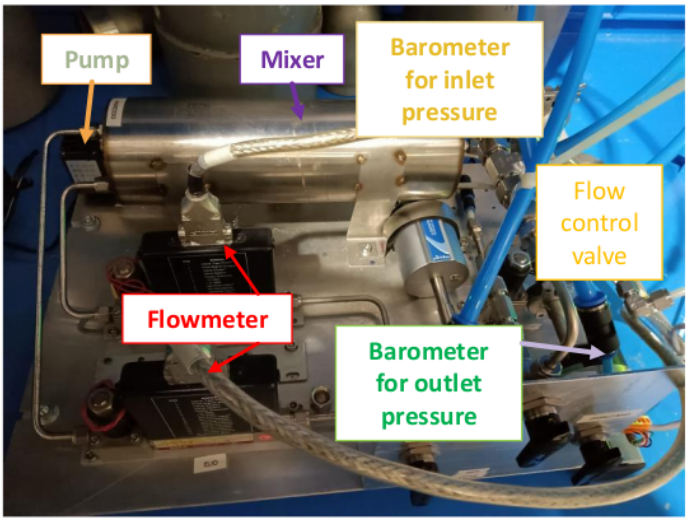

Figure 7.26: Portable gas system.

The Wave Dream Board

The flagship of the acquisition system is the Wave Dream Board (WDB), developed at PSI. It contains 16 channels with variable gain amplification and flexible shaping through a programmable pole-zero cancellation [88, 133] .
Two DRS4 chips are connected to two 8-channel ADCs, which are read out by a Field-Programmable Gate Array (FPGA). In normal operation, the DRS4 chips work in "transparent mode", where they sample the input signals continuously at a speed up to 5 GSPS in an analogue ring buffer. At the same time, a copy of the input signal is sent to the DRS4 output, where it is digitized continuously by the ADCs at 80 MSPS with a resolution of 12 bits. The output stream of the ADCs is used in the FPGA to perform complex trigger algorithms such as a threshold cut on the sum of all input channels. The WDB can be used in stand-alone mode, where it is read out through Gigabit Ethernet. An ultra-low noise bias voltage generator has been implemented in the WDB to power up SiPMs, through the signal cables.

Figure 7.27: The Wave dream board from MEG II experiment.

The most interesting feature of the WDB is its interface which is completely similar to the one of an oscilloscope with 16 channel, as shown in Figure 7.28, where a typical event of a track passing through the 6 drift tubes with 1 cm cell size is visible.

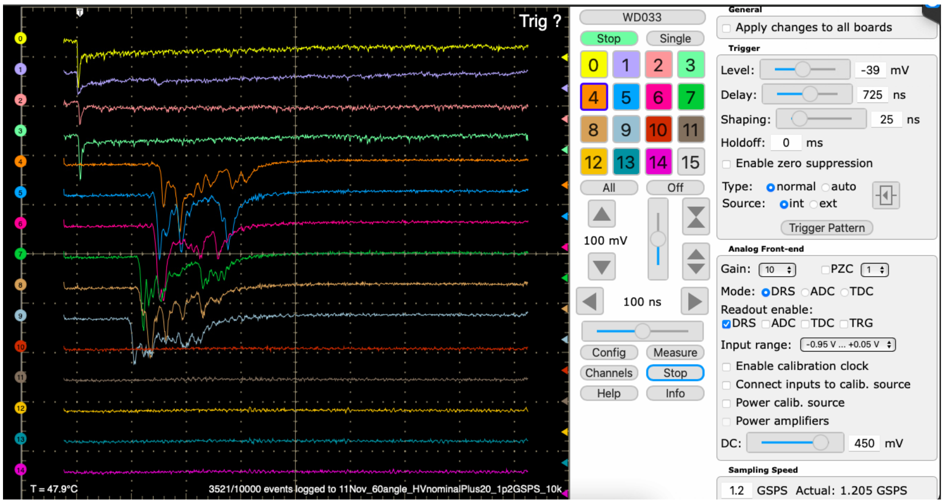

Figure 7.28: WDB interface. The channel from 0 to 3 correspond to the 4 signals from the two scintillator tiles, the ones from 4 to 10 correspond to the 6 tubes with 1 cm cell size, the ones from 11 to 12 correspond to the tubes with 3 cm cell size, the ones from 13 to 15 correspond to the tubes with 3 cm cell size.

The WDB stores data in binary format, which are then converted in a custom ROOT format to accomplish the data analysis.

The advantages of a simple setup

The setup chosen for the beam test, shown in its completeness in Figure 7.29, is quite simple, but extremely functional.

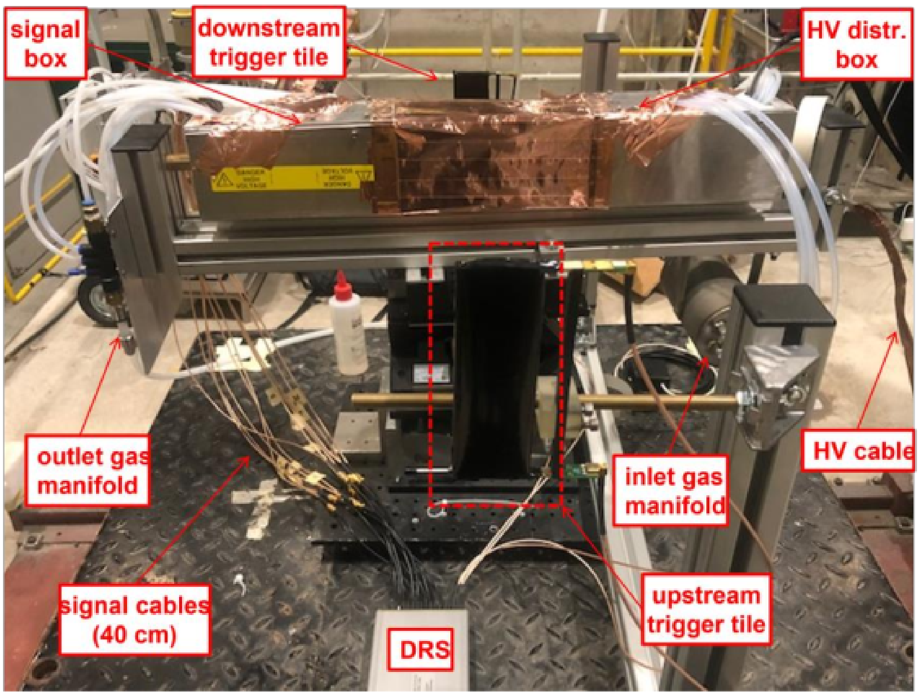

Figure 7.29: A picture of the setup used during the beam test.

This setup has a few of advantages:

- no need of external trackers: the important features is the constant path length inside the drift tubes active volume;
- no need of internal tracking, like t0 calibration, alignment, track finding and fitting algorithms;
- no need to convert time to distance, the goal is to count clusters in time domain;
- no worry of multiple scattering, which is irrelevant for path length differences at these moment;
- no need of particle tagging in hadron beams, only muon beam were used;

7.4.2 The data collected during the first test beam

During the first test beam, a 165 GeV/c muon beam has been used to collect data with two different gas mixtures, at different angles between the wire direction and the beam line and by performing a HV scan. Table 7.1 summarizes the data collected at the different configurations, where nominal HV is the HV corresponding to 2×10^5 gas gain. In table 7.1 the nominal HV

Table 7.1: Data collected during the first beam test.

Gas mixture	HV scan	Angle scan
90%He-10% iC_4H_{10}	nominal HV, ±10,±20,+30	0°,15°,30°,45°,60°
80%He-20% iC_4H_{10}	nominal HV, 10,±20	0°,15°,30°,45°,60°

is referred to the voltage suggested by Garfield++ simulations for the different kind of tubes arranged in the tube pack, the 0° refers to the wire direction perpendicular to the beam line. Unfortunately the data referred to the 80:20 mixture cannot be used for the analysis because the nominal voltage values suggested by Garfield++ were underestimated. Neither the data referred to the drift tubes with 3 cm cell size can be used because the signal acquisition window was out of the signal range.

7.4.3 The counting peaks algorithm

The strategy to prove the potentials of the cluster counting technique and to solve any doubts about the simulations results relies in finding an algorithm that can count the number of clusters per each event collected during the data taking.
An algorithm named "*derivative algorithm*" (DERIV) have been implemented, based on the imposition of cuts on the maximum waveform amplitude. In details, it searches for a peak in a waveform by comparing the amplitude, the first and the second derivative with a proper threshold, chosen by studying RMS value. Figure 7.30 shows a typical event, corresponding to a 90-10 mixture, nominal HV+20V and 0°.

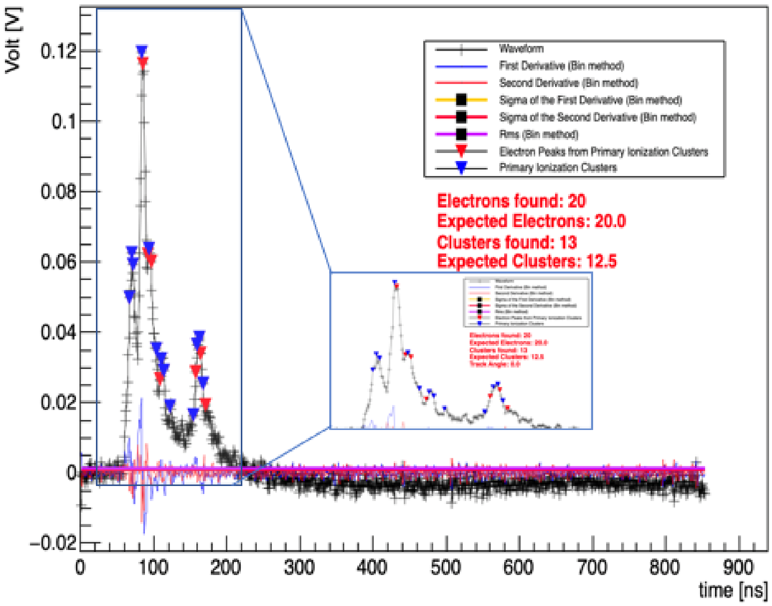

Figure 7.30: A typical waveform collected with 90-10 mixture, nominal HV+20V and 0° with a tube of 1 cm cell size and 20 μm wire diameter.

In Figure 7.30 the black line represents the waveform, the violet one the first derivative, the brown one the second derivative, the straight yellow one the sigma of the first derivative, the straight orange one the sigma of the second derivative and the straight pink one the RMS. The red triangles represent the peaks found by the algorithm.
The number of peaks expected can be calculated according to the relation (7.7):

$$\begin{aligned} N_{peaks} = & \delta cluster/cm(M.I.P.) \times \\ & drift\,tube\,size[cm] \times \\ & relativistic\,rise \times \\ & electrons/clusters \times \\ & 1/\cos(\alpha) \end{aligned} \tag{7.7}$$

where

- $\delta cluster/cm(M.I.P.)$ changes from 12 to 18 respectively for 90-10 and 80-20 mixtures,
- drift tube size changes from 0.8 to 1.8 respectively for 1 cm and 2 cm cell size tube,
- relativistic rise is 1.3
- electrons/clusters is 1.6
- α is the angle between the drift tubes pack and the beam line.

The distribution of the number of peaks found by the algorithm have been studied, two examples are reported in Figure 7.31.

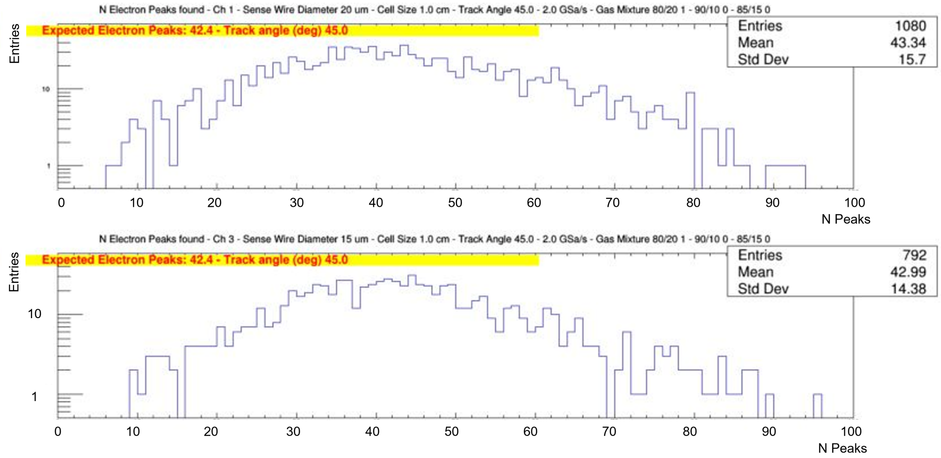

Figure 7.31: Number of peaks distribution for 1 cm drift cell tubes filled with 90-10 mixture, at nominal voltage, at 45 ° with 20 μm (top), 15 μm (bottom) diameter wire.

As shown in Figure 7.31 the number of peaks found by the algorithm are compatible with the one expected .

7.4.4 The clusterization algorithm

The derivative algorithm finds the number of electron peaks, but another algorithm, named "*clusterization algorithm*", was implement to convert the peaks found in clusters. The procedure of the algorithm consists of:

- Association of electron peaks consisting in consecutive bins (difference in time == 1 bin) to a single electron in order to eliminate fake electrons.
- Considering the contiguous electrons peaks which are compatible with the electrons diffusion time (2.5 ns or 3 bins) as belonging to the same ionization cluster.

An example of the result obtained with the clusterization algorithm is illustrated in Figure 7.32, where the red triangles marked the peaks found by the derivative algorithm and the blue triangles marked the number of clusters found by the clusterization algorithm.

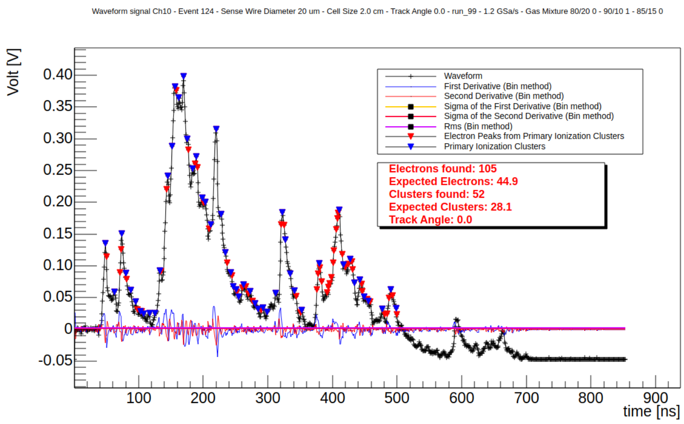

Figure 7.32: The figure shows a typical event acquired with a 2 cm cell size drift tube. The red triangles mark the peaks found by the derivative algorithm. The blue triangles mark the number of clusters found by the clusterization algorithm.

The distribution of the clusters found by the clusterization analysis for the different configuration have been studied. An example, is reported in Figure 7.33.

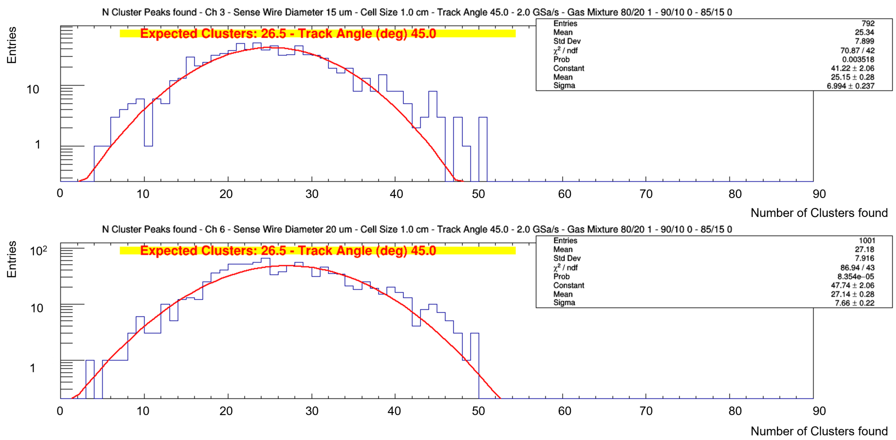

Figure 7.33: The figure shows the number of cluster distribution by applying the clusterization algorithm on the peaks found by the derivative algorithm for 1 cm drift cell tubes filled with 90-10 mixture, at nominal voltage, at 45 ° with 15 μm (top), 20 μm (bottom) diameter wire.

The red lines depicted on the plots of Figure 7.33 is the results of a Gaussian fit. In both cases, the mean value is compatible with the one expected and the sigma value correspond to the root square of the mean value proving the expected Poisson nature of the clusters distribution.
The cluster counting efficiency has been evaluated for 1 cm drift size cells and 2 cm drift size cells, at different track angles, as shown in Figure 7.34.

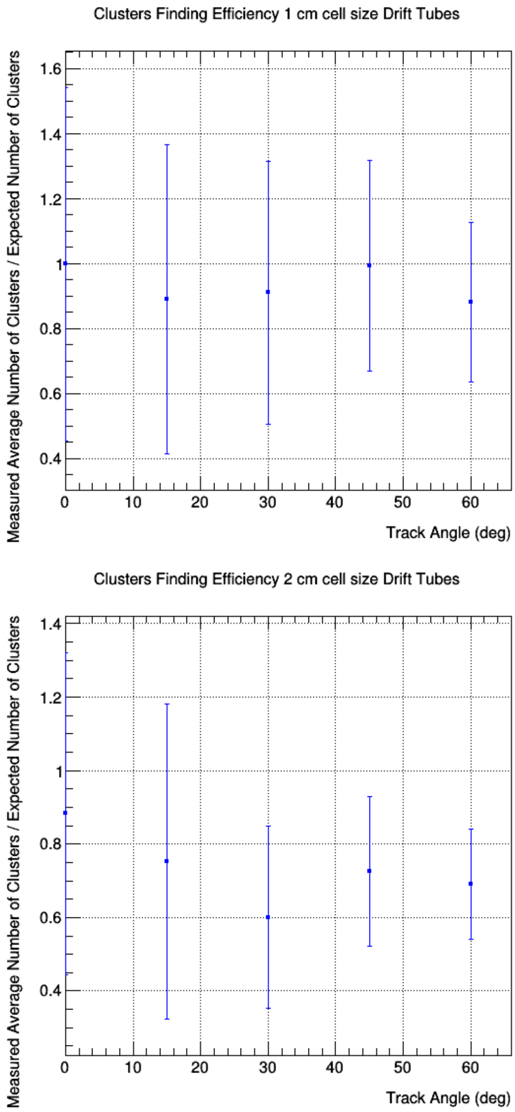

Figure 7.34: Cluster counting efficiency for 1 cm (top) and 2 cm (bottom) drift size cells, for the gas mixture of 90 % He and 10 % iC_4H_{10} vs the angle scan.

7.4.5 The second beam test

The first beam test gave promising results: a reasonable number of data have been collected and analyzed, a promising algorithm has been implemented and the distributions obtained are compatible with the ones expected from the physics of the ionization process. Anyway, a single beam energy has been exploited and the parasitic mode prevented different tests, with different gas mixture percentages. The second beam test aimed to collect data at different beam energy, even if the relativistic rise could not be exploited.
The setup for the second beam test is similar to the one used for the first test: a pack of drift tubes, with different cell size and wire diameter and material, as depicted in Figure 7.35.

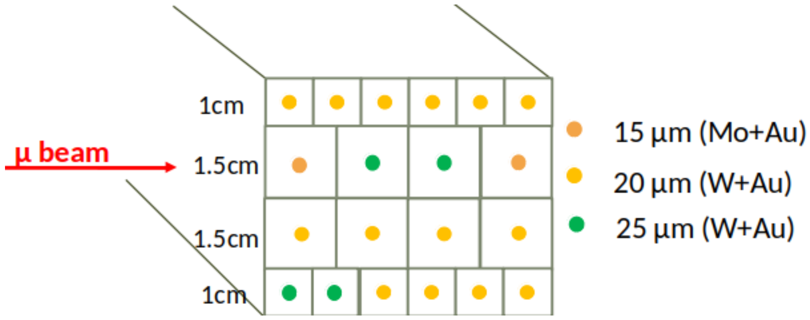

Figure 7.35: Pictorial representation of the drift tube pack used during the second beam test.

The connecting scheme and the DAQ maintain the same logic used during the first beam test. Unfortunately some of the tubes broke: instead of 20 tubes, 14 have been used. Figure 7.36 shows a picture of the setup used during the test. 7.36.

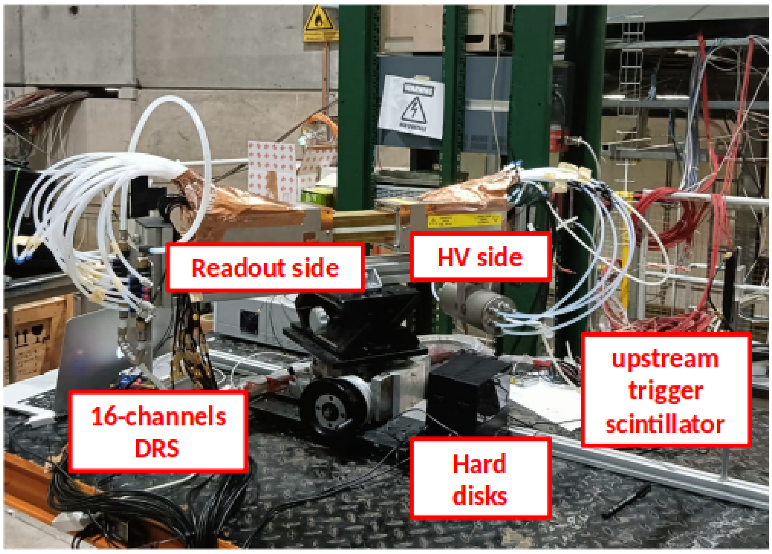

Figure 7.36: A picture of the experimental setup used during the second beam test.

During the beam test, a large data set ($\sim$ 700000 events) at different configurations have been collected, by varying not only the high voltage, the angle between the beam and the drift tubes pack and the gas mixture, but also the sampling rate, as summarize in the table 7.2.

Table 7.2: Data collected during the second beam test

Gas mixture (He-iC4H10)	μ beam energy	Sampling rate	Angle scan	HV scan
90:10	180	1,1.5,2	0,30,45,60	nominal,+10,+20,-10
	80	1	45	nominal
	40	1	0, 45	nominal
80:20	180	1.5, 2	0,30,45,60	nominal,+10,+20,-10
	40	1	0,45	nominal
85:15	180	1,2	0,45	nominal,+10,+20,-10

The DERIV and the Clusterization algorithm have been used to analyze thee new data. Figure 7.37 presents the cluster counting efficiency for 1 cm and 1.5 cm cell size drift tubes, collected with the gas mixture of 80 % He and 20 % iC_4H_{10}, the sampling rate of 2 GSps, at the nominal HV vs the angle scan.

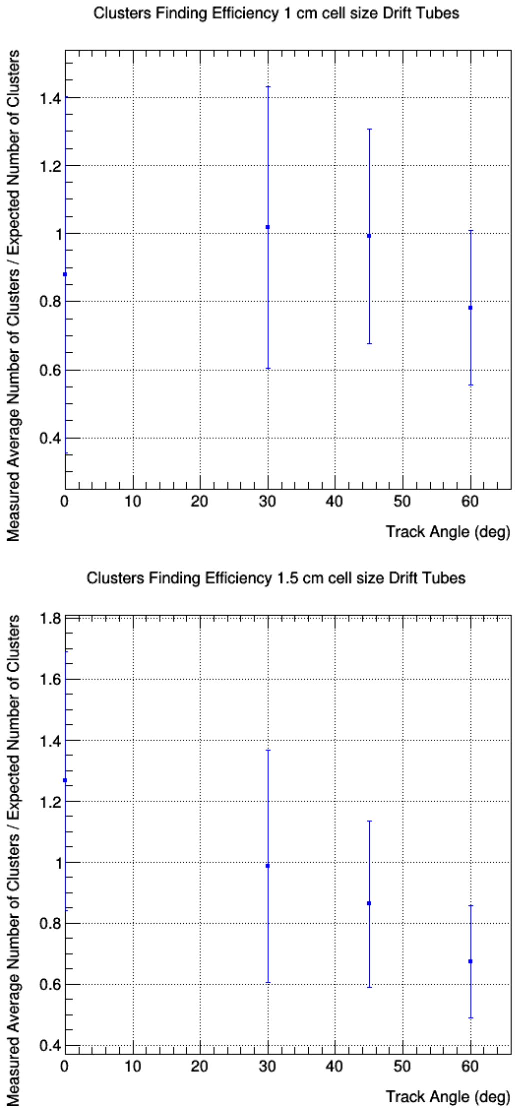

Figure 7.37: Cluster finding efficiency for 1 cm (top) and 1.5 cm (bottom) cell size drift tubes, with the gas mixture of 80 % He and 20 % iC_4H_{10}, the sampling rate of 2 GSps, at the nominal HV vs the angle scan.

Once again, the results obtained are compatible with the ones expected from the physics of the ionization process, even if a lower efficiency can be observed at 60 ° and need to be further investigated.
Figure 7.38 presents the cluster counting efficiency for 1 cm and 1.5 cm cell size drift tubes, with the mixture of 80 % He and 20 % iC_4H_{10}, at the angle of 45° and the sampling rate of 2 GSps vs the HV scan.

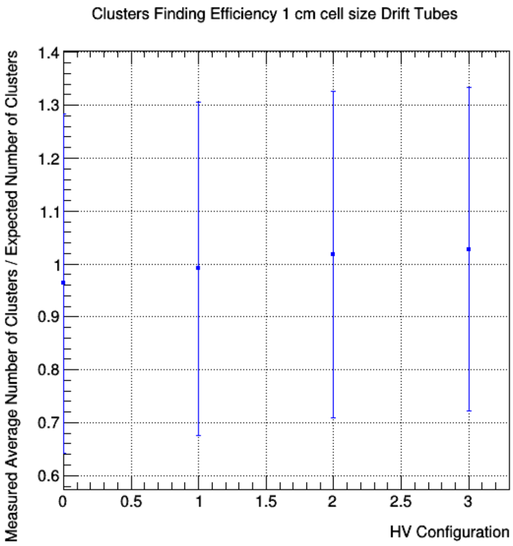

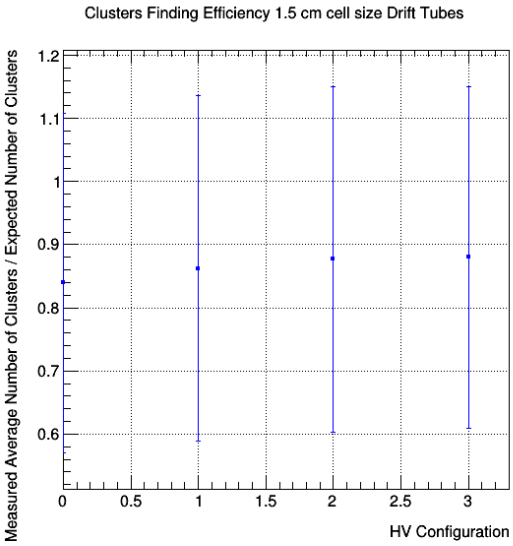

Figure 7.38: Cluster finding efficiency for 1 cm (top) and 1.5 cm (bottom) cell size drift tubes, with the mixture of 80 % He and 20 % iC_4H_{10}, the sampling rate of 2 GSps, at the angle of 45° vs the HV scan. HV configurations range from 0 to 3 which represent the HV scan from nominal HV -10V up to nominal HV +20V as reported in Table 7.2

Figure 7.39 presents the cluster counting efficiency for 1 cm and 1.5 cm cell size drift tubes, with the gas mixture of 90 % He and 10 % iC_4H_{10}, at the angle of 45° vs the sampling rate scan.

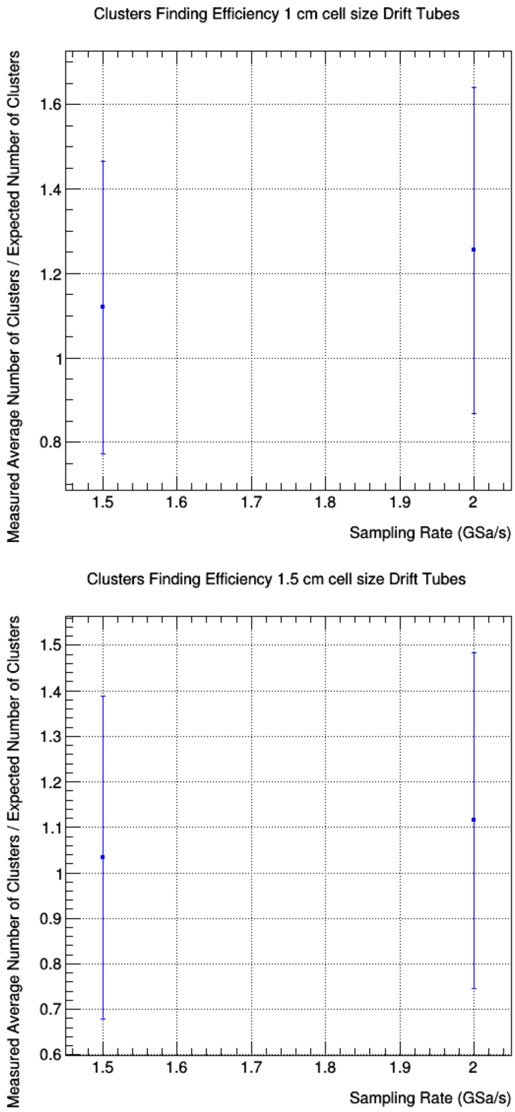

Figure 7.39: Cluster finding efficiency for 1 cm (top) and 1.5 cm (bottom) cell size drift tubes, with the mixture of 90 % He and 10 % iC_4H_{10}, at the angle of 45° vs the sampling rate scan.

A higher number of clusters has been found by increasing the sampling rate, as expected.
The analysis of the data collected during this test is still ongoing.
Moreover the collaboration with other group in the CEPC and FCC collaboration allows to apply and test machine learning techniques, which are very promising for the cluster peaks identification.
Other beam tests will be conducted to study the relativistic rise of the Bethe and Bloch function, in order to ascertain the doubts arisen from the simulations results obtained with Garfield++ and Geant4.

Conclusions

Ultralight drift chambers are powerful tools for high energy physics and for all the experiments that try to ascertain the existence of Physics beyond the Standard Model.
The MEG experiment, with its first phase of operations at the Paul Scherrer Institut (PSI), set the most stringent constraint on the Charged Lepton Flavour Violating $\mu^+ \longrightarrow e^+\gamma$ decay process. Its upgrade, the MEGII experiment, has the goal of reaching a sensitivity enhancement on the decay process of about one order of magnitude, compared to the present MEG results. One of the key ingredient for this purpose is its tracker, the ultralight drift chamber, focus of this thesis.
In particular, to improve the performances of the MEGII experiments two ingredients have been proposed: a monitoring drift chamber and a new set of time-to-space relations.
The monitoring chamber allows to measure drift velocity variation at per mil level in few minutes, to prevent that any kinds of contamination by impurities or any change in temperature and pressure influence the positron track reconstruction.
The time-to-space relations play a key role in the tracking framework of the MEGII experiment. So far, an old version has been used, which was referred to a completely different gas mixture. I developed instead a new set of tables, which have been simulated for the currently used gas mixture. Moreover, I implemented a series of improvements in the MEGII tracking framework, which can provide better performances of the positron tracks reconstruction.
The successful operation of the MEGII drift chamber makes this detector the best candidate for the IDEA tracker at future colliders.
Indeed, the second part of this thesis deals with the two main tasks necessary for a high performative ultralight drift chamber: the mechanical design and the implementation of the cluster counting/timing technique.
I developed he mechanical design of the CMD3 drift chamber as case of study for the IDEA drift chamber, trying to reduce the amount of budget material to minimize the contribution from the multiple Coulombian scattering.
A great effort has been spent to study the cluster counting technique in order to prove its potential for the particle identification performances. The analysis starts with detailed simulation by using Garfield++ and Geant4 and ends with two beam tests performed at CERN/H8, which are providing extremely promising results.
In details, starting from analytical results, I simulated, by using Garfield++ software, the ionization phenomenon inside Helium/Isobutane gas mixture. The simulations results have been used to developed an algorithm which can simulate the number of clusters and the cluster size in Geant4 software toolkit. The two beam tests provided us a huge amount of data to validate the test beam results and to provide experimental measurement of the ionization phenomenon inside the helium based drift chambers. The results obtained by analyzing the data collected are compatible with what expected from the physics of the phenomenon.

There's still plenty of room for improvement and a lot of work has to be done: the monitoring drift chamber has to be installed at PSI, the tracking framework of he MEG II experiment need to be reinforced, the algorithm for the cluster counting has to be imported in the full simulation of the IDEA drift chamber and other beam tests are necessary to study the relativistic rise of the dN/dx and dE/dx curves.
Anyway the research project fully demonstrates that the ultralight drift chambers will provide an extremely powerful tool to investigate the rich and diverse physics landscape and hopefully to find hint of Physics Beyond the Standard Model.

Appendix A

The algorithms workflow for the cluster counting simulation in Geant4

The goal of reproducing the number of clusters and the cluster size distribution in Geant4 is of crucial importance to simulate properly the cluster counting technique in the IDEA drift chamber full simulation. It is possible to implement physics model in Geant4, but this could require a great space disk occupation and a long computational time. So that, an algorithm which by using the energy deposit information provided by Geant4 to reproduce the number of cluster and the cluster size in the helium based gas mixture seems to be a valid way to follow.
Actually, three different algorithms have been implemented to simulate properly the ionization process in Geant4 and in this appendix some technical details about their implementation are presented.

A.1 The machinery ingredients for the algorithms in Geant4

A list of variables from Garfield++ simulations have been used for the implementation of the algorithms, here listed:

- maxExEcl : total kinetic energy spent to create clusters with cluster size higher than one,
- ExECl : kinetic energy generated per cluster,
- Ncl1 : number of clusters with cluster size equal to one
- Nclp : number of clusters with cluster size higher than one
- maxCut : energy value equivalent to the range cut set in Geant4 (1 keV)
- totExECl : total kinetic energy reconstructed to create clusters with cluster size higher than one
- Eloss : energy loss from a track passing through the cell
- ClSz : cluster size
- Eizp : primary ionization energy, 15.8 eV

- Eizs : secondary ionization energy, 25.6 eV

These variables will be widely used in the next section to describe the details of the algorithms development.

A.2 The first algorithm

The first algorithm, if maxExEcl is higher than zero, generates the kinetic energy for clusters with cluster size higher than one by using its distribution and evaluates cluster size. This procedure is repeated until the sum of primary ionization energy and kinetic energy per cluster saturate the maxExEcl of the event. Then, using the remaining energy (Eloss-maxExEcl), the algorithm creates clusters with cluster size equal to one by assigning their kinetic energy according to the proper distribution.
The reconstruction of clusters with cluster size equal to one remains the same for all next algorithms.
The workflow for the first algorithm is illustrated in the scheme in Figure A.1.

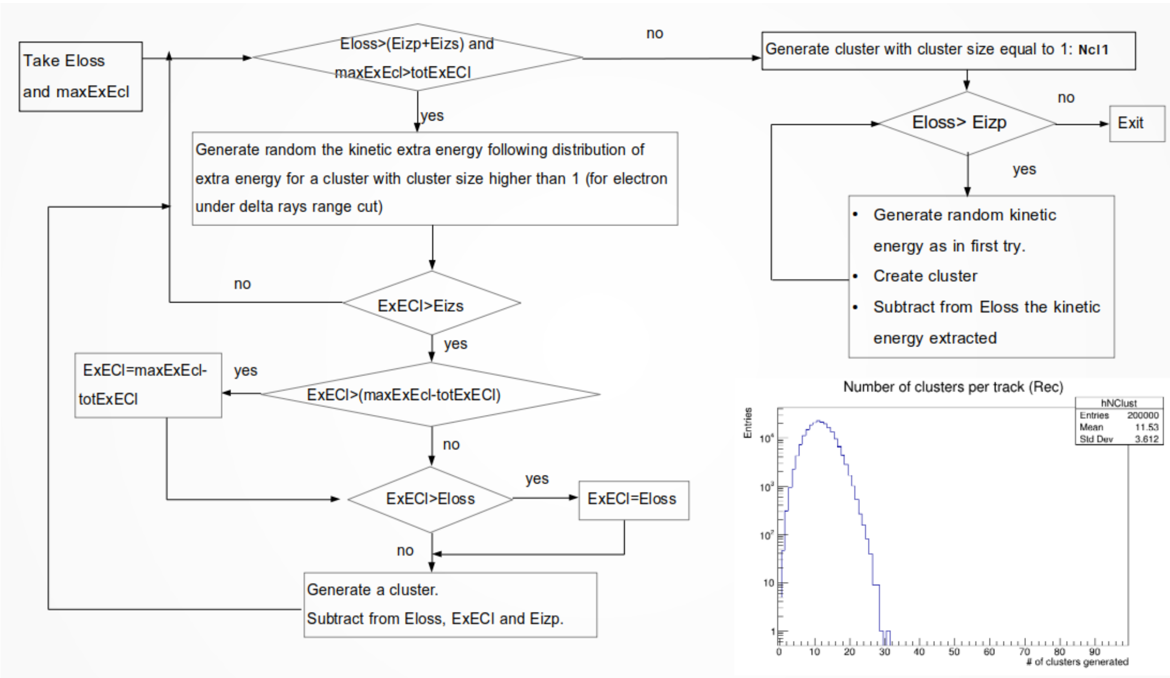

Figure A.1: Workflow for the first algorithm implementation.

The second algorithm (similar to the previous), during the generation of clusters with cluster size higher than 1, assigns the kinetic energy to them, choosing the best over five extractions that makes the total kinetic energy for cluster with cluster size higher than 1 better approximating the *maxExEcl*.

A.2.1 The evaluation of the cluster size

The evaluation of the cluster size has been implemented by studying the relation between extra energy (kinetic energy) and cluster size for clusters with cluster size higher than 1 (delta rays are included). In Figure A.2 an example of the correlations plots between the extra energy and the cluster size are presented.

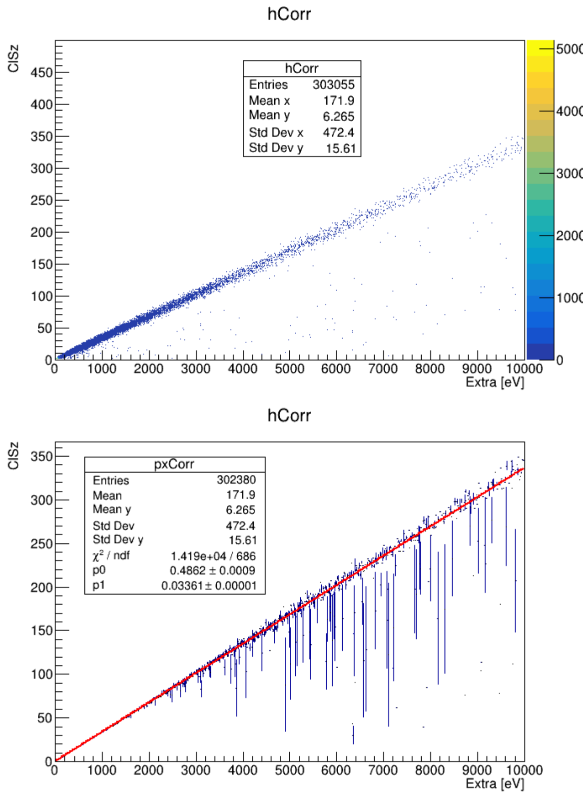

Figure A.2: Relation between extra energy and cluster size for clusters with cluster size higher than 1.

The correlation trend has been fitted with a first degree polynomial. To evaluate the cluster size for clusters with more than one electron, the dispersion for 10 different slices of extra energy up to delta rays cut range (1000 eV) has been studied with the following relation:

$$(ExEcl \times p1 + p0) - ClSz \tag{A.1}$$

The Figure A.3 shows an example of a slice of the extra energy between 900 and 1000 eV.

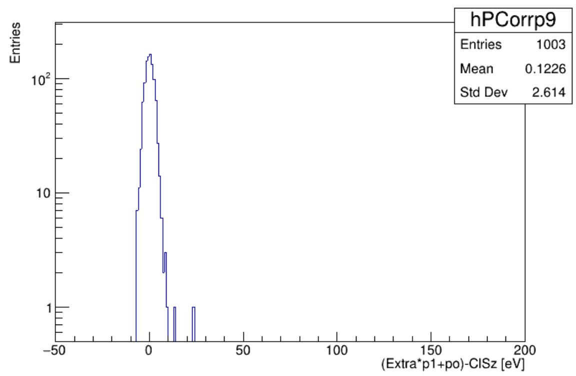

Figure A.3: Example for extra energy between 900 and 1000 eV.

So that, the cluster size is evaluated as :

$$(ExEcl * p1 + p0) - RndExtr \tag{A.2}$$

where RndExtr represent a random extraction from the 10 correlation plot slices. Same evaluation is performed for cluster size generated by delta rays.
The dispersion for different slice of extra energy above the value of delta rays cut range (1000 eV) has been studied by following the same relation (A.1). The Figure A.4 shows a example for extra energy between 9 and 10 keV. At the end, the cluster size is evaluated with the same

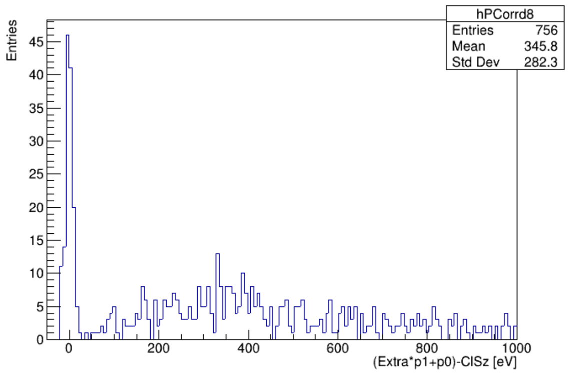

Figure A.4: Example for extra energy between 9 and 10 keV.

relation (A.2).
The second algorithm (similar to the previous), during the generation of clusters with cluster size higher than one, assigns the kinetic energy to them, choosing the best over five extractions that makes the total kinetic energy for cluster with cluster size higher than one approximating better the maxExEcl. To correct a systematic underestimation of the mean number of clusters, an additional correction to the residual energy for generating cluster with clusters size equal to one can be used. The workflow is like the one for the first algorithm.

A.3 The third algorithm

The third algorithm follows a different methodology. Indeed it uses the total kinetic energy of the event to evaluate *a priori* the number of clusters, applying the most likelihood *criterium*. The workflow for this algorithm is illustrated in Figures A.5, A.6, A.7.

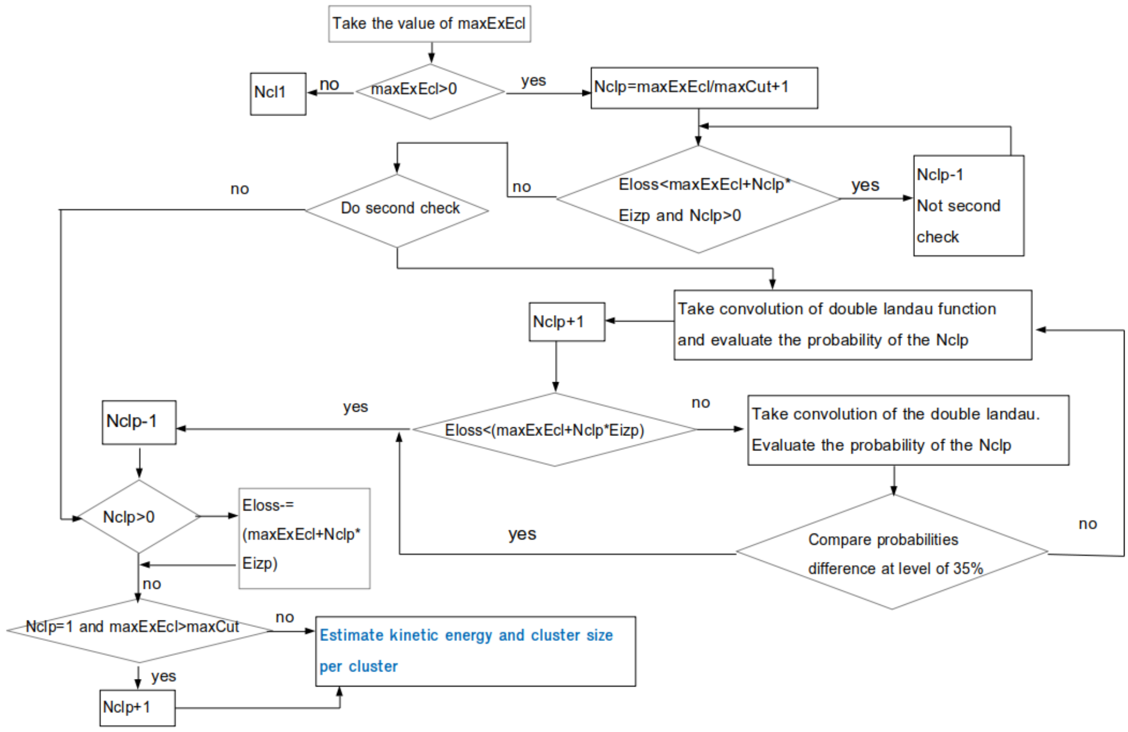

Figure A.5: Workflow for the third algorithm implementation.

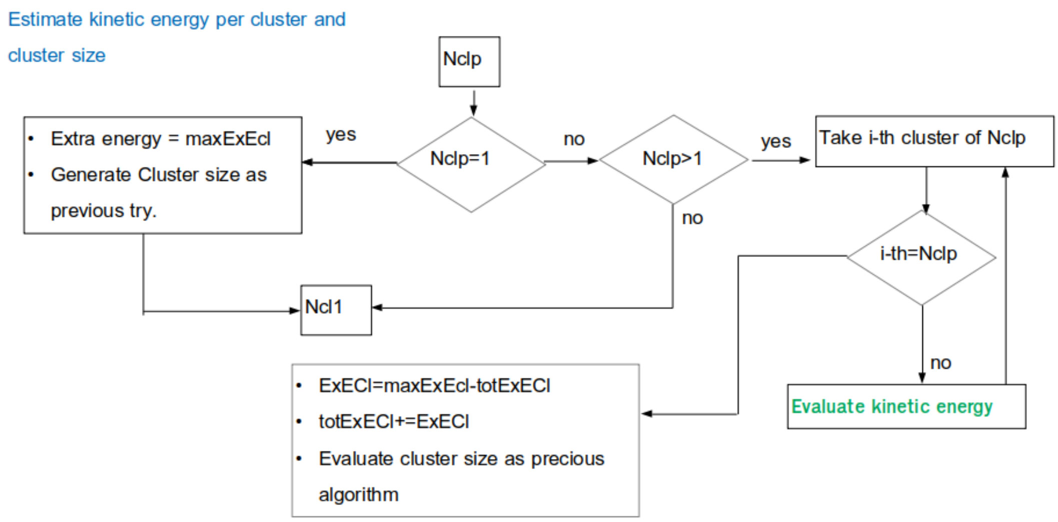

Figure A.6: Workflow for the third algorithm implementation: details on the procedure to estimate the kinetic energy per cluster and cluster size.

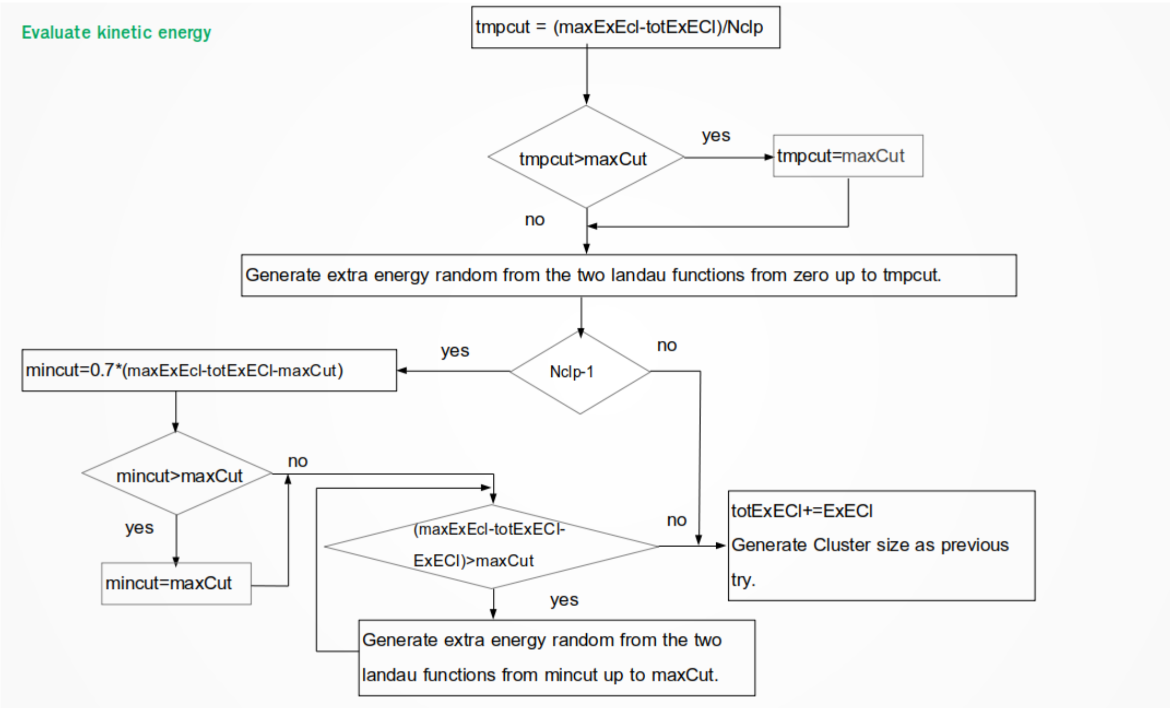

Figure A.7: Workflow for the third algorithm implementation: details on the procedure to evaluate kinetic energy.

Appendix B

The Kalman Filter algorithm

In the GENFIT package[1], the KF algorithm and its extension algorithms like Deterministic Annealing Filter are available for the track fitting.
The key of the algorithm is to use both the estimation from the physics model (the positron's interaction among the materials with the gradient magnetic field) and measurement from the detectors. The KF starts from a certain state vector called seed, which is the starting point of the recursive steps. It plays a key role in the tracking performance since a wrong initial state results in a wrong estimation. The state vector at the next step (or plane) is estimated from the previous state and its physics models, for example the extrapolation from the previous plane to the next plane. Then the estimated state and the measured state are combined with the factor called Kalman gain. After that the updated (combined) state is used for the next estimation step and these steps are repeated.
This appendix describes in details the Kalman filter operation.

B.1 Kalman Filter (KF)formalism

The KF is a progressive fitting algorithm commonly used to fit tracks in particle spectrometers. It provides better performance with respect to global minimization algorithms in presence of materials and non-homogeneous magnetic fields.
The states of the positron tracks at each point can be expressed by the five parameters (one for the momentum, two for the direction, and two for the position) in GENFIT [134]:

$$\vec{x_k} = \left[\frac{q}{|\vec{p}|}, \frac{du}{dw}, \frac{dv}{dw}, u, v\right]^T \tag{B.1}$$

where k is the index of the measurement (hit index in the track),$\vec{x_k}$ is the state of k-th measurement, q is the particle charge, p is the momentum. u, v, w are the coordinates system on the detector plane defined in the GENFIT, as shown in Figure B.1.

[1] GENFIT is a generic toolkit for track reconstruction for experiments in particle and nuclear physics [134]

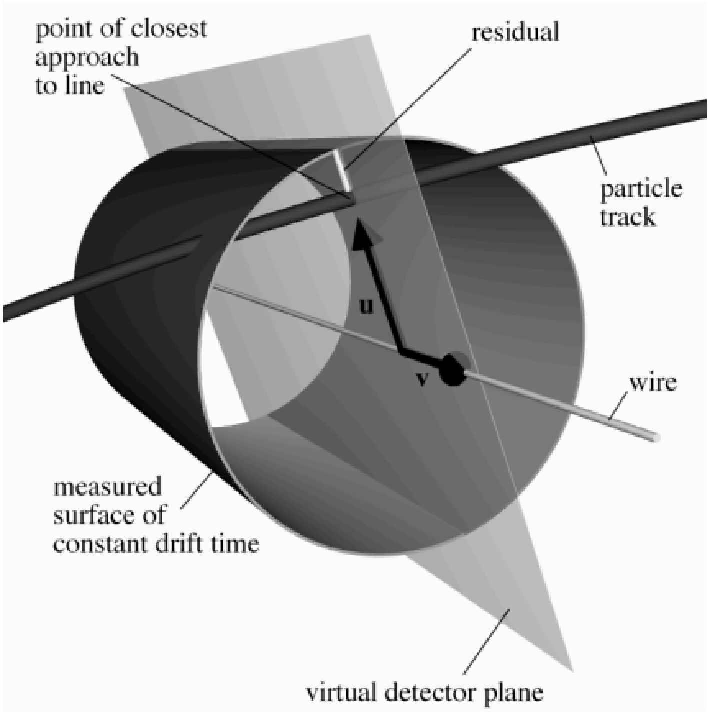

Figure B.1: The coordinate system of the wire measurement in GENFIT [134].

The k-h state of the positron track is estimated by using the information of the (k - 1)-th state:

$$\vec{x_k} = f_{k-1}(\vec{x_{k-1}}) + \vec{w}_{k-1} \tag{B.2}$$

where f_{k-1} is a transport matrix from the (k - 1)-th state to the k-th state, $\vec{w}_{k-1}$ the white noise [2]. The measurement state,$\vec{m_k}$, can be described with the projection matrix Hk:

$$\vec{m_k} = H_k\vec{x_k} + \vec{\epsilon_k} \tag{B.3}$$

where the $\vec{\epsilon_k}$ is the measurement uncertainty. The contribution of the multiple scattering, bremsstrahlung, and the other stochastic processes are taken into account in $\vec{w}_{k-1}$. The KF algorithm performs two steps recursively: "prediction step" with the mathematical model and "update step" with the measurement information. The schematics is described in Figure B.2. This recursive characteristics is suitable for the particle tracking: the k-th state include all the information up to the k - 1-th state.

[2]The KF algorithm assumes the linear dynamic system, but the particle representation under the magnetic field is not a linear system. In this case, the system equation is approximated by a linear function with the Taylor expansion. This extended algorithm to the non-linear system is called "Extended Kalman Filter".

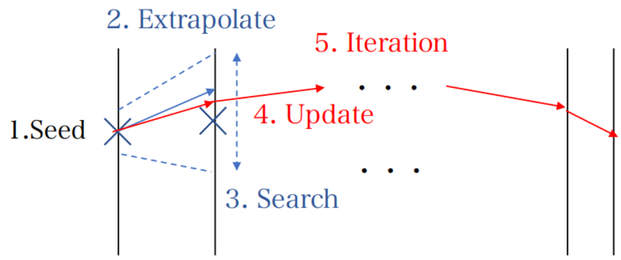

Figure B.2: The sketch of KF algorithm.

The prediction step estimates the k-th state from the k - 1-th state which already includes all of the information untill the k - 1-th measurement and described as $x_{k-1|k-1}$. The predicted state,$\vec{x}_{k|k-1}$, and its covariance, $C_{k|k-1}$, are calculated as following:

$$\vec{x}_{k|k-1} = f_{k-1}(x_{k-1|k-1}) \tag{B.4}$$

$$C_{k|k-1} = f_{k-1}C_{k-1|k-1}f_{k-1}^T + Q_{k-1} \tag{B.5}$$

where the Q_{k-1} is the covariance matrix of $\vec{w}_{k-1}$.
Then the predicted state is updated to $\vec{x}_{k|k}$ and the covariance to $C_{k|k}$ with the information of the k-th measurement:

$$\vec{x}_{k|k} = \vec{x}_{k|k-1}K_k[\vec{m_k} - H_k\vec{x}_{k|k-1}] \tag{B.6}$$

$$C_{k|k} = [I_k - K_kH_k]C_{k|k-1} \tag{B.7}$$

where K_k is the Kalman Gain matrix, which determines the best weight for the measurement and the prediction:

$$K_k = C_{k|k-1}H_k^T[H_kC_{k|k-1}H_k^T + V_k]^{-1} \tag{B.8}$$

where V_k is the covariance matrix of $\vec{\epsilon_k}$.
The crucial information for the positron tracking comes from the calculation of the χ^2 for the track. The χ^2 value at each point, after the updated step, χ_k^2, is evaluated as following:

$$\chi_k^2 = \vec{r}_{k|k}^T R_{k|k}^{-1}\vec{r}_{k|k} \tag{B.9}$$

The $\vec{r}_{k|k}$ is the residual of the state vector after the k-th update step, $R_{k|k}$ is the residual of the covariance matrix:

$$\vec{r}_{k|k} = \vec{m_k} - H_k\vec{x}_{k|k} \tag{B.10}$$

$$R_{k|k} = V_k - H_kC_{k|k}H_k^T \tag{B.11}$$

The χ^2 of the positron track is obtained by the sum of χ_k^2 at each step. After completing the iteration to the final state, the KF performs the same iteration from the last state to the first state (backward steps). This process is called the "smoothing step". The weight for the smoothing step at k-th state, A_k, is described as following:

$$A_k = C_{k|k}F_k^TC^-1_{k+1|k} \tag{B.12}$$

After the smoothing step, the state, covariance matrix, and residuals can be calculated as following, respectively:

$$\vec{x_{k|n}} = \vec{x}_{k|k} + A_k[x_{k+1|n} - x_{k+1|k}] \tag{B.13}$$

$$C_{k|n} = C_{k|k} A_k [C_{k+1|n} - C_{k+1|k}] A_k^T \tag{B.14}$$

$$\vec{r}_{k|n} = \vec{m_k} - H_k \vec{x_{k|n}} \tag{B.15}$$

$$R_{k|n} = Vk - H_k C_{k|n} H_k^T \tag{B.16}$$

B.2 Deterministic Annealing Filter (DAF)

The Deterministic Annealing Filter or DAF [135] is the extension of the Kalman Filter algorithm to avoid the wrong measurement assignment in the same layer. As an example, a single CDCH hit has two competing hits in the same layer: a "left-measurement" and a "right-measurement" and only one of both is the true one.

The concept of the DAF is to use the predicted residuals of the measurement for the re-weighted observations. The prolongation part is actually identical to the KF case, but the assignment probabilities of all competing measurements can be computed in every layer. Assume that there are n_k measurements in the layer k and their index is written with i, like $\vec{m}_k^i (i = 1 ... n_k)$. The prediction $\vec{x}_{k|k-1}$ is updated with the observation, $\vec{m}_k^i$, with the assignment probability of p_k^i:

$$\vec{x}_{k|k} = \vec{x}_{k|k-1} + K_k \sum_{i=1}^{n_k} [p_k^i [\vec{m}_k - H_k \vec{x}_{k|k-1}]] \tag{B.17}$$

To allow the zero-weights of the measurements, the Kalman gain matrix has to be written in terms of inverse covariance (or weight matrix):

$$K_k = [C_{k|k-1}^{-1} + p_k H_k^T V^{-1} 1_k H_k]^{-1} H_k^T + V_k^{-1} \tag{B.18}$$

where p_k is the sum of all weights p_k^i. The covariance matrix of the updated state is defined as:

$$C_{k|k} [C_{k|k-1}^{-1} + p_k H_k^T V_k^{-1} H_k] \tag{B.19}$$

After the smoothing step, the prediction $x_{k|n}^*$ using all the measurementS except the ones at the k-th layer can be obtained along with its covariance matrix $C_{k|n}^*$. By using this prediction and covariance matrix, the assignment probabilities of the measurements can be computed as following:

$$p_k^i \propto \phi(\vec{m}_k^i; H_k \vec{x}_{k|n}^*, Vk + H_k C^* k|n H_k^T) \tag{B.20}$$

where ϕ(measurement;mean,covariance)means the multivariate gaussian probability function. A simpler formula could be obtained if the covariance matrix after the smoothing step is neglected:

$$p_k^i \propto \phi(\vec{m}_k^i; H_k \vec{x}_{k|n}^*, Vk + H_k C^* k|n H_k^T) \equiv \phi_k^i \tag{B.21}$$

the V_k is replaced with TV_k, where T is the parameter to control the global optimization of the assignment probabilities and called “temperature”. Practically, the weights are normalized as following:

$$p_k^{i*} = \frac{\phi_k^i}{\Lambda(T, \lambda) + \sum_{j=0}^{n_k} \phi_k^j} \tag{B.22}$$

where λ is the parameter which defines the cut-off value. The meaning of the temperature is illustrated in Figure B.3: the algorithm starts from the high temperature, resulting in the similar weights for all measurements, then the updated step is iterated at the lower temperature, and finally, the assignments will be frozen out.

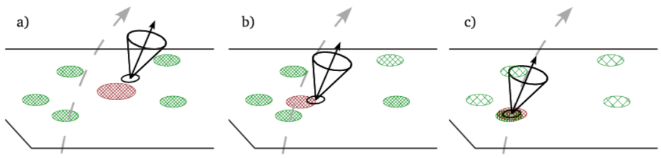

Figure B.3: Illustration of the probability assignment with deterministic annealing filter [136]. (a) The algorithm starts with high temperature and all measurements (green circles) in the same layer have the similar weight. (b) At the lower temperature, the measurements far from the estimate obtain the lower assignment probabilities. (c) Finally, the assignments are frozen out.

Acknowledgments

I would like to express my sincere gratitude to my supervisors: dr. Giovanni Francesco Tassielli, prof. Marco Panareo, dr. Francesco Grancagnolo and prof. Nicola De Filippis.
Then I would like to thank MEG, FCC and CEPC collaborations, in particular dr. Francesco Renga, dr. Fedor Ignatov, dr. Atsushi Oya, Dylan Palo for their support.
I am also grateful to Alessandro Miccoli, Alessandro Corvaglia and Gianluigi Chiarello for their feedback sessions and moral support.
In the end, I would be remiss in not mentioning my family, especially my parents, my partner, my beloved brother and all my friends and colleagues. Their belief in me has kept my spirits and motivation high during this process.

"The fact that we live at the bottom of a deep gravity well, on the surface of a gas covered planet going around a nuclear fireball 90 million miles away and think this to be normal is obviously some indication of how skewed our perspective tends to be."
Douglas Adams

«***Allons-y***»

Bibliography

[1] J. Ellis, "Outstanding questions: Physics beyond the Standard Model," *Phil. Trans. Roy. Soc. Lond.*, vol. A370, pp. 818–830, 2012.

[2] F. Jegerlehner, "The hierarchy problem and the cosmological constant problem revisited," *Foundations of Physics*, pp. 1–57, 2019.

[3] A. Mazumdar, "The origin of dark matter, matter-anti-matter asymmetry, and inflation," 06 2011.

[4] S. F. King, A. Merle, S. Morisi, Y. Shimizu, and M. Tanimoto, "Neutrino mass and mixing: from theory to experiment," *New Journal of Physics*, vol. 16, p. 045018, apr 2014.

[5] J.-P. Uzan, "Inflation in the standard cosmological model," *Comptes Rendus Physique*, vol. 16, no. 10, pp. 875–890, 2015.

[6] F. J. Yndurain, *The Theory of Quark and Gluon Interactions*. Theoretical and Mathematical Physics, Berlin, Germany: Springer, 2006.

[7] S. L. Glashow, "Partial-symmetries of weak interactions," *Nuclear Physics*, vol. 22, no. 4, pp. 579–588, 1961.

[8] S. Weinberg, "A Model of Leptons," *Phys. Rev. Lett.*, vol. 19, pp. 1264–1266, 1967.

[9] C. N. Yang and R. L. Mills, "Conservation of isotopic spin and isotopic gauge invariance," *Phys. Rev.*, vol. 96, pp. 191–195, Oct 1954.

[10] O. Nachtmann, *Elementary Particle Physics, Concepts and Phenomena*. Springer-Verlag Berlin Heidelberg, 1990.

[11] F. Englert and R. Brout, "Broken Symmetry and the Mass of Gauge Vector Mesons," *Phys. Rev. Lett.*, vol. 13, pp. 321–323, 1964.

[12] P. W. Higgs, "Broken Symmetries and the Masses of Gauge Bosons," *Phys. Rev. Lett.*, vol. 13, pp. 508–509, 1964.

[13] G. S. Guralnik, C. R. Hagen, and T. W. B. Kibble, "Global Conservation Laws and Massless Particles," *Phys. Rev. Lett.*, vol. 13, pp. 585–587, 1964.

[14] L. Cadamuro, "Search for Higgs boson pair production in the $b\bar{b}\tau^+\tau^-$ decay channel with the CMS detector at the LHC. Recherche de la production de paires de bosons de Higgs dans le canal de désintégration $b\bar{b}\tau^+\tau^-$ avec le détecteur CMS auprès du LHC," 2017. Presented 05 Oct 2017.

[15] P. Williams, "Naturalness, the autonomy of scales, and the 125gev higgs," *Studies in History and Philosophy of Science Part B: Studies in History and Philosophy of Modern Physics*, vol. 51, pp. 82–96, 2015.

[16] G. L. Kane and M. A. Shifman, "Introduction to 'The supersymmetric world: The Beginnings of the theory'," *arXiv*, 2001.

[17] R. Mohapatra, "Supersymmetry and r-parity: an overview," *Physica Scripta*, vol. 90, 08 2015.

[18] A. Cohen, D. Kaplan, and A. Nelson, "The more minimal supersymmetric standard model," *Physics Letters B*, vol. 388, no. 3, pp. 588–598, 1996.

[19] D. Croon, T. E. Gonzalo, L. Graf, N. Košnik, and G. White, "GUT Physics in the Era of the LHC," *Frontiers in Physics*, vol. 7, 2019.

[20] E. R. Paudel, "Problems of standard model, review," *BMC Journal of Scientific Research*, vol. 4, Dec. 2021.

[21] S. Raby, *Supersymmetric Grand Unified Theories: From Quarks to Strings via SUSY GUTs*, vol. 939. Springer, 2017.

[22] A. Pérez-Lorenzana, "An introduction to extra dimensions," *Journal of Physics: Conference Series*, vol. 18, p. 224, jan 2005.

[23] K. Becker, M. Becker, and J. Schwarz, *String Theory and M-Theory: A Modern Introduction.* Cambridge University Press, 2006.

[24] A. M. Baldini *et al.*, "Search for the lepton flavour violating decay $\mu^+ \to \mathrm{e}^+\gamma$ with the full dataset of the MEG experiment," *Eur. Phys. J. C*, vol. 76, no. 8, p. 434, 2016.

[25] U. Bellgardt and other, "Search for the decay $\mu^+ \to e^+e^+e^-$," *Nuclear Physics B*, vol. 299, no. 1, pp. 1–6, 1988.

[26] P. Wintz, "Status of muon electron conversion at PSI," in *Joint U.S. Japan Workshop on New Initiatives in Muon Lepton Flavor Violation and Neutrino Oscillation with High Intense Muon and Neutrino Sources*, pp. 72–79, 10 2000.

[27] L. Willmann *et al.*, "New bounds from searching for muonium to anti-muonium conversion," *Phys. Rev. Lett.*, vol. 82, pp. 49–52, 1999.

[28] B. Aubert *et al.*, "Searches for Lepton Flavor Violation in the Decays $\tau \longrightarrow e\gamma$ and $\tau \longrightarrow \mu\gamma$," *Phys. Rev. Lett.*, vol. 104, p. 021802, 2010.

[29] K. Hayasaka *et al.*, "Search for Lepton Flavor Violating Tau Decays into Three Leptons with 719 Million Produced Tau+Tau- Pairs," *Phys. Lett. B*, vol. 687, pp. 139–143, 2010.

[30] E. Abouzaid *et al.*, "Search for lepton-flavor-violating decays of the neutral kaon," *Physical Review Letters*, vol. 100, apr 2008.

[31] D. Ambrose *et al.*, "New limit on muon and electron lepton number violation from $K_0^L \longrightarrow \mu^{pm}e^{mp}$ decay," *Phys. Rev. Lett.*, vol. 81, pp. 5734–5737, 1998.

[32] A. Sher *et al.*, "Improved upper limit on the decay $k^+ \longrightarrow \pi^+\mu^+e^-$," *Physical Review D*, vol. 72, 07 2005.

[33] ATLAS Collaboration, "Search for the charged-lepton-flavor-violating decay $Z \rightarrow e\mu$ in pp collisions at $\sqrt{s} = 13$ TeV with the ATLAS detector," 2022.

[34] R. Akers *et al.*, "A Search for lepton flavor violating Z0 decays," *Z. Phys. C*, vol. 67, pp. 555–564, 1995.

[35] P. Abreu *et al.*, "Search for lepton flavor number violating Z0 decays," *Z. Phys. C*, vol. 73, pp. 243–251, 1997.

[36] L. Calibbi and G. Signorelli, "Charged Lepton Flavour Violation: An Experimental and Theoretical Introduction," *Riv. Nuovo Cim.*, vol. 41, no. 2, pp. 71–174, 2018.

[37] N. Cabibbo, "Unitary Symmetry and Leptonic Decays," *Phys. Rev. Lett.*, vol. 10, pp. 531–533, 1963.

[38] M. Kobayashi and T. Maskawa, "CP Violation in the Renormalizable Theory of Weak Interaction," *Prog. Theor. Phys.*, vol. 49, pp. 652–657, 1973.

[39] Z. Maki, M. Nakagawa, and S. Sakata, "Remarks on the unified model of elementary particles," *Prog. Theor. Phys.*, vol. 28, pp. 870–880, 1962.

[40] B. Pontecorvo, "Inverse beta processes and nonconservation of lepton charge," *Zh. Eksp. Teor. Fiz.*, vol. 34, p. 247, 1957.

[41] R. L. Workman and Others, "Review of Particle Physics," *PTEP*, vol. 2022, p. 083C01, 2022.

[42] R. Bernstein and P. S. Cooper, "Charged lepton flavor violation: An experimenter's guide," *Physics Reports*, vol. 532, pp. 27–64, nov 2013.

[43] A. de Gouvêa and P. Vogel, "Lepton flavor and number conservation, and physics beyond the standard model," *Progress in Particle and Nuclear Physics*, vol. 71, pp. 75–92, jul 2013.

[44] Y. Amhis *et al.*, "Averages of b-hadron, c-hadron, τ -lepton properties as of summer 2016," *The European Physical Journal C*, vol. 77, dec 2017.

[45] E. P. Hincks and B. Pontecorvo, "Search for gamma-radiation in the 2.2-microsecond meson decay process," *Phys. Rev.*, vol. 73, pp. 257–258, 1948.

[46] T. Kinoshita and A. Sirlin, "Polarization of electrons in muon decay with general parity-nonconserving interactions," *Phys. Rev.*, vol. 108, pp. 844–850, Nov 1957.

[47] C. Bouchiat and L. Michel, "Theory of μ-meson decay with the hypothesis of nonconservation of parity," *Phys. Rev.*, vol. 106, pp. 170–172, Apr 1957.

[48] Papa, Angela, "Charged lepton flavour violation searches at the Paul Scherrer Institut: Status of the MEGII and Mu3e experiments," *EPJ Web Conf.*, vol. 179, p. 01018, 2018.

[49] Y. Kuno and Y. Okada, "Muon decay and physics beyond the standard model," *Rev. Mod. Phys.*, vol. 73, pp. 151–202, 2001.

[50] F. Cei and D. Nicolo, "Lepton flavour violation experiments," *Advances in High Energy Physics*, vol. 2014, pp. 1–31, 03 2014.

[51] A. Gando *et al.*, "Constraints on θ_{12} from a three-flavor oscillation analysis of reactor antineutrinos at KamLAND," *Physical Review D*, vol. 83, mar 2011.

[52] R. Barbieri and L. Hall, "Signals for supersymmetric unification," *Physics Letters B*, vol. 338, pp. 212–218, oct 1994.

[53] J. Hisano, T. Moroi, K. Tobe, and M. Yamaguchi, "Exact event rates of lepton flavor violating processes in supersymmetric SU(5) model," *Phys. Lett. B*, vol. 391, pp. 341–350, 1997.

[54] R. Barbieri, L. Hall, and A. Strumia, "Violations of lepton flavour and CP in supersymmetric unified theories," *Nuclear Physics B*, vol. 445, pp. 219–251, jul 1995.

[55] A. Abada *et al.*, "FCC Physics Opportunities: Future Circular Collider Conceptual Design Report Volume 1," Tech. Rep. 6, 2019.

[56] M. Benedikt *et al.*, "FCC-ee: The Lepton Collider: Future Circular Collider Conceptual Design Report Volume 2. Future Circular Collider," tech. rep., CERN, Geneva, Dec 2018.

[57] The CEPC Study Group, "CEPC Conceptual Design Report: Volume 1 - Accelerator," tech. rep., 2018.

[58] T. C. S. Group, "CEPC Conceptual Design Report: Volume 2 - Physics and Detector," tech. rep., 2018.

[59] X. Lou, M. Boscolo, and F. Zimmermann, "Status of the e^+e^- Collider Projects in Asia and Europe: CEPC and FCC-ee," *JACoW*, vol. IPAC2022, p. TUIZSP1, 2022.

[60] P. Azzurri, G. Bernardi, S. Braibant, D. d'Enterria, J. Eysermans, P. Janot, A. Li, and E. Perez, "A special higgs challenge: measuring the mass and production cross section with ultimate precision at FCC-ee," *The European Physical Journal Plus*, vol. 137, dec 2021.

[61] P. F. Monni and G. Zanderighi, "QCD at the FCC-ee," *Eur. Phys. J. Plus*, vol. 136, no. 11, p. 1162, 2021.

[62] P. Janot, "Top-quark electroweak couplings at the FCC-ee. Top-quark electroweak couplings at the FCC-ee," *JHEP*, vol. 04, p. 182. 16 p, Mar 2015.

[63] A. Blondel and P. Janot, "FCC-ee overview: new opportunities create new challenges," 2021.

[64] T. Lesiak, "Flavour Physics at the FCC-ee," *Acta Phys. Polon. B*, vol. 49, pp. 1241–1246, 2018.

[65] C. W. Fabjan and H. Schopper, eds., *Particle Physics Reference Library: Volume 2: Detectors for Particles and Radiation*. Cham: Springer Nature, 2020.

[66] G. F. Knoll, *Radiation detection and measurement; 4th ed.* New York, NY: Wiley, 2010.

[67] W. Blum, W. Riegler, and L. Rolandi, *Particle detection with drift chambers; 2nd ed.* Berlin: Springer, 2008.

[68] A. Walenta, J. Fischer, H. Okuno, and C. Wang, "Measurement of the ionization loss in the region of relativistic rise for noble and molecular gases," *Nuclear Instruments and Methods*, vol. 161, no. 1, pp. 45–58, 1979.

[69] G.Charpak and F.Sauli, "Multiwire proportional chambers and drift chambers," *Nuclear Instruments and Methods*, no. 162, pp. 405–428, 1979.

[70] J. J. Lowke and J. H. Parker, "Theory of electron diffusion parallel to electric fields. ii. application to real gases," *Phys. Rev.*, vol. 181, pp. 302–311, May 1969.

[71] T. Ferbel, *Experimental techniques in high-energy nuclear and particle physics; 2nd ed.* Singapore: World Scientific, 1991.

[72] A. Breskin, G. Charpak, F. Sauli, M. Atkinson, and G. Schultz, "Recent observations and measurements with high-accuracy drift chambers," *Nuclear Instruments and Methods*, vol. 124, no. 1, pp. 189–214, 1975.

[73] W. Farr, J. Heintze, K. Hellenbrand, and A. Walenta, "Space resolution of drift chambers operated at high gas pressure," *Nuclear Instruments and Methods*, vol. 154, no. 1, pp. 175–181, 1978.

[74] C. Fronsdal and H. Überall, "μ-meson decay with inner bremsstrahlung," *Phys. Rev.*, vol. 113, pp. 654–657, Jan 1959.

[75] A. Baldini, F. Cei, C. Cerri, S. Dussoni, L. Galli, M. Grassi, D. Nicolo, F. Raffaelli, F. Sergiampietri, G. Signorelli, F. Tenchini, D. Bagliani, M. De Gerone, F. Gatti, E. Baracchini, Y. Fujii, T. Iwamoto, D. Kaneko, T. Mori, and N. Kuchinksy, "MEG Upgrade Proposal," 01 2013.

[76] J. Adam *et al.*, "The MEG detector for $\mu \to e^+\gamma$ decay search," *The European Physical Journal C*, vol. 73, apr 2013.

[77] W. Wagner, M. Seidel, E. Morenzoni, F. Groeschel, M. Wohlmuther, and M. Daum, "PSI status 2008—Developments at the 590MeV proton accelerator facility," *Nuclear Instruments and Methods in Physics Research Section A: Accelerators, Spectrometers, Detectors and Associated Equipment*, vol. 600, no. 1, pp. 5–7, 2009.

[78] J. Adam *et al.*, "New constraint on the existence of the $\mu^+ \to e^+\gamma$ decay," *Phys. Rev. Lett.*, vol. 110, p. 201801, 2013.

[79] A. Baldini *et al.*, "The design of the MEG II experiment," *The European Physical Journal C*, 01 2018.

[80] G. Cavoto, G. Chiarello, M. Hildebrandt, A. Hofer, K. Ieki, M. Meucci, S. Milana, V. Pettinacci, F. Renga, and C. Voena, "A photogrammetric method for target monitoring inside the MEG II detector," *Review of Scientific Instruments*, vol. 92, no. 4, p. 043707, 2021.

[81] P. W. Cattaneo *et al.*, "Development and commissioning of the 30 ps time resolution meg ii pixelated timing detector," *Nuclear Instruments and Methods in Physics Research Section A: Accelerators, Spectrometers, Detectors and Associated Equipment*, vol. 936, 09 2018.

[82] M. D. Gerone *et al.*, "Development and commissioning of the timing counter for the MEG experiment," *IEEE Transactions on Nuclear Science*, vol. 59, pp. 379–388, apr 2012.

[83] G. Boca, P. Cattaneo, M. De Gerone, F. Gatti, M. Nakao, M. Nishimura, W. Ootani, M. Rossella, Y. Uchiyama, M. Usami, and K. Yanai, "Timing resolution of a plastic scintillator counter read out by radiation damaged sipms connected in series," *Nuclear Instruments and Methods in Physics Research Section A: Accelerators, Spectrometers, Detectors and Associated Equipment*, vol. 999, p. 165173, 2021.

[84] R. Sawada, "Performance of liquid xenon gamma ray detector for meg," *Nuclear Instruments and Methods in Physics Research Section A: Accelerators, Spectrometers, Detectors and Associated Equipment*, vol. 623, no. 1, pp. 258–260, 2010. 1st International Conference on Technology and Instrumentation in Particle Physics.

[85] S. Ogawa, "Liquid Xenon calorimeter for MEG II experiment with VUV-sensitive MPPCs," *Nuclear Instruments and Methods in Physics Research Section A: Accelerators, Spectrometers, Detectors and Associated Equipment*, vol. 845, pp. 528–532, 2017. Proceedings of the Vienna Conference on Instrumentation 2016.

[86] A. Baldini *et al.*, "The Search for $\mu^+ \longrightarrow e^+\gamma$ with 10^{-14} Sensitivity: The Upgrade of the MEG Experiment," *Symmetry*, vol. 13, p. 1591, 08 2021.

[87] L. Galli *et al.*, "Wavedaq: An highly integrated trigger and data acquisition system," *Nuclear Instruments and Methods in Physics Research Section A: Accelerators, Spectrometers, Detectors and Associated Equipment*, vol. 936, pp. 399–400, 2019. Frontier Detectors for Frontier Physics: 14th Pisa Meeting on Advanced Detectors.

[88] S. Ritt, R. Dinapoli, and U. Hartmann, "Application of the DRS chip for fast waveform digitizing," *Nuclear Instruments and Methods in Physics Research Section A: Accelerators, Spectrometers, Detectors and Associated Equipment*, vol. 623, no. 1, pp. 486–488, 2010. 1st International Conference on Technology and Instrumentation in Particle Physics.

[89] M. Chiappini *et al.*, "The new drift chamber of the MEG II experiment," *Nuclear Instruments and Methods in Physics Research Section A: Accelerators, Spectrometers, Detectors and Associated Equipment*, vol. 936, pp. 501–502, 2019. Frontier Detectors for Frontier Physics: 14th Pisa Meeting on Advanced Detectors.

[90] A. Baldini *et al.*, "A new cylindrical drift chamber for the MEG II experiment," *Nuclear Instruments and Methods in Physics Research Section A: Accelerators, Spectrometers, Detectors and Associated Equipment*, vol. 824, pp. 589–591, 2016. Frontier Detectors for Frontier Physics: Proceedings of the 13th Pisa Meeting on Advanced Detectors.

[91] G. Tassielli *et al.*, "The drift chamber of the MEG II experiment," *Journal of Instrumentation*, vol. 15, pp. C09051–C09051, 09 2020.

[92] M. Cascella, F. Grancagnolo, and G. Tassielli, "Cluster counting/timing techniques for drift chambers," *Nuclear Physics B - Proceedings Supplements*, vol. 248-250, pp. 127–130, 2014. 1st Conference on Charged Lepton Flavor Violation.

[93] A. Ferrari, "The kloe drift chamber," *Nuclear Instruments and Methods in Physics Research Section A: Accelerators, Spectrometers, Detectors and Associated Equipment*, vol. 494, no. 1, pp. 163–172, 2002. Proceedings of the 8th International Conference on Instrumentatio n for Colliding Beam Physics.

[94] A. Baldini *et al.*, "Single-hit resolution measurement with meg ii drift chamber prototypes," *Journal of Instrumentation*, vol. 11, pp. P07011–P07011, jul 2016.

[95] G. Cataldi, F. Grancagnolo, and S. Spagnolo, "Cluster counting in helium based gas mixtures," *Nuclear Instruments and Methods in Physics Research Section A: Accelerators, Spectrometers, Detectors and Associated Equipment*, vol. 386, no. 2, pp. 458–469, 1997.

[96] A. Baldini, G. Cavoto, F. Cei, M. Chiappini, G. Chiarello, A. Corvaglia, M. Francesconi, L. Galli, F. Grancagnolo, M. Grassi, M. Hildebrandt, M. Meucci, A. Miccoli, D. Nicoló, A. Papa, M. Panareo, C. Pinto, F. Raffaelli, F. Renga, G. Signorelli, G. Tassielli, and C. Voena, "The ultra light drift chamber of the meg ii experiment," *Nuclear Instruments and Methods in Physics Research Section A: Accelerators, Spectrometers, Detectors and Associated Equipment*, vol. 958, p. 162152, 2020. Proceedings of the Vienna Conference on Instrumentation 2019.

[97] G. Chiarello *et al.*, "The construction technique of the new meg ii tracker," *Nuclear Instruments and Methods in Physics Research Section A: Accelerators, Spectrometers, Detectors and Associated Equipment*, vol. 936, pp. 495–496, 2019. Frontier Detectors for Frontier Physics: 14th Pisa Meeting on Advanced Detectors.

[98] R. Assiro *et al.*, "Assembly techniques for ultra-low mass drift chambers," *Nuclear Physics B - Proceedings Supplements*, vol. 248-250, pp. 124–126, 2014. 1st Conference on Charged Lepton Flavor Violation.

[99] G. Chiarello *et al.*, "The full stereo drift chamber for the MEG II experiment," *Journal of Instrumentation*, vol. 12, pp. C03062–C03062, 03 2017.

[100] M. Panareo *et al.*, "The front end electronics for the drift chamber readout in MEG experiment upgrade," *JINST*, vol. 15, no. 07, p. C07009, 2020.

[101] A. Baldini *et al.*, "Gas distribution and monitoring for the drift chamber of the meg-ii experiment," *Journal of Instrumentation*, vol. 13, 04 2018.

[102] A. Baldini *et al.*, "Detailed analysis of chemical corrosion of ultra-thin wires used in drift chamber detectors," *Journal of Instrumentation*, vol. 16, p. T12003, 12 2021.

[103] M. Chiappini *et al.*, "Commissioning of the MEG II tracker system," *Journal of Instrumentation*, vol. 15, pp. C06056–C06056, jun 2020.

[104] F. Cuna, G. Chiarello, A. Corvaglia, N. D. Filippis, F. Grancagnolo, M. Manta, I. Margjeka, A. Miccoli, M. Panareo, and G. Tassielli, "A 10^{-3} drift velocity monitoring chamber," *Journal of Instrumentation*, vol. 15, pp. C09007–C09007, sep 2020.

[105] P. Bernardini, G. Fiore, R. Gerardi, F. Grancagnolo, U. von Hagel, F. Monittola, V. Nassisi, C. Pinto, L. Pastore, and M. Primavera, "Precise measurements of drift velocities in helium gas mixtures," *Nuclear Instruments and Methods in Physics Research Section A: Accelerators, Spectrometers, Detectors and Associated Equipment*, vol. 355, no. 2, pp. 428–433, 1995.

[106] V. Golovatyuk, F. Grancagnolo, and R. Perrino, "Influence of oxygen and moisture content on electron life time in helium–isobutane gas mixtures," *Nuclear Instruments and Methods in Physics Research Section A: Accelerators, Spectrometers, Detectors and Associated Equipment*, vol. 461, no. 1, pp. 77–79, 2001. 8th Pisa Meeting on Advanced Detectors.

[107] F. Cuna, G. Chiarello, A. Miccoli, A. Corvaglia, N. D. Filippis, E. Gorini, F. Grancagnolo, M. Panareo, M. Primavera, G. Tassielli, and A. Ventura, "A 10^{-3} drift velocity monitoring chamber for the MEG II experiment," *Nuclear Instruments and Methods in Physics Research Section A: Accelerators, Spectrometers, Detectors and Associated Equipment*, vol. 1046, p. 167737, 2023.

[108] P. DeVries, P. DeVries, and J. Hasbun, *A First Course in Computational Physics*. Jones & Bartlett Learning, 2011.

[109] T. Kinoshita and A. Sirlin, "Radiative corrections to fermi interactions," *Phys. Rev.*, vol. 113, pp. 1652–1660, Mar 1959.

[110] M. Antonello, "IDEA: A detector concept for future leptonic colliders," *Nuovo Cimento C*, vol. 43, p. 27. 6 p, 2020.

[111] P. Azzi and E. Perez, "Exploring requirements and detector solutions for FCC-ee," 2021.

[112] G. Gaudio, "The IDEA detector concept for FCCee," *PoS*, vol. ICHEP2022, p. 337, 11 2022.

[113] M. Keil, "Upgrade of the ALICE Inner Tracking System," *JINST*, vol. 10, p. C03012. 11 p, 2015.

[114] M. Mager, "Alpide, the monolithic active pixel sensor for the alice its upgrade," *Nuclear Instruments and Methods in Physics Research Section A: Accelerators, Spectrometers, Detectors and Associated Equipment*, vol. 824, pp. 434–438, 2016. Frontier Detectors for Frontier Physics: Proceedings of the 13th Pisa Meeting on Advanced Detectors.

[115] G. Aglieri Rinella, "The alpide pixel sensor chip for the upgrade of the alice inner tracking system," *Nuclear Instruments and Methods in Physics Research Section A: Accelerators, Spectrometers, Detectors and Associated Equipment*, vol. 845, pp. 583–587, 2017. Proceedings of the Vienna Conference on Instrumentation 2016.

[116] G. Bencivenni, R. D. Oliveira, G. Morello, and M. P. Lener, "The micro-resistive WELL detector: a compact spark-protected single amplification-stage MPGD," *Journal of Instrumentation*, vol. 10, pp. P02008–P02008, feb 2015.

[117] N. Akchurin, F. Bedeschi, A. Cardini, M. Cascella, F. Cei, D. De Pedis, R. Ferrari, S. Fracchia, S. Franchino, M. Fraternali, G. Gaudio, P. Genova, J. Hauptman, L. La Rotonda, S. Lee, M. Livan, E. Meoni, A. Moggi, D. Pinci, A. Policicchio, J. G. Saraiva, F. Scuri, A. Sill, T. Venturelli, and R. Wigmans, "The electromagnetic performance of the RD52 fiber calorimeter," *Nucl. Instrum. Methods Phys. Res., A*, vol. 735, pp. 130–144. 15 p, 2014.

[118] L. Pezzotti and A. Villa, "IDEA Dual-Readout Calorimeter Simulation," *PoS*, vol. EPS-HEP2021, p. 777, 2022.

[119] I. Pezzotti, H. Newman, J. Freeman, J. Hirschauer, R. Ferrari, G. Gaudio, G. Polesello, R. Santoro, M. Lucchini, S. Giagu, F. Bedeschi, S. Lee, P. Harris, C. Tully, A. Jung, N. Akchurin, A. Belloni, S. Eno, J. Qian, B. Zhou, J. Zhu, J. S. H. Lee, I. Vivarelli, R. Hirosky, and H. Yoo, "Dual-readout calorimetry for future experiments probing fundamental physics," 2022.

[120] S. Braibant and P. Giacomelli, "Muon detection at FCC-ee," *Eur. Phys. J. Plus*, vol. 136, no. 11, p. 1143, 2021.

[121] F. Cuna *et al.*, "A proposal of a He based Drift Chamber as central tracker for the IDEA detector concept for a future e^+e^- collider," *PoS*, vol. EPS-HEP2021, p. 786, 2022.

[122] G. F. Tassielli, "A proposal of a drift chamber for the IDEA experiment for a future e^+e^- collider," *PoS*, vol. ICHEP2020, p. 877, 2021.

[123] F. Cuna *et al.*, "Simulation of particle identification with the cluster counting technique," in *International Workshop on Future Linear Colliders*, 5 2021.

[124] F. Grancagnolo *et al.*, "Drift chamber for the CMD-3 detector," *Nucl. Instrum. Meth. A*, vol. 623, pp. 114–116, 2010.

[125] M. Passera, W. J. Martiano, A. Sirlin, P. Ko, and D. Ki Hong, "The muon g-2 discrepancy: errors or new physics?," *AIP Conference Proceedings*, 2008.

[126] G. W. Bennett, B. Bousquet, H. N. Brown, G. Bunce, R. M. Carey, P. Cushman, G. T. Danby, P. T. Debevec, M. Deile, H. Deng, and et al., "Measurement of the negative muon anomalous magnetic moment to 0.7 ppm," *Physical Review Letters*, vol. 92, Apr 2004.

[127] F. Cuna *et al.*, "The central tracker of SCTF and CMD3 detectors," *Nucl. Instrum. Meth. A*, vol. 1040, p. 167229, 2022.

[128] A. Barnyakov, "The project of the Super Charm-Tau Factory in Novosibirsk," *Journal of Physics: Conference Series*, vol. 1561, p. 012004, jun 2020.

[129] F. Cuna, G. Chiarello, A. Miccoli, A. Corvaglia, N. De Filippis, E. Gorini, F. Grancagnolo, M. Panareo, M. Primavera, G. Tassielli, and A. Ventura, "The Central Tracker of the CMD3 detector," *Nuclear Instruments and Methods in Physics Research Section A: Accelerators, Spectrometers, Detectors and Associated Equipment*, vol. 1045, p. 167655, 2023.

[130] C. Lippmann, "Particle identification," *Nuclear Instruments and Methods in Physics Research Section A: Accelerators, Spectrometers, Detectors and Associated Equipment*, vol. 666, pp. 148–172, feb 2012.

[131] F. Cuna *et al.*, "Particle identification with the cluster counting technique for the IDEA drift chamber," *PoS*, vol. ICHEP2022, p. 335, 2022.

[132] C. Caputo, G. Chiarello, A. Corvaglia, F. Cuna, B. D'Anzi, N. D. Filippis, W. Elmetenawee, E. Gorini, F. Grancagnolo, M. Greco, S. Gribanov, K. Johnson, M. Maggi, A. Miccoli, M. Panareo, A. Popov, M. Primavera, A. Taliercio, G. Tassielli, A. Ventura, and S. Xin, "Particle identification with the cluster counting technique for the idea drift chamber," *Nuclear Instruments and Methods in Physics Research Section A: Accelerators, Spectrometers, Detectors and Associated Equipment*, p. 167969, 2022.

[133] S. Ritt, "The DRS chip: cheap waveform digitizing in the GHz range," *Nuclear Instruments and Methods in Physics Research Section A: Accelerators, Spectrometers, Detectors and Associated Equipment*, vol. 518, no. 1, pp. 470–471, 2004. Frontier Detectors for Frontier Physics: Proceedin.

[134] C. Höppner, S. Neubert, B. Ketzer, and S. Paul, "A novel generic framework for track fitting in complex detector systems," *Nuclear Instruments and Methods in Physics Research Section A: Accelerators, Spectrometers, Detectors and Associated Equipment*, vol. 620, no. 2, pp. 518–525, 2010.

[135] R. Frühwirth and A. Strandlie, "Track fitting with ambiguities and noise: A study of elastic tracking and nonlinear filters," *Computer Physics Communications*, vol. 120, no. 2, pp. 197–214, 1999.

[136] S. Fleischmann, *Track reconstruction in the ATLAS experiment: The deterministic annealing filter*. PhD thesis, Wuppertal U., 2006.